VOLUME 76 AUGUST 3, 1972 NUMBER 16

JPCHAx

THE JOURNAL OF PHYSICAL CHEMISTRY

PUBLISHED BIWEEKLY BY THE AMERICAN CHEMICAL SOCIETY

THE JOURNAL OF

PHYSICAL CHEMISTRY

AMERICAN CHEMICAL SOCIETY, *1155 Sixteenth St., N.W., Washington, D. C. 20036*

Books and Journals Division
JOHN K CRUM, *Director*
JOSEPH H. KUNEY, *Head, Business Operations Department*
RUTH REYNARD, *Assistant to the Director*

 Published biweekly by the American Chemical Society at 20th and Northampton Sts., Easton, Pa. 18042. Second-class postage paid at Washington, D. C., and at additional mailing offices.

All manuscripts should be sent to *The Journal of Physical Chemistry*, Department of Chemistry, University of Minnesota, Minneapolis, Minn. 55455.

Additions and Corrections are published once yearly in the final issue. See Volume 75, Number 26 for the proper form.

Extensive or unusual alterations in an article after it has been set in type are made at the author's expense, and it is understood that by requesting such alterations the author agrees to defray the cost thereof.

The American Chemical Society and the Editor of *The Journal of Physical Chemistry* assume no responsibility for the statements and opinions advanced by contributors.

Correspondence regarding accepted copy, proofs, and reprints should be directed to Editorial Production Office, American Chemical Society, 20th and Northampton Sts., Easton, Pa. 18042. Manager: CHARLES R. BERTSCH. Assistant Editor: EDWARD A. BORGER. Editorial Assistant: JOSEPH E. YURVATI.

Advertising Office: Centcom, Ltd. (formerly Century Communications Corporation), 142 East Avenue, Norwalk, Conn. 06851.

Business and Subscription Information

Remittances and orders for subscriptions and for single copies, notices of changes of address and new professional connections, and claims for missing numbers should be sent to the Subscription Service Department, American Chemical Society, 1155 Sixteenth St., N.W., Washington, D. C. 20036. Allow 4 weeks for changes of address. Please include an old address label with the notification.

Claims for missing numbers will not be allowed (1) if received more than sixty days from date of issue, (2) if loss was due to failure of notice of change of address to be received before the date specified in the preceding paragraph, or (3) if the reason for the claim is "missing from files."

Subscription rates (1972): members of the American Chemical Society, $20.00 for 1 year; to nonmembers, $60.00 for 1 year. Those interested in becoming members should write to the Admissions Department, American Chemical Society, 1155 Sixteenth St., N.W., Washington, D. C. 20036. Postage to Canada and countries in the Pan-American Union, $5.00; all other countries, $6.00. Single copies for current year: $3.00. Rates for back issues from Volume 56 to date are available from the Special Issues Sales Department, 1155 Sixteenth St., N.W., Washington, D. C. 20036.

This publication and the other ACS periodical publications are now available on microfilm. For information write to: MICROFILM, Special Issues Sales Department, 1155 Sixteenth St., N.W., Washington, D. C. 20036.

Notice to Authors last printed in the issue of June 22, 1972

THE JOURNAL OF

PHYSICAL CHEMISTRY

Volume 76, Number 16 August 3, 1972

JPCHAx 76(16) 2187–2342 (1972)

COMMUNICATIONS TO THE EDITOR

AUTHOR INDEX

In papers with more than one author the name of the author to whom inquiries about the paper should be addressed is marked with an asterisk in the by-line.

ANNOUNCEMENT

On the last two pages of this issue you will find reproduced the table of contents of the July 1972 issue of the *Journal of Chemical and Engineering Data.*

THE JOURNAL OF
PHYSICAL CHEMISTRY

VOLUME 76, NUMBER 16 AUGUST 3, 1972

Unimolecular Processes Subsequent to Recoil Tritium Reactions with Spiropentane[1]

by Y. Y. Su and Yi-Noo Tang*

Department of Chemistry, Texas A&M University, College Station, Texas 77843 *(Received August 16, 1971)*

Publication costs assisted by the U. S. Atomic Energy Commission

Spiropentane-*t* molecules, excited by the T*-for-H substitution, underwent unimolecular processes by two different routes: one is direct decomposition to C_2H_3T and allene-*t* while the other is a consecutive isomerization–decomposition reaction which proceeds through its isomer, methylenecyclobutane, to give the same end products. The unimolecular nature of the decomposition was verified by pressure studies from 100 to 1500 Torr. The C_3H_3T/C_2H_3T ratios from these samples were all approximately equal to 1.0. According to the reaction mechanism, this means the RRKM postulate of energy randomization before decomposition is a useful approximation for the recoil tritium excited systems at the employed pressure range.

The major interest of the present work lies in the hot atom excitation studies of spiropentane[2,3] and the search for possible energy nonrandomization in its unimolecular decomposition. Spiropentane, when excited, is known either to decompose to ethylene and allene as in (1) or to isomerize to methylenecyclobutane as in (2).[4,5] Flowers and Frey[4] have studied the thermal decomposition of spiropentane in a temperature range of 360–410° and a pressure range of 25–350 Torr and have measured the activation energy for (2) to be 57.57 kcal/mol with an A factor of $10^{15.68}$. They have

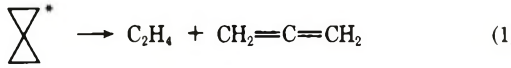

(1)


(2)

observed that (1) is much slower than (2) and has a higher energy of activation. On the other hand, Burkhardt[5] has studied the same processes at a much lower pressure range and has observed much higher yields of C_2H_4 and C_3H_4, especially at the lowest employed pressures. This points to a conclusion that (1) is the lower energy process. One of the purposes of this work is to examine the dilemma and to see how the recoil tritium excitation results will fit into the picture.

The decomposition of spiropentane initiated by recoil tritium substitution will also furnish information about the extent of energy randomization before unimolecular reactions. The kinetic model proposed by Rice, Ramsperger, Kassel, and Marcus (RRKM) for unimolecular reactions postulates that intramolecular transfer of energy between vibrational degrees of freedom is very rapid compared to the rate of reaction,[6] while on the other hand, Slater assumes that the former process is slow.[7]

(1) Presented in part at the 160th National Meeting of the American Chemical Society, Chicago, Ill., Sept 1970.

(2) For recoil tritium reactions, see, for example, R. Wolfgang, *Progr. React. Kinet.*, **3**, 97 (1965); *Ann. Rev. Phys. Chem.*, **16**, 15 (1965).

(3) For hot atom excitation studies, see, for example, F. S. Rowland, "Proceedings of the International School of Physics, 'Enrico Fermi' Course XLIV—Molecular Beam and Reaction Kinetics," Ch. Schlier, Ed., Academic Press, New York, N. Y., 1970.

(4) M. C. Flowers and H. M. Frey, *J. Chem. Soc.*, 5550 (1960).

(5) P. J. Burkhardt, "The Kinetics of the Thermal Decomposition of Spiropentane and Methylenecyclobutane," Ph.D. Dissertation, University of Oregon, 1962.

Among several early reports, probably the most convincing experimental supports for the RRKM model were performed by Butler and Kistiakowsky[8] and by Harrington, Rabinovitch, and Frey.[9] They employed different chemical reactions to produce either excited methylcyclopropane molecules (BK) or excited *sec*-butyl radicals (HRF) with different distributions of excitation energy, but a change in the distribution of the isomerization products or a variation in the rate of decomposition was not observed in either one of the above two cases. Recently, Rynbrandt and Rabinovitch[10] have produced chemically symmetrical, vibrationally excited hexafluorobicyclopropyl-d_2 by the addition of either CH_2 or CD_2 to the corresponding compounds, and have followed its unimolecular decomposition by using the D-atom tracers to distinguish the two rings. Their results, at a pressure less than 100 Torr, indicate conclusions similar to the previous reports.[10a] However, a failure of complete energy randomization was observed at higher pressures.[10b]

A symmetrical distribution of energy in initially unsymmetrically excited spiropentane to give the isomerization product methylenecyclobutane was recently confirmed by Doering, Gilbert, and Leermakers.[11] In the present work, we would like to report a similar study on the energy randomization process for the unimolecular decomposition of spiropentane to ethylene and allene excited by the recoil tritium excitation method. Since hot atom substitution deposits larger amounts of localized energy than that encountered in the previous work,[11] it will be of interest to find out whether nonrandomized decomposition can be observed in the present spiropentane system.

An indication about energy randomization in recoil tritium excitation studies has been previously obtained from the isopropyl chloride system.[3,12] However, the experimental uncertainty introduced by the position-isomer separation and other complications renders it less conclusive than the present spiropentane case.

Experimental Section

These experiments were carried out by the usual techniques employed in studying recoil tritium reactions.[13] High energy tritium atoms were produced by the reactions $^3He(n,p)^3H$ in the gas phase and $^6Li(n,\alpha)^3H$ in the heterogeneous liquid–solid system. Gas samples containing ^3He, spiropentane, and other additives were prepared with a high vacuum system and then sealed in a Pyrex 1720 bulb. Oxygen was normally employed as a scavenger. Bromine and iodine were also employed in several samples to observe the scavenged species. For the high pressure samples, either CO or CF_4 were used as pressure builders. For liquid samples the components were condensed onto LiF at the bottom of a capillary tube. DPPH and I_2 were used as liquid phase scavengers; as I_2 adds to C=C bonds, it complicated the system. These samples were irradiated at the Texas A&M University Nuclear Center Research Reactor with a neutron flux of 1×10^{12} neutrons cm^{-2} sec^{-1} for 5 and 15 min for gas sample and liquid sample, respectively.

The analyses of tritium-labeled products after irradiation were performed by radio gas chromatography.[14] The analyses were made primarily on the following two columns: (1) 50-ft DMS: 35% dimethylsulfolane on 30–60 mesh firebrick, for separation of total hydrocarbons and operated at room temperature (25°). The products were (H_2 + CH_4 + C_2H_4), acetylene, allene, methylacetylene, spiropentane, and methylenecyclobutane. (2) 50-ft PCA: 9.6% propylene carbonate on 30–50 mesh activated alumina, for separation of lightest hydrocarbons and operated at 0°. The products were H_2, CH_4, acetylene, allene, and methylacetylene.

Spiropentane was obtained from the Chemical Sample Co. with less than 0.5% impurity, confirmed by gas chromatography. Helium-3 with a tritium content of less than 2×10^{-11}% was obtained from Monsanto Research Corp. Matheson CP grade CO and CF_4 were used.

Results

Pressure Dependence of Products from Recoil Tritium Reactions with Spiropentane. The primary reactions expected from recoil tritium reactions with spiropentane are as shown below. However, the spiropentane-*t*

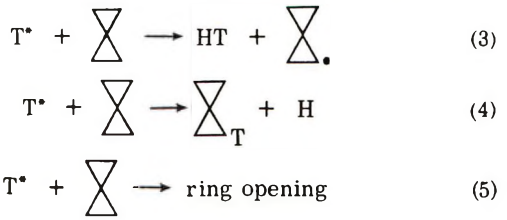

molecules from (4) may have enough excitation energy to undergo unimolecular decomposition or isomerization processes analogous to (1) and (2) to yield C_2H_3T, C_3H_3T, or methylenecyclobutane-*t*. To verify the

(6) See, for example, (a) I. Amdur and G. G. Hammes, "Chemical Kinetics: Principles and Selected Topics," McGraw-Hill, New York, N. Y., 1967; (b) B. S. Rabinovitch and D. W. Setser, *Advan. Photochem.*, **3**, 1 (1964).

(7) N. B. Slater, "Theory of Unimolecular Reactions," Cornell University Press, Ithaca, N. Y., 1959.

(8) J. N. Butler and G. B. Kistiakowsky, *J. Amer. Chem. Soc.*, **82**, 759 (1960).

(9) R. E. Harrington, B. S. Rabinovitch, and H. M. Frey, *J. Chem. Phys.*, **33**, 1271 (1960).

(10) (a) J. D. Rynbrandt and B. S. Rabinovitch, *ibid.*, **54**, 2275 (1971); (b) J. D. Rynbrandt and B. S. Rabinovitch, *J. Phys. Chem.*, **74**, 4175 (1970); **75**, 2164 (1971).

(11) W. Von E. Doering, J. C. Gilbert, and P. A. Leermakers, *Tetrahedron*, **24**, 6863 (1968).

(12) Y.-N. Tang and F. S. Rowland, *J. Phys. Chem.*, **72**, 707 (1968).

(13) See, for example, Y.-N. Tang, Ph.D. Dissertation, University of Kansas, 1964.

(14) J. K. Lee, E. K. C. Lee, B. Musgrave, Y.-N. Tang, J. W. Root, and F. S. Rowland, *Anal. Chem.*, **34**, 741 (1962).

Table I: Relative Yields of Products from Recoil Tritium Reactions with Spiropentane

	Gas pressure, Torr					
Spiropentane	50	64	150	108	190	252
O_2	22	28	52	91	97	52
^3He	7	10	20	32	31	28
	Total pressure					
	79	102	222	231	318	332
	Relative Yields[a]					
HT	1000	1000	1000	1000	1000	1000
C_2H_3T	313 ± 3	295 ± 2	270 ± 1	274 ± 1	261 ± 1	260 ± 2
Allene-*t*	258 ± 2	233 ± 1	225 ± 2	224 ± 2	225 ± 2	205 ± 2
Propyne-*t*	66 ± 25	54 ± 30	45 ± 20	43 ± 8	52 ± 25	60 ± 20
Spiropentane-*t*	589 ± 5	568 ± 2	630 ± 3	649 ± 3	691 ± 1	663 ± 4
Methylenecyclobutane-*t*	NM[b]	34 ± 2	44 ± 2	35 ± 1	NM[b]	42 ± 1
C_3H_3T/C_2H_3T	1.04 ± 0.08	0.97 ± 0.10	1.00 ± 0.07	0.97 ± 0.03	1.06 ± 0.09	1.02 ± 0.08

[a] Yields relative to HT as 1000. [b] NM = not measured.

unimolecular nature for the formation of these products, a pressure study was carried out. The HT yield from (3) should be pressure independent and therefore serve as a good internal standard for comparison.[15] Data in Table I reveal that spiropentane-*t*, the stabilization product, increases, while the decomposition products such as C_2H_3T and allene-*t* decrease with increasing pressure.

All the samples included in Table I are extremely well-scavenged. As a result, products expected from (5), the ring-opening process, are completely removed while they are free radicals. For the samples listed in Table I, the only unexpected products observed are a minor yield of C_2HT and trace amounts of CH_3T and propene-*t*.

Sources of Propyne-t. As indicated in Table I, not only allene-*t*, but also propyne-*t* was observed. The latter might be formed either directly by some processes in the system or from the isomerization of the former *via* one of the following three routes: (1) isomerization from allene-*t* formed with enough excitation energies;[16,17] (2) conversion from allene-*t* during irradiation; and (3) conversion from allene-*t* during the storage and/or the sample-transferring period.

There is convincing experimental evidence that the majority of the propyne-*t* yield was derived from allene-*t* *via* route (3). For most of the samples, the second aliquot always showed a higher propyne-*t* yield than the first one, and a complementary relation between propyne-*t* and allene-*t* yields was always found between the two aliquots. In an extreme case, when two aliquots of the same sample were analyzed 6 days apart while stored in a Hg-containing sample break-up tube under room light, the propyne-*t*/allene-*t* ratio changes from 0.16 to 1.4. However, the sum of their yields relative to that of HT was approximately the same for the two aliquots.

The upper limit for the contribution to the propyne-*t* yield by all the other possible routes, direct processes included, amounted to 15% of the total allene-*t* formed as evidenced by the lowest observed propyne-*t* yield from all the analyzed samples. However, the actual contribution from these processes should be much less because it seems to be inevitable even for the sample with a minimum propyne-*t* yield to have certain contribution by the above described third route isomerization.

From the above discussion, it is impossible to deny that a certain amount of propyne-*t* may be formed *via* a direct process and *not* originated from allene-*t*. However, such contribution, if any, at most amounts to a few per cent. Moreover, one of the most likely direct processes for propyne-*t* formation should be

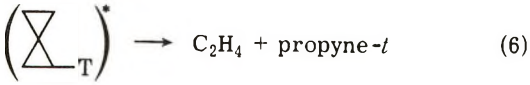

(6)

This means the amount of propyne-*t* formed directly is also a counterpart of the C_2H_3T yield.

Therefore, it seems to be justified to use the sum of the allene-*t* and propyne-*t* yields to evaluate the total C_3H_3T yield when the C_3H_3T/C_2H_3T ratio is calculated. However, it should be kept in mind that the actual C_3H_3T/C_2H_3T ratio might be lower than the calculated one by a few per cent due to the possible formation of propyne-*t* from other sources.

Recoil Tritium Reactions with Spiropentane at High Pressures. The vapor pressure of spiropentane at room temperature is about 0.5 atm. To study the recoil tritium reactions with spiropentane at a pressure higher than that, some additives must be employed. Two different kinds of pressure builders were tried in these experiments—CO and CF_4. In each case, suffi-

(15) Y.-N. Tang, E. K. C. Lee, and F. S. Rowland, *J. Amer. Chem. Soc.*, 86, 1280 (1964).

(16) D. A. Frank-Kamenetskii and V. G. Markovich, *Acta Physiochim. USSR*, 17, 308 (1942).

(17) J. F. Cordes and H. Günzler, *Chem. Ber.*, 92, 1055 (1959).

Table II: Percentage Yields of T-for-H Substitution Products at High Pressures

	Gas pressure, Torr					
Spiropentane	214	224	219	161	161	245
O_2	100	96	74	75	69	70
CO	502	504	0	0	0	0
CF_4	0	0	600	1270	1340	1385
^3He	28	28	20	30	40	35
	Total pressure					
	844	862	913	1536	1610	1735
	Percentage Yields[a]					
C_2H_3T	19.9 ± 0.2	23.0 ± 0.1	19.6 ± 0.4	20.3 ± 1.3	20.4 ± 0.4	15.6 ± 0.1
Allene-*t*	13.9 ± 0.2	16.0 ± 0.2	15.3 ± 0.4	10.9 ± 0.4	12.8 ± 0.4	12.7 ± 0.1
Propyne-*t*	6.1 ± 0.2	6.3 ± 1.3	5.8 ± 0.3	5.9 ± 0.6	5.6 ± 0.2	6.0 ± 0.1
Spiropentane-*t*	57.5 ± 3.0	52.7 ± 0.2	53.9 ± 0.1	60.4 ± 0.6	59.0 ± 0.4	63.8 ± 0.1
Methylenecyclobutane-*t*	2.6 ± 0.2	2.0 ± 0.1	5.4 ± 0.4	2.5 ± 0.3	(2.2)[b]	1.9 ± 0.1
C_3H_3T/C_2H_3T	1.00 ± 0.02	0.97 ± 0.06	1.08 ± 0.03	0.83 ± 0.06	0.90 ± 0.02	1.19 ± 0.01

[a] The sum of all the listed products have a yield of 100%. [b] Assumed to be an average of 2.5 and 1.9%.

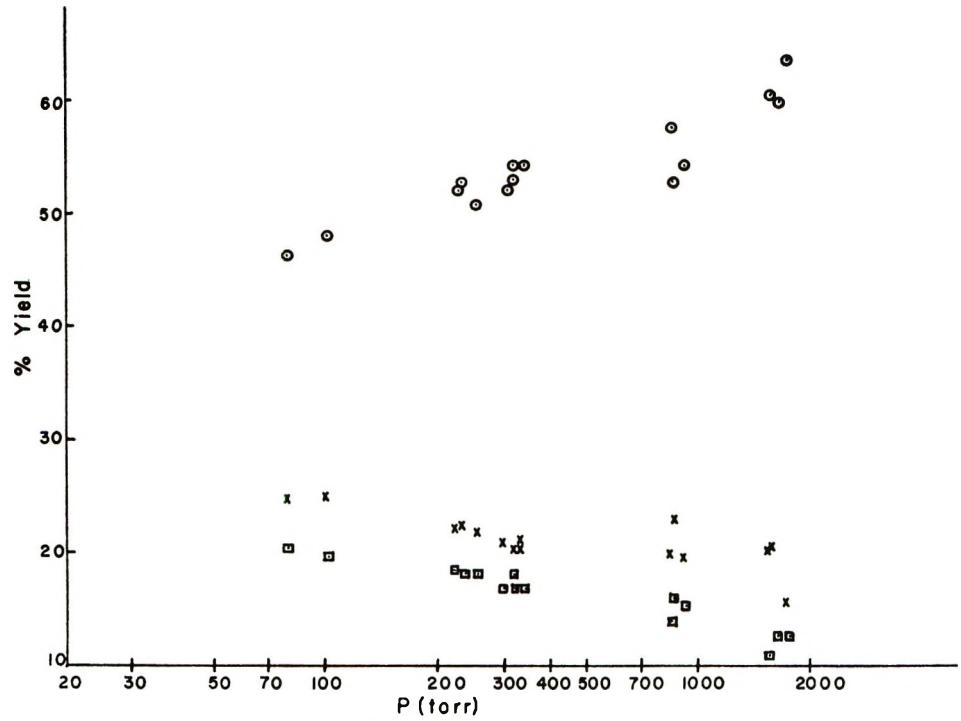

Figure 1. Pressure dependence of stabilization and decomposition products: ⊙, spiropentane-*t*; ×, C_2H_3T; ⊡, allene-*t*.

cient O_2 was added to ensure scavenging. These experiments, as shown in Table II, have been carried out to a maximum pressure of only 1730 Torr because of the technical problem involved in irradiating very high pressure samples with a nuclear reactor. In this table, the percentage yields instead of the relative yields were used, where the sum of all the stabilization, decomposition, and isomerization products were set as 100%. The effect on the product spectrum by the increased pressure is essentially a continuation of that on the samples shown in Table I. The overall pressure effect on the percentage yields of the stabilization product, spiropentane-*t*, and the decomposition products, C_2H_3T and allene-*t*, is illustrated in Figure 1—the former increasing with increasing pressure, while the latter pair decreases.

Data in Figure 1 summarize not only all the results listed in Tables I and II, but also a number of others whose numerical values are not shown in the tables.

Liquid Phase Experiments. For the stabilization of excited products, the liquid phase can be treated as a continuation of the very high pressure gas systems.[15] Both DPPH and I_2 scavenged recoil tritium reactions with spiropentane in the liquid phase have been tried. However, only the former type of scavenged samples are fruitful due to the addition of I_2 to unsaturated

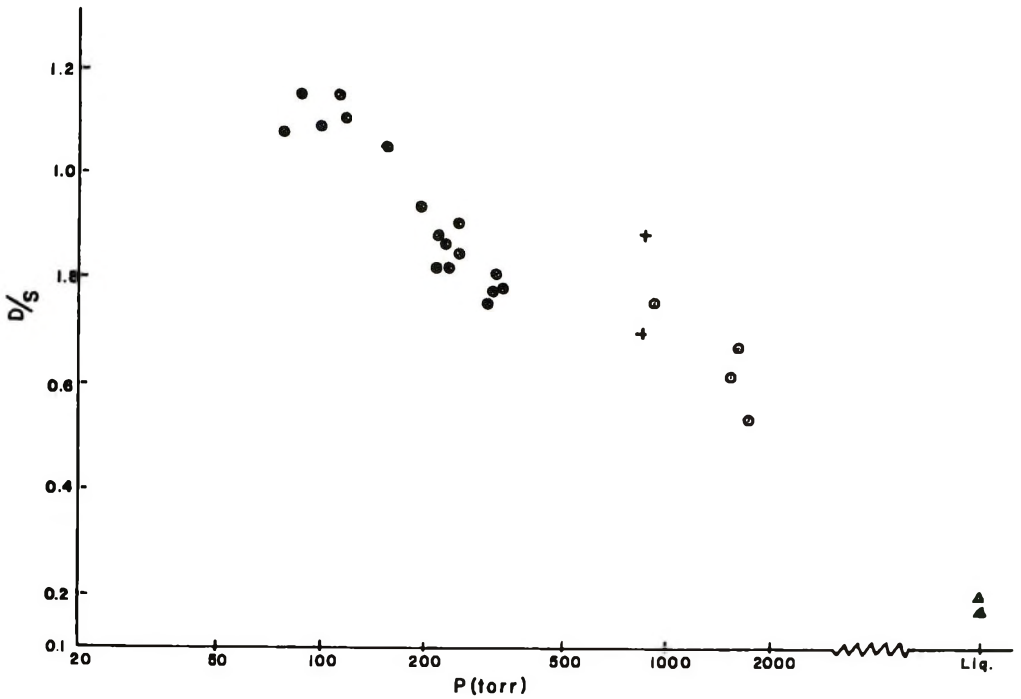

Figure 2. Pressure dependence of the decomposition/stabilization ratio: ⊗, spiropentane–O_2 system; +, spiropentane–O_2–CO system; ⊙, spiropentane–O_2–CF_4 system; Δ, liquid spiropentane–DPPH system.

compounds in the latter type of samples. For the DPPH samples, since scavenging is not necessarily complete in the liquid, spiropentane-*t* instead of HT was chosen as a comparison standard. The yields relative to spiropentane-*t* as 1000 are C_2H_3T, 72 ± 12; allene-*t*, 64 ± 4; propyne-*t*, 52 ± 2; methylenecyclobutane-*t*, 55 ± 12. These results reveal that decomposition and isomerization are insignificant in the liquid.

The C_3H_3T/C_2H_3T ratio from the liquid samples will not be employed in the graph plotting due to the possibility of incomplete scavenging in the system.

In Figure 2, the decomposition/stabilization ratio, (D/S), of all the samples including the liquid ones is plotted as a function of pressure.

Halogen-Scavenged Experiments. Both bromine and iodine scavenged gas samples were tried, but all of them were unfruitful. Besides the problem of their addition to unsaturated bonds, they also reacted directly with spiropentane before or during irradiation to give various halides.

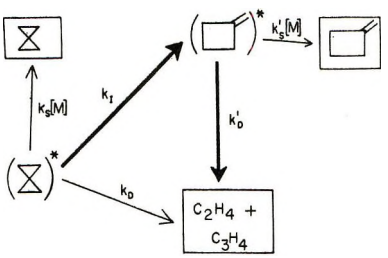

Figure 3. Scheme for excited spriopentane to decompose, isomerize, and be stabilized.

Discussion

Unimolecular Isomerization and Decomposition of Excited Spiropentane. The spiropentane-*t* formed in reaction (4) should have a rather wide energy distribution spectrum with a median energy of about 115 kcal/mol.[18] This should enable unimolecular processes similar to (1) and (2) to take place.

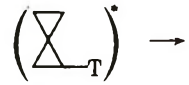

(7)

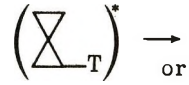

$\rightarrow CH_2 = CHT + CH_2{=}C{=}CH_2$ (8a)

or $CH_2 = CH_2 + CH_2{=}C{=}CHT$ (8b)

As summarized in Table III, the relative percentage of decomposition to C_2H_4 and C_3H_4 and isomerization to methylenecyclobutane from excited spiropentane varied tremendously according to the method and condition of excitation. It ranges from 7% decomposition in Flowers and Frey's thermolysis work[4] to 93% decomposition in our hot atom excitation studies. The other two sets of data presented involve Burkhardt's low pressure thermolysis work[5] and the Hg6($^3P_1$) photosensitization work by De Mare and coworkers.[19] In each of the latter two cases, values at three typical pressures were quoted. It is observed that, for these two systems, the percentage decomposition and isomerization are very sensitive to the total pressure.

(18) E. K. C. Lee and F. S. Rowland, *J. Amer. Chem. Soc.*, **85**, 897 (1963).

(19) G. R. De Mare, L. G. Walker, O. P. Strausz, and H. E. Gunning, *Can. J. Chem.*, **44**, 457 (1966).

Table III: Percentage Yields of Decomposition and Isomerization Processes for Excited Spiropentane

Method of excitation	Conditions	Decomposition, %	Isomerization, %	Reference
Thermal	360°, 25–350 Torr	7	93	Flowers and Frey[4]
	408°, 25–350 Torr	9	91	
	390°, 5.0 Torr	23	77	Burkhardt[5]
	390°, 0.40 Torr	50	50	
	390°, 0.013 Torr	81	19	
Hg6($^3P_1$), photosensitization	50 Torr	80	20	De Mare and coworkers[19]
	160 Torr	50	50	
	300 Torr	26	74	
Recoil tritium excitation	200 Torr	93	7	This work

Scheme of Unimolecular Processes. To explain the large variation of percentage decomposition and percentage isomerization observed in Table III, a scheme for the unimolecular processes for excited spiropentane is proposed and illustrated in Figure 3. The excited parent compound might be stabilized by collision with rate constant k_S or either isomerize or decompose with rate constants k_I and k_D, respectively. On the other hand, the isomerization product, methylenecyclobutane, is also excited and might either be stabilized with rate constant k_S' or decompose according to reaction 9 with a rate constant k_D'.[5,20-22]

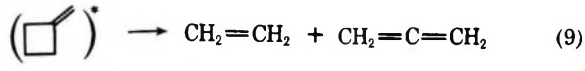

(9)

The reason why the newly formed methylenecyclobutane must be highly excited follows from a thermodynamic consideration of the isomerization process. The heat of formation of spiropentane is 44.25 ± 0.08 kcal/mol,[23] while that of methylenecyclobutane is unknown. However, it can be estimated from the additivity rules by Benson and coworkers[24] and from the heat of formation values and the strain energy values for c-C_3H_8, c-C_4H_{10}, c-C_5H_{12}, methylenecyclopropane, and methylenecyclopentane to be 34.7 ± 3.0 kcal/mol.[25] This gives a heat of reaction for eq 2 as −9.55 ± 3.0 kcal/mol. It means that the initially formed methylenecyclobutane will not only have all the excitation the spiropentane originally possessed, but will be some 10 kcal/mol higher.

Potential Energy Diagram for the Consecutive Unimolecular Decomposition. According to the above discussion, the unimolecular decomposition of spiropentane by the methylenecyclobutane route is actually a consecutive series consisting of (2) followed by (9). The potential energy diagram for this consecutive reaction is shown in Figure 4.

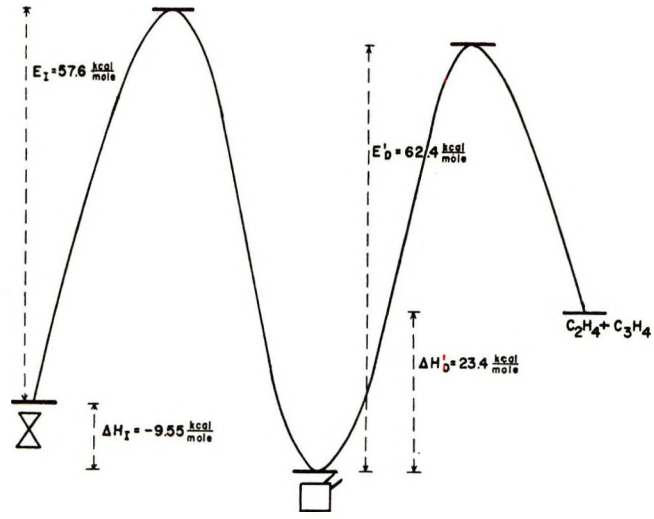

Figure 4. Potential energy diagram for the consecutive unimolecular decomposition of spiropentane.

The activation energies for (2) and (9) are 57.6[4] and 62.4 ± 1.1 kcal/mol,[26] respectively, while the heat of reaction for (9) is +23.4 kcal/mol.[27] From the diagram, it is obvious that any excited spiropentane molecule with enough energy to overcome the barrier for the isomerization step should also have enough energy to overcome the barrier for the follow-up decomposition step unless it is immediately stabilized by collisions.

Clue for the Presence of Direct Decomposition. For the two possible unimolecular processes shown in Figure 3 of excited spiropentane, Flowers and Frey's thermolysis results give definite confirmation only to the isomerization route through the direct observation of methylenecyclobutane.[4] The presence of ethylene and allene in minor amounts does not necessarily confirm the presence of the direct decomposition route because they also may result from the consecutive process. Although the authors have attributed only 4%

(20) R. L. Brandaure, B. Short, and S. M. E. Kellner, *J. Phys. Chem.*, **65**, 2269 (1961).

(21) J. P. Chesick, *ibid.*, **65**, 2170 (1961).

(22) W. von Doering and J. C. Gilbert, *Tetrahedron Suppl.*, **5**, 397 (1966).

(23) J. D. Cox and G. Pilcher, "Thermochemistry of Organic and Organometallic Compounds," Academic Press, New York, N. Y., 1970.

(24) S. W. Benson, *et al.*, *Chem. Rev.*, **69**, 279 (1969).

(25) The strain energies for the following compounds in kilocalories per mole are c-C_3H_6, 27.6; c-C_4H_8, 26.2; c-C_5H_{10}, 6.3; methylenecyclopropane, 40.9; methylenecyclopentane, 6.4. By assuming that the increment in strain energy from c-C_4H_8 to methylenecyclobutane is intermediate between those of the other two pairs, the strain energy of methylenecyclobutane is estimated to be 32.9 kcal/mol. This value, coupled with the heat of formation for the various groups in methylenecyclobutane from ref 24, gives an estimated heat of formation for this compound as 34.7 ± 3.0 kcal/mol.

(26) The activation energy for reaction 9 was evaluated as 61.5 kcal/mol from ref 20 and 63.3 kcal/mol from ref 21. The average of these two values is used here.

(27) From ref 23, the heats of formation values for ethylene and allene are 12.45 and 45.63 kcal/mol, respectively.

of the observed ethylene and allene to the secondary decomposition of methylenecyclobutane,[4] this decomposition route might account for all the observed ethylene and allene if the authors have overlooked the 9.55 kcal/mol exothermicity of reaction 2.[25]

There is no other positive evidence for the occurrence of the direct decomposition of spiropentane to ethylene and allene besides this doubtful one. However, if it does take place, it is surely the higher energy process of the two, because of the limited amount of products detected at lower temperatures.

Low Pressure Thermolysis Results. Burkhardt's low pressure thermolysis results can be explained completely by isomerization–decomposition consecutive processes.[5] As shown on the reaction scheme, the excited methylenecyclobutane molecules can either be stabilized or decompose. At the extremely low pressure range employed by Burkhardt, k_D' becomes much more pronounced in comparison with $k_S'[M]$ because [M] is very small. This explains the high yields of ethylene and allene. The observed pressure dependence of products is also what would have been expected from such a stabilization–decomposition competition. The higher energy direct decomposition process is evidently not responsible for the ethylene and allene formation in this case.

Recoil Tritium Excitation Results. The T-for-H substitution reaction will deposit energies (of a very wide spectrum) with a median at about 115 kcal/mol on the resulting spiropentane molecules.[18] The ones with energy below 57.6 kcal/mol will end up as spiropentane-*t*. The ones with higher energies may be either stabilized as spiropentane-*t* or isomerize to excited methylenecyclobutane-*t* which in turn may either be stabilized or decompose to C_2H_3T and C_3H_3T. The higher the excitation energy, the less chance there will be for preserving methylenecyclobutane-*t*. Moreover, for the ones with high enough energy to overcome the barrier for direct decomposition of spiropentane-*t*, C_2H_3T, and C_3H_3T might be obtained without going through the methylenecyclobutane-*t* route.

A combination of the above described processes at a given pressure will give rise to the observed product pattern at that pressure. The very low yield of methylenecyclobutane-*t* is expected because of the very large amount of energy deposited.

As a result, the observed C_2H_3T and C_3H_3T yields in these recoil tritium experiments probably come from a combination of the two decomposition routes of spiropentane.

Reaction Intermediate. Data shown in Table III on the $Hg6(^3P_1)$ photosensitized reactions of spiropentane are not only similar to the other described systems, but also can be explained on a similar basis when bearing in mind that the amount of excitation is in between the thermal and the recoil excited systems.[19] Since a biradical is definitely involved in this case, it is likely that the decomposition of spiropentane in the other systems also involved biradical intermediates.

The initial step of spiropentane decomposition is generally believed to involve the cleavage of a C–C bond to give such a biradical as in (10) which then proceeds to give the final products.[5,11,28] Two types of homolysis are possible: the radial and the peripheral. There is no direct measurement on the relative prob-

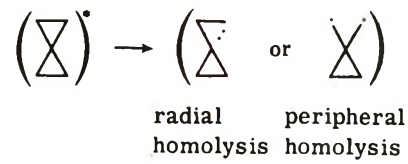

(10)

ability of these two types of homolysis in spiropentane. However, from Flowers and Frey's work on 1,1-dimethylcyclopropane,[29] which shows that the former is favored by a factor of 100, it is likely that the radial homolysis is also heavily favored in spiropentane if the excitation energy is in the same range as those employed by Flowers and Frey. However, for the present recoil tritium excitation studies, the energy deposited on spiropentane is much higher.[18] In the extreme case of infinitive excitation, the "high energy limit" in C–C bond cleavage is likely to be the statistical breakage of the three C–C bonds involved in the ring, *i.e.*, two radial and one peripheral. This means for recoil tritium excitation studies where a wide spectrum of excitation is involved, the overall radial/peripheral cleavage ratio should lie somewhere between 2 and about 100. Even if the "high energy limit" for the radial to peripheral cleavage is 1:1, the observed *overall* radial/peripheral cleavage ratio should be *larger* than 1.0 and *not* equal to 1.0 because a wide spectrum of excitation including a significant fraction of relatively low excitation is involved in the recoil tritium excitation studies.[18]

Energy Randomization—The Direct Decomposition Case. Consideration of the energy randomization problem will be separated into two cases: (1) the direct decomposition and (2) the consecutive isomerization–decomposition, owing to the fact that both might contribute to the C_2H_3T and C_3H_3T yields.

In the excited spiropentane-*t* molecules obtained from (4), let us call the ring where the T-for-H substitution occurs ring 1 and the other ring 2. In the extreme case of 100% localized decomposition, C–C bonds in ring 1 are the only ones which will cleave. For the direct decomposition case, a radial homolysis will produce C_2H_3T and C_3H_4 while a peripheral homolysis will result in C_2H_4 and C_3H_3T. As a result, the expected relative yields of C_2H_3T and C_3H_3T from this extreme case should be proportional to the relative probability of radial and peripheral homolyses. Since the former homolysis is expected to be favored, the

(28) J. C. Gilbert, *Tetrahedron*, 25, 1459 (1969).

(29) M. C. Flowers and H. M. Frey, *J. Chem. Soc.*, 3953 (1959).

expected ratio of C_3H_3T/C_2H_3T should therefore be smaller than 1.0 if the energy is not randomized before decomposition.

On the other hand, if the energy is completely randomized before decomposition, barring tritium isotope effects, we should always obtain a C_3H_3T/C_2H_3T ratio of 1.00 because both rings would have an equal chance for cleavage. (For the C–C bond cleavage in ring 2, a radial homolysis will produce C_2H_4 and C_3H_3T, while a peripheral homolysis will give C_2H_3T and C_3H_4. If ring 1 and ring 2 have the same chance for cleavage, the sum of C_2H_3T produced should be equal to the sum of C_3H_3T formed.) Any significant contribution by the localized nonrandomized decomposition will cause the above ratio to deviate from unity.

Energy Randomization—The Consecutive Isomerization–Decomposition Case. Next we shall consider the formation of C_2H_3T and C_3H_3T by the consecutive isomerization–decomposition route. Again if we assume the extreme case of 100% localized reaction, C–C bonds in ring 1 will be the only ones to cleave. By applying the knowledge that radial homolysis is favored, the following cleavage should be the commonly observed situation

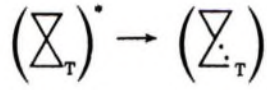

(11)

I

It is generally believed that this diradical (I) will further isomerize to the tetramethylene diradical (II) which possesses additional allyl radical stabilization.[5] The carbon atoms in II are arbitrarily numbered.

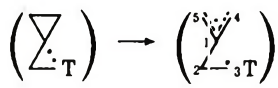

(12)

II

The combination of C_3 with either C_4 or C_5 will convert II into the final product, methylenecyclobutane (III), with the tritium atom at the third carbon. Further decomposition of III will give C_2H_3T and C_3H_4 with the

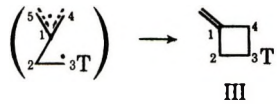

(13)

III

tritium atom in ethylene. Therefore, as a result, energy nonrandomization before unimolecular homolysis tends to favor the formation of C_2H_3T over that of C_3H_3T in the present case.

On the other hand, if the energy is completely randomized before the C–C bond homolysis, both rings should have an equal chance for cleavage. As a result, barring tritium isotope effects, we should always obtain a C_3H_3T/C_2H_3T product ratio of exactly 1.00, because any inequality in the C_2H_3T and C_3H_3T yields created by the cleavage of one ring should be completely counterbalanced by the cleavage of the other ring. Therefore, any deviation of the above ratio from unity is an indication of an appreciable amount of energy nonrandomization process.

Energy Randomization in Recoil Tritium Excitation Studies. From the above two sections on the two modes of unimolecular decomposition for recoil tritium excited spiropentane to give C_2H_3T and C_3H_3T, it can be concluded that in the case of complete energy randomization, a C_3H_3T/C_2H_3T ratio of 1.00 should be obtained. Any deviation from unity, most likely in the direction of a value less than 1.00, would indicate appreciable amounts of nonrandomization.

The C_3H_3T/C_2H_3T ratios of all the well-scavenged samples listed in the results section are plotted in Figure 5 as a function of the total pressure of the system. It is obvious that up to a total pressure of about 2 atm, this ratio still does not deviate by any significant amount from unity.[30] This means, for the recoil tritium excited spiropentane system under ordinary conditions, the RRKM postulate about energy randomization is still a generally useful approximation. Even if we take into account that the actual C_3H_3T/C_2H_3T ratio might be a few per cent lower than unity, the above generalization still holds. However, it may mean that there is a certain amount of nonrandomized process which is only a very small fraction of the total decomposition.

Comparison with the Work by Doering, Gilbert, and Leermakers on Energy Randomization in Spiropentane. The work performed by Doering and coworkers on energy randomization in spiropentane involved the addition of methylene to a double bond in a hydrocarbon.[11] From the estimation by Butler and Kistiakowsky, the excitation energy, E^*, is 95 kcal/mol[8] and nearly monoenergetic. The unimolecular isomerization of spiropentane employed by them has an activation energy of 57.6 kcal/mol.[4] Define "relative excess excitation," E_{re}, as

$$E_{re} = \frac{E^* - E_a}{E_a} \tag{14}$$

This quantity should be directly related to the probability of observing energy nonrandomization. The evaluated "relative excess excitation" value for Doering's system is 0.65 while in our study of spiropentane, the median energy is approximately 115 kcal/mol[18] and the activation energy is 62.4 kcal/mol[26] so that the "relative excess excitation" is estimated at 0.84. Another major feature of the present study is that there is a wide energy distribution.[18] This means that more than half of the spiropentane-t molecules have excitation energies of 100 kcal/mol or above with a certain fraction of them having energies over 200 kcal/mol.

(30) Recent data indicate that the 1.19 point (1735 Torr) in Figure 5 could be in error so that a deviation for C_3H_3T/C_2H_3T ratio from unity may be real starting from about 2 atm total pressure.

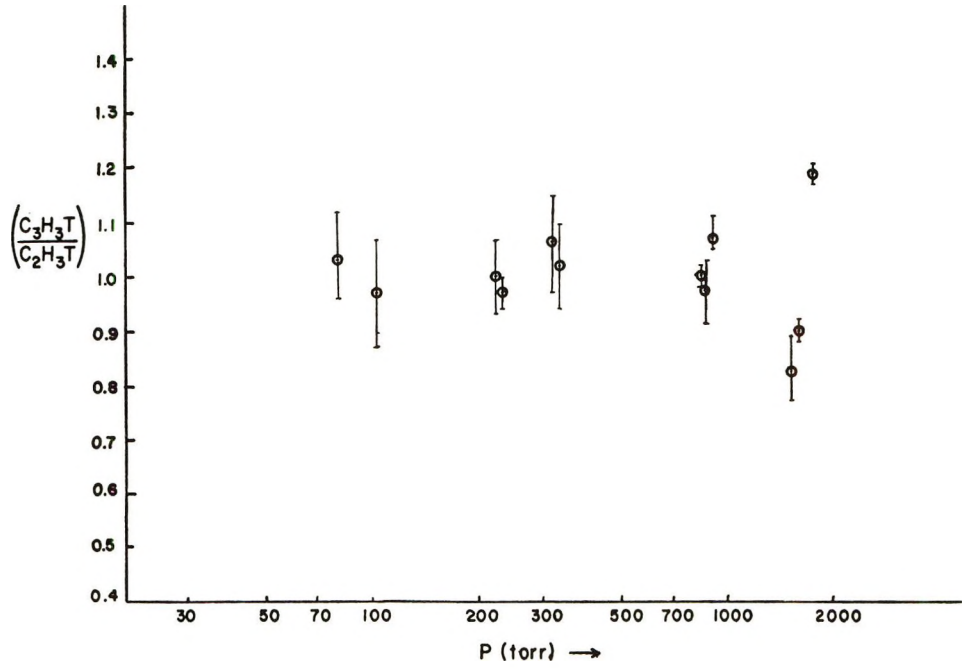

Figure 5. C_3H_3T/C_2H_3T product ratio from recoil tritium reactions with spiropentane as a function of total pressure of the system.

Because of this, the recoil tritium excitation method holds more promise as a means for detecting energy nonrandomization than does the method employed by Doering and coworkers.

Possibility for Observing Nonrandomized Decomposition. In the work performed by Rynbrandt and Rabinovitch, the monoenergetic excitation is about 111 kcal/mol and the unimolecular process has a critical threshold of about 46.5 kcal/mol.[10b] Therefore, their results concluded that when a "relative excess excitation" of 1.4 was deposited nonrandomly in hexafluorobicyclopropyl, about 3.5% of the product was formed *via* a nonrandom decomposition which could be unmistakably detected at a pressure higher than 100 Torr.

In the present spiropentane system, nonrandomized decomposition was not observed at a pressure up to about 1000 Torr. However, this is not unexpected because the "relative excess excitation" value (0.84) of the present case is much lower than the 1.4 value for the hexafluorobicyclopropyl system. It is very likely that at pressures somewhat higher than 1000 Torr, energy nonrandomized decomposition of spiropentane can be experimentally detected.

Acknowledgment. This research is supported by AEC Contract No. At-(40-1)-3898. The constructive suggestions of Professors F. S. Rowland and A. S. Rodgers were deeply appreciated.

Half-Quenching Pressures in the Association of Methyl Radicals-d_0 and -d_3

by P. C. Kobrinsky and G. O. Pritchard*

Department of Chemistry, University of California, Santa Barbara, California 93106 *(Received December 8, 1971)*

Publication costs borne completely by The Journal of Physical Chemistry

Cross-combination studies are reported for CF_3 and CH_3 (or CD_3) radicals to determine the half-quenching pressures, $P_{1/2}$, when the decomposition rate equals the collisional stabilization rate, for C_2H_6* and C_2D_6*. The results are not consistent and appear to depend upon the nature of the photolytic source molecules. CF_3COCH_3 and $CF_3N_2CH_3$ were used in this work to produce C_2H_6*, and $P_{1/2}$ values differing by a factor of 10 were obtained at 25 and 120°. An isotope effect of about 10 is indicated for C_2D_6* decomposition *vs.* C_2H_6* decomposition at 25 and 120°, using ketones as photolytic radical sources.

Waage and Rabinovitch (WR),[1] have recently given an extensive discussion of the unimolecular dissociation of ethane and the reverse process, the bimolecular recombination of methyl radicals. A novel method of determining the half-quenching pressure, $P_{1/2}$, for the methyl association

$$CH_3 + CH_3 \underset{k_{-r}}{\overset{k_r}{\rightleftharpoons}} C_2H_6^*(+M) \xrightarrow{k_M} C_2H_6(+M) \quad (1)$$

has been developed by Grotewold, Lissi, and Neumann (GLN)[2] and Casas, *et al.*,[3] who determined the falloff in the cross-combination ratio, ψ, at reduced pressures for CH_3 and a heavier radical, X, where

$$\psi = R_{XCH_3}/(R_{C_2H_6} \cdot R_{X_2})^{1/2}$$

There is a wide divergence between the experimental data of GLN[2] at 15° (where X = C_2H_5) and 60° (where X = isopropyl) and previous experimental data of Toby and Weiss (TW),[4] and the theoretical calculations of WR[1] using RRKM theory. GLN used appropriate mixtures of azo compounds as photolytic sources of the radicals. Very recently we[5] have reported on the pressure dependence of ψ, for X = CF_3, at 25 and 120°. CF_3COCH_3 and mixtures of $(CH_3)_2CO$ and $(CF_3)_2CO$ were used as photolytic sources. We found $P_{1/2} \simeq 0.8 \pm 0.2$ mm at both temperatures; the value at 120° is in very close agreement with WR's calculations, while the lower limit at 25° is in reasonable agreement (see Figure 1 of ref 1).[6-8] Grotewold, *et al.*,[2,3] propose a more "rigid" C_2H_6* activated complex to account for their results. Herein we report measurements of $P_{1/2}$ down to −50° in an attempt to test the theories and check the data of the various workers. We also report on a possible isotope effect for C_2D_6*, as indicated by other recent data of Cala and Toby (CT).[9]

Experimental conditions are as given previously,[5] except that an Hg-containing, as well as an Hg-free, apparatus was used. This caused no detectable difference in our results. $(CF_3)_2CO$, $(CD_3)_2CO$, $(CH_3)_2CO$, CF_3COCH_3, and $CH_3N_2CF_3$ were used as photolytic radical sources. The azo compound was prepared from CH_3NH_2 and CF_3NO.[10] For the experiments at about −50°, a cylindrical Pyrex reactor (900 cm³, 5.8 cm diameter) was filled on the vacuum line and placed in a large insulated box containing Dry Ice, throughout which the air was vigorously circulated. The reaction cell had thermocouples taped to the outside and was mounted on cork spacers within a cylindrical metal sheath. The average temperature recorded on the thermocouples was −52 ± 3°.

The experimental data for C_2H_6* are recorded in Figure 1 as a plot of $(\psi_\infty/\psi)^2$ *vs.* the logarithm of pressure.[11] The ordinate is equivalent to $k_M[M]/(k_{-r} + k_M[M])$, with the normalization factor ψ_∞ = 2.54. The data obtained using $CF_3N_2CH_3$ lead to a value of $P_{1/2} \simeq 0.06 \pm 0.02$ mm, *independent of the temperature*. Such a value at −50° agrees well with an extrapolation of WR's theoretical curve. The unexpected nature of the results led us to reexamine the ketone system. These data are also included in Figure 1, mainly for a temperature of 120°. It is not feasible

(1) E. V. Waage and B. S. Rabinovitch, *Int. J. Chem. Kinet.*, **3**, 105 (1971).

(2) J. Grotewold, E. A. Lissi, and M. G. Neumann, *J. Chem. Soc. A*, 375 (1968).

(3) F. Casas, C. Previtali, J. Grotewold, and E. A. Lissi, *ibid.*, 1001 (1970).

(4) S. Toby and B. H. Weiss, *J. Phys. Chem.*, **68**, 2492 (1964).

(5) P. C. Kobrinsky, G. O. Pritchard, and S. Toby, *J. Phys. Chem.*, **75**, 2225 (1971).

(6) The extremely high values depicted at 216 and 300°, taken from the data of Shaw, *et al.*,[7] depend upon how $P_{1/2}$ is determined. Lower values, in more general agreement with the other data, are obtained by direct inspection of Figure 3 in ref 7.[8]

(7) H. Shaw, J. H. Menczel, and S. Toby, *J. Phys. Chem.*, **71**, 4180 (1967).

(8) S. Toby, private communication.

(9) F. R. Cala and S. Toby, *J. Phys. Chem.*, **75**, 837 (1971).

(10) A. H. Dinwoodie and R. N. Haszeldine, *J. Chem. Soc.*, 2268 (1965). We thank Drs. N. C. Craig and D. W. Setser for their modified procedure.

(11) For runs at 1 mm or below, $\psi = R_{CF_2CH_2}/(R_{C_2F_6} \cdot R_{C_2H_6})^{1/2}$ as the CF_3CH_3* undergoes HF elimination. The CF_3CH_3 varied from a trace product up to <3% of the CF_2CH_2 formation.

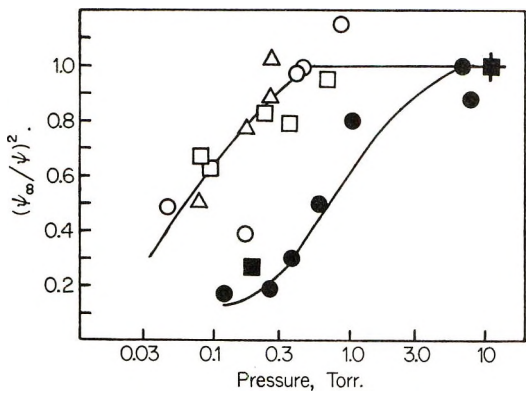

Figure 1. Semilog plot of $(\psi_\infty/\psi)^2$ *vs.* pressures for C_2H_6*. $CF_3N_2CH_3$ as the photolytic source: ○, 120°; □, 25°; and △, −50°; ✚, average of 13 high-pressure runs, see text. Ketone (CF_3COCH_3, CH_3COCH_3, CF_3COCF_3) sources: this work, ●, 120°; and ■, 25°. Right-hand line is from previous work, ref 5.

to use the ketones below room temperature. The line drawn through the ketone data is taken from our previous work,[5] and it represents a large number of runs carried out at 25 and 120°. We quite readily corroborate the previous value of $P_{1/2} \simeq 0.8 \pm 0.2$ mm.[12]

TW[4] concluded that acetone was approximately two to three times more efficient than azomethane in deactivating the excited ethane complex. A later reevaluation of the data[7] indicated that the efficiencies were the same. At $P_{1/2}$, where $k_{-r} = k_M[M]$, we see in Figure 1 that CF_3COCH_3 appears to be ten times less efficient than $CF_3N_2CH_3$! This is unsupported and contrary to the usual strong collision assumption concerning vibrational deexcitation of highly excited polyatomic molecules, particularly by polyatomic quenchers;[13] prior evidence indicates that ketones are strong collisional quenchers for C_2H_6*.[4,5,14] However, we found the azo system results to be reproducible. Similarly, although the lower temperature data of GLN have been criticized,[1,5,15] it may well be that their data also constitute valid experimental observations under their conditions, where they[2] find $P_{1/2} = 0.012$ at 15°. This indicates a quenching efficiency factor of 70, which is even more unreasonable. Attempts to use the data to establish a model for the C_2H_6* activated complex[2,3] are therefore extremely questionable. We conclude that although a study of the variation in ψ with pressure appears to be an ingenious and simple method[9] for the measurement of $P_{1/2}$, some as yet unrealized factor(s) cause(s) large variations in the determinations, at least with azo compounds at lower temperature.

A referee has suggested that other possible reactions in the azo systems should be considered which may contribute to the apparently anomalous behavior. CF_3H was absent at room temperature in the $CF_3N_2CH_3$ experiments, and at higher pressures Chang, Craig, and Setser (CCS)[16] also found that abstraction by CF_3 and CH_3 radicals was negligible. A direct group abstraction, *e.g.*

$$CH_3 + CH_3N_2CF_3 \longrightarrow C_2H_6 + N_2 + CF_3 \quad (2)$$

has little precedent, and if it occurred it should increase in importance with increasing pressure. The high-pressure limit for ψ obtained by CCS[16] is normal (see Figure 1[17]). On the other hand, the facile addition of CF_3 radicals to $(CF_3)_2N_2$ is well documented,[18] and the addition of CH_3 to $(CF_3)_2N_2$, with the possible decomposition of the vibrationally excited intermediate to produce CF_3

$$CH_3 + (CF_3)_2N_2 \longrightarrow (CH_3)(CF_3)N_2CF_3^* \longrightarrow CF_3 + CH_3N_2CF_3 \quad (3)$$

has been suggested.[19] In keeping with these observations the addition of CF_3, and probably CH_3, to $CF_3N_2CH_3$ has been reported,[10,16] which leads to the possible formation of four vibrationally excited intermediates. The decomposition of these intermediates (before stabilization and removal by radical addition to form hydrazines[10]) could occur at low pressures, but it seems unlikely that a C_2H_6 or C_2F_6 molecule is formed directly *via* such a decomposition. (A radical producing sequence, as in (3) above, would seem more plausible.) For instance, the predominant occurrence of one, or both, of the reaction sequences

$$CF_3 + CF_3N_2CH_3 \longrightarrow (CF_3)(CF_3)N_2CH_3^* \longrightarrow C_2F_6 + N_2 + CH_3 \quad (4)$$

$$CH_3 + CF_3N_2CH_3 \longrightarrow CF_3N_2(CH_3)(CH_3)^* \longrightarrow CF_3 + N_2 + C_2H_6 \quad (5)$$

could account for the shift in the half-quenching pressure that we have observed. Removal of the stabilized intermediate in reaction 4 by CH_3 addition (or

(12) For the older data[5] $\psi_\infty = 2.67$. The slight change in the average high-pressure limit for the cross-combination ratio probably reflects a change in chromatographic conditions.

(13) B. S. Rabinovitch, H. F. Carroll, J. D. Rynbrandt, J. H. Georgakokas, B. A. Thrush, and R. Atkinson, *J. Phys. Chem.*, **75**, 3376 (1971).

(14) R. E. Dodd and E. W. R. Steacie, *Proc. Roy. Soc., Ser. A*, **223**, 283 (1954).

(15) K. J. Hole and M. F. R. Mulcahy, *J. Phys. Chem.*, **73**, 177 (1969); A. N. Dunlop, R. J. Kominar, and S. J. W. Price, *Can. J. Chem.*, **48**, 1269 (1970).

(16) H. W. Chang, N. L. Craig, and D. W. Setser, *J. Phys. Chem.*, **76**, 954 (1972).

(17) This point constitutes the average of 13 experiments carried out over a total pressure range of 9.2 to 750 Torr at room temperature. The $CF_3N_2CH_3$ was diluted with approximately ten times as much c-C_4F_8; however, the non-occurrence of *any* direct group abstraction to form any of the ethanes is verified.

(18) J. R. Dacey and D. M. Young, *J. Chem. Phys.*, **23**, 1302 (1955); G. O. Pritchard, H. O. Pritchard, H. I. Schiff, and A. F. Trotman-Dickenson, *Trans. Faraday Soc.*, **52**, 849 (1956); J. R. Dacey, R. F. Mann, and G. O. Pritchard, *Can. J. Chem.*, **43**, 3215 (1965); S-L. Chong and S. Toby, *J. Phys. Chem.*, **74**, 2801 (1970).

(19) L. Batt and J. M. Pearson, *Chem. Commun.*, 575 (1965); R. L. Thommarson and G. O. Pritchard, *J. Phys. Chem.*, **70**, 2307 (1966); J. D. Reardon and C. E. Waring, *ibid.*, **75**, 735 (1971).

in (5) by CF_3 addition) results in the formation of 1,1-bistrifluoromethyldimethylhydrazine,[10] but the reported product may well be (or contain) the 1,2- compound,[10] which arises from

$$CH_3 \text{ or } CF_3 + CF_3N_2CH_3 \longrightarrow (CH_3)(CF_3)N_2CH_3^* \text{ or } CF_3N_2(CH_3)(CF_3)^* \quad (6)$$

followed by stabilization and radical combination. The decomposition mode corresponding to (4) or (5) for either intermediate produces CF_3CH_3. However, under our conditions we see only $CF_2{=}CH_2$, and Batt and Pearson and Reardon and Waring[19] report the absence of CF_3CH_3 in their experiments on reaction 3. Even if they do occur, it would seem that reaction sequences (4) and (5) may be very difficult to establish, although perhaps our present results could be taken as inferential evidence for their occurrence. The reaction sequences would decrease in importance with decreasing temperature, suggesting that we attach the most validity to the $-50°$ data.

The data of GLN cannot be rationalized on the above basis. Radical addition and hydrazine formation are much less significant in $(CH_3)_2N_2$ photolysis, and the extensive studies of Toby and his coworkers[4,7,20] do not indicate a group abstraction to produce ethane. It should also be noted that the ψ values of GLN are normal at high (>0.1 mm) pressures in the $CH_3 + C_2H_5$ study at room temperature. GLN observed that the direct intramolecular elimination of ethane in the primary photolytic step[20]

$$(CH_3)_2N_2 + h\nu \longrightarrow C_2H_6 + N_2$$

did not cause a significant correction under their conditions. In the present work we did not observe significant amounts of CF_3CH_3, so that there is no need to consider the possible primary intramolecular split, at least under our conditions.

The data on $C_2D_6^*$ are presented in Figure 2 for 25 and 120°. The results at the higher temperature are rather scattered at low pressures, so that a semilogarithmic plot is not employed. However, an isotope

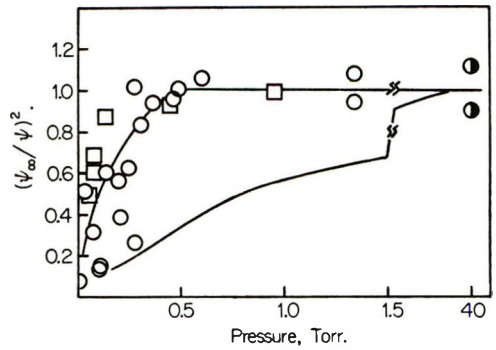

Figure 2. Plot of $(\psi_\infty/\psi)^2$ *vs.* pressure for $C_2D_6^*$. $CD_3COCD_3 + CF_3COCF_3$ source: ○, 120°; and □, 25°; ◑, from G. O. Pritchard and M. J. Perona, *Int. J. Chem. Kinet.*, **2**, 281 (1970). Right-hand line is $C_2H_6^*$ data, this work and ref 5.

effect is clearly indicated. We estimate $P_{1/2}(C_2D_6^*) \simeq 0.1 \pm 0.05$ mm at 25 and 120°. There is some evidence for a trend with temperature, which is in the right direction,[1] and the lower limit of $P_{1/2}$ may very well correspond better to the lower temperature and the upper limit to the higher temperature. With the scatter involved, there is not a firm basis for this conclusion. Since $P_{1/2}(C_2H_6^*) \simeq 0.8 \pm 0.2$ mm, an isotope effect of about 10 (between 4 and 20, taking the extreme values) is indicated at these temperatures. CT[9] report 1.5–6 for this isotope effect at 300°, which included a cross-combination falloff determination. Any further interpretation of the isotope effect would not appear to be warranted at this juncture, due to the large variations in the values reported in these studies.

Acknowledgments. We thank the National Science Foundation and the Clapp Foundation (Milford, Connecticut) for support. We further thank Professor S. Toby for helpful discussions and Mr. F. Servedio for the preparation of $CF_3N_2CH_3$. Our thanks are also due to Professor D. W. Sester for a pre-publication copy of his paper.

(20) S. Toby and J. Nimoy, *J. Phys. Chem.*, **70**, 867 (1966); S-L. Cheng, J. Nimoy, and S. Toby, *ibid.*, **71**, 3075 (1967); F. R. Cala, S-L. Chong, H. P. Sperling, and S. Toby, *Can. J. Chem.*, **48**, 357 (1970).

The Hydrogen–Oxygen Reaction on Lanthanide Oxides. II. The Stoichiometric Hydrogen–Oxygen Reaction on Neodymium Oxide, Dysprosium Oxide, and Erbium Oxide

by John F. Read* and Reid E. Conrad

Department of Chemistry, Mount Allison University, Sackville, New Brunswick, Canada *(Received November 9, 1971)*

Publication costs assisted by Mount Allison University

The reaction between a stoichiometric mixture of hydrogen and oxygen has been studied over neodymium oxide, dysprosium oxide, and erbium oxide catalysts. The reaction was studied over neodymium oxide in the temperature range 68–150° at pressures from 0.68 to 14.22 Torr, over dysprosium oxide in the temperature range 85–150° at pressures from 2.04 to 3.20 Torr, and over erbium oxide in the temperature range 109–191° at pressures from 0.20 to 9.17 Torr. The kinetics over all three oxides obey a similar pattern. Below a certain temperature the kinetics are zero order, and above this temperature the apparent order changes during the course of each reaction from zero to a value in the range 0.5–1. The results are explained in terms of a general kinetic expression based on the Langmuir isotherm, namely $-dP_T/dt = (A_mP_T)^m/(1 + BP_T)^m$, where A_m and B are temperature-dependent constants, P_T is the total pressure of hydrogen plus oxygen, and m is an integer of value 1 to 3. The best fit between experimental and theoretical data is obtained when $m = 1$. The most likely mechanism is one which involves the fraction of active surface covered by molecular hydrogen as a rate-determining step.

Introduction

Although the catalyzed reaction between hydrogen and oxygen has been extensively studied, there is no consistent mechanism or kinetic expression that can be applied in all cases.

In many instances the order with respect to hydrogen is between zero and unity, and the order with respect to oxygen is zero. For example, an overall order of zero has been postulated by Gray and Darby[1] with excess oxygen over nickel oxide and by Read, *et al.*,[2] over neodymium sulfide. An order greater than zero but less than one in hydrogen has been observed by Bulgakov, *et al.*,[3] over iron(III) oxide and by Mamedov, *et al.*,[4] with excess oxygen over iron(III) oxide, chromium(III) oxide, vanadium(V) oxide, copper(II) oxide, cobalt(II) oxide, cobalt(III) oxide, manganese (IV) oxide, titanium(IV) oxide, and zinc oxide. Dry and Stone[5] have reported an order of one in hydrogen over nickel oxide and Ostrovskii[6] has reported an order of one in hydrogen over silver. However, it should be noted that many of these investigations were carried out in excess oxygen, and this could mask the dependency on oxygen pressure.

Kinetic expressions that are not independent of oxygen pressure have been observed. For example, in the reaction over platinum[7] the kinetics are derived assuming that the rate is proportional to the cube of the surface covered by the reactants, and that the Langmuir isotherm is obeyed.

The catalytic activity of the lanthanide oxides for the hydrogen–oxygen reaction has been studied, but a detailed kinetic analysis has not been attempted. Bakumenko,[8] Bakumenko and Chashechnikova,[9] and Antoshin, *et al.*,[10] have compared the activity of various lanthanide oxides towards the hydrogen–oxygen reaction and have noted that the highest activity is associated with the greatest oxygen mobility in the catalyst. In addition, Antoshin, *et al.*,[11] have compared the hydrogen–oxygen reaction, the hydrogen–deuterium reaction, and the exchange of isotopic oxygen over doped lanthanum oxide. They observed a first-order dependence on the hydrogen pressure. A first-order dependence has also been noted by Bakumenko and Chashechnikova[9] over neodymium oxide.

(1) T. J. Gray and P. W. Darby, *J. Phys. Chem.*, **60**, 209 (1965).

(2) J. F. Read, W. H. Bouma, and S. E. Robertson, *J. Catal.*, **19**, 1 (1970).

(3) N. N. Bulgakov, Z. R. Ismagilov, V. V. Popovskii, and G. K. Boreskov, *Kinet. Katal.*, **11**, 638 (1970).

(4) E. A. Mamedov, V. V. Popovskii, and G. K. Boreskov, *ibid.*, **10**, 852 (1969); **11**, 969 (1970); **11**, 979 (1970).

(5) M. E. Dry and F. S. Stone, *Discuss. Faraday Soc.*, **No. 28**, 192 (1959).

(6) V. E. Ostrovskii, *Kinet. Katal.*, **8**, 371 (1967).

(7) Yu. A. Balovnev, S. Z. Roginskii, and I. I. Tretyakov, *Dokl. Akad. Nauk SSSR*, **163**, 394 (1965).

(8) T. T. Bakumenko, *Kinet. Katal.*, **6**, 74 (1965).

(9) T. T. Bakumenko and I. T. Chashechnikova, *ibid.*, **10**, 796 (1969).

(10) G. V. Antoshin, Kh. M. Minachev, and R. V. Dmitriev, *Izv. Akad. Nauk SSSR, Ser. Khim.*, **8**, 1864 (1967).

(11) G. V. Antoshin, Kh. M. Minachev, and M. E. Lokhuary, *J. Catal.*, **22**, 1 (1971).

In this contribution, data are presented on the stoichiometric reaction between hydrogen and oxygen over neodymium oxide, dysprosium oxide, and erbium oxide. These data, together with the hydrogen and oxygen adsorption results presented in an earlier paper,[12] will form the basis of a detailed study of the nonstoichiometric hydrogen–oxygen reaction over lanthanide oxides. By comparing the results obtained over different members of the series it should be possible to obtain a better understanding of the role of the catalyst.

Experimental Section

The apparatus comprised a conventional high-vacuum system. Stoichiometric mixtures of hydrogen and oxygen (assayed grade, supplied by The British Oxygen Co.) were prepared and allowed onto the catalyst. The reaction was followed by measuring the total pressure in the closed reaction chamber every 3 min, using a McLeod gauge. Variations in the measuring procedure and in the apparatus assured that the pressure readings were valid and that there were no problems associated with the mass transport of reactants or products. Mass spectral analysis confirmed that only hydrogen, oxygen, and water vapor were involved in the reaction and that the reaction was stoichiometric. Runs were followed up to 90 min. A trap, surrounded by liquid nitrogen, protected the catalyst from contamination and allowed the water produced in the reaction to be condensed.

The reaction was studied over the temperature range 68–150° for neodymium oxide, 85–150° for dysprosium oxide, and 109–191° for erbium oxide. Runs were performed throughout these temperature ranges at an approximately constant initial total pressure of between 2 and 3 Torr. In addition, the reaction was studied varying the initial pressure in the range 1–14 Torr over neodymium oxide and erbium oxide.

The three catalysts used in the present study were of "Specpure" grade supplied by Johnson Matthey. X-Ray and ir analysis confirmed that all three oxides possessed the C-type structure[13] although neodymium oxide appeared to be hydrated.[12] There was no change in structure during the experiments and sintering did not occur.[14] Surface areas were measured by the BET method using krypton.

The oxides were conditioned by heating for 7 days at 550° and $<10^{-6}$ Torr of pressure. Reproducible results were obtained by evacuating the system for 10 min between runs at the same temperature and for at least 3 hr between runs at different temperatures.

An IBM 1130 computer was used for the calculations, the reaction rates being determined by cubic spline interpolation.[15] The kinetics were determined by calculating the apparent order at each data point and by plotting the appropriate form of the integrated rate expression with specified values for the apparent order.

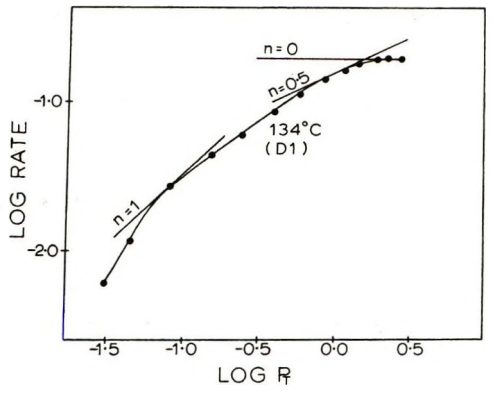

Figure 1. The logarithm of the rate of reaction *vs.* the logarithm of the total pressure over dysprosium oxide.

Results

The experimental data were initially analyzed using the general equation

$$-\frac{dP_T}{dt} = kP_T^n \qquad (1)$$

where P_T is the total pressure of hydrogen plus oxygen in Torr, t is the time in minutes, k is the rate constant, and n is the overall order of the reaction. The rate and order were determined at each data point. In general, the order increased during any particular reaction from a value of zero up to a value in the range 0.5–1, though a few values went as high as 3. The change in order can be seen from the log rate *vs.* log P_T plot shown in Figure 1 for the hydrogen–oxygen reaction over dysprosium oxide at 134° (run D1). The slope of the graph is equal to n; lines are drawn in at $n = 0$, $n = {}^1/_2$, and $n = 1$. At an approximately constant initial pressure of 2 ± 1 Torr, there was a particular temperature for each oxide below which the order for all the runs remained constant at zero up to at least 50% of the reaction. This temperature is shown in Table I. Several reactions at higher temperatures and higher pressures also gave a constant order of zero.

For clarity of presentation the results are tabulated according to eq 1, with n equal to 0, ${}^1/_2$, and 1. The absolute rate constants (that is, k, corrected for the volume of the system and the total surface area of the catalyst), k_0, $k_{1/2}$, and k_1, respectively, are given for the linear portion of eq 1. For reactions which did not give a linear portion when $n = 0$, k_0 was calculated from the initial rates. When a linear portion was not shown

(12) J. F. Read, *Can. J. Chem.*, **50**, 490 (1972).

(13) H. R. Hoekstra, *Inorg. Chem.*, **5**, 754 (1966).

(14) D. R. Ashmead, D. D. Eley, and R. Rudham, *J. Catal.*, **3**, 280 (1964).

(15) L. G. Dunfield and J. F. Read, *J. Chem. Phys.*, in press.

Table I: Relative Activity of the Catalysts

Oxide	Ionic radius of metal ion, Me^{3+}, Å	Temperature below which zero-order kinetics are obeyed for 50% reaction, °C	Temperature range in which reproducible results were obtained, °C	Temperature at which $k_{1/2} = 2.5 \times 10^{-2}$ cm $Torr^{1/2}$ min^{-1}, °C
Nd_2O_3	1.15	80	68–150	129
Dy_2O_3	1.07	110	85–150	137
Er_2O_3	1.04	130	109–191	170

with $n = {}^1/_2$ or $n = 1$, no values for $k_{1/2}$ or k_1 are reported in the tables. Many reactions obey zero-order kinetics initially and then change to a higher order. The pressure at which half-order kinetics are obeyed instead of zero-order kinetics is indicated in the tables of results.

Each of the oxides studied decreased in activity during the initial reactions. The initial activity could never be regained, but a constant activity could be maintained by baking out the oxide at 300° for 3 days between each run. A lower, constant activity could be maintained by evacuating the system for 10 min between runs at the same temperature and for 3 hr between runs at different temperatures. The latter procedure was adopted throughout the present work. Several runs were usually performed at each pressure and temperature (the number being indicated in parentheses after the run number in the tables). The average result is presented.

Neodymium Oxide. The results are summarized in Table II. The initial pressure, $(P_T)_{t\to 0}$, decreased slightly for each successive run up to and including run N17. Above 100°, overall half-order kinetics were obeyed at all times. Below this temperature, the reaction obeyed overall zero-order kinetics above a certain pressure, before slowly changing to overall half-order kinetics. At the lower temperatures, the initial rate was very slow, overall zero-order kinetics being obeyed only after the first few minutes. This was particularly noticeable at the lowest temperature of 68°, as shown in Figure 2. Both the overall zero- and overall half-order graphs for run N13 are also shown in Figure 2. These graphs clearly show the order changing from zero to one-half. Extra doses were added to runs N16 and N17 after about 15 min. The slope of the half-order plot was identical before and after this dose was added. The initial stoichiometric pressure was varied in runs N18, N19, and N20. The rate constants from the overall zero- and half-order plots remained tolerably constant over a wide range of initial pressures. The tendency for overall zero-order kinetics to be obeyed at lower temperatures and higher pressures was demonstrated.

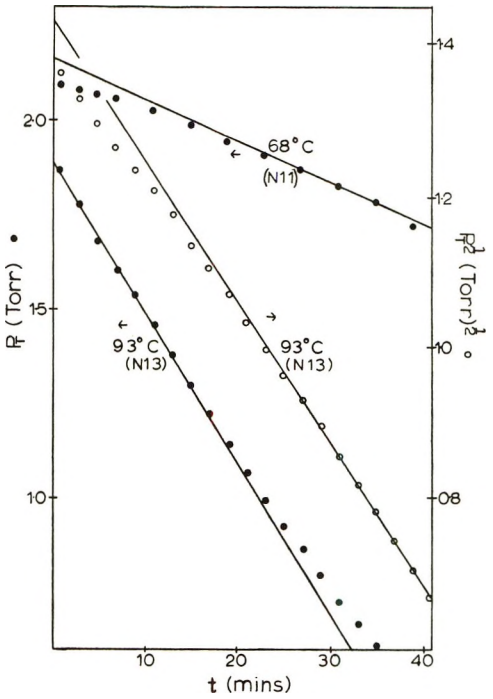

Figure 2. Zero- and half-order plots for the hydrogen–oxygen reaction over neodymium oxide.

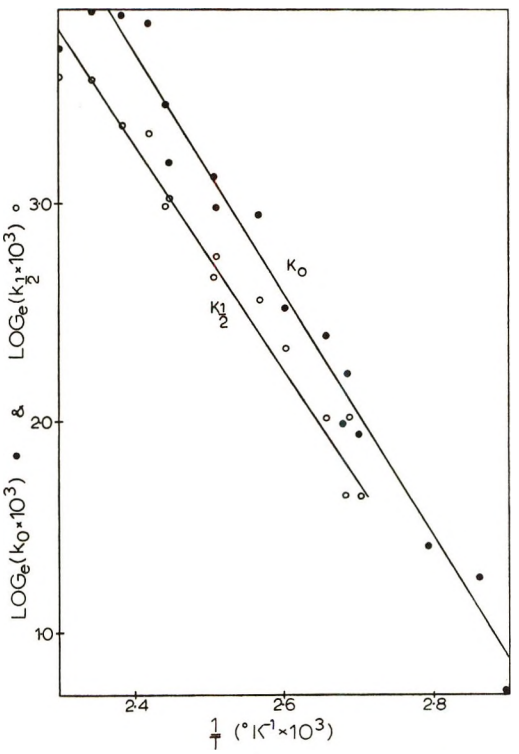

Figure 3. Arrhenius plots using zero- and half-order rate constants for the hydrogen–oxygen reaction over neodymium oxide.

The overall order with respect to concentration, calculated from initial rate data at various initial pressures, is one-half. The Arrhenius plots using the zero- and half-order rate constants are shown in Figure

Table II: Hydrogen–Oxygen Reaction on Neodymium Oxide (Total surface area = 0.136 m²; Volume of reaction vessel = 258 cm³)

Run	Temp, °C	Average $(P_T)_{t\to 0}$, Torr	$k_0 \times 10^3$, cm Torr min^{-1}	$k_{1/2} \times 10^3$, cm Torr$^{1/2}$ min^{-1}	Low pressure limit of zero-order obeyance, Torr	$A_1 \times 10^2$
N1 (5)	106	3.64	31.1	16.0	...	
N2 (4)	114	3.57	40.9	18.7	...	
N3 (6)	121	3.37	49.1	19.5	...	
N4 (6)	130	2.86	47.6	28.1	...	29.9
N5 (3)	143	2.72	50.4	36.4	...	43.0
N6 (3)	136	2.52	49.5	29.2	...	36.3
N7 (3)	109	2.58	19.3	13.1	...	12.0
N8 (3)	97	2.23	11.1	7.50	2.0	9.56
N9 (2)	91	2.29	6.93	5.25	1.8	5.64
N10 (2)	72	2.22	3.56	2.62	1.6	
N11 (2)	68	2.10	2.06		1.0[a]	
N12 (2)	80	1.93	4.12	3.75	1.5	
N13 (2)	93	1.92	9.18	7.50	1.8	
N14 (2)	104	1.84	12.6	10.5	...	
N15 (2)	117	1.82	20.1	16.1	...	
N16 (2)	126	1.73	24.7	21.0	...	
N17 (2)	150	1.68	42.5	36.7	...	
N18.1	127	1.64	25.5	20.2	...	
18.2		2.63	32.4	20.6	...	28.3
18.3		3.69	35.6	20.6	...	
18.4		4.56	28.5	17.2	2.2	
18.5		14.22	30.5	19.5	3.5	
N19.1	117	1.02	12.4	13.1	...	
19.2		2.72	23.1	14.6	...	20.6
19.3		10.70	15.7	15.7	4.5	
19.4		8.84	20.6		4.3[a]	
N20.1	94	0.62	4.69	5.62	...	
20.2		7.28			5.3[a]	
20.3		5.48			4.1[a]	
20.4		1.99	2.44	5.25	1.1	
20.5		3.44	7.31		1.8[a]	

[a] The reaction was only followed up to this pressure.

Table III: Hydrogen–Oxygen Reaction on Dysprosium Oxide (Total surface area = 0.139 m²; Volume of reaction vessel = 253 cm³)

Run	Temp, °C	Average $(P_T)_{t\to 0}$, Torr	$k_0 \times 10^3$, cm Torr min^{-1}	$k_{1/2} \times 10^3$, cm Torr$^{1/2}$ min^{-1}	$k_1 \times 10^3$, cm min^{-1}	Low pressure limit of zero-order obeyance, Torr	$A_1 \times 10^2$
D1 (4)	134	3.20	43.2	28.3		...	
D2 (3)	123	3.05	37.1	21.4	30.3	...	
D3 (2)	111	2.91	27.1	16.7	21.5	...	
D4 (2)	101	2.83	22.9	13.1	12.3	...	
D5 (1)	90	2.80	2.31			0.7[a]	
D6 (1)	85	2.71	1.64			1.7[a]	
D7 (1)	95	2.70	2.87	2.03		1.2	
D8 (1)	105	2.68	5.27	3.92		1.3	
D9 (4)	117	2.60	24.5	15.6	20.3	...	11.4
D10 (2)	128	2.46	28.7	19.6	27.8	...	16.8
D11 (2)	137	2.41	32.9	24.7	41.4	...	24.5
D12 (2)	150	2.33	40.7	45.8	61.4	...	35.3
D13 (2)	145	2.23	38.3	44.3	52.5	...	31.2
D14 (2)	123	2.20	25.8	17.8	27.1	...	15.3
D15 (2)	111	2.13	20.3	14.5	15.4	...	8.98
D16 (1)	95	2.04	3.58	2.47		1.3	

[a] The reaction was only followed up to this pressure.

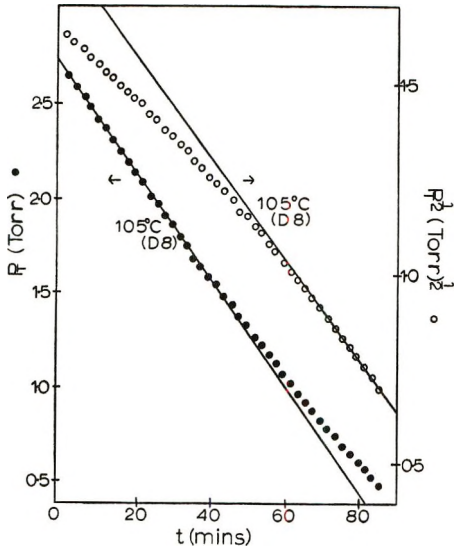

Figure 4. Zero- and half-order plots for the hydrogen–oxygen reaction over dysprosium oxide.

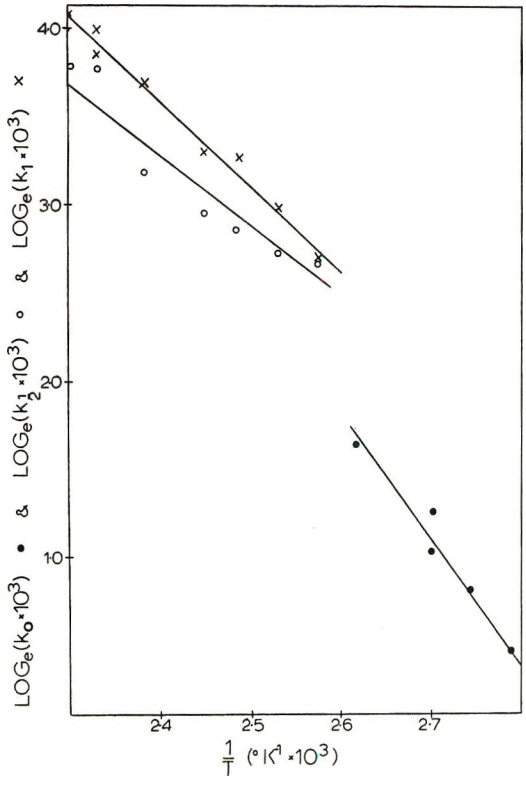

Figure 5. Arrhenius plots using zero-, half-, and first-order rate constants for the hydrogen–oxygen reaction over dysprosium oxide.

3. The first three runs (N1, N2, and N3) were relatively faster than the rest, indicating that the sample had not reached a level of constant activity. The activation energies using the zero- and half-order rate constants are 13 ± 2 and 11 ± 2 kcal mol^{-1}, respectively.

Dysprosium Oxide. The results are summarized in Table III. As for neodymium oxide the data could be

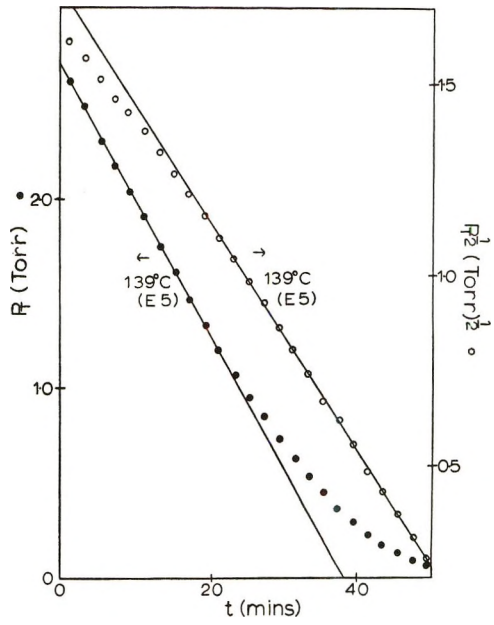

Figure 6. Zero- and half-order plots for the hydrogen–oxygen reaction over erbium oxide.

fitted to overall zero- and/or half-order kinetics. In addition, in the latter stages of many of the reactions at high temperatures, the data could be fitted to first-order kinetics. The runs below 105° had a slow initial rate before they became zero order. The change from overall zero order to overall half order for run D8 is shown in Figure 4. Above 110°, overall half-order kinetics were obeyed up to about 60% reaction.

The Arrhenius plots from the zero-order, half-order, and first-order rate constants are shown in Figure 5. The first four runs (D1, D2, D3, and D4) were relatively faster than the rest. The values for the activation energies using the zero-order, half-order, and first-order rate constants are 13 ± 3, 8 ± 3, and 10 ± 2 kcal mol^{-1}, respectively.

Erbium Oxide. The results are summarized in Table IV. As the temperature decreased to 109°, a very slow initial rate became apparent. Zero-order kinetics were obeyed after a few minutes. In Figure 6, the change from zero-order to half-order kinetics for run E5 at 139° is shown. Above 150°, the runs obeyed overall half-order kinetics. In some cases, linearity was maintained up to 90% reaction.

In runs E13 and E14, zero-order kinetics were obeyed at the higher pressures. The rate was initially slow at these pressures; the higher the pressure the longer the time before zero-order kinetics were obeyed. It was difficult to calculate the initial slope of the zero-order graphs. From a comparison of the half-order rate constants, it is clearly seen that the initial pressure had very little effect on the rate constant.

The overall order with respect to concentration, calculated from initial rate data at various initial pressures, is one-half.

Table IV: Hydrogen–Oxygen Reaction on Erbium Oxide (Total surface area = 0.132 m^2; Volume of reaction vessel = 254 cm^3)

Run	Temp, °C	Average $(P_T)_{t\to 0}$, Torr	$k_0 \times 10^3$, cm Torr min^{-1}	$k_{1/2} \times 10^3$, cm $Torr^{1/2}$ min^{-1}	Low pressure limit of zero-order obeyance, Torr	$A_1 \times 10^2$
E1 (2)	148	3.38	16.4	14.5	1.6	
E2 (4)	161	3.16	31.7	21.4	...	
E3 (3)	186	3.08	51.0	35.1	...	49.3
E4 (3)	176	2.85	47.0	29.4	...	43.3
E5 (2)	139	2.69	14.3	11.1	1.4	20.2
E6 (2)	130	2.64	10.9	7.64	1.2	14.9
E7 (2)	116	2.57	4.58		1.3	
E8 (1)	109	2.51	0.57		1.3	
E9 (2)	125	2.47	5.92		1.2	
E10 (3)	155	2.38	22.5	16.0	...	27.6
E11 (2)	191	2.30	51.2	35.1	...	51.8
E12 (2)	168	2.27		23.3	...	32.4
E13.1	156	0.77	9.74	14.5	...	
13.2		9.17	20.8		4.8[a]	
13.3		6.56	22.9	12.2	2.6	
13.4		1.97	17.8	13.7	1.5	
E14.1	168	3.76	34.4	21.8	2.8	
14.2		2.74	32.5	22.2	...	36.7
14.3		1.16	21.0	21.8	...	
14.4		1.98	9.55	16.8	...	
14.5		0.20	24.8	21.8	...	

[a] The reaction was only followed up to this pressure.

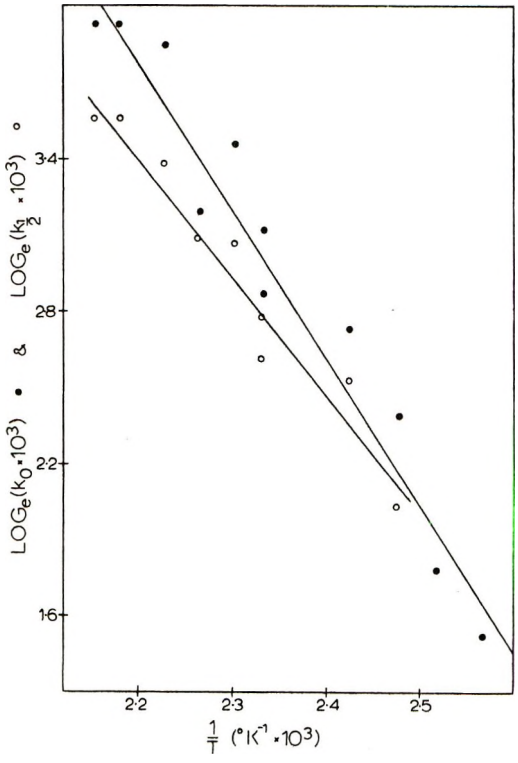

Figure 7. Arrhenius plots using zero- and half-order rate constants for the hydrogen–oxygen reaction over erbium oxide.

The Arrhenius plots using the zero- and half-order rate constants are shown in Figure 7. The activation energies using the zero- and half-order rate constants are 15 ± 2 and 9 ± 2 kcal mol^{-1}, respectively.

Discussion

Activity. The sites on the surface of the oxides are not all equally active. One set of very active sites is readily, irreversibly poisoned. For example, the reaction was measurable at room temperature on a freshly baked-out sample of neodymium oxide. After a few runs had been performed, the reaction was no longer measurable at room temperature, even after prolonged baking out at high temperatures. A second set of sites is slowly poisoned, and the activity of the surface decreases to a constant value with successive runs. The first three runs for neodymium oxide and the first four runs for dysprosium oxide are relatively faster than the subsequent runs.

The relative activity of the three oxides can be seen from the data in Tables I and V. There is no overall pattern to the activities of these oxides except that the reaction proceeds at the lowest temperature on the oxide with the highest ionic radius. Bakumenko and Chashechnikova[9] report that the activity of neodymium oxide is anomalously high and suggest the possibility of the formation of a higher oxide.

Kinetics and Mechanism. The kinetics obeyed on all three oxides follow a similar pattern. Below the temperature indicated in Table I zero-order kinetics are obeyed up to at least 50% of the reaction at initial

Table V: Activation Energies Using Different Kinetic Models

Oxide	E_A using k_0, kcal mol^{-1}	E_A using $k_{1/2}$, kcal mol^{-1}	E_A using k_1, kcal mol^{-1}	E_A using A_1, kcal mol^{-1}
Nd_2O_3	13 ± 2 (0.971)	11 ± 2 (0.993)	...	12 ± 2 (0.990)
Dy_2O_3	13 ± 3 (0.947)	8 ± 3 (0.959)	10 ± 2 (0.975)	11 ± 2 (0.999)
Er_2O_3	15 ± 2 (0.976)	9 ± 2 (0.972)	...	8 ± 2 (0.992)

pressures in the range 2 ± 1 Torr. In addition, zero-order kinetics are obeyed over neodymium oxide at 94° with $(P_T)_{t\to 0}$ at 3.44, 5.48, and 7.28 Torr, at 117° with $(P_T)_{t\to 0}$ at 8.84 and 10.70 Torr, and at 127° with $(P_T)_{t\to 0}$ at 4.56 and 14.22 Torr. Zero-order kinetics are also obeyed over erbium oxide at 156° with $(P_T)_{t\to 0}$ at 6.56 and 9.17 Torr and at 168° with $(P_T)_{t\to 0}$ at 3.76 Torr. At low temperatures, a very slow initial rate becomes apparent before zero-order kinetics are obeyed. This is caused by the increased time necessary to reach steady-state conditions.

For about 10 to 20° above the temperatures shown in Table I and at initial pressures in the range 2 ± 1 Torr, the order changes gradually from zero to one-half during the course of each reaction. At higher temperatures still the order changes more rapidly from zero to a value in the range 0.7–1. In these cases, linear plots can usually be obtained for half-order kinetics (*i.e.*, $P_T^{1/2}$ *vs.* t) up to about 70% of the reaction.

The general tendency towards zero-order kinetics at low temperatures and high pressures is observed over all the oxides.

The activation energies, E_A, calculated from the zero-order, half-order, and first-order rate constants are shown in Table V. The correlation is shown in parentheses. The activation energies using $k_{1/2}$ are lower than those obtained using k_0. This could be due to the fact that many of the values for k_0 are calculated from initial rates which are often anomalously low.

The results can be explained by assuming that the rate is dependent on the fraction of active surface covered by molecular hydrogen and/or oxygen, and that adsorption obeys the Langmuir isotherm.

A general equation can be derived of the form

$$-\frac{dP_T}{dt} = \frac{k(b_{O_2}P_{O_2})^x(b_{H_2}P_{H_2})^y}{(1 + b_{O_2}P_{O_2} + b_{H_2}P_{H_2})^{x+y}} \qquad (2)$$

where k is a proportionality constant, $x = 0$ or 1, $y = 0$, 1, or 2, b_{O_2} and b_{H_2} are the adsorption coefficients for oxygen and hydrogen, respectively, and P_{O_2} and P_{H_2} are the pressures of oxygen and hydrogen, respectively.

For a stoichiometric reaction, eq 2 can be expressed as

$$-\frac{dP_T}{dt} = \frac{(A_mP_T)^m}{(1 + BP_T)^m} \qquad (3)$$

where A_m and B are temperature-dependent constants, with B decreasing as temperature increases, and $m = 1$, 2, or 3.

Equation 3 will give rise to a change in apparent order during the course of a reaction from zero order when $BP_T \gg 1$ to m order when $BP_T \ll 1$. At low temperatures and high pressures BP_T will have a relatively large value and hence zero-order kinetics would be expected.

In an attempt to determine the value of m the data were analyzed for the three values of m. The constants B and A_1 ($m = 1$), A_2 ($m = 2$), and A_3 ($m = 3$) were evaluated from the differential and integrated forms of eq 3.

The value of m cannot be obtained from the differential form of eq 3. The data obey the three equations ($m = 1$, 2, or 3) equally well. Calculated values for A_1, A_2, and A_3 are of the correct order of magnitude and vary appropriately with temperature. The constants show a slight pressure dependence.

The integrated forms of eq 3 were fitted by the method of least squares, and all of the plots are linear. This is not unexpected in that all these equations have the same form; if the data fits eq 3 with $m = 1$, then the extra term in eq 3 with $m = 2$ will allow an even better fit. Analysis of the constants A_1, A_2, and A_3 show that they are in agreement with the values obtained by the previous method. However, eq 3 with $m = 1$ yields the most consistent results for the constant A_m and shows the most appropriate variation with temperature. The constants A_2 are often negative, and there is poor agreement between the values calculated by different methods. The constants A_3 are better than A_2, but there are several negative values and there is poor agreement between values calculated from runs at similar temperatures. All three constants again show a pressure dependence. The values for A_1 at a constant initial pressure of approximately 2.7 Torr are shown in Tables II, III, and IV for neodymium oxide, dysprosium oxide, and erbium oxide, respectively. The values have not been calculated when zero-order kinetics are obeyed. The apparent activation energies have been obtained by plotting log A_1 *vs.* $1/T$. The graphs are shown in Figure 8, and the activation energies are given in Table V. It can be seen that the values obtained from $k_{1/2}$, k_1, and A_1 agree within experimental error. Also, as shown in Table VI, the values agree well with those obtained by other

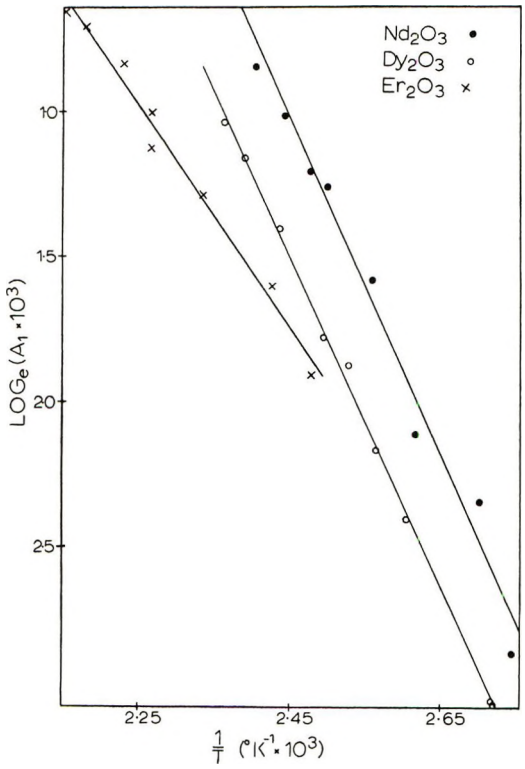

Figure 8. Arrhenius plots using the constant from eq 6 with $m = 1$, for the hydrogen–oxygen reaction over neodymium oxide, dysprosium oxide, and erbium oxide.

Table VI: Comparison of Activation Energies

Oxide	Average E_A using $k_{1/2}$, k_1, and A_1, kcal mol^{-1}	E_A,[a] kcal mol^{-1} Excess oxygen	Excess hydrogen	E_A,[b] kcal mol^{-1} Excess hydrogen
Nd_2O_3	11	17	10	7
Dy_2O_3	10	47	13	
Er_2O_3	9			8

[a] Reference 8. [b] Reference 9.

workers, except for the high values in excess oxygen.

In summary, the experimental data can best be explained by assuming a kinetic expression of the form shown in eq 3. Although there is some evidence for apparent orders greater than one, the most likely value for m is unity. The constant A_1, calculated from eq 3, shows some pressure dependence indicating that there may be a deactivation process occurring. The overall results are in line with the work of Antoshin, *et al.*,[11] who obtained an order of one over doped lanthanum oxide, and Bakumenko and Chashechnikova,[9] who obtained an order of one or less in hydrogen over several lanthanide oxides.

From the experimental data it is not possible to determine whether $x = 1$ and $y = 0$, or $x = 0$ and $y = 1$ in eq 2. Hydrogen and oxygen adsorption studies over neodymium oxide and dysprosium oxide[12] show that, at the pressures and temperatures involved in the present study, hydrogen adsorption is nondissociative whereas oxygen adsorption is dissociative. In addition, oxygen adsorption over dysprosium oxide is very small. Preliminary studies of the effect of catalyst pretreatment indicate that hydrogen pretreatment increases the rate whereas oxygen pretreatment either decreases the rate slightly or has no effect. This is in line with the activation energies shown in Table VI calculated in excess oxygen and excess hydrogen. In view of the above, and the fact that Bakumenko and Chashechnikova[9] suggest that the rate depends on the hydrogen pressure, the most likely kinetic expression is eq 2 with $x = 0$ and $y = 1$. However, adsorption studies indicate that at slightly higher temperatures than those involved in the present study, oxygen adsorption increases and, over neodymium oxide, the rate of oxygen adsorption is no longer instantaneous. Therefore, a slight change in temperature may affect the mechanism and hence the kinetics. There is evidence for apparent orders as high as three at 150° over neodymium oxide and dysprosium oxide. At these temperatures, it is possible that the data are best expressed in the form of eq 2 with $x = 1$ and $y = 2$.

Possible mechanisms which would give rise to this equation are those with a rate-determining step involving two adsorbed molecules of hydrogen and one adsorbed molecule of oxygen. A mechanism involving the intermediate production of adsorbed hydrogen peroxide would also give rise to this kinetic expression.

Conclusion

The experimental data presented in this paper obey the general kinetic expression

$$-\frac{dP_T}{dt} = \frac{(A_m P_T)^m}{(1 + BP_T)^m}$$

with the most consistent and appropriate values for A_m and B being obtained when $m = 1$. Further experiments are being conducted using nonstoichiometric ratios of hydrogen and oxygen, and the results will be presented in a subsequent paper.

Acknowledgment. Appreciation is expressed for considerable help given by Dr. R. Rudham, Chemistry Department, Nottingham University, England.

The Precursors of the Metal-Complexed Hydroperoxyl Radical[1]

by A. Samuni

Radiation Research Laboratories and Center for Special Studies, Mellon Institute of Science, Carnegie-Mellon University, Pittsburgh, Pennsylvania 15213 *(Received February 14, 1972)*

Publication costs assisted by Carnegie-Mellon University and the U. S. Atomic Energy Commission

The precursors of the metal-complexed paramagnetic intermediates generated in the course of redox reactions of hydrogen peroxide with metal ions have been studied by esr spectroscopy using *in situ* radiolysis. Thus the necessity of adding H_2O_2 and the interference of the resulting peroxy complexes were avoided. No complexed species were formed from the free metal ion in the absence of HO_2 radicals. However, when peroxy-metal complexes were present in the system both $\cdot OH$ and HO_2 gave rise to the same secondary species. The results indicate that the complexed radicals are formed through direct addition of HO_2 radical to the metal ion as well as *via* one-electron oxidation of peroxy-metal complexes by $\cdot OH$ and HO_2. These results support the formulation of the species produced in all cases as M–O–O·. It was found also that Zr^{IV} and Hf^{IV} in each case react with HO_2 to yield two different paramagnetic transients similar to those obtained from Ti^{IV}.

Introduction

Since the assignment of the two esr singlets observed[2] on mixing Ti^{III} ions with H_2O_2 as the spectrum of free radicals coordinated with Ti^{IV} ions,[3] a number of experiments have been performed to study similar metal-stabilized free radicals.[4-11] These studies were mainly carried out by generating HO_2 radicals in a flow system *via* redox reactions of H_2O_2 with various metal ions and following the reaction by esr spectroscopy. Although many of the transition-metal ions of the Sc, Ti, V, and Cr groups in their highest stable oxidation states were searched for the purpose of identifying the corresponding complexed radicals, in some of the systems investigated the transients have escaped detection. A better understanding of the formation and decay mechanisms of the complexed transients, as well as knowledge of their precursors, are prerequisite to the choice of the optimal experimental conditions under which these transients can be detected by esr spectroscopy. All previous studies were made in the presence of excess H_2O_2 so that it was not possible to predict whether $\cdot OH$ or HO_2 (or both) were involved in the reaction. Moreover, most of the metal ions studied form, in the presence of H_2O_2, various peroxy-metal complexes, and it would be helpful to know whether it is the metal ion or its peroxy complex that reacts with the primary radicals to yield the secondary ones. It was recently shown[12,13] that inadequate understanding of the metal ion + H_2O_2 redox system has led to many erroneous interpretations. Therefore, in view of the wide use of these redox reactions as a source of free radicals and the frequent occurrence of the complexed transients throughout the reactions, a further study of these systems seemed warranted. The present work was undertaken to investigate the origin of transition-metal complexed radicals which might be formed *via* several different mechanisms. An attempt is also made to account for the contradictory experimental reports and interpretations regarding the appearance of a two-lined spectrum in the case of the elements of group IV (Ti^{IV}, Zr^{IV}, Hf^{IV}). The complexed radical was produced through a steady-state, *in situ* radiolysis of the acid aqueous solutions of the metal ions. Using this technique it was possible to avoid the necessity of adding hydrogen peroxide to the system. Thus the interference of peroxy-metal complexes in the reactions was prevented. Moreover, by properly choosing experimental conditions, the formation of either $\cdot OH$ or HO_2 radicals in the irradiated solution was controlled thus enabling us to distinguish among the various formation mechanisms of the radicals.

The results obtained in the present study indicate that in the absence of H_2O_2 no detectable reaction of $\cdot OH$ with any of the transition metal ions studied takes

(1) Supported in part by the U. S. Atomic Energy Commission.

(2) (a) W. T. Dixon and R. O. C. Norman, *Nature (London)*, **196**, 891 (1962); (b) W. T. Dixon and R. O. C. Norman, *J. Chem. Soc.*, 3119 (1963).

(3) Y. S. Chiang, J. Craddock, D. Mickewich, and J. Turkevich, *J. Phys. Chem.*, **70**, 3509 (1969).

(4) M. S. Bains, J. C. Arthur, Jr., and O. Hinojosa, *Inorg. Chem.*, **9**, 1570 (1970).

(5) M. S. Bains, J. C. Arthur, Jr., and O. Hinojosa, *J. Amer. Chem. Soc.*, **91**, 4673 (1969).

(6) (a) M. C. R. Symons, *J. Chem. Soc. A*, 1889 (1970); (b) Y. Shimizu, T. Shiga, and K. Kuwata, *J. Phys. Chem.*, **74**, 2929 (1970).

(7) R. W. Brandon and C. S. Elliott, *Tetrahedron Lett.*, **44**, 4375 (1967).

(8) T. Ozawa, Y. Kirino, M. Setaka, and T. Kwan, *Nippon Kagaku Zasshi*, **95**, 304 (1971).

(9) V. F. Shuvalov, N. M. Bazhin, V. M. Berdnikov, A. P. Merkulov, and V. K. Fedorov, *Zh. Strukt. Khim.*, **10**, 548 (1969).

(10) M. Setaka, Y. Kirino, T. Ozawa, and T. Kwan, *J. Catal.*, **15**, 209 (1969).

(11) A. Samuni and G. Czapski, *J. Phys. Chem.*, **74**, 4592 (1970).

(12) G. Czapski, *ibid.*, **75**, 2957 (1971).

(13) G. Czapski, A. Samuni, and D. Meisel, *ibid.*, **75**, 3271 (1971).

place to yield complexed radicals. On the other hand, some metal ions such as Th^{IV}, U^{VI}, Ti^{IV}, Zr^{IV}, Hf^{IV}, and Ce^{III}, react with HO_2 to form the complexed hydroperoxyl radical. In the presence of hydrogen peroxide the complexed radicals are generated probably *via* one-electron oxidation of the peroxy–metal complexes by both ·OH and HO_2 radicals.

Experimental Section

Reagents. Reagent grades were used when available (Fisher Scientific Co. Certified thorium nitrate; Fisher Scientific Co. Purified ammonium vanadate, uranyl sulfate, zirconium sulfate, and titanium sulfate; Research Inorganic Chemicals lanthanum nitrate, zirconium nitrate, sodium metavanadate, hafnium nitrate, and niobium pentoxide; G. Frederick Smith Chemical Co. thorium perchlorate, zirconyl perchlorate, lanthanum perchlorate, uranyl perchlorate, and cerous perchlorate; and Baker Analyzed Reagents hydrogen peroxide 30% and perchloric acid). All the chemicals were used without further purification. The niobium pentoxide was dissolved in sulfuric acid as described formerly.[14] Acidities were adjusted (to pH 1, unless otherwise stated) using perchloric acid. Solutions were prepared with doubly distilled water. Regularly the perchlorate salts of the metal ions studied were used, but no differences in the obtained results were found when the perchlorate was replaced by the sulfate anion. When peroxy–metal complexes were studied, the metal ion solutions were mixed with hydrogen peroxide prior to irradiation. Introduction of oxygen into the solution was carried out by bubbling a nitrogen–oxygen mixture rather than pure oxygen since the oxygenation of the solution resulted in a considerable broadening of the esr lines. On measuring the esr spectra in deaerated and aerated solutions, the line widths were found to be practically the same. Deoxygenation of the solutions was done by bubbling with Airco prepurified nitrogen.

The steady-state, *in situ* radiolysis esr technique and the experimental setup have been described elsewhere.[15,16] A conventional X-band spectrometer was used and the radiation source a 2.8-MeV Van de Graaff accelerator. The flow rate of the sample solution was about 1–0.5 cc/sec. All experiments were carried out at ~15°.

Results and Discussion

There is some controversy in the literature concerning the formation, reactions, and chemical nature of the complexed radicals. For instance, the eight-lined spectrum which appears during the oxidation of VO^{2+} by H_2O_2 has been accounted for in different ways

$$VO_2^+ + HO_2 \longrightarrow VO_2^+\text{–}HO_2 \quad (1)^{8,10}$$

$$VO(O_2)^+ + \cdot OH \longrightarrow VO(\cdot O_2)^{2+} + OH^- \quad (2)^{17}$$

$$VO(O_2)^+ + HO_2 \longrightarrow VO(\cdot O_2)^{2+} + HO_2^- \quad (3)^{11}$$

while in the case of titanium + H_2O_2 the number of the reaction schemes suggested was even higher. Denoting schematically the metal ion (VO_2^+), its peroxy complex ($VO(O_2)^+$), and the complexed radical formed (VO_2^+–HO_2) as M, M–H_2O_2, and ·P, respectively, the various mechanisms can be written generally for all metals as follows

$$M + \cdot OH \longrightarrow \cdot P \quad (4)$$

$$M + HO_2 \longrightarrow \cdot P \quad (5)$$

$$M\text{–}H_2O_2 + \cdot OH \longrightarrow \cdot P \quad (6)$$

$$M\text{–}H_2O_2 + HO_2 \longrightarrow \cdot P \quad (7)$$

$$M\text{–}H_2O_2 + \cdot OH \longrightarrow OH^- + \cdot P \quad (8)$$

$$M\text{–}H_2O_2 + HO_2 \longrightarrow HO_2^- + \cdot P \quad (9)$$

where reactions 4–7 are addition reactions and reactions 8 and 9 are one-electron redox processes. (The schematic notations M and M–H_2O_2 are adopted for the metal ion and its peroxy complex(es), irrespective of their hydrolyzed forms, both in the highest stable oxidation state of the metal. ·P represents the complexed paramagnetic species, and no attempt has been made here to draw any conclusions concerning the various ionic species, either of the metal ion or ·P, present in the reaction mixtures.) Although there is some evidence that most of the complexed radicals detected hitherto might be produced in the absence of ·OH radicals, it was not yet made clear whether reactions 4, 6, and 8 should be excluded also when ·OH radicals do occur in the system.[3,18–22] To check the existence of reactions 4–9 the occurrence of the possible reacting species (M, M–H_2O_2, ·OH, HO_2) was controlled by choosing proper experimental conditions and the solutions of the metal ions studied were irradiated in the following manner: (a) in the absence of both O_2 and H_2O_2 where neither HO_2 nor M–H_2O_2 were present; (b) in the presence of O_2 where both HO_2 and ·OH do occur in the solution; (c) in the presence of both O_2 and H_2O_2 (excess) (As a result the dominant species were HO_2 and M–H_2O_2.); (d) in the presence of a low [H_2O_2] and in the absence of oxygen (in such a case neither M nor HO_2 were present in the solution due to binding of the H_2O_2 molecules by the metal ions).

(14) N. Adler and C. F. Hiskey, *J. Amer. Chem. Soc.*, **79**, 1827, 1831, 1834 (1957).

(15) R. W. Fessenden and R. H. Schuler, *J. Chem. Phys.*, **39**, 2147 (1963).

(16) K. Eiben and R. W. Fessenden, *J. Phys. Chem.*, **75**, 1186 (1971).

(17) H. B. Brooks and F. Sicilio, *Inorg. Chem.*, **10**, 2530 (1971).

(18) K. Takakura and B. Ranby, *J. Phys. Chem.*, **72**, 164 (1968).

(19) F. Sicilio, R. E. Florin, and L. A. Wall, *ibid.*, **70**, 47 (1966).

(20) J. Stauff and H. J. Huster, *Z. Phys. Chem.*, (*Frankfurt am Main*), **55**, 39 (1967).

(21) N. C. Verma, K. P. Mishra, and B. B. Singh, *Indian J. Chem.*, **9**, 882 (1971).

(22) V. H. Fischer, *Ber. Bunsenges. Phys. Chem.*, **71**, 685 (1967).

Table I: Esr Signals in Irradiated Aqueous Solutions Containing 4 m*M* Metal Ion in 0.1 *M* $HClO_4$

Conditions	Metal ion							
	Th^{IV}	U^{VI}	Ti^{IV}	Zr^{IV}	Hf^{IV}	Ce^{III}	V^{V}	Nb^{V}[a]
Deaerated solution	...	...	...	...	...	...	...	...
Aerated solution	Single line	Single line	Two lines	Two lines	Two lines	Single line	...	...
	$g = 2.01828$	$g = 2.0209$	$g_1 = 2.01339$	$g_1 = 2.01485$	$g_1 = 2.01653$	$g = 2.01829$		
	$\Delta H = 1.05$ G	$\Delta H = 1.2$ G	$\Delta H_1 = 0.6$ G	$\Delta H_1 = 1.0$ G	$\Delta H_1 = 1.0$ G	$\Delta H = 1.05$ G		
			$g_2 = 2.01184$	$g_2 = 2.01391$	$g_2 = 2.01487$			
			$\Delta H_2 = 0.5$ G	$\Delta H_2 = 0.6$ G	$\Delta H_2 = 0.7$ G			
Aerated solution $\frac{[H_2O_2]}{[M]} = 5$	Single line	Single line	Two lines	Single line	Two lines	Single line	Eight lines	Ten lines
	$g = 2.01828$	$g = 2.0209$	$g_1 = 2.01339$	$g_1 = 2.01510$	$g_1 = 2.01653$	$g = 2.01829$	$g = 2.0109$	$g = 2.0110$
	$\Delta H = 1.05$ G	$\Delta H = 1.2$ G	$\Delta H_1 = 0.6$ G	$\Delta H_1 = 2.2$ G	$\Delta H_1 = 1.0$ G	$\Delta H = 1.05$ G	$\Delta H = 0.74$–0.66 G	$\Delta H = 0.8$ G
			$g_2 = 2.01184$		$g_2 = 2.01487$		$a = 4.5$ G	$a = 6.2$ G
			$\Delta H_2 = 0.5$ G		$\Delta H_2 = 0.7$ G			
Deaerated solution $\frac{[M]}{[H_2O_2]} = 5$	Single line	Single line	Two lines	Three lines	Two lines	Single line	Eight lines	Ten lines
	$g = 2.01828$	$g = 2.0209$	$g_1 = 2.01339$	$g_1 = 2.01485$	$g_1 = 2.01653$	$g = 2.01829$	$g = 2.0109$	$g = 2.0110$
	$\Delta H = 1.05$ G	$\Delta H = 1.2$ G	$\Delta H_1 = 0.6$ G	$\Delta H_1 = 1.0$ G	$\Delta H_1 = 1.0$ G	$\Delta H = 1.05$ G	$\Delta H = 0.74$–0.66 G	$\Delta H = 0.8$ G
			$g_2 = 2.01184$	$g_2 = 2.01391$	$g_2 = 2.01487$		$a = 4.5$ G	$a = 6.2$ G
			$\Delta H_2 = 0.5$ G	$\Delta H_2 = 0.6$ G	$\Delta H_2 = 0.7$ G			
				$g_3 = 2.01258$				
				$\Delta H_3 = 0.5$ G				

[a] At 0.1 *M* H_2SO_4.

a. Deaerated Solutions. The esr signals of the radicals present during the steady-state irradiation of the acid (0.1 *M* $HClO_4$) aqueous solutions containing 4 m*M* metal ion were recorded for the following transition metal ions: Ti^{IV}, Zr^{IV}, Th^{IV}, Ce^{III}, V^{V}, Nb^{V}, U^{VI}, and Hf^{IV}. The irradiations were carried out first in acid solutions in the absence of oxygen where ·H and ·OH radicals are the only species which react with the solute. Under these experimental conditions no esr signals due to metal-complexed radicals were observed in any of the irradiated solutions. Considering the high production rate[16] of the primary radicals and the slow decay of the secondary ones searched, the absence of any detectable signal leads to the exclusion of the possibility formerly suggested[20] that ·P is directly formed *via* reaction 4. This result is also in accord with previous conclusions based on the similarity between the esr signals of ·P formed from vanadium[6a] and titanium[6b] and those of peroxy species (M–O–O·) rather than monoxy (M–O·) species.[23] Therefore, it is possible to conclude that no detectable addition reaction of ·OH radical to any of the metal ions studied takes place.

b. Aerated Solutions. Acid aqueous solutions of the metal ions have been irradiated in the presence of oxygen, the esr spectra were recorded, and the results are summarized in Table I. Under those experimental conditions all ·H atoms are converted into $H\dot{O}_2$ radicals

$$\cdot H + O_2 \longrightarrow H\dot{O}_2 \qquad (10)$$

leaving [·OH] practically unaffected. Hence, the formation of the observed complexed radicals undoubtedly involves a direct addition of the $H\dot{O}_2$ radical to the metal ion (*i.e.*, reaction 5), a conclusion which agrees with former results.[4,9,11] It is seen in Table I that Th^{IV}, U^{VI}, Ti^{IV}, Zr^{IV}, Hf^{IV}, and Ce^{III} react directly with the $H\dot{O}_2$ radical. In the case of Zr^{IV} and Ce^{III} the present experimental results differ considerably from those previously reported.[4,9,11] Furthermore, the complexed species thought to be[8-10] formed from $H\dot{O}_2$ and vanadium(V) ions (VO_2^+) was *not* detected even when O_2 was introduced into the solution, a result which indicates that neither ·OH nor $H\dot{O}_2$ react with VO_2^+ to yield the complexed radical. These discrepancies could stem from the fact that premixing of the metal ion with H_2O_2 is essential in some cases (as for V^{V}) but unnecessary in others. To check this possibility, the experiments were repeated when hydrogen peroxide was added to the solutions.

c. Aerated Solutions Containing H_2O_2. In the presence of an excess of H_2O_2 the ·OH radicals also are converted into $H\dot{O}_2$ radicals through reaction 11

$$\cdot OH + H_2O_2 \longrightarrow H_2O + H\dot{O}_2 \qquad (11)$$

(23) P. R. Edwards, S. Subramanian, and M. C. R. Symons, *Chem. Commun.*, 799 (1968).

Figure 1. The esr spectra (second derivative) obtained on radiolysis of aerated 0.1 M $HClO_4$ solutions containing 4 mM of (a) Ti^{IV}, (b) Zr^{IV}, and (c) Hf^{IV}. Field increases from left to right. The relative positions of the lines in the different radicals are properly indicated (see Table I for g values).

thus increasing the HO_2 chemical yield by a factor of 1.8 compared with the oxygenated H_2O_2-free solutions (primary yields of ·H, ·OH, and e_{aq}^- are about 0.6, 2.8, and 2.8, respectively). Furthermore, peroxy–metal ion complexes were present in the irradiated solution due to the presence of the hydrogen peroxide[24-28] (see Table II). As a result the complexed-transients involving V^V and Nb^V have become detectable, indicating that peroxy complexes are, in this case, the precursors of ·P rather than the metal ions themselves, *i.e.*, reactions 7 and/or 9.

The results shown in Table I and the interpretation given above can be compared with previous ones[8,9,11] attributing the complexed species formed to the metal ions and/or their peroxy complexes. The contradictory explanations stem from the role of hydrogen peroxide in the metal ion–H_2O_2 redox systems. To demonstrate the complications which arise from studying the complexed radical using the (widely used) rapid-mixing technique, let us consider the titanium(III) + H_2O_2 redox system. The reactions which take place at 0.1 M $HClO_4$ are

$$Ti^{III} + H_2O_2 \xrightarrow{k_{12}} Ti^{IV} + OH^- + \cdot OH \quad (12)$$

$$Ti^{III} + \cdot OH \xrightarrow{k_{13}} Ti^{IV} + OH^- \quad (13)$$

$$Ti^{IV} + H_2O_2 \underset{k_{-14}}{\overset{k_{14}}{\rightleftharpoons}} Ti^{IV}\text{–}H_2O_2 \quad (14)$$

as well as reaction 11, taking into account, of course, the self-recombination and cross-recombination reactions of ·OH and HO_2. Now, considering the corresponding rate constants ($k_{12} = 5 \times 10^2\ M^{-1}\ sec^{-1}$,[29] $k_{13} = 3 \times 10^9\ M^{-1}\ sec^{-1}$,[29] $k_{14} = 1.2 \times 10^2\ M^{-1}\ sec^{-1}$,[25] $k_{11} = 1.2 \times 10^7\ M^{-1}\ sec^{-1}$,[30] $\log K_{14} = 4$[25]) it seems evident that reactions 11–14 take place concurrently. Consequently, provided $[H_2O_2] > [Ti^{III}]$, titanous ions, titanic ions, peroxy–titanic ions, as well as ·OH and HO_2 radicals are all present in the system simultaneously. Thus the formation of the peroxy–metal complexes, before the primary reaction is over, makes it almost impossible to ascertain which are the precursors of the long-lived secondary radicals.

Table II: Peroxy Complexes[a] of the Metal Ions at 0.1 M $HClO_4$

Metal ion	Composition of complex	Log K_{eq}	Reference	Remarks
Ti^{IV}	Monoperoxy	4.27	24	
V^V	Monoperoxy	4.54	25	
	Diperoxy	0.11	25	
Nb^V	Monoperoxy	12.7	26, 14	$<H_2SO_4$ 40%
	Diperoxy		14	$>H_2SO_4$ 40%
U^{VI}	Monoperoxy	32	27	
	Diperoxy	60	27	
Zr^{IV}	Mono- and diperoxy		28	

[a] Except in the case of Ti^{IV}, additional complexes with different ratio of peroxy group per metal ion do exist, but at the low metal ion concentration and pH used, the mono- and diperoxy complexes are dominant. See ref 28 for detailed description.

The comparison of the results obtained in the presence and in the absence of H_2O_2 (Table I) indicates that, in the case of group V metals, reaction 5 probably does not occur (to any detectable extent)—a conclusion which supports previous similar suggestions.[11] It is also seen in Table I that the esr spectra of the radicals formed from U^{VI}, Th^{IV}, Ce^{III}, Ti^{IV}, and Hf^{IV} were not changed on the addition of H_2O_2 into the solution. It might suggest that the same complexed paramagnetic

(24) E. Gastinger, *Z. Anorg. Allg. Chem.*, **275**, 331 (1954).

(25) M. Orhanovic and R. Wilkins, *J. Amer. Chem. Soc.*, **89**, 278 (1967).

(26) L. G. Sillen, "Stability Constants of Metal Ion Complexes," *Chem. Soc. Spec. Publ.*, **No. 17**, 206 (1964).

(27) A. I. Moskvin, *Radiokhimiya*, **10**, 13 (1968).

(28) J. A. Connor and B. A. V. Ebsworth, *Advan. Inorg. Chem. Radiochem.*, **6**, 279 (1964).

(29) G. Czapski, A. Samuni, and D. Meisel, submitted for publication.

(30) M. Anbar and P. Neta, *Int. J. Appl. Radiat. Isotopes*, **18**, 493 (1967).

species are formed in the presence and in the absence of H_2O_2.

It is noteworthy that H_2O_2 formed by the ionizing radiation was present in the system throughout all of the experiments. Nevertheless, no esr signals due to the complexed radicals were observed unless either oxygen or hydrogen peroxide was added to the solution prior to irradiation (see Table I). Indeed, the calculation of the $[H_2O_2]$ produced through the irradiation and the $[M\text{–}H_2O_2]$ consequently formed shows that $[\cdot P]$ was too low to be detected (for the case of $M = Ti^{IV}$).

d. Deaerated Solutions, $[H_2O_2] < [M]$. The complexed radicals have already been obtained in systems where ·OH radicals were absent as by $Ce^{IV} + H_2O_2$[4,9,11] reaction or *via* electrolytic oxidation of peroxy titanium.[31] Since ·OH is a more efficient oxidant than $H\dot{O}_2$, such a mechanism implies that ·P radicals formed through mere oxidation of peroxy metals would be formed from ·OH radical also. This possibility was studied by irradiating deaerated solutions where $[H_2O_2] < [M]$. Under such experimental conditions no $H\dot{O}_2$ radicals are formed through reactions 10 or 11 either, provided the peroxy complex formed between the metal ion and H_2O_2 is very stable. As a result, the reacting species in the system turn out to be $M\text{–}H_2O_2$ and ·OH rather than M and $H\dot{O}_2$. Considering Table II it is seen that some of the metal ion investigated forms very stable peroxy complexes with H_2O_2. Nevertheless, as shown in Table I, all metal ions yielded observable esr signals in deaerated solutions where $[H_2O_2] < [M]$, indicating the formation of the complexed radical also from $M\text{–}H_2O_2$ and ·OH. Again, the complexed species formed through addition of $H\dot{O}_2$ to M (reaction 5) were indistinguishable, except for the case of Zr^{IV}, from those produced from ·OH and $M\text{–}H_2O_2$. Therefore, *assuming* the radicals formed through the various mechanisms are identical implies the exclusion of the existence of reactions 6 and 7. This conclusion suggests the following formation mechanisms for the metal ions investigated: (a) reaction 5 in the case of Ce^{III} and maybe Th^{IV}, too

$$Ce^{3+} \text{ (or } CeOH^{2+}) + H\dot{O}_2 \longrightarrow Ce(\cdot O_2)^{2+} + H^+$$

(b) reactions 8 and 9 in the cases of V^V and Nb^V

$$VO(O_2)^+ + H\dot{O}_2 \longrightarrow HO_2^- + VO(\cdot O_2)^{2+}$$
$$VO(O_2)^+ + \cdot OH \longrightarrow OH^- + VO(\cdot O_2)^{2+}$$

(c) reactions 5, 8, and 9 in the cases of Ti^{IV}, Hf^{IV}, U^{VI}, and Zr^{IV}

$$TiO^{2+} + H\dot{O}_2 \longrightarrow TiO(\cdot O_2)^+ + H^+$$
$$TiO(O_2) + H\dot{O}_2 \longrightarrow TiO(\cdot O_2)^+ + HO_2^-$$
$$TiO(O_2) + \cdot OH \longrightarrow TiO(\cdot O_2)^+ + OH^-$$

e. Transients with Higher Peroxide Content. Most of the metal ions investigated are capable of forming complexes with peroxide-to-metal ratios higher than 1:1. Nevertheless, the monoperoxy complexes are dominant in the solutions (except for U^{VI}) provided $[H_2O_2] < [M]$. On introducing H_2O_2 into the metal ion solution no change in the magnetic parameters of the obtained spectra was observed. These results suggest, as mentioned above, that complexed radicals formed in the presence and the absence of H_2O_2 are either identical or indistinguishable by esr spectroscopy. The latter possibility is supported by the observation of the invariance of the spectra, even under a hundredfold increase of the H_2O_2 concentration. In other words, the unpaired electron being located on a peroxy group associated with the metal ion is presumably affected very little by coordination of an additional peroxy group to that ion. Evidently this is not the case with zirconium(IV), since increasing $[H_2O_2]$ in the Zr^{IV} ion solution resulted both in the disappearance of the high-field line as well as the broadening of the low-field line and shifting it towards a lower field. Hence, the previously detected[4,9,11] broad line in the $Zr^{IV} + H_2O_2$ systems is probably attributable to higher peroxy complex(es) of this ion.

f. Two-Lined Spectra. In view of the close similarity between certain of the transition metals of group IV, particularly Ti, Zr, and Hf, the previously reported marked differences among the esr signals of their complexes with $H\dot{O}_2$ seemed obscure. The two esr lines (2.5 G apart) appearing in the Ti system are ascribed by all recent workers to two different paramagnetic intermediates involving the Ti^{IV} ion. On the other hand, the Zr^{IV} ion was found to yield a comparatively wide *single* line[4,9,11] with $\Delta H > 2$ G. In the case of Hf^{IV}, a two-lined spectrum (2.5 G apart) has been observed[4] and was attributed to a *single* species whose esr line has been split due to a hyperfine interaction.[4] Previously, Fischer[22] related the very weak "satellite" lines accompanying the intense pair of lines formed from Ti^{IV} to hyperfine splitting caused by the metal ion. Since Zr and Hf as well as Ti are labeled by nonzero nuclear spin isotopes roughly at the same level (^{47}Ti, $I = {}^5/_2$, natural abundance: 7.75%; ^{49}Ti, $I = {}^7/_2$, 5.51%; ^{91}Zr, $I = {}^5/_2$, 11.23%; ^{177}HF, $I = {}^7/_2$, 18.39%; ^{179}Hf, $I = {}^9/_2$, 13.78%), it would be reasonable to anticipate similar behavior of these three systems. As shown in Figure 1, each of the three metal ions, Ti, Zr, and Hf, when irradiated in the presence of O_2 gave rise to an esr spectrum consisting of a pair of lines separated by 2.54, 1.54, and 2.72 G, respectively. Previously it was reported[4] that no change in the intensities ratio of the two-lined spectrum of $Hf^{IV}\text{–}H\dot{O}_2$ was observed when the experimental conditions were varied. This result led Bains, *et al.*,[4] to relate the spectrum to a single species. However, the results obtained in the course of the present study show that

(31) H. B. Brooks and F. Sicilio, *J. Phys. Chem.*, **74**, 4565 (1970).

this is not the case. On changing the concentration of the metal ion, the relative intensity of the high-field line compared with that of the low-field line was not kept constant in the cases of Zr and Hf. These results exclude the assignment of the Hf^{IV}–$H\dot{O}_2$ two line spectrum to a line splitting and indicate that two different complexed radicals are formed by the $H\dot{O}_2$ addition to the metal ion. As to the Ti^{IV}–$H\dot{O}_2$, several attempts have been made to account for the appearance of its "doublet" spectrum. The two lines were atrributed to: (1) $H\dot{O}_2$ and ·OH radicals;[32] (2) $H\dot{O}_2$ radical and ·OH or $H\dot{O}_2$ radical associated with Ti^{IV};[33] (3) ·OH radical and ·OH radical complexed with Ti^{IV};[19] (4) ·OH and $H\dot{O}_2$ radicals, both complexed with Ti^{IV};[3,9,20,34,35] (5) ·OH and $H\dot{O}_2$ radicals, both complexed with peroxy–Ti^{IV};[18] (6) Ti^{IV}–OO· and a dimeric species Ti^{IV}–O–O–Ti^{IV}–OO·;[22] (7) $H\dot{O}_2$ radicals coordinated with Ti^{IV}–$(H_2O_2)_n$ complexes of different types.[6b] Recently it was even suggested[21] that these long-lived paramagnetic species are formed from Ti^{III}–OH–Ti^{IV} or Ti^{III}–$H\dot{O}_2$–Ti^{IV} complexes.

In view of the results obtained in the present work, it appears that both lines can be generated in the absence of peroxy complexes of the metal ions (Ti, Zr, and Hf), *i.e.*, from M ions and $H\dot{O}_2$ radicals solely. Regarding the pair of esr lines appearing in the Ti system, it is almost generally accepted to relate the low-field line to the Ti^{IV}–$H\dot{O}_2$ radical ($TiO(\cdot O_2)^+$). Indeed, the present results confirm that assignment. But it seems that the suggested complexes of Ti^{IV}–(·OH),[3,9,20,34] Ti^{III}–OH–Ti^{IV},[21] and Ti^{IV}–$(H_2O_2)_n$–HO_2[6b] should be ruled out on the grounds of the experimental results. However, the possibility of an existence of a dimeric form as previously suggested[22] cannot be excluded as is the assignment of the two lines to different hydrolyzed forms of the metal ions. (The same arguments hold for Zr^{IV} and Hf^{IV} as well.)

g. Short-Lived Complexed Radicals. The lifetime of the complexed $H\dot{O}_2$ radicals has been shown[5-11] to be very long compared with the decay time of the free $H\dot{O}_2$. This fact was one of the reasons which made it easier to detect these species. Hence, a complexed radical with a shorter lifetime might sometimes escape detection. Recently the esr spectra of the very unstable complexed radicals Nb^V–$H\dot{O}_2$ and La^{III}–$H\dot{O}_2$ were identified[36] and previous failure to detect them[4] was accounted for. The difficulty caused by the fast decay rate of the radicals was overcome in the present study by generating the radicals at the observation point by *in situ* radiolysis. As can be seen in Table I the ten-lined spectrum of Nb^V–$H\dot{O}_2$ (^{93}Nb, $I = {}^9/_2$, natural abundance = 100%) was observed on irradiating the peroxy–niobium solution. On the other hand, no esr signal due to La^{III}–$H\dot{O}_2$[36] was observed even on the addition of high La^{III} concentrations. The failure to detect the La^{III}–$H\dot{O}_2$ could stem from the following reasons: (a) the loss of sensitivity by an order of magnitude due to the splitting of the line (^{139}La, $I = {}^7/_2$, natural abundance = 100%); (b) the too low steady-state concentration of the radicals caused either by a very fast decay rate or a very low stability of the complex La^{III}–$H\dot{O}_2$. This explanation is in accord with the very poor signal-to-noise ratio achieved when the La^{III}–$H\dot{O}_2$ was produced by the rapid mixing technique.[36]

The Ce^{III}–$H\dot{O}_2$ complexed radical has been shown[37,38] to be a short-lived radical too; nevertheless, it was detected previously[32,37,38] using the rapid-mixing esr technique. On comparing the magnetic parameters of the Ce^{III}–$H\dot{O}_2$ and the Th^{IV}–$H\dot{O}_2$ signals (Table I), the two spectra seemed to be identical and the possibility that one of the metal ions was contaminated by the other was considered. Since both signals were observed even at low concentrations of the metal ions and their intensities were of the same order of magnitude, the possibility that one species only is responsible for both signals seemed unlikely. The incompatibility of the present result with those previously reported[4] where Ce^{III}–$H\dot{O}_2$ was not found can be explained as follows. The use of sulfuric acid by Bains, *et al.*,[4] for adjusting the pH prevented the detection of this species while, where $HClO_4$ was used, the Ce^{III}–$H\dot{O}_2$ was observable.[37,38] To verify this explanation sulfuric acid has been added to the aerated solution of Ce^{III} prior to irradiation. This resulted in a complete disappearance of the Ce^{III}–$H\dot{O}_2$ esr signal, even at $[H_2SO_3] = 0.1\ M$, while Th^{IV}–$H\dot{O}_2$ signal was observed even in sulfuric acid. (The different behavior in the various acids has already been discussed elsewhere.[39]) It should be noted that exclusion of a Ce^{IV}–$H\dot{O}_2$ stable radical by Bains, *et al.*,[4] is apparently correct, since $H\dot{O}_2$ reduces Ce^{IV} very rapidly in both sulfuric and perchloric media.[39]

Conclusions

It would be justifiable to refer to the various complexed species produced in the metal–H_2O_2 system as hydroperoxyl radicals complexed by metal ions (M–O–O·).

Transition metal ions form complexed radicals through direct addition of $H\dot{O}_2$ radical but *not* of ·OH radical.

When H_2O_2 is present in the system, the secondary

(32) L. H. Piette, G. Bulow, and K. Loeffler, American Chemical Society, Division of Petroleum Chemistry, C9–C19 (1964).
(33) A. R. Metcalf and W. A. Waters, *J. Chem. Soc. B*, 340 (1967).
(34) M. S. Bains, J. C. Arthur, Jr., and O. Hinojosa, *J. Phys. Chem.*, 72, 2250 (1968).
(35) W. A. Armstrong, *Can. J. Chem.*, 47, 3737 (1969).
(36) G. Czapski and A. Samuni, unpublished results.
(37) G. Czapski and A. Samuni, *Israel J. Chem.*, 7, 361 (1969).
(38) G. Czapski, H. Levanon, and A. Samuni, *ibid.*, 7, 375 (1969).
(39) A. Samuni and G. Czapski, *ibid.*, 8, 551 (1970).

paramagnetic species are produced *via* an oxidation of the peroxy complexes of the metal ions by both HO_2 and ·OH radicals.

The complexed radicals produced from different peroxy complexes of the same metal ion are (except for Ze^{IV}) indistinguishable by esr spectroscopy.

Ti^{IV}, Zr^{IV}, and Hf^{IV} exhibit similarity by yielding two different complexed radicals each on addition of HO_2 to the metal ion, even in the absence of H_2O_2. This is probably due to different hydrolyzed or dimeric forms of the metal ions.

Nb^{V} and V^{V} do not form complexed radicals through the reaction of the free metal ions but *via* their peroxy complexes only.

Measurement of the Rate Constant for H + H_2CO → H_2 + HCO at 297–652°K

by A. A. Westenberg* and N. deHaas

Applied Physics Laboratory, The Johns Hopkins University, Silver Spring, Maryland 20910 *(Received February 14, 1972)*

Publication costs assisted by the Bureau of Naval Ordnance

Absolute measurements of the rate constant for the reaction H + H_2CO → H_2 + HCO (k_1) over the temperature range 297–652°K are reported. A fast-flow reactor with esr detection for H atom decay was used. The Arrhenius expression obtained was $k_1 = 1.35 \times 10^{13} \exp(-3760/RT)$ cm^3 mol^{-1} sec^{-1}. Comparisons with other data are made.

The rate constant of the reaction

$$H + H_2CO \longrightarrow H_2 + HCO \qquad (1)$$

has been measured directly only at room temperature,[1] while k_1 relative to other reactions has been determined by more complex photolysis[2,3] and explosion limit[4] studies at higher temperatures. We report here the direct measurement of k_1 over a temperature range 297–652°K.

The technique was that used in several previous studies from this laboratory, which has been adequately described.[5-7] It is a fast-flow system with movable stable gas (H_2CO) injector and a fixed esr cavity (outside the heated reactor) to monitor H decay, the latter being furnished by a microwave discharge in a trace of H_2 (<0.5%) in helium carrier. The quartz reactor was coated with H_3BO_3 to reduce H loss on the walls, although all first-order losses of H (not dependent on the presence of H_2CO) cancel out in this technique. H_2CO was supplied directly and continuously from paraformaldehyde heated to 60–80° in a thermostatically controlled oven and throttled to the injector through a needle valve. The tubes between the supply of paraformaldehyde in the oven and the injector did not require heating, and a steady, reproducible flow of H_2CO was readily furnished in this way. Metering was accomplished after each run by transferring the H_2CO flow to a calibrated volume and timing the pressure rise. As usual in this technique, the (H_2CO) was always in large excess over (H) so that the decay of (H) could be treated as pseudo first order.

The logarithmic (H) decay slopes were uniformly excellent straight lines over a factor of 3–10 decrease in (H). This was accomplished by moving the H_2CO injector typically over distances of 20–70 cm depending on conditions. From the slope, the linear velocity, and the known (H_2CO), a value of nk_1 was determined for each run. Several runs at each reactor temperature were usually performed at different H_2CO and He flows and pressures. Corrections of a few per cent for axial diffusion[6] were applied.

The value of n in this system was assumed to be 2, since reaction 1 is clearly followed by the fast secondary step H + HCO → H_2 + CO and, in the case where H_2CO is in excess, no other appreciable secondary reactions are likely. That CO is the only major product (other than H_2) formed and is equal to the H_2CO con-

(1) W. R. Brennen, I. D. Gay, G. P. Glass, and H. Niki, *J. Chem. Phys.*, **43**, 2569 (1965).

(2) R. Klein, J. R. McNesby, M. D. Scheer, and L. J. Schoen, *ibid.*, **30**, 58 (1959).

(3) J. R. McNesby, M. D. Scheer, and R. Klein, *ibid.*, **32**, 1814 (1960).

(4) R. R. Baldwin and D. W. Cowe, *Trans. Faraday Soc.*, **58**, 1768 (1962).

(5) A. A. Westenberg and N. deHaas, *J. Chem. Phys.*, **46**, 490 (1967).

(6) A. A. Westenberg and N. deHaas, *ibid.*, **47**, 1393 (1967).

(7) A. A. Westenberg and N. deHaas, *ibid.*, **50**, 707 (1969).

Table I: Summary of Measurements of k_1 for $H + H_2CO \rightarrow H_2 + HCO$[a]

T, °K	P, Torr	v, cm/sec	(H_2CO), mol/cm³	k_1, cm³ mol⁻¹ sec⁻¹
297	1.17	2630	8.78×10^{-10}	2.6×10^{10}
	0.76	2110	10.4×10^{-10}	2.5×10^{10}
	1.52	2020	11.5×10^{-10}	2.8×10^{10}
	2.14	3030	12.7×10^{-10}	2.8×10^{10}
	1.17	2660	14.7×10^{-10}	2.7×10^{10}
	0.76	2130	14.8×10^{-10}	2.5×10^{10}
				$(2.6 \pm 0.1) \times 10^{10}$
358	0.88	2640	6.52×10^{-10}	5.4×10^{10}
	1.40	3320	8.99×10^{-10}	6.0×10^{10}
	0.87	2690	9.43×10^{-10}	5.8×10^{10}
	1.82	2560	11.2×10^{-10}	6.4×10^{10}
				$(5.9 \pm 0.3) \times 10^{10}$
380	1.71	3780	5.71×10^{-10}	8.5×10^{10}
	1.71	3780	9.10×10^{-10}	8.9×10^{10}
				$(8.7 \pm 0.2) \times 10^{10}$
437	1.50	4160	1.79×10^{-10}	18.6×10^{10}
448	1.17	3780	3.02×10^{-10}	2.1×10^{11}
	1.17	3770	3.12×10^{-10}	2.1×10^{11}
	1.50	4290	4.41×10^{-10}	2.1×10^{11}
	1.64	2700	4.44×10^{-10}	2.1×10^{11}
	1.89	3420	5.74×10^{-10}	2.2×10^{11}
				$(2.1 \pm 0.0) \times 10^{11}$
599	1.08	4870	3.56×10^{-10}	6.0×10^{11}
	1.08	5050	4.51×10^{-10}	6.0×10^{11}
608	1.74	5940	3.70×10^{-10}	6.7×10^{11}
	1.74	5960	4.92×10^{-10}	6.1×10^{11}
				$(6.4 \pm 0.3) \times 10^{11}$
652	2.13	6840	2.63×10^{-10}	6.0×10^{11}
	0.86	4660	4.45×10^{-10}	5.2×10^{11}
	1.07	5370	4.54×10^{-10}	6.8×10^{11}
	1.31	5850	4.54×10^{-10}	8.7×10^{11}
	0.80	4650	4.94×10^{-10}	6.0×10^{11}
	2.08	6980	5.12×10^{-10}	7.9×10^{11}
				$(6.7 \pm 1.0) \times 10^{11}$

[a] All runs in helium carrier (>95%). Values of k_1 have been corrected for axial diffusion.

sumed in this system has been demonstrated earlier.[1] Thus the overall reaction was taken to be $2H + H_2CO \rightarrow 2H_2 + CO$.

The results are summarized in Table I and the mean values at each temperature are plotted in Figure 1. The Arrhenius expression is $k_1 = 1.35 \times 10^{13} \exp(-3760/RT)$ cm³ mol⁻¹ sec⁻¹.

Our room temperature value $k_1 = 2.6 \times 10^{10}$ is in excellent agreement with that reported by Brennen, *et al.*,[1] who also found $k_1 = 2.6 \times 10^{10}$. Their experiment was essentially the same as our own, except that mass spectrometric detection for H was used.

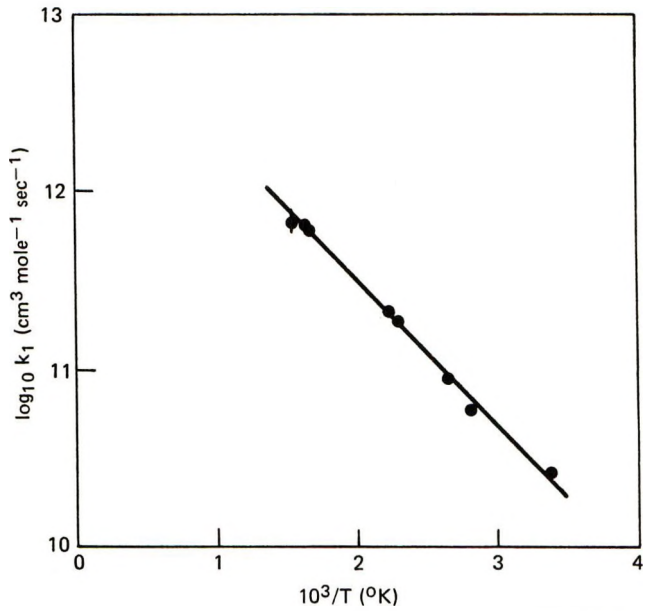

Figure 1. Arrhenius plot of data on k_1 for $H + H_2CO \rightarrow H_2 + HCO$. The data obey $k_1 = 1.35 \times 10^{13} \exp(-3760/RT)$.

Of the high temperature studies in the literature, McNesby, *et al.*,[3] combined their photolysis results on H_2CO–D_2CO mixtures over the range 520–670°K with analogous results by Klein, *et al.*,[2] on H_2–D_2CO mixtures, with the help of isotopic rate constant ratio theory, to derive the ratio $k(D + H_2)/k_1 = 3 \exp(-3400/RT)$. Using our recent experimental result[6] $k(D + H_2) = 4.4 \times 10^{13} \exp(-7600/RT)$, which encompassed the same temperature range, the photolysis experiments predict $k_1 = 1.5 \times 10^{13} \exp(-4200/RT)$. This is good agreement with our preexponential factor but a somewhat higher activation energy. At 650°K the above expression gives $k_1 = 6 \times 10^{11}$, and at room temperature (far outside the photolysis range) the predicted value is 1.4×10^{10}. The corresponding results from our own Arrhenius expression are $k_1(650°) = 7.3 \times 10^{11}$ and $k_1(300°) = 2.6 \times 10^{10}$, so that the agreement is fair at temperatures within the actual range of the photolysis work.

The other high-temperature work on k_1 is that of Baldwin and Cowe[4] on the inhibition of H_2–O_2 explosion limits by H_2CO at 813°K, from which they arrived at a ratio $k_1/k(H + O_2) = 320$. If the recommended value from the Leeds review[8] (which, to be sure, relies somewhat on the result in ref 4) is used for $k(H + O_2)$, *i.e.*, 6.8×10^9 at 813°K, the inhibition work yields $k_1 = 2.2 \times 10^{12}$. Our own Arrhenius relation yields $k_1 = 1.3 \times 10^{12}$ at this temperature. We are unaware of any other reliable data in the literature for comparison.

(8) "High Temperature Reaction Rate Data," University of Leeds, Report No. 3, April 1969.

Relative Rate Constants for O + HCO → OH + CO and O + HCO → H + CO_2

by A. A. Westenberg* and N. deHaas

Applied Physics Laboratory, Johns Hopkins University, Silver Spring, Maryland 20910 *(Received February 14, 1972)*

Publication costs assisted by the Bureau of Naval Ordnance

A simple analysis is given showing how the measurement of O atoms consumed and CO_2 formed in the O + H_2CO reaction system, with $(O)_0 \gg (H_2CO)_0$, can be related to the rate constant ratio k_3/k_2 for the alternate pathways O + HCO → OH + CO (k_2) and O + HCO → H + CO_2 (k_3). Experimental results in a fast-flow system at room temperature give the value $k_3/k_2 = 0.73 \pm 0.15$.

In a previous paper[1] we pointed out how the measurement of the absolute concentrations of "steady-state" intermediates could be used to determine the relative importance of various reaction rates involving the HO_2 radical. A somewhat different approach is exploited here in regard to the HCO radical, the actual intermediate concentrations not being required for the desired result.

When O atoms react with H_2CO in a fast-flow system the primary step is surely the simple abstraction

$$O + H_2CO \longrightarrow OH + HCO \qquad (1)$$

which is then followed by the fast steps

$$O + HCO \longrightarrow OH + CO \qquad (2)$$

$$O + HCO \longrightarrow H + CO_2 \qquad (3)$$

$$O + OH \longrightarrow O_2 + H \qquad (4)$$

This sequence has been discussed by Niki[2] in connection with his measurement of k_1. We shall be interested only in the situation where the initial concentration $(O)_0$ is in large excess compared to $(H_2CO)_0$, and in this case one can reasonably argue that other conceivable secondary reactions are unimportant. The reaction H + H_2CO → H_2 + HCO is about half as fast as (1) at room temperature[3,4] and could not compete in excess (O). While H + HCO → H_2 + CO should have a rate constant comparable to k_2 and k_3, it also would be unlikely to compete appreciably in excess (O). Furthermore, H_2 is not found as a product.[2] The reaction OH + H_2CO → H_2O + HCO was supposedly ruled out by Niki[2] in contributing to the H_2O formed, although it has since been found to be very fast[5] ($k \simeq 10^{13}$ cm^3 mol^{-1} sec^{-1}). Nevertheless, neither it nor OH + HCO → H_2O + CO would be expected to compete for OH removal with the still faster[6] reaction 4 in excess (O).

Using reactions 1–4, the only source of CO_2 is (3), the reaction CO + OH → CO_2 + H ($k \simeq 10^{11}$) being negligible in excess (O). Assuming steady-state concentrations of HCO and OH it is straightforward to derive the relation

$$\frac{(O)_0 - (O)_f}{(CO_2)_f} = \frac{4 + 3k_3/k_2}{k_3/k_2}$$

where $(O)_f$ and $(CO_2)_f$ refer to concentrations existing after all the H_2CO has been consumed and both (O) and (CO_2) attain constant "final" values (*i.e.*, "final" as far as these four reactions are concerned). Measurement of the left-hand quantity above would then permit the ratio k_3/k_2 to be determined.

As a check on the validity of the analysis using only reactions 1–4, the "complete" mechanism including the other four possible reactions discussed above in addition to (1)–(4) was programmed for rigorous solution on a computer; *i.e.*, the set of simultaneous rate equations for all species (without the steady-state approximation for the intermediates) was solved using known or estimated values for the rate constants. The rigorously computed quantity $[(O)_0 - (O)_f]/(CO_2)_f$ was shown to be within 10% of the quantity $[4 + 3k_3/k_2]/(k_3/k_2)$ for any ratio $(O)_0/(H_2CO)_0 > 4$.

An alternate method is possible in principle, since the same analysis is easily shown to lead to the relation $[(O)_0 - (O)_f]/(H_2CO)_0 = [4 + 3k_3/k_2]/[1 + (k_3/k_2)]$. This is far less desirable, however, since the measurable quantity on the left only varies in the range 4 → 3 as k_3/k_2 takes on the possible values 0 → ∞. It is, therefore, very insensitive compared to the CO_2 method in which the measurable quantity varies as ∞ → 3 as $k_3/k_2 = 0 \rightarrow \infty$.

Experiments were performed in our usual discharge flow system[7] with a fixed esr cavity to measure (O) and a mass spectrometer inlet with continuous sampling

(1) A. A. Westenberg and N. deHaas, *J. Phys. Chem.*, **76**, 1586 (1972).

(2) H. Niki, *J. Chem. Phys.*, **45**, 2330, 3468 (1966).

(3) W. Brennen, I. D. Gay, G. P. Glass, and H. Niki, *ibid.*, **43**, 2569 (1965).

(4) A. A. Westenberg and N. deHaas, *J. Phys. Chem.*, **76**, 2213 (1972).

(5) E. D. Morris, Jr., and H. Niki, *J. Chem. Phys.*, **55**, 1991 (1971).

(6) A. A. Westenberg, N. deHaas, and J. M. Roscoe, *J. Phys. Chem.*, **74**, 3431 (1970).

(7) A. A. Westenberg and N. deHaas, *J. Chem. Phys.*, **47**, 1393 (1967).

Table I: Summary of Measurements of k_3/k_2 at Various $(O)_0/(H_2CO)_0$ Ratios (All Runs Were at Room Temperature in 97–98% Argon Carrier)

P, Torr	$(O)_0$, mol/cm³	$(CO_2)_f$, mol/cm³	$(O)_f/(O)_0$	$(O)_0/(H_2CO)_0$	k_3/k_2
1.11	8.4×10^{-10}	0.58×10^{-10}	0.38	4.7	0.68
1.80	12.3×10^{-10}	0.63×10^{-10}	0.62	5.1	0.92
1.87	14.8×10^{-10}	0.74×10^{-10}	0.53	5.9	0.63
1.87	14.3×10^{-10}	0.31×10^{-10}	0.66	6.7	0.32
1.88	13.4×10^{-10}	0.45×10^{-10}	0.64	8.0	0.52
1.49	12.6×10^{-10}	0.53×10^{-10}	0.68	9.4	0.85
1.49	6.1×10^{-10}	0.31×10^{-10}	0.63	9.6	0.96
1.90	13.5×10^{-10}	0.43×10^{-10}	0.74	10.6	0.80
1.65	14.4×10^{-10}	0.51×10^{-10}	0.70	16.7	0.72
1.49	12.3×10^{-10}	0.25×10^{-10}	0.85	19.9	0.86
				Av	0.73 ± 0.15

downstream of the cavity for the CO_2 produced. O atoms were furnished by a microwave discharge in argon carrier containing 1–2% of O_2. H_2CO was generated from paraformaldehyde heated to 60–80° and metered directly to a movable injector through a needle valve. The H_2CO flow was measured after each run by transferring it to a calibrated volume and timing the pressure rise. No special problems with metering and handling the H_2CO were encountered, except that cleaning the needle valve was occasionally necessary. Steady flows of H_2CO could be readily introduced to the main flow system in this way, as was proved by monitoring the m/e 30 peak in the mass spectrometer. The CO_2 formed was monitored at m/e 44, and the mass spectrometer was calibrated after each run by adding a metered flow of CO_2 to the main flow. Absolute (O) values were measured by esr in our usual way,[8] using a separate filling of pure O_2 for calibration.

For each run the flows and injector position were adjusted so that the (H_2CO) was completely consumed by the time the mixture reached the esr cavity, as evidenced both by attainment of a constant O signal upon moving the injector farther away from the cavity, and the disappearance of H_2CO in the mass spectrometer. This O signal was proportioned to $(O)_f$, and the corresponding m/e 44 peak to $(CO_2)_f$. The H_2CO was then bypassed out of the reactor and an esr integral taken, which gave $(O)_0$. These were converted to absolute concentrations by the above calibration procedures, and a value of k_3/k_2 was determined.

Results of a number of such runs are given in Table I. A limited total pressure range could be covered due to physical limitations of the system while still meeting the basic requirement that there be no further reaction beyond the cavity. The more important variable, the initial $(O)_0/(H_3CO)_0$ ratio, was varied over a rather wide range of 4.7–19.9. The average of 10 runs gave a value $k_3/k_2 = 0.73 \pm 0.15$ at room temperature, with no significant trend as $(O)_0/(H_2CO)_0$ was varied.

The simple abstraction reaction 2, which is 73 kcal/mol exothermic, is thus slightly faster than the substitution reaction 3, which has an exothermicity of 99 kcal/mol. The latter represents a somewhat more complex process, so that we do not consider the result $k_2 > k_3$ to be surprising, with the aid of hindsight. This is similar to the results obtained[1] in the $H + HO_2$ reaction, where the substitution path $H + HO_2 \rightarrow H_2O + O$ was found to be slower than either of the alternate abstraction reactions.

The only other value for k_3/k_2 in the literature is that of Niki, *et al.*,[9] in a study of the $O + C_2H_4$ reaction, where H_2CO and then HCO are formed in the secondary reactions. From their mechanism they derived $(CO_2)_f/(H)_f = (k_3/k_2)/2[1 + (k_3/k_2)]$, and from the measured quantity on the left they obtained $k_3/k_2 = 0.25 \pm 0.16$. This is lower than our ratio, although not much beyond the respective quoted error limits. Since the measurable quantity $(CO_2)_f/(H)_f$ varies only as $0 \rightarrow 0.5$ as $k_3/k_2 = 0 \rightarrow \infty$, this is a very insensitive method and based on a more complex system. This, plus the fact that their mass spectrometric (H) measurement calibrated against the $H + NO_2$ titration was not very reliable (as they note), leads us to prefer the present value for k_3/k_2.

(8) A. A. Westenberg and N. deHaas, *J. Chem. Phys.*, **40**, 3087 (1964).
(9) H. Niki, E. E. Daby, and B. Weinstock, "Twelfth Symposium on Combustion," The Combustion Institute, Pittsburgh, Pa., 1969, p 277.

Reactivities of Solvated Electrons in Ethylene Glycol–Water Glass

by Harald B. Steen* and Magne Kongshaug[1]

Norsk Hydro's Institute for Cancer Research, Montebello, Oslo 3, Norway *(Received November 30, 1971)*

Publication costs assisted by Norsk Hydro's Institute for Cancer Research

The effect of various electron-scavenging solutes, $CuCl_2$, H_2O_2, $NaNO_3$, CCl_3COONa, CCl_3COOH, and HCl, on the isothermal decay of stabilized electrons (e_s^-)[2] in ethylene glycol–water glass has been studied at 123 K by continuous measurements of the optical density (OD) during and after X-irradiation. The decay kinetics of the OD are similar for all solutes indicating that e_s^- is the only diffusible species. The decay of OD is independent of wavelength over the major part of the absorption spectrum of e_s^-. The decay kinetics are nonexponential so that the rate of reaction of e_s^- with the various scavengers, which is derived on the basis of the observation that the scavenging kinetics is exponential with regard to solute concentration, decreases by a factor of 4 during the first 200 sec of the decay whereupon it becomes approximately constant. The reactivities of e_s^- with the various scavengers are not proportional to those of dry (e^-) or mobile electrons (e_m^-) previously measured in the same glass. In particular the hydronium ion, which reacts very slowly with e^- and e_m^-, is a very efficient scavenger of e_s^-. The results indicate that coulombic effects may possibly contribute to the difference between the reactivities of e^-, e_m^-, and e_s^-.

Introduction

There is increasing experimental evidence to indicate that radiation-induced electrons in polar media may react with sufficiently concentrated solutes before they become stabilized by solvation or trapping. With present day techniques the electrons cannot be observed directly during the extremely short period prior to stabilization. Their existence as reactive species is postulated mainly on the basis of experiments showing how the yields of hydrated (e_{aq}^-) and solvated or trapped electrons (e_s^-)[2] are reduced by the presence of various solutes which are known to be efficient electron scavengers. Thus, it is usually assumed that the reactive precursor of stabilized electrons must be free or quasifree electrons moving with thermal—or higher—energy.

The precursor of e_{aq}^- has been termed the "dry electron" (e^-), while the precursor of e_s^- in glasses is usually called the "mobile electron" (e_m^-). It seems appropriate to retain this distinction. Thus, the reactivities of e^- in aqueous solutions at 300 K, measured by Wolff, *et al.*,[3] are not the same, or not even proportional to the reactivities of e_m^- in polar glasses at 77 K.[4] This difference seems to reflect a real difference between e^- and e_m^- rather then the different conditions under which the reactivities were measured. Thus, attributing the quenching of the spontaneous X-ray-induced recombination luminescence of indole in a glycol–water glass at 77 K by various electron scavengers to the scavenging of the recombining electron, it was found[5] that the reactivities of these electrons are proportional to those reported by Wolff, *et al.*, for e^-. On the other hand, the reactivities for e_m^-, determined by studying the effect of the same electron scavengers on the yield of e_s^- under identical conditions,[4] are not the same and not proportional to those found for e^-.

It has been suggested[6] that the time dependence of reaction rate constants predicted by the diffusion model may explain the differences in reactivities between e^- and e_{aq}^- observed by Wolff, *et al.* Although this effect may have contributed to the difference between e^- and e_{aq}^-, recent data from these authors[3b] seem to show that it is hardly the main reason. Thus, if it was, the difference between the rate constants attributed to e^- and e_{aq}^- should generally decrease with their absolute magnitude. As pointed out by these authors, no such systematic variation is apparent from their list of 18 solutes.[3b]

The same argument applies to the difference between e^- and e_m^- observed in glycol–water glass. And in this case it is more clear-cut since in the glass the electron is the only diffusible species. There is no systematic correlation between the magnitude of the scavenging efficiencies and the difference between the values observed for e^- and e_m^-. Hence, it appears that the state of the electron observed by the recombination luminescence experiments, which we denote e^-, must be different from that of e_m^- as studied from

(1) Fellow of the Norwegian Cancer Society.

(2) As discussed below the stabilized (trapped) electron observed in the present experiments appears to be essentially similar to the solvated electron at room temperature except for its larger stability, *i.e.*, larger lifetime, which is due primarily to the higher viscosity of the medium at low temperatures. Hence, we have used the term e_s^- also for the stabilized electron studied here.

(3) (a) R. K. Wolff, M. J. Bronskill, and J. W. Hunt, *J. Chem. Phys.*, **53**, 4211 (1970); (b) J. E. Aldrich, M. J. Bronskill, R. K. Wolff, and J. W. Hunt, *ibid.*, **55**, 530 (1971).

(4) H. B. Steen, O. Kaalhus, and M. Kongshaug, *J. Phys. Chem.*, **75**, 1941 (1971).

(5) H. B. Steen, *ibid.*, **74**, 4059 (1970).

(6) H. A. Schwarz, *J. Chem. Phys.*, **55**, 3647 (1971).

the effects of scavengers on the yield of e_s^-. For example it is conceivable that e^- are electrons with energies above the thermal one, as suggested by Wolff, *et al.*,[3a] whereas e_m^- represent thermalized electrons.

Kevan[7] reported that the reactivities of the precursor of radiation-induced trapped H atoms in acidic glasses, which seems to be an electron, were approximately proportional to those of e_{aq}^- at room temperature. This is definitely not the case for e_m^- in glycol–water glass.[4] As discussed below this apparent discrepancy may be explained by assuming that whereas e_m^- observed in glycol–water glass is essentially a free particle, the electron studied by Kevan may be a solvated electron which is so unstably trapped that it can move rapidly in the medium. Thus, the difference between these two states of the electron may be primarily in the degree of solvation.

In the present communication we report on the reactivity of the electron in the final stage of its energy degradation, that is the reactivity of e_s^-. Thus, we have found that in the glycol–water glass referred to above, e_s^- is not completely stable, even at 77 K, but decays very slowly, *i.e.*, in the matter of days, apparently due to a slow reaction of e_s^- in the matrix of the glass. The rate of this decay is increased significantly by the presence of various electron scavengers. We have studied here this effect at a somewhat higher temperature where the decay is somewhat faster and therefore more convenient to study. Thus, we have measured the rate of decay of e_s^- as a function of the concentration of various scavengers at 123 K and thereby determined relative values for the reactivity of e_s^-. These values are not proportional to the previously reported reactivities of e^- and e_m^-, whereas they correlate well with rate constants for e_s^- at room temperature.

Experimental Section

The ethylene glycol–water solvent (EG/H_2O) was a mixture, 1:1 by volume, of ethylene glycol ("Chromatoquality" from Matheson Coleman and Bell) and doubly distilled water. $CuCl_2$, H_2O_2, $NaNO_3$, CCl_3COOH, and HCl were all *pro analysi* reagents from Merck, while CCl_3COOHa was from Schuchardt.

Samples (50-μl) in gilded Perspex cups, 1 mm deep, were irradiated under vacuum by 50-kV X-rays at 123 K, and the optical density at a chosen wavelength was measured continuously during the irradiation as well as subsequent to it by the intensity of a monochromatic light beam reflected from the bottom of the sample. The dose rate, as measured by the Fricke dosimetry, was 80 krads/min (8.3×10^{11} eV/g sec).

Details of the apparatus and experimental procedure are given elsewhere.[8] The samples were usually irradiated until OD $\approx$ 0.18 which corresponds to an overall concentration of e_s^- approximately equal to 5×10^{-5} M. The exposure time thus varied between 15 and 150 sec depending on the solute and its concentration.

By increasing the intensity of the analyzing light beam far above its normal level, it was confirmed that the effect of optical bleaching can be disregarded in the present experiments.

Results

Electron Yields. The radiation-induced absorption at 585 nm, which is close to the absorption maximum of e_s^- (λ_{max} $\sim$565 nm at 123 K), appears to be due almost exclusively to this species. None of the products formed by the reaction of electrons with the various scavengers seem to contribute noticeably to the absorption at this wavelength. Thus, when irradiating samples with scavenger concentrations roughly ten times higher than those necessary to halve $G(e_s^-)$, the optical density at 585 nm grew at a rate which was never more than a few per cent of that obtained in the actual experiments. Furthermore, the decay of OD_{585nm} during optical bleaching at this temperature was strictly exponential, indicating that only one absorbing species is present.[9]

In Figure 1 are shown typical recorder traces of the OD during and after irradiation as observed for pure EG/H_2O and samples containing HCl and $NaNO_3$. $G(e_s^-)$ is proportional to the initial slope of that part of the curves which was recorded during irradiation. The absolute value of $G(e_s^-)$ can be found if one knows the extinction coefficient ϵ of e_s^-, the optical path length of the analyzing light beam and the dose rate. If we assume ϵ = 13,700 $(M \text{ cm})^{-1}$ in accordance with Higashimura, *et al.*,[10] we obtain $G(e_s^-)$ = 2.0 at 77 K in excellent agreement with the value reported by these authors.

Decay Kinetics. It may be seen from Figure 1 that in the pure glass OD increases linearly with dose while for samples containing scavenger, the curves deviate noticeably from straight lines. This deviation becomes more pronounced with increasing scavenger concentrations. The deviation can be explained by the second part of the curves in Figure 1 which demonstrates the decay of OD subsequent to irradiation. Thus, making the obvious assumption that a similar decay goes on during irradiation as well, the deviation from a linear relationship between OD and dose can be quantitatively accounted for. Our comments to Figure 1 apply to all the other scavengers as well.

Figure 2 shows decay curves for a variety of samples. As seen also in Figure 1, there is a significant decay of

(7) L. Kevan in "Radiation Chemistry of Aqueous Systems," G. Stein, Ed., Wiley-Interscience, New York, N. Y., 1968, pp 21–71.

(8) H. B. Steen, O. I. Sorensen, and J. Aa. Holteng, *Int. J. Radiat. Phys. Chem.*, in press.

(9) H. B. Steen, unpublished results.

(10) T. Higashimura, M. Noda, T. Warashina, and H. Yoshida, *J. Chem. Phys.*, **53**, 1152 (1970).

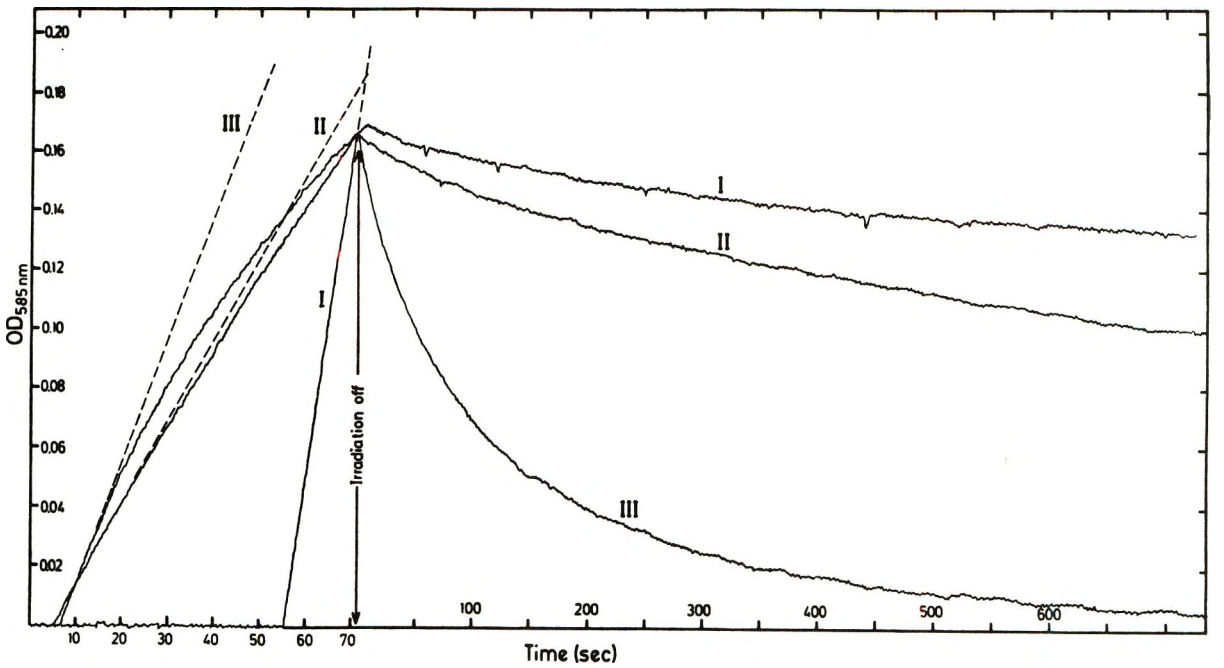

Figure 1. The OD at 585 nm of EG/H_2O glass with various solutes after X-irradiation at 123 K: curve I, no solute; curve II, 0.12 *M* $NaNO_3$; curve III, 0.15 *M* HCl. The optical path length is approximately 2 mm. The curves are reproductions of actual recorder traces to indicate the actual signal-to-noise ratio. Note the different time scales before and after interruption of the irradiation.

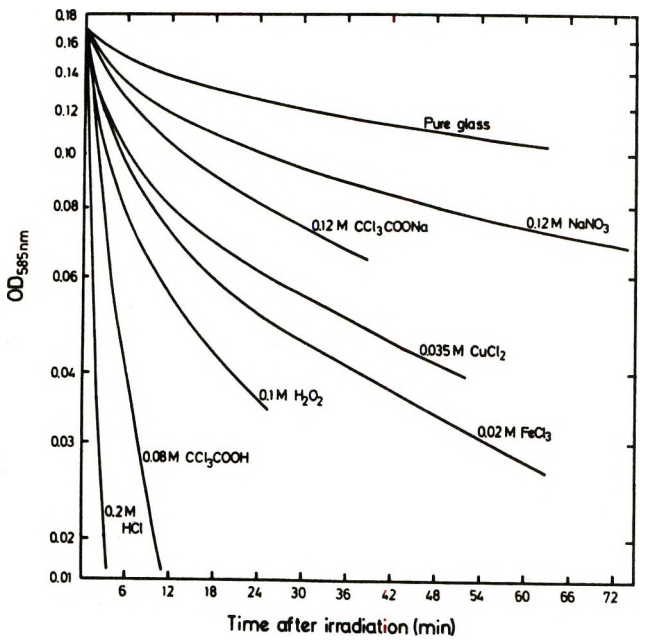

Figure 2. Decay of OD at 585 nm after X-irradiation at 123 K for EG/H_2O glass with various solutes.

e_s^- also in the absence of any solute. This is supposedly due partly to recombination with the positive hole and partly to reaction of e_s^- with the solvent. The latter process appears to be strongly dominant. Thus, previous studies of e_s^- in this glass by esr techniques demonstrated that by thermal activation the disappearing electrons are replaced by the same number (within 10%) of ethyl radicals apparently associated with ethylene glycol.[11] Furthermore, the number of light quanta emitted as recombination luminescence, *i.e.*, the afterglow and thermoluminescence which seem to be due to recombination between e_s^- and positive holes, is only a few per cent of the number of e_s^-.[12] Hence, when scavenger molecules are present, there is a competition for e_s^- between scavenging and reaction with the solvent, while hole recombination is unimportant.

Evidently, the decay curves in Figure 2 are not exponential. Thus, the rate of decay decreases significantly with time. All the curves can be decomposed into two exponential components—a relatively fast initial one and a second slower one. However, such a decomposition of curves covering less than one decade is hardly conclusive.

As noted above, all samples were irradiated to the same OD. This implies that for samples which required a longer irradiation time, because of low yield of e_s^- caused by the presence of scavenger, a larger part of the fast component of the decay was lost during irradiation, and the decay observed after irradiation was affected accordingly. In most cases this effect was small since usually the irradiation time was short as compared to the decay time. For some samples, however, the effect was significant as shown by an extreme example in Figure 1 (curve III). The extent of the decay of e_s^- during irradiation puts an upper limit

(11) H. B. Steen, *Photochem. Photobiol.*, 9, 479 (1969).
(12) J. Moan and H. B. Steen, *J. Phys. Chem.*, 75, 2887 (1971).

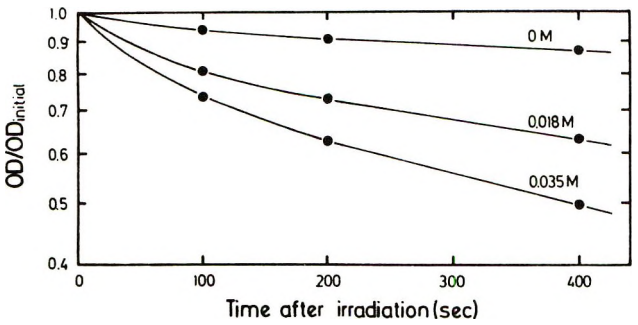

Figure 3. Decay of OD at 585 nm for X-irradiated samples with different concentrations of $CuCl_2$. Each curve represents the average of four separate experiments. The temperature is 123 K.

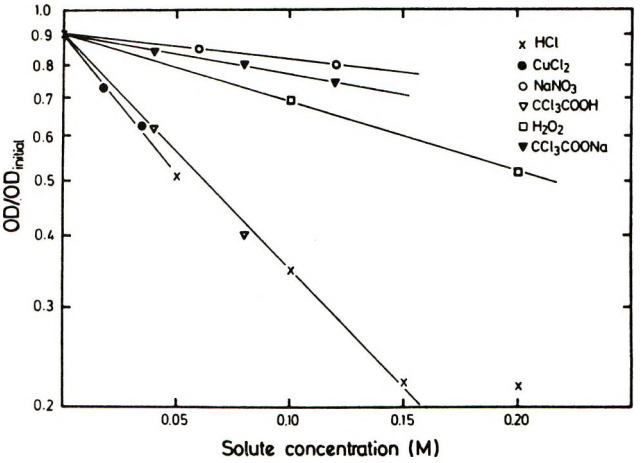

Figure 4. The OD at 585 nm 200 sec after irradiation at 123 K relative to the OD at the end of the irradiation as a function of the concentration of various solutes. Each point represents the average of at least four separate experiments.

to the scavenger concentrations which could be used in the present experiments.

Except for this effect the decay kinetics were independent of dose as observed for a fivefold increase of the dose. This is in accordance with the fact that even with the highest dose, the overall concentration of e_s^- ($\approx 5 \times 10^{-4}$ *M*) was at least one order of magnitude smaller than that of the solutes. The results, including the values of $G(e_s^-)$, were also independent of dose rate as observed for tenfold decrease of this parameter.

As noted below the decay kinetics appear to be the same for all solutes and all concentrations studied.

For each of the scavengers four curves of the type shown in Figure 1 were obtained for every scavenger concentration, *i.e.*, each experiment was repeated four times. The reproducibility of single experiments was within 10%. Mean values of the OD were calculated for different times after irradiation, and decay curves which have been drawn from these mean values are depicted in Figure 3.

The decay of OD at 123 K was studied also at 470 and 700 nm. The decay kinetics and the effects of the various solutes at these wavelengths were the same as those observed at 585 nm. This result is in accordance with a recent study[9] of the effects of thermal and optical bleaching of e_s^- at various temperatures. Thus, it was found that, in contrast to what is the case at lower temperatures, the shape of the absorption spectrum observed at 123 K and above is not changed noticeably either by optical bleaching with monochromatic light of various wavelengths or during isothermal decay. These results indicate that at 123 K all e_s^- have the same trap depth, probably because the viscosity of the medium is low enough to allow complete relaxation of all occupied traps. These findings demonstrate that the decay of the OD at 585 nm, as well as at any other wavelength within the absorption spectrum of e_s^-, is indeed representative for the decay of the totality of e_s^-, and furthermore, that the nonexponential kinetics of the isothermal decay cannot be explained by a trap-depth dependent decay rate.

Scavenging Kinetics. Figure 4 depicts the OD at 200 sec after irradiation relative to that recorded at the end of the irradiation as a function of the scavenger concentration. Thus, this is a measure of the rate of decay during the first 200 sec after irradiation. Within the rather limited range of scavenger concentrations which could be studied in the present experiments, the results appear to be in accordance with exponential scavenging kinetics. By plotting the OD at 100 and 400 sec after irradiation in the same manner, curves similar to those in Figure 4 were obtained except that the slopes were different, *i.e.*, the slopes, of course, increase with time.

Scavenging Efficiencies. Defining scavenging efficiency as being proportional to the slope of the curves in Figure 4 (see below), relative values for this parameter have been determined, and the results for three different decay times are given in Table I. It can be seen that although the scavenging efficiency increases continuously with time (see below), the ratios between the values obtained for the various solutes are independent of the decay time. This means that, at least within the time range of Table I, the decay kinetics were the same for all scavengers as well as for the pure glass. This finding seems to exclude the possibility that some of the scavengers are able to diffuse in the glass. Thus, one would expect the decay kinetics resulting from the reaction between two diffusible species to be different from that of a reaction between a diffusible and a fixed species. Since it seems highly improbable that molecules like CCl_3COO^- should be able to diffuse under the present conditions (this was indeed excluded by conductivity measurements), we conclude that all scavengers were immobile, leaving e_s^- as the only reactive species which was able to diffuse.

It should be noted that the scavenging efficiency for CCl_3COOH is similar to that of HCl while it is almost

Table I: Scavenging Efficiencies of e_s^- in EG/H_2O Glass at 123 K Measured at Various Decay Times as the Reduction of OD at 585 nm Relative to This Reduction in the Pure Glass[a]

Solute	100 sec	200 sec	400 sec	Mean value
$CuCl_2$	9.8	11.2	11.2	10.7
HCl	9.3	9.6	10.8	9.9
H_2O_2	2.7	2.7	2.5	2.7
$NaNO_3$	1.0	1.0	1.0	1.0
CCl_3COOH	7.6	9.5	10.0	9.0
CCl_3COONa	1.9	1.6	1.4	1.6

[a] The values have been normalized so that the value for $NaNO_3$ is unity in all cases.

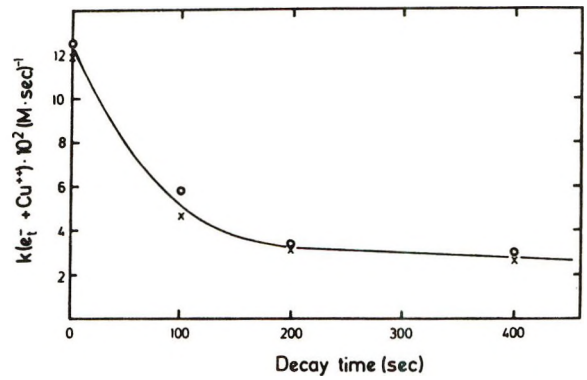

Figure 5. The time dependence of the rate constant of the reaction of e_s^- with solute at 123 K as observed for two different concentrations of $CuCl_2$: O, 0.018 *M*; ×, 0.035 *M*.

one order of magnitude larger than that of CCl_3COONa. This supports our previous assumption[4] that CCl_3COOH is fully dissociated and shows that H^+ is a much more efficient scavenger of e_s^- than the acetate ion. As discussed below this is in conspicuous contrast to the scavenging of e^- and e_m^- for which the scavenging efficiency of the acetate ion is more than one order of magnitude larger than that of H^+.

Time Dependence of the Rate Constants. According to the results in Figure 4, the scavenging kinetics can be adequately described by eq 1

$$OD/OD_0 = e^{-K[S]} \quad (1)$$

where OD and OD_0 denote the OD observed at a certain time t after irradiation in the presence and absence of scavenger, respectively. K is the scavenging efficiency in accordance with the definition above, and [S] is the scavenger concentration. This type of scavenging kinetics was observed for the precursor of e_{aq}^- by Wolff, *et al.*[3a] A theoretical basis for eq 1 was given by these authors and will be discussed in more detail elsewhere.[13] It should be noted that K is time dependent, and furthermore that the relative values of K given in Table I are derived directly from the experimental data without any assumptions about the reaction mechanisms or kinetics.

According to eq 1, K is the probability that e_s^- will have reacted with a scavenger of unit concentration within the time t. Defining the reaction rate constant k as the probability of reaction of e_s^- with scavenger per unit time and scavenger concentration, we have eq 2

$$k = dK/dt \quad (2)$$

Deriving eq 1 with respect to t gives eq 3

$$\frac{1}{OD}\frac{d(OD)}{dt} - \frac{1}{OD_0}\frac{d(OD_0)}{dt} = -\frac{dK}{dt}[S] = -k[S] \quad (3)$$

In a semilogarithmic plot of OD *vs.* time, as in Figure 3, the first two terms in this equation are the slopes of such curves at the time t as obtained in the presence and absence of scavenger. Thus, we have determined k as a function of time from eq 3 by measuring the slopes of the respective decay curves at various values of the decay time. The results obtained for $CuCl_2$ are depicted in Figure 5. It can be seen that the rate constant decreases by a factor of 4 during the first 200 sec after irradiation whereupon it approaches a constant value in accordance with the approximately exponential decay observed for extended decay times. Furthermore, it appears that the rate constant is independent of the scavenger concentration within the range studied. The small difference obtained for the two concentrations of $CuCl_2$, seen in Figure 5, is probably due to the aforementioned decay of e_s^- during irradiation by which the sample with the higher scavenger concentration loses slightly more of the fast decay component.

Since, according to Table I, the ratios between the scavenging efficiencies observed for different scavengers are independent of t, it follows from eq 2 that the time dependence of the reaction rate constant will be similar to that in Figure 5 for all scavengers. The absolute magnitudes of the rate constants are proportional to the scavenging efficiencies calculated above and may therefore be found by comparing Table I and Figure 5.

Discussion

In Table II the scavenging efficiencies obtained for e_s^- at 123 K are compared on a relative scale to those of e^- and e_m^- in EG/H_2O glass at 77 K. The scavenging efficiencies of e^- and e_m^- have been reported elsewhere[3b,4] except for the values for e_m^- with $CuCl_2$ and CCl_3COONa, which are reported for the first time here. The conspicuous property of both e^- and e_m^- is their low reactivity with hydronium ions as compared to that of e_s^- and e_{aq}^-. The present experiments show that in contrast to e^- and e_m^-, e_s^- is scavenged very efficiently by hydronium ions. This result is supported by our previous observation of the effect of $NaNO_3$ and HCl on the yield of thermoluminescence of

(13) M. Kongshaug, O. Kaalhus, J. Moan, and H. B. Steen, manuscript in preparation.

photoionized tryptophan in EG/H_2O glass which indicated that hydronium ions react more efficiently with the recombining electrons giving rise to this luminescence than did NO_3^-.[12] The high reactivity of hydronium ions with e_s^- as opposed to e_m^- demonstrates that the diffusion of e_s^- as observed here does not occur by activation of the electron to a mobile state comparable to e_m^- as is the case when the activation is optically induced. This indicates that the stabilized electron observed here and the solvated electron at room temperature are similar not only in their optical absorption properties but also with regard to reactivity. This similarity is indeed confirmed by our finding that the scavenging efficiencies for e_s^- presented here are approximately proportional to the reaction rate constants for e_s^- in EG/H_2O at room temperature as measured by pulse radiolysis.[9]

Table II: Relative Scavenging Efficiencies for e^-, e_m^-, and e_s^- in EG/H_2O Glass[a]

Solute	Relative scavenging efficiency		
	e^-	e_m^-	e_s^-
$CuCl_2$	...	3.5	4.0
H_2O_2	1.0	1.0	1.0
$NaNO_3$	3.2	1.3	0.37
$ClCH_2COOH$	0.9	0.18	...
CCl_3COONa	...	2.2	0.6
CCl_3COOH	3.8	2.4	3.3
HCl	<0.1	0.11	3.7

[a] To facilitate comparison the values have been normalized so that the value for H_2O_2 is unity in all cases. The absolute values for e^- and e_m^- are given in ref 4.

According to Table II the scavenging efficiencies for e_s^- are clearly not proportional to those for e_m^- even if one disregards the hydronium ion. Hence, the reactivities of these two states of the electron appear to be generally different in the present glass.

In contrast Kevan found that in $H_2PO_4^-$ and HSO_4^- glasses at 77 K the reactivities of the precursor of trapped H atoms, which appears to be a mobile electron, are proportional to those of e_{aq}^- at room temperature, and on this basis he argued for a structural similarity between this mobile electron and e_{aq}^-.[7,14,15] A corresponding similarity between e_m^- and e_s^- does not seem to exist for these entities as observed here. It seems possible, therefore, that while the e_m^- studied by the present experiments probably is a free electron in its pretrapped state, the electron studied by Kevan is a stabilized electron, essentially similar to e_s^- in the present glass, but so loosely bound that it diffuses and decays completely during irradiation. Since e_s^- apparently reacts efficiently with hydronium ions, and since 10^{-3} M of other efficient scavengers of e_s^- reduces $G(H_T)$ significantly, this hypothesis requires that the concentration of hydronium ions in $H_2PO_4^-$ and HSO_4^- glasses is low, *i.e.*, 10^{-3} M. For phosphate glass this seems quite probable since the pK of $H_2PO_4^-$ in water at 25° is 7.2.[16] For HSO_4^-, on the other hand, the pK at 25° is 1.9.[16] It is not known how these pK's vary with temperature. However, it has been suggested that polymerization at low temperature in $H_2SO_4^-$ glasses may cause a large increase in pK.[17]

The reasons for the differences in the reactivities of e_m^- and e_s^- are not known. It should be noted, however, that when the scavenging efficiencies are normalized to that of the only neutral scavenger, H_2O_2, it can be seen (Table II) that the rates of scavenging of e_s^- by the positive scavengers, H_3O^+ and Cu^{2+}, are increased relative to those of the e_m^- scavenging, while for all the negative scavengers the opposite is the case. This may indicate that the difference between the reactivities of e_m^- and e_s^- can be due, at least in part, to coulombic effects. Thus, one should expect this effect to increase with decreasing velocity of the electron, *i.e.*, in going from e_m^- to e_s^-. Similarly, a corresponding decrease in relative scavenging efficiency of the negative scavengers can be seen (Table II) also going from e^- to e_m^- for which the energy probably decreases in this order. It must be emphasized, however, that these indications of coulombic effects are only qualitative, and for the hydronium ion it seems particularly unlikely that they are the main reason for the different reactivities of e_m^- and e_s^-. Additional solutes, especially positive and neutral ones, should be investigated to test the hypothesis further.

The mechanism of the diffusion of the stabilized electron under the present conditions is not clear. As noted above, thermal activation of the electron to a mobile state comparable to e_m^- can be disregarded, and we are left with the following three possibilities.

(1) The electron may be tunneling from its trap directly into the vacant orbital of the scavenger. It seems improbable that a major fraction of e_s^- decays by this mechanism because it implies tunneling over distances of the order of 15 Å. Furthermore, this mechanism alone offers no reasonable explanation for the strong temperature dependence of the decay rate observed above 110 K, *i.e.*, an increase by roughly one order of magnitude between 110 and 123 K.[9] It seems quite possible, however, that a smaller fraction of e_s^- *i.e.*, those incidentally trapped fairly close to scavenger molecules, decay in this way.

(2) The electron may be tunneling from one trap to another until a scavenger molecule is encountered.

(14) L. Kevan, P. N. Moorthy, and J. J. Weiss, *J. Amer. Chem. Soc.*, 86, 771 (1964).

(15) L. Kevan, *ibid.*, 89, 4238 (1967).

(16) "Handbook of Chemistry and Physics," 45th ed, The Chemical Rubber Co., Cleveland, Ohio, 1964.

(17) D. M. Brown and F. S. Dainton, *Trans. Faraday Soc.*, 62, 1139 (1966).

However, if it is assumed that the trap density of the present glass is approximately 10^{-2} M, as seems to be the case for 10 M NaOH glass,[7,18] such tunneling must take place over distances of the order of 25 Å in order to explain a major fraction of the decay of e_s^-. Hence, if the estimate of trap density is of the correct order of magnitude, this mechanism is probably not important here.

(3) The stabilized electron may move as such. That is, the electron trap with the electron in it may be randomly moving by dielectric relaxation of the medium. This possibility is supported by the sharp rise in the decay rate of e_s^- which is observed in the temperature region where the glass begins to soften.

As already noted, it is of course possible that the diffusion of e_s^- occurs by a combination of these mechanisms. Thus, it is conceivable that diffusion over relatively large distances, say >10 Å, occurs primarily by mechanism 3, and that the dominance of this mechanism increases with temperature, while short-range displacements may take place by tunneling processes, primarily the tunneling from trap to scavenger, which should be relatively more important at low temperatures.

Such a combination of diffusion mechanisms may be one reason for the time-dependent reaction rate of e_s^- as shown in Figure 5. Thus, it seems possible that the relatively fast initial decay is associated mainly with tunneling of part of e_s^- directly into the scavenger molecule, *i.e.*, that part of e_s^- which is trapped sufficiently close to scavenger molecules, while the slower decay component is due to diffusion of e_s^- as such, *i.e.*, by mechanism 3 above. This hypothesis is indeed supported by the observation that the temperature dependence of these two decay components appears to be different.[9]

A further study of the reaction kinetics of e_s^- in glasses may possibly shed some light on the more general problem of the time dependence of the reaction of e_{aq}^- in its early stages (*i.e.*, in very concentrated solutions) which so far seems to be based primarily on theoretical arguments.

Acknowledgment. We are indebted to Professor Aa. Ore and Mrs. J. Mossige for constructive criticism of the manuscript.

(18) B. G. Ershov and A. K. Pikaev, *Radiat. Res. Rev.*, **2**, 1 (1969).

The Photochemical Behavior of Cobalt Complexes Containing Macrocyclic (N_4) Ligands. Oxidation–Reduction Chemistry of Dihalogen Radical Anions[1]

by Sally D. Malone and John F. Endicott*

Department of Chemistry, Wayne State University, Detroit, Michigan 48202 *(Received February 18, 1972)*

Publication costs assisted by the Public Health Service

The electron transfer reactions of dihalogen radical anions, X_2^-, have been examined with cobalt(III) and with cobalt(II) substrates. The X_2^- oxidations of Co(*trans*[14]diene)$^{2+}$ all proceed at nearly diffusion-controlled rates. The observation of this reaction for I_2^- substantiates the prediction that I_2^- is a stronger oxidant than I_2 or I_3^-. No direct evidence for X_2^- reduction of cobalt(III) complexes has been obtained. Indirect evidence is presented that I_2^- reduces $Co(NH_3)_5I^{2+}$.

Introduction

Following the classical study of Grossweiner and Matheson[2] the spectral and kinetic properties of the dihalogen radical anions, I_2^-,[2] Br_2^-,[3,4] and Cl_2^- [3-5] have been reasonably well characterized.[6] These radicals have often been postulated as likely intermediates in one-equivalent reactions of various metal ions with aqueous solutions of the halogens[7-9] or halides.[10] Despite their ease of generation and detection, and despite their apparent mechanistic importance, there have been few direct observations of the reactions of

(1) Partial support of this research by the Public Health Service (Grant AM 14341) is gratefully acknowledged.

(2) L. I. Grossweiner and M. S. Matheson, *J. Phys. Chem.*, **61**, 1089 (1957).

(3) M. S. Matheson, W. A. Mulac, and J. Rabani, *ibid.*, **69**, 2613 (1965).

(4) M. E. Langmuir and E. Hayon, *ibid.*, **71**, 3308 (1967).

(5) M. Anbar and J. K. Thomas, *ibid.*, **68**, 3829 (1964).

dihalide radical anions with transition metal substrates.[4,11-13] There has been some direct evidence for the X_2^- oxidations of transition metal substrates.[11-13] It is to be observed, however, that the irreversibility of their redox disproportionation reactions[2-5] (1) suggests that these species may in principle also function as reducing agents.

$$2X_2^- \longrightarrow X_2 + 2X^- \qquad (1)$$

We have undertaken photochemical investigations of cobalt(III) complexes of the type *trans*-Co^{III}(*trans*-[14]diene)X_2[14] in order to examine some aspects of the kinetics and energetics of recombination reactions involving dihalogen radical anions and Co^{II}(*trans*[14]-diene)[15-17] species. Since the tetradentate macrocyclic *trans*[14]diene ligand remains coordinated to cobalt(II) for long periods in aqueous solution,[16,17] radical recombination reactions are expected to be an extremely im-

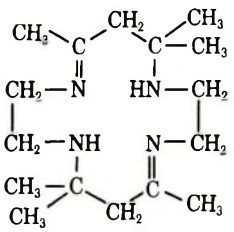

trans[14]diene

portant component of the charge transfer to metal (CTTM) photochemistry of the *trans*-Co^{III}(*trans*[14]-diene)X_2 species. Furthermore Co^{II}(*trans*[14]diene) species are known to be weakly reducing[16-18] and low spin,[17] so these are good model systems in which to examine the reactivity of low spin ($3d^7$) cobalt(II) complexes with simple radicals.

In addition to the X_2^- oxidations of Co^{III}(*trans*-[14]diene), we have looked for evidence of X_2^- reductions of cobalt(III) complexes.

Experimental Section

A. Materials. Reagent grade acids and simple salts were used without further purification. Distilled water, redistilled from permanganate in Pyrex apparatus, was used for all solutions. For solution deaeration, tank nitrogen was passed through a chromous–perchloric acid scrubber to remove the last traces of oxygen. The $Co(NH_3)_6^{3+}$,[19] $Co(NH_3)_5Br^{2+}$,[19] and $Co(NH_3)_5I^{2+}$ [20] complexes were prepared as described in the literature and metathesized to the perchlorate salts by recrystallizing from dilute perchloric acid when desired. Preparations of (*trans*[14]diene)$\cdot 2HClO_4$ [21] and $Na_3[Co(CO_3)_3]\cdot 3H_2O$,[22] used to prepare [Co(*trans*[14]-diene)CO_3]ClO_4 and subsequently [Co(*trans*[14]diene)-X_2]ClO_4 or Co(*trans*[14]diene)X_3 were followed as previously described.[23,24] The preparation of [Co(*trans*-[14]diene)$(O_2CCH_3)OH$]ClO_4 has been described elsewhere.[16] The [Co(*trans*[14]diene)]$(ClO_4)_2$ was prepared in an inert atmosphere,[17] and the compound stored in stoppered containers under nitrogen until use.

B. Apparatus. The instrumentation used to generate and record flash photolysis data has been described,[11] as have the various continuous photolysis apparatuses.[25-27] Absorption spectra were measured using a Cary 14 recording spectrophotometer. The 20-cm cells used for flash photolysis were made with quartz windows and jacketed with a quartz tube concentric with the sample cell.[27,28] The flash pulse had about a 50-μsec detectable duration for 250-J pulses.[11] For less intense pulses the pulse duration was shorter, becoming about 15 μsec for a 50-J pulse.

C. Procedures. To eliminate oxygen from solutions to be photolyzed, flasks containing the weighed amount of solid to be dissolved were evacuated then filled with Cr^{2+}-scrubbed nitrogen. The appropriate amount of previously deaerated solvent was quickly added by pipet, and the solutions were then transferred *via* pipet or syringe and serum cap into previously N_2 flushed systems. Samples for spectral measurements were syringed into preflushed 1-cm silica cells with round tops onto which serum caps were fixed. Each solution

(6) For recent reviews see: (a) A. Treinin, "Radical Ions," E. T. Kaiser and L. Kevan, Ed., Interscience, New York, N. Y., 1968, Chapter 12, pp 544–551; (b) J. K. Thomas, *Adv. Radiation Chem.*, 1, 103 (1969).

(7) P. R. Carter and N. Davidson, *J. Phys. Chem.*, **56**, 877 (1952).

(8) J. H. Crabtree and W. P. Schaeffer, *Inorg. Chem.*, **5**, 1348 (1966).

(9) W. H. Woodruff, D. C. Weatherburn, and D. W. Margerum, *ibid.*, **10**, 2102 (1971).

(10) A. J. Fudge and K. W. Sykes, *J. Chem. Soc.*, 119 (1952).

(11) G. Caspari, R. G. Hughes, J. F. Endicott, and M. Z. Hoffman, *J. Amer. Chem. Soc.*, **92**, 6801 (1970).

(12) A. T. Thornton and A. S. Lawrence, *Chem. Commun.*, 443 (1970).

(13) (a) T. L. Kelly and J. F. Endicott, *J. Amer. Chem. Soc.*, **92**, 5733 (1970); (b) *ibid.*, **94**, 1797 (1972).

(14) *trans*[14]diene = 5,7,7,12,14,14-hexamethyl-1,4,8,11-tetraazacyclotetradeca-4,11-diene.

(15) The axial coordination positions of the cobalt(II) complex are labile, and there is some limited evidence[16,17] that at equilibrium there are no ligands strongly bonded in the axial positions in these complexes.

(16) M. P. Liteplo and J. F. Endicott, *Inorg. Chem.*, **10**, 1420 (1971).

(17) D. P. Rillema and J. F. Endicott, *J. Amer. Chem. Soc.*, submitted for publication and unpublished observations.

(18) D. P. Rillema, J. F. Endicott, and E. Papaconstantinoe, *Inorg. Chem.*, **10**, 1739 (1971).

(19) W. C. Fernelius, *Inorg. Syn.*, **2**, 217 (1940); H. S. Booth, *ibid.*, **1**, 186 (1939).

(20) R. G. Yalman, *Inorg. Chem.*, **1**, 16 (1962).

(21) N. F. Curtis and R. W. Hay, *Chem. Commun.*, 524 (1966).

(22) H. F. Bauer and W. C. Drinkard, *J. Amer. Chem. Soc.*, **82**, 5031 (1960).

(23) N. Sadasivan and J. F. Endicott, *ibid.*, **88**, 5468 (1966).

(24) N. Sadasivan, J. A. Kernohan, and J. F. Endicott, *Inorg. Chem.*, **6**, 770 (1967).

(25) J. F. Endicott and M. Z. Hoffman, *J. Amer. Chem. Soc.*, **87**, 3348 (1965).

(26) J. F. Endicott, M. Z. Hoffman, and L. S. Beres, *J. Phys. Chem.*, **74**, 1021 (1970).

(27) W. L. Wells and J. F. Endicott, *ibid.*, **75**, 3075 (1971).

(28) See ref 13.

from which kinetic measurements were taken was flashed only once and then discarded. In some cases we have used cut-off filter solutions[13] to prevent irradiation of deep ultraviolet absorption bands or to minimize the amount of decomposition during a single flash. Flash photolysis data were recorded in the usual manner.[11] After converting observed transmittance values into absorbance values and correcting for substrate absorbances, data were treated in either first-order (log $(A - A_\infty)$ *vs.* time) or second-order ($1/A$ *vs.* time) manner. The order of reaction was determined from plots of log A_0 *vs.* $t_{1/2}$.[11]

Results

A. Continuous Photolysis. The 254-nm irradiation of solutions of Co(*trans*[14]diene)$(OH_2)_2^{3+}$ and Co(*trans*[14]diene)Cl_2^+ results in the formation of Co(*trans*[14]diene)$^{2+}$. Overall quantum yields are estimated as $(3.5 \pm 1.2) \times 10^{-3}$ (in 0.1 *M* $HClO_4$) and $(3 \pm 1) \times 10^{-3}$ (in 0.1 *M* $HClO_4$, 0.9 *M* KCl), respectively, for the diaquo and dichloro complexes.

The determination of *primary* quantum yields in these systems is extremely difficult for at least three reasons. (1) As reported in detail below Co(*trans*[14]diene)$^{2+}$ is oxidized efficiently by many of the primary and secondary radicals and by oxidized ligand species (*e.g.*, X_2) formed from photoreduction of Co^{III}(*trans*[14]diene)X_2. (2) Co(*trans*[14]diene)$^{2+}$ is very readily oxidized by O_2 especially at high halide concentrations. (3) The absorption maxima of the Co(*trans*[14]diene)$^{2+}$ product ($\epsilon_{325} = 2.6 \times 10^3$; $\epsilon_{250} = 1 \times 10^3$) and original substrates (*e.g.*, for Co(*trans*[14]diene)Cl_2^+, $\epsilon_{325} = 1.6 \times 10^3$; $\epsilon_{250} = 1.4 \times 10^4$) are not sufficiently different that the yields of products can be readily determined for small extents of photolysis. To attempt a better estimate of the primary quantum yield we have also photolyzed Co(*trans*[14]diene)Cl_2^+ in pure methanol. Under these conditions one expects reactions 2 and 3[4,11]

$$\text{Co(}trans\text{[14]diene)}Cl_2^+ + h\nu \longrightarrow \text{Co(}trans\text{[14]diene)}^{2+} + Cl\cdot + Cl^- \quad (2)$$

$$Cl\cdot + CH_3OH \longrightarrow HCl + \cdot CH_2OH \quad (3)$$

in competition with (4) and followed by (5)[29] through (7). Since these experiments in methanol were per-

$$Cl\cdot + Cl^- \rightleftharpoons Cl_2^- \quad (4)$$

$$\cdot CH_2OH + \text{Co(}trans\text{[14]diene)}Cl_2^+ \longrightarrow \text{Co(}trans\text{[14]diene)}^{2+} + 2Cl^- + CH_2O + H^+ \quad (5)$$

$$Cl_2^- + \text{Co(}trans\text{[14]diene)}^{2+} \longrightarrow \text{Co(}trans\text{[14]diene)}Cl_2^+ \quad (6)$$

$$Cl\cdot + Cl_2^- \longrightarrow Cl_2 + Cl^- \quad (7)$$

formed at very low $[Cl^-]$, (4), (6), and (7) can be assumed to be relatively unimportant. We have not observed (5), but assume that it may account for half the observed cobalt(II).[29] The overall quantum yield of Co(*trans*[14]diene)$^{2+}$ observed under these conditions was $(3 \pm 1) \times 10^2$ which implies a primary yield of about $(1.5 \pm 1) \times 10^{-2}$.

The 254-nm irradiation of Co(*trans*[14]diene)$(O_2CCH_3)OH^+$ in neutral solution or in NaO_2CCH_3 solution (0.1 or 0.01 *M*) led to the formation of Co(*trans*[14]diene)$^{2+}$. Although we were unable to purge sample solutions of CO_2 before photolysis (the hydrolysis of this cobalt(III) complex is acid catalyzed), we did find that CH_4 and C_2H_6 were not detectable as photolysis products. We estimate the quantum yield for formation of Co(*trans*[14]diene)$^{2+}$ to be (0.12 ± 0.03) for this complex.

When [Co(*trans*[14]diene)$(N_3)_2$]ClO_4 was irradiated at 254 nm, the absorbance changes at 560 nm were consistent with $\phi_{\text{Co(}trans\text{[14]diene)}^{2+}} = 0.04$.

B. Flash Photolysis Studies. Dihalide Radical Anion Decay Rates. To be able to compare values of the X_2^- decay rate constants (k_1) appropriate to our experimental conditions we have generated Cl_2^-, Br_2^-, and I_2^- from several sources. These results are summarized in Table I. Values of k_1 in Table I have 15–20% precision except in the cases noted.

Dihalide Radical Anion Reactions with Co(trans[14]diene)$^{2+}$. As noted in Table I, transients generated from Co(*trans*[14]diene)Cl_2^+ and Co(*trans*[14]diene)Br_2^+ do not exhibit a simple second-order decay over more than one reaction half-life. The observed curvature of the second-order plots is consistent with a competition between the natural decay mode (1) and reaction 8 with the cobalt(II) fragment which formed in the photoreduction of Co(*trans*[14]diene)X_2^-.[15,30] To ob-

$$Y + \text{Co(}trans\text{[14]diene)}^{2+} + X_2^- \longrightarrow Co^{III}\text{(}trans\text{[14]diene)}XY + X^- \quad (8)$$

tain reliable rates of reaction 8 we have examined the pseudo-first-order decay rates of X_2^- in the presence of variable amounts of Co(*trans*[14]diene)$^{2+}$. From a plot of the pseudo-first-order decay constants of X_2^- *vs.* [Co(*trans*[14]diene)$^{2+}$] we have obtained the values of k_8 in Table II.

With regard to the data in Table II it should be noted that Co(*trans*[14]diene)I_2^+ is unstable (in excess I^-) with respect to I_3^- and Co(*trans*[14]diene)$^{2+}$.[16,18,31] Since Co(*trans*[14]diene)$^{2+}$ has appreciable absorptivity in the near-ultraviolet, we have used solutions of the highly absorbing ion pair $(Co(NH_3)_6^{3+}, I^-)$[32,33] as our

(29) D. Meyerstein, private communication.

(30) The nature of the axial ligands in the immediate cobalt(III) products is not known.

(31) W. Latimer, "Oxidation Potentials," Prentice-Hall, Englewood Cliffs, N. J., 1952.

(32) M. G. Evans and G. H. Nancollas, *Trans. Faraday Soc.*, **49**, 363 (1949).

(33) M. T. Beck, *Coord. Chem. Rev.*, **3**, 91 (1968).

Table I: Dihalide Radical Anion Decay Rate Constants[a]

Species irradiated	$[X^-]$, M	$[X_2^-]_{t=0} \times 10^6$,[b] M	Ionic strength	$k_1 \times 10^{-9}$, M^{-1} sec^{-1}
Cl^- [c,d]	1.0	1.2	1.1	8.4
Co(*trans*[14]diene)Cl_2^+ [e]	1.0	1	1.1	8.2 ± 4
Br^- [c,d]	1.0	4.1	1.1	5.8
$Co(NH_3)_5Br^{2+}$	0.20	1–3	0.20	3.2
Co(*trans*[14]diene)Br_2^+ [e]	0.10	1–10	0.20	6.4 ± 0.8
Co(tetraen)Br^{2+}	0.20	4	0.20	3.0
I^- [c,f]	0.010	2–5	0.020	7
$Co(NH_3)_6^{3+}$, I^- [g]	0.010	9	0.020	3.5
$Co(NH_3)_5I^{2+}$	1.0×10^{-3}	1	0.10	5.4
	(2×10^{-6})[h]	7	0.12	*i*

[a] pH 1 except as indicated. Mean values of k_1 are quoted. Average deviations were ±20% except as indicated. [b] Extrapolated concentration. A range of $[X_2^-]_{t=0}$ is indicated in cases that several experiments gave differing values. [c] Potassium salt. [d] Solutions saturated with N_2O. [e] Second-order plots generally were significantly curved; k_1 estimated from initial slope. [f] pH 3. [g] Ion pair. [h] $[I^-]$ inferred from $[I_2^-]_{t=0}$, $K_9 = 8 \times 10^4$ M^{-1} and the amount of $Co(NH_3)_5I^{2+}$ decomposed in the flash. [i] At very low $[I^-]$ the decay of I_2^- becomes first order; see ref 2. The first-order rate constant was 2.8×10^4 sec^{-1}.

Table II: Rate Constants for Oxidations of Co(*trans*[14]diene)$^{2+}$ by Dihalide Radical Anions

X_2^-	Source of X_2^-	$[X^-]$, M[a]	Ionic strength	Range of added $[Co(trans[14]diene)^{2+}]$, M[b]	$k_8 \times 10^{-9}$, M^{-1} sec^{-1}
Cl_2^-	Co(*trans*[14]diene)Cl_2^+	1.0 (Cl^-)	1.1	$(0–3.5) \times 10^{-5}$ (3)	1.0 ± 0.4
Br_2^-	Co(*trans*[14]diene)Br_2^+	0.2 (Br^-)	0.2	$(0–3.5) \times 10^{-5}$ (4)	1.4 ± 0.1
	$Co(NH_3)_5Br^{2+}$	0.2 (Br^-)	0.2	$(0.5–1.8) \times 10^{-5}$ (5)	1.5 ± 0.1
I_2^-	$Co(NH_3)_6^{3+}$, I^- [c]	0.02 (I^-)	0.03	$(1–10) \times 10^{-6}$ (10)	7.2 ± 0.8

[a] pH 1; halide in parentheses. [b] Number of trials in parentheses. [c] Ion pair; pH 2.

source of I_2^- for these experiments. It has previously been established that the $(Co(NH_3)_6^{3+}, I^-)$ ion pair is efficiently photodecomposed into Co^{2+} and I_2.[25,34] The ammine complexes of cobalt(II) equilibrate with solvent in acidic aqueous solution rapidly enough that they cannot be involved in a back reaction with I_2^- or I_3^-. In this system we do observe that the pseudo-first-order rate constant for decay of I_2^- increases with $[Co(trans[14]diene)^{2+}]$; however, following this reaction we observe a very slow increase in the absorptivity due to I_3^-. This slower reaction is apparently the result of I^- reduction of the (*trans*[14]diene)cobalt(III) complexes formed in the initial step (8). The apparent second-order rate constant for this latter reaction is about 35 M^{-1} sec^{-1} under our reaction conditions.

$Co(NH_3)_5I^{2+}$. We have carefully re-examined[35] the flash photolysis behavior of this complex to determine (1) if the radical implicated[25,36,37] in the thermal reduction of $Co(NH_3)_5I^{2+}$ can be identified as $I\cdot$ or I_2^- and (2) whether $Co(NH_3)_5I^{2+}$ is a convenient source of I_2^-.

We find that if $[Co(NH_3)_5I](ClO_4)_2$ is dissolved in 0.1 M $HClO_4$, if all solutions are handled in the dark and if solutions approximately 10^{-5} M in $Co(NH_3)_5I^{2+}$ are flashed in less than 15 min after dissolving the complex, then *no* transient absorbance is observed in the near-ultraviolet spectral region. If solutions are permitted to stand more than about 30 min, so that some I^- may be formed from the thermal hydrolysis,[38] or if small amounts of I^- ($[I^-] \leq 10^{-3}$ M) are introduced into the solution before photolysis, then the I_2^- transient is always observed. The decay characteristics of the I_2^- transient formed from $Co(NH_3)_5I^{2+}$ depend on the (estimated) ratio of $[I\cdot]$ to $[I_2^-]$ as expected,[2] but do not depend on the $[Co(NH_3)_5I^{2+}]$ remaining after flashing. When perchlorate solutions (from which I^- has been excluded as rigorously as possible) of $Co(NH_3)_5I^{2+}$ are only partially (about 50% using a 50-J pulse) decomposed by flash photolysis, the substrate absorbance at 390 nm changes only during the light pulse (pulse lifetimes were 10–20 μsec); in our experiments the substrate absorbance was observed to be constant after 10–15 μsec.

We found that solutions of $Co(NH_3)_5I^{2+}$ were too difficult to handle to be convenient as a source of I_2^-.

(34) J. F. Endicott and M. Z. Hoffman, *J. Phys. Chem.*, **70**, 3389 (1966).

(35) S. A. Penkett and A. W. Adamson, *J. Amer. Chem. Soc.*, **87**, 2514 (1965).

(36) A. Haim and H. Taube, *ibid.*, **85**, 495 (1963).

(37) V. Balzani and V. Carassiti, "Photochemistry of Coordination Compounds," Academic Press, New York, N. Y., 1970, p 205.

(38) F. Basolo and R. G. Pearson, "Mechanism of Inorganic Reactions," 2nd ed, Wiley, New York, N. Y., 1967.

Discussion

A. Photoredox Behavior of Cobalt(III) Complexes Containing Macrocyclic Ligands. The estimated primary yield of about 0.02 for photoreduction of Co(*trans*[14]diene)Cl_2^+ can be compared to yields of about 0.2 for $Co(NH_3)_5Cl^{2+}$,[11,25] 0.1 for *trans*-$Co(en)_2Cl_2^+$ [25] and 0.03 for Co(tetraen)Cl^+ [11] (tetraen is tetraethylenepentamine). Although this variation in quantum yields cannot be easily rationalized at the present time, it is clear that all these systems must have very efficient mechanisms for nonradiative relaxation of their charge-transfer excited states; the efficiency of deactivation varies only from 80 to 98%.

As we had expected, thermal back reactions are very important when macrocyclic complexes of cobalt(III) are photoreduced. We have capitalized on this fact to examine some features of dihalogen radical anion reactions with metal complexes.

B. Dihalogen Radical Anion Reactions with Metal Complexes. The X_2^- oxidations of Co(*trans*[14]diene)$^{2+}$ all occur with second-order rate constants which are very near to the diffusion-controlled limit. Such variations in k_8 as we have recorded in Table II appear to arise from differences in the ionic strength rather than from differences in the reactivities of the various X_2^- species. When we commenced this study, we had expected some variations in reactivity since the X_2^- radical anions vary in their oxidizing potentials (Table III) and the Co(*trans*[14]diene)$(OH_2)_2^{3+,2+}$ self-exchange rate is very slow ($k_{Co} = 2 \times 10^{-7}$ M^{-1} sec^{-1} at 70°).[39] Thus, in principle, values of k_8 might have been used in connection with the Marcus[40] cross relation[41] to determine the validity of potentials estimated in Table III. More recently, however, it has been shown that the activation barriers observed in cobalt(III)–(II) self-exchange reactions are not simply related to the activation barriers observed in either reductions of cobalt(III)[42] complexes or the oxidations of cobalt(II)[17] complexes. The value of $k_8 \geq 10^9$ M^{-1} sec^{-1} observed for X_2^- oxidations of Co(*trans*[14]diene)$^{2+}$ can be compared to the second-order rate constant of approximately 10^6 M^{-1} sec^{-1} observed for both the Ce^{IV} ($E° = 1.44$ V)[31] and the $Ru(bipy)_3^{3+}$ ($E° = 1.26$ V)[43] oxidations of this same substrate.[17] Allowing for the differences in reactant charge types there is less than two orders of magnitude difference in these reactivities.

One aspect of the potentials estimated in Table III is clearly confirmed by this study. Despite the similarity of potentials for the Co(*trans*[14]diene)$(OH_2)_2^{3+,2+}$ [16] and the I_2/I^- [31] couples and despite the observation that excess I^- reduces Co(*trans*[14]diene)$(OH_2)_2^{3+}$,[44] we find that I_2^- oxidizes Co(*trans*[14]diene)$^{2+}$ (in excess iodide), demonstrating that I_2^- is a significantly stronger oxidant than I_2. The thermodynamic argument that X_2^- radical anions are generally more powerful oxidants than the X_2 or X_3^- species seems unimpeachable.

Table III: Reduction Potentials for Aqueous Halogen and Dihalide Radicals

Radical couple	Estimated reduction potentials, V[a] X = Cl	X = Br	X = I
$X\cdot + e^- \rightleftharpoons X^-$	2.6	2.2	1.4[b]
$X_2^- + e^- \rightleftharpoons 2X^-$ [c]	2.3	1.9	1.1
$X_2 + e^- \rightleftharpoons X_2^-$	0.6	0.3	0.3

[a] Using standard free energies of formation of X·(gas), and X^-(aq) as tabulated in ref 31. Standard free energies of solution of X· were approximated using solubility data of the nearest noble gas (J. H. Hildebrand, J. M. Prausnitz, and R. L. Scott, "Regular and Related Solutions," Van Nostrand-Reinhold, Princeton, N. J., 1970, p 204). [b] A value of 1.27 V was estimated for this couple in ref 36. [c] For $K = [X_2^-]/[X\cdot][X^-]$ we have used $K \simeq 10^5$ M^{-1} in each case (ref 6b). For Br_2^-, K has been reported to be greater than 10^7 M^{-1} (B. Cercek, M. Ebert, C. W. Gilbert, and A. J. Swallow, "Pulse Radiolysis," Academic Press, New York, N. Y., 1965, p 83) and for Cl_2^- greater than of equal to 10^2 M^{-1} (ref 25).

It is much more difficult to find direct evidence that X_2^- radical anions function as reducing agents. We have found that the presence of Co(*trans*[14]diene)$(OH_2)_2^{3+}$ does not change the Br_2^- decay rate. On the other hand, the observation that the cobalt(II) yield from irradiation of $Co(NH_3)_5I^{2+}$ is dependent on the incident light intensity[25,37,45] suggests that some such X_2^- reaction may occur in this system;[46] thus

$$Co(NH_3)_5I^{2+} + h\nu \xrightarrow{H^+} Co^{2+} + I\cdot + 5NH_4^+ \quad (\phi I_a)$$

$$I\cdot + I^- \rightleftharpoons I_2^- \quad (9)$$

(39) D. P. Rillema, J. F. Endicott, and N. A. P. Kane-Maguire *J. Chem. Soc., Chem. Commun.*, 495 (1972).

(40) For pertinent reviews see: (a) R. A. Marcus, *Ann. Rev. Phys. Chem.*, **15**, 155 (1965); (b) W. L. Reynolds and R. W. Lumry, "Mechanisms of Electron Transfer," Ronald Press, New York, N. Y., 1966.

(41) In the present case, this would be $k_8 = (k_{Co}k'K_8f_8)^{1/2}$ where k' is a "self-exchange" rate constant for I_2/I_2^-, K_8 is the equilibrium constant for K_8 and $\log f_8 = (\log K_8)^2/4 \log (k_{Co}k'/Z^2)$ (for Z the collision frequency).

(42) D. P. Rillema, J. F. Endicott, and R. C. Patel, *J. Amer. Chem. Soc.*, **94**, 394 (1972); (b) J. F. Endicott, R. R. Schroeder, and D. R. Ferrier, *J. Phys. Chem.*, submitted for publication; (c) D. P. Rillema and J. F. Endicott, *Inorg. Chem.*, in press.

(43) See D. A. Buckingham and A. M. Sargeson, "Chelating Agents and Metal Chelates," R. P. Dwyer and D. P. Mellor, Ed., Academic Press, New York, N. Y., 1964, Chapter 6, Bipy is bipyridine.

(44) J. A. Kernohan, Ph.D. Dissertation, Boston University, 1969. Also note the similar inference recorded in the Results section, above.

(45) Valentine (*Advan. Photochem.*, **6**, 123 (1968), footnote 64) has attributed to one of the present authors (J. F. E.) a statement that this intensity dependence is not real. At one time this author did verbally discuss the possibility of ambiguities resulting from the techniques employed by Endicott and Hoffman.[22] The effect in question has been substantiated in the more careful work of Balzani and coworkers.[37]

(46) Haim and Taube[36] have presented evidence that the enhanced reduction of $Co(NH_3)_5I^{2+}$ is brought about by iodine atoms (I·); see following discussion.

$$I_2^- + Co(NH_3)_5I^{2+} \xrightarrow{H^+} I_3^- + Co^{2+} + 5NH_4^+ \quad (10)$$

$$2I_2^- \longrightarrow I_3^- + I^- \quad (11)$$

$$I_2^- + I \longrightarrow I_2 + I^- \quad (12)$$

$$2I \longrightarrow I_2 \quad (13)$$

We have therefore re-examined aspects of the photochemistry of $Co(NH_3)_5I^{2+}$ in order to determine whether evidence for reaction 10 can be found. Flash photolysis of $Co(NH_3)_5I^{2+}$ produces I_2^- except when I^- is rigorously excluded from the photolyte. When I_2^- is observed, the amount is compatible with the thermal aquation of $Co(NH_3)_5I^{-}$ [38] and the high stability of I_2^- ($K_9 = 8 \times 10^4\ M^{-1}$ [6b]). Under flash conditions (*i.e.*, high I_a and $[Co(NH_3)_5I^{2+}] \leq 5 \times 10^{-5}\ M$), we find no evidence for either (10) and (14). If these reactions

$$I\cdot + Co(NH_3)_5I^{2+} \xrightarrow{H^+} I_2 + Co^{2+} + 5NH_4^+ \quad (14)$$

were diffusion controlled (*i.e.*, k_{10} or k_{14} about 10^{10} M^{-1} sec^{-1}), we should have observed a transient ($t_{1/2}$ > 10 μsec) corresponding to the change in substrate absorbance (at 390 nm in the absence of I^- or at 580 nm when I^- was present), but we have not been able to detect such an absorbance change.[47] We therefore conclude that reactions 10 and 14 are too slow to compete with (11)–(13) at such high radical concentrations. This is of course consistent with the previously observed intensity dependence[25,37] of the cobalt(II) yields since these continuous photolyses have indicated that even with $I_a \simeq 5 \times 10^{-3}$ einstein l.$^{-1}$ min^{-1} (about 1/10^3 of our flash intensities) (10) and (14) are not competitive with (11)–(13). Although neither (10) nor (14) is observed directly, some relatively straightforward considerations suggest that observed intensity dependence of the cobalt(II) yield can only arise from (10). In the continuous photolysis experiments $[Co(NH_3)_5I^{2+}] \simeq 10^{-3}\ M$ and 10–20 min after preparing such solutions $[I^-] \simeq 10^{-5}\ M$.[38] A photostationary state treatment of $[I\cdot]$ and $[I_2^-]$ in the above mechanism leads to

$$[I\cdot] \simeq \frac{\phi I_a + k_{-9}[I_2^-]}{k_9[I^-] + k_{14}[Co(NH_3)_5I^{2+}] + k_{12}[I_2^-] + k_{13}[I\cdot]}$$

Since k_9, k_{12}, and k_{13} are all of the same magnitude (10^9 to 10^{10} M^{-1} sec^{-1})[2] and since $[I^-] \sim 10^{-5}\ M \gg ([I_2^-] + [I\cdot])$, we have approximately (neglecting the contribution from $k_{-9}[I_2^-]$)[48] $[I\cdot] \simeq \phi I_a/(k_9[I^-] + k_{14}[Co(NH_3)_5I^{2+}])$. Thus if $I\cdot$ were the radical reattacking the substrate, the overall quantum yield, $\phi_{Co^{2+}} = (\phi I_a + k_{14}[I\cdot][Co(NH_3)_5I^{2+}])/I_a$ should be independent of I_a, and for the $I\cdot/Co(NH_3)_5I^{2+}$ reaction $k_{14} \geq 10^5\ M^{-1}$ sec^{-1}. From our flash photolysis studies we can only say that $k_{14} < 10^9\ M^{-1}$ sec^{-1}. However $\phi_{Co^{2+}}$ has been found to be I_a dependent, so $I\cdot$ must not be the implicated radical.

Our flash photolysis studies of $Co(NH_3)_5I^{2+}$ show that: (1) no reduction of $Co(NH_3)_5I^{2+}$ (as monitored at 390 and 580 nm) is observed (after the light pulse) on the flash photolysis time scale, and (2) that I_2^- is formed even when $[I^-] \ll [Co(NH_3)_5I^{2+}] \leq 10^{-5}\ M$. We therefore infer that reaction 10 predominates over (14). Assuming that $k_9[I^-] > k_{14}[Co(NH_3)_5I^{2+}]$, then a photostationary state treatment gives

$$[I_2^-] \simeq \frac{\phi I_a}{k_{10}[Co(NH_3)_5I^{2+}] + k_{11}[I_2^-] + k_{12}\phi I_a/k_9[I^-]}$$

The proposed mechanism is compatible with the observed intensity dependence of

$$\phi_{Co^{2+}} \simeq \frac{\phi I_a + k_{10}[I_2^-][Co(NH_3)_5I^{2+}]}{I_a}$$

if

$$k_{10}[Co(NH_3)_5I^{2+}] \simeq \{k_{11}[I_2^-] + k_{12}\phi I_a/k_9[I^-]\}$$

when $I_a \simeq 10^{-6}$ einstein l.$^{-1}$ sec^{-1}. Further substituting $[I^-] \simeq 10^{-5}\ M$, $[Co(NH_3)_5I^{2+}] \simeq 10^{-3}\ M$, and $k_{12} \simeq k_7 \simeq 10^{10}\ M^{-1}$ sec^{-1}, and $k_{11} \simeq 5 \times 10^9\ M^{-1}$ sec^{-1}, we find $[I_2^-] \simeq 5 \times 10^{-9}\ M$ and $k_{10} \simeq 2.5 \times 10^4\ M^{-1}$ sec^{-1}. It is clear that the observed intensity dependence of ϕ in this system can be related to a radical/substrate reaction only if this reaction has a relatively small (compared to k_9, k_{11}, k_{12}, or k_{13}) second-order rate constant.

Our very rough estimate of a reasonable value of k_{10} may be compared to the observed value of $6.7 \times 10^3\ M^{-1}$ sec^{-1} for the $Ru(NH_3)_6^{2+}$ ($E^\circ = 0.1$ V)[49] reduction of $Co(NH_3)_5I^{2+}$.[50] Since the I_2/I_2^- self-exchange reaction must be slower than or equal to diffusion controlled ($k_{ex} \leq 10^{10}\ M^{-1}$ sec^{-1}), the apparent similarities in the rates of the $Ru(NH_3)_6^{2+}$ and I_2^- reductions of $Co(NH_3)_5I^{2+}$ does indicate that I_2^- is a relatively good reducing agent; *i.e.*, using the Marcus[41] square root relation, $k_{12} = (k_{11}k_{22}K_{12})^{1/2}$, we estimate $E^\circ \leq 0.45$ V for the I_2/I_2^- couple.[46,47,49-52] This limit is consistent with the estimate for this couple in Table III.

C. Mixed Dihalogen Radical Anions. The potentials estimated in Table III permit some inferences regarding the formation and stability of radical anions of the type XY^-, where $X \neq Y$. Such a radical anion

(47) Note that our experimental conditions were adjusted so that the observed transmittance changed from about 0% T to about 30% T during a single flash. This change in transmittance corresponds to about 50% decomposition of the $Co(NH_3)_5I^{2+}$ substrate.

(48) The term $k_{-9}[I_2^-]$ can make a significant contribution only if k_{12} is about the same magnitude as k_9. Our experimental observations rule out this possibility.

(49) T. J. Meyer and H. Taube, *Inorg. Chem.*, **7**, 2369 (1968).

(50) J. F. Endicott and H. Taube, *J. Amer. Chem. Soc.*, **86**, 1686 (1964).

(51) Employed in this calculation are values of $E^\circ = 0.1$ V[48] and $k_{exch} = 10^3\ M^{-1}$ sec^{-1} [47,49] for the $Ru(NH_3)_6^{3+}/Ru(NH_3)_6^{2+}$ couple.

(52) G. Navon and D. Meyerstein, *J. Phys. Chem.*, **74**, 4067 (1970).

may be formed in either of two ways, (15) or (16). It follows then that the ratio of the corresponding formation constants, K_{15} and K_{16}, and the first-order dissociation rate constant, k_{-15} and k_{-16}, will depend on whether X· or Y· is the better oxidant; *i.e.*

$$X\cdot + Y^- \rightleftharpoons XY^- \quad (15)$$

$$X^- + Y\cdot \rightleftharpoons XY^- \quad (16)$$

$$K_{15}/K_{16} = \frac{[X^-][Y\cdot]}{[X\cdot][Y^-]} \simeq \frac{k_{-16}}{k_{-15}}$$

As an example consider the case of IBr^-. Clearly Br· is a far more powerful oxidant than I·, and from the estimates in Table III we find $[Br\cdot][I^-]/[Br^-][I\cdot] \simeq 1.7 \times 10^{-14}$. Thus IBr^- can only be formed from the reaction of Br· with I^- and would be expected decay into Br^- and I· with a large first-order rate constant. For example, we find that when $Co(NH_3)_5Br^{2+}$ is flash photolyzed in the presence of I^- only the I_2^- transient is observed.

Finally, the mere observation of radical anions of the XY^- type helps bracket the potential of the Y·/Y^- couples. Thus the observation of Schoneshofen and Henglein[53] that both $(ISCN)^-$ and $(BrSCN)^-$ have appreciable lifetimes indicates that the NCS·/NCS^- couple is pretty much central ($E^\circ \simeq 1.8$ V) between the I·/I^- and the Br·/Br^- couples. On the other hand, our observations that flash photolysis of $Co(NH_3)_5N_3^{2+}$ in I^- produces I_2^-, and a new transient ($\lambda_{max} \sim 420$ nm), presumably BrN_3^-, in 1.0 *M* Br^- suggests that N_3· is only a little poorer oxidant than Br··.

(53) (a) M. Schoneshofen and A. Henglein, *Ber. Bunsenges. Phys. Chem.*, **74**, 393 (1970); (b) *ibid.*, **73**, 289 (1969).

Biphotonic Ionization Processes in Nonpolar Solutions of *N,N,N′,N′*-Tetramethyl-*p*-phenylenediamine

by A. Alchalal, M. Tamir, and M. Ottolenghi*

Department of Physical Chemistry, The Hebrew University, Jerusalem, Israel *(Received January 10, 1972)*

Publication costs assisted by the U. S. National Bureau of Standards

Photoconductivity experiments, using pulsed nitrogen-laser excitation at 3371 Å, are carried out in fluid hydrocarbon solutions of TMPD (*N,N,N′,N′*-tetramethyl-*p*-phenylenediamine). The effects of light intensity and of added quenchers indicate that TMPD undergoes ionization in a biphotonic process involving both excited singlet and triplet states as photoactive intermediates. TMPD solutions containing naphthalene and biphenyl as fluorescence quenchers are found to be photoconductive, exhibiting a second power dependence on the laser light intensity. The photocurrents are attributed to light absorption by the resulting fluorescent exciplexes. The details of this process are discussed in terms of the exciplex absorption spectrum.

Introduction

Excited aromatic molecular systems in fluid solutions may undergo ionization *via* two alternative paths represented schematically by

$$D^* \longrightarrow D^+ + e_s^- \text{ (or } R^-) \quad (1)$$

$$D^* + A \longrightarrow D^+ + A^- \quad (2)$$

The first process involves electron transfer from an excited donor molecule (D*) to the solvent, followed by the formation of the D^+ radical cation and a solvated electron (e_s^-).[1] In some cases[2] dissociative electron capture may occur, leading to the formation of solvent radical fragments (R^-). Process 2 involves the interaction between an excited donor and a solute acceptor molecule (or *vice versa*) leading, in polar solvents, to the solvated D^+ and A^- radical ions.[3]

(1) J. Jortner, M. Ottolenghi, and G. Stein, *J. Amer. Chem. Soc.*, **85**, 2712 (1963); J. Eloranta and H. Linschitz, *J. Chem. Phys.*, **38**, 2214 (1963); L. I. Grossweiner and H. I. Joscheck, *J. Amer. Chem. Soc.*, **88**, 3261 (1966); H. S. Pilloff and A. C. Albrecht, *Nature (London)*, **212**, 499 (1966).

(2) C. Chachaty, D. Schoemaker, and R. Bensasson, *Photochem. Photobiol.*, **12**, 317 (1970); M. Ottolenghi, *Chem. Phys. Lett.*, **12**, 339 (1971).

(3) H. Leonhardt and A. Weller, *Z. Phys. Chem. (Frankfurt am Main)*, **29**, 277 (1961); *Ber. Bunsenges. Phys. Chem.*, **67**, 791 (1963); H. Knibbe, D. Rehm, and A. Weller, *ibid.*, **72**, 257 (1968); K. H. Grellmann, A. R. Watkins, and A. Weller, *J. Luminescence*, **1,2**, 678 (1970).

When excitation is carried out with near-uv light in solvents of very low polarity ($\epsilon < 3$), the energy requirements for both processes can be satisfied only by assuming that at least two light quanta are involved in each one-electron ionization. This has been recently confirmed for process 1 with D ≡ TMPD, by a pulsed-laser photoconductivity study,[4] showing that the two quantum process involves the consecutive absorption of two photons, rather than the interaction between two one-photon excited molecules. Process 2 has not yet been distinguished in nonpolar systems.

It is the purpose of the present work to elucidate the mechanism and to identify the photoactive intermediates in the two quantum ionization of TMPD *via* processes 1 and 2 in nonpolar liquids. Conductivity detection methods are applied since their higher sensitivity, relative to absorbance measurements, is essential for monitoring the low yield photoionization products in nonpolar solvents.

Experimental Section

The pulsed N_2 laser photolysis techniques with absorbance or conductivity detection methods have been previously described.[4,5] A fast response (~15 nsec) detection system (Figure 1) for transient conductivity signals, employing a Motorola MC 1445 amplifier, was employed when high time resolution was required. All experiments were carried out using single shots with energy of $\sim 5 \times 10^{-4}$ J. The pulse reproducibility was better than 5%. The laser beam cross section after focusing was of about 6 mm². Maximum peak photocurrents measured under an applied field of 0.5 kV, with a 10^4 Ω load resistor, were about 5 μA.

Eastman Kodak TMPD, naphthalene, and biphenyl were zone refined. Matheson spectrograde solvents were used without further purification. All experiments were carried out at room temperature.

Results and Discussion

(1) *TMPD in Isopentane.* In a previous work, applying a pulsed N_2 laser photoconductivity technique, we have shown that TMPD in isopentane undergoes photoionization *via* the consecutive absorption of two 3371-Å photons.[4] It was suggested that in such a process both lowest singlet and triplet states may act as photoactive intermediates. With the purpose of clarifying the exact roles of these two states in the photoionization process, we have now carried out pulsed laser experiments using selective quenchers of singlet and triplet states. From absorbance lifetime measurements in 3-methylpentane (3MP) (Figure 2), we have established that piperylene efficiently quenches the TMPD triplet state ($^3T^*$) with a rate constant of $1.1 \pm 0.4 \times 10^{10}\ M^{-1}\ \text{sec}^{-1}$. However, the fluorescence of TMPD was found to be unaffected by piperylene concentrations as high as 0.1 *M*. Figure 3 shows the effect of piperylene on the photoconductivity after pulsing a

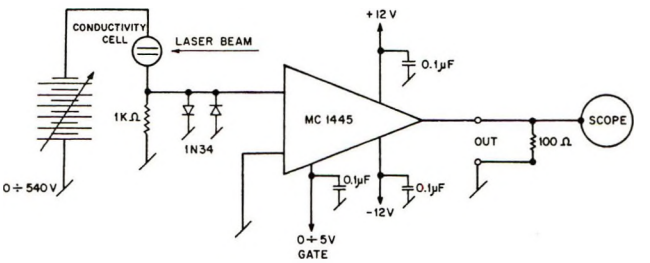

Figure 1. Fast response photoconductivity circuit.

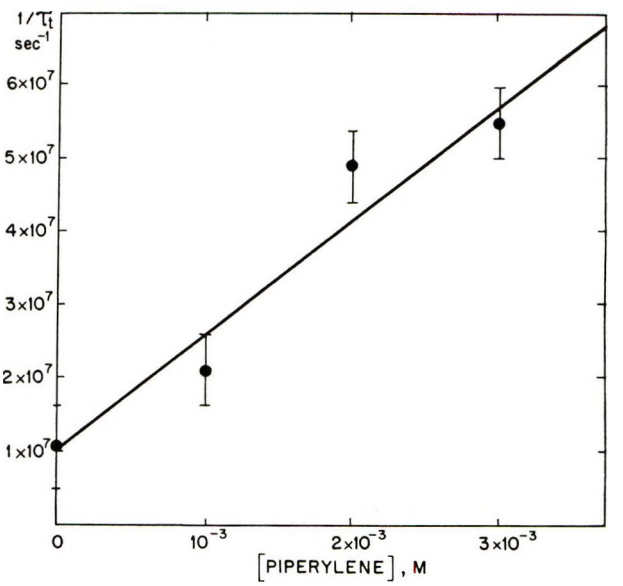

Figure 2. The effect of piperylene on the half-life of the triplet state in a deaerated 10^{-3} *M* solution of TMPD in 3MP.

deaerated 1.5×10^{-3} *M* solution of TMPD in 3MP. The photoconductivity signal is constant as long as the piperylene concentration is below $\sim 5 \times 10^{-2}$ *M*. At higher concentrations the photocurrent decreases, reaching a constant limiting value when [piperylene] < ~0.1 *M*. An important conclusion from the data of Figure 3 is that, even when substantial quenching of $^3P^*$ takes place, as long as the triplet lifetime is long compared to the duration of the laser pulse (~10 nsec), the photocurrent is independent of the piperylene concentration. In other words, the photocurrent starts to be affected only when the triplet lifetime (τ_t) becomes comparable to the duration of the laser pulse (τ_p). A residual value is observed when $\tau_t < \tau_p/10$. Such a behavior is entirely consistent with a biphotonic ionization involving the triplet state, *i.e.*

$$^3T^* \xrightarrow{h\nu} T^+ + e_s^-$$

excluding, in the present low polarity system, triplet–triplet annihilation[6] as a possible path of charge

(4) M. Tamir and M. Ottolenghi, *Chem. Phys. Lett.*, **6**, 369 (1970).
(5) C. R. Goldschmidt, M. Ottolenghi, and G. Stein, *Israel J. Chem.*, **8**, 29 (1970).
(6) L. P. Gary, K. de Groot, and R. C. Yarganin, *J. Chem. Phys.*, **49**, 1577 (1968).

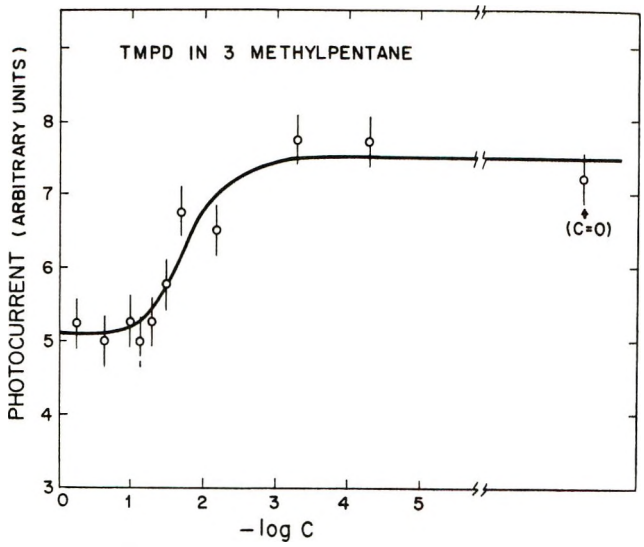

Figure 3. The effect of piperylene concentration (C in moles per liter) on the peak photocurrent in a deaerated 1.5 $\times$ 10^{-3} M solution of TMPD in 3MP.

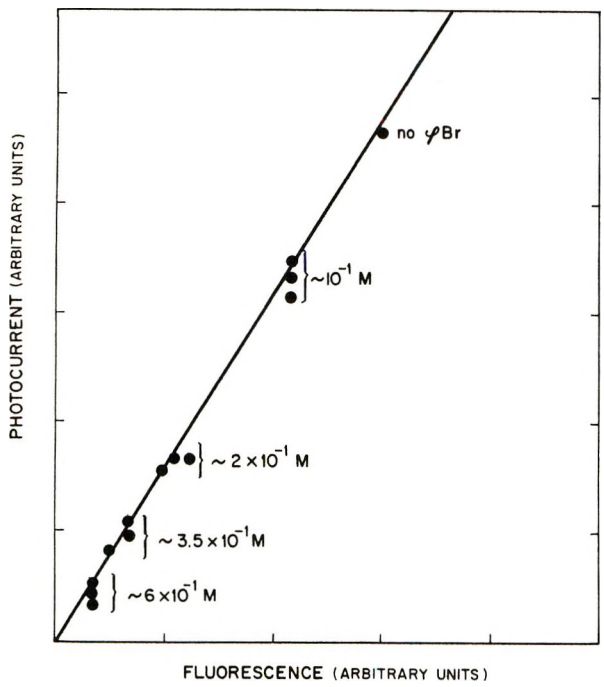

Figure 4. Peak photocurrent (P) as function of fluorescence intensity (I) in a 2 $\times$ 10^{-3} M solution of TMPD in isopentane. The fluorescence was quenched by adding bromobenzene (concentrations are reported in the figure) in the presence of 0.1 M piperylene.

carrier formation. Saturation of TMPD–isopentane solutions with air does not affect the photoconductivity. Since in air-saturated solutions $\tau_t \cong 30$ nsec $> \tau_p$, this is in keeping with the proposed mechanism.

The residual (~70%) photocurrent left after total quenching of the triplet should be attributed to a second absorbing species present during the laser pulse. The most plausible intermediate is the fluorescent singlet state for which, in 3MP, $\tau_s \cong 4$ nsec. To check this assumption we have investigated the effect of added bromobenzene on the photocurrent. The linear relation in Figure 4 shows that the quenching of fluorescence by bromobenzene is accompanied by a drop in the system's photoconductivity. Piperylene was added to scavenge triplet molecules resulting from the heavy atom quenching process. These data establish the second ionization path as due to light absorption by the thermalized singlet state, *i.e.*

$$^1T^* \xrightarrow{h\nu} T^+ + e_s^-$$

In keeping with our previous conclusions,[4] these results rule out the simultaneous absorption of two photons as a route leading to ionization.

The biphotonic processes involving $^3T^*$ and $^1T^*$ imply considerable extinction coefficients for the corresponding species at 3371 Å. For $^3T^*$ the value ϵ(3371 Å) $\cong 4 \times 10^3$ has been reported.[7] The absorption spectrum of $^1T^*$ obtained by pulsed laser photolysis is shown in Figure 5. Unfortunately, due to the interference of fluorescence and of the absorption of ground state TMPD, the measurements could not be

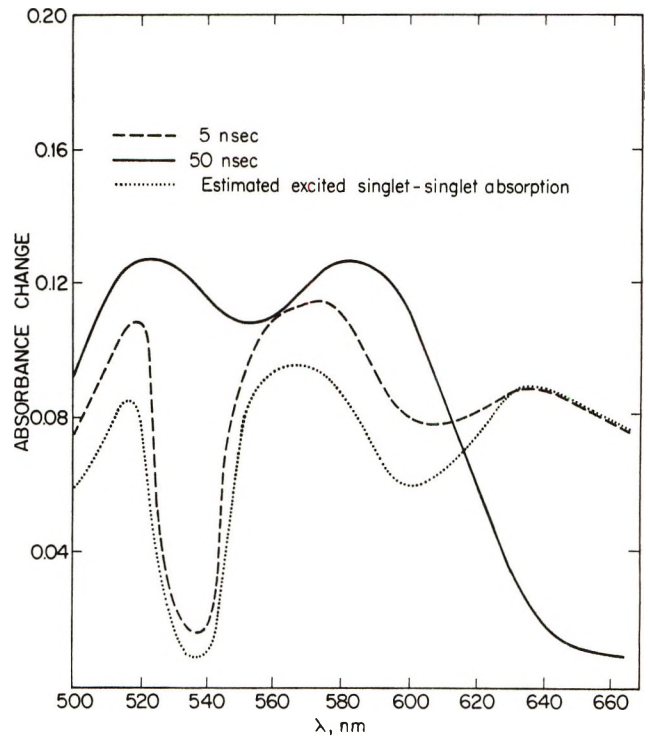

Figure 5. Absorbance changes in the laser photolysis of 10^{-3} M TMPD in deaerated isopentane. The spectrum recorded 50 nsec after pulsing is that of $^3T^*$. The spectrum after 5 nsec is the superposition of the absorptions due to $^1T^*$ and $^3T^*$. The spectrum of $^1T^*$ has been estimated by substracting the triplet contribution as described by D. S. Kliger and A. C. Albrecht, *J. Chem. Phys.*, **50**, 4109 (1969).

(7) K. D. Cadogan and A. C. Albrecht, *J. Phys. Chem.*, **73**, 1868 (1969).

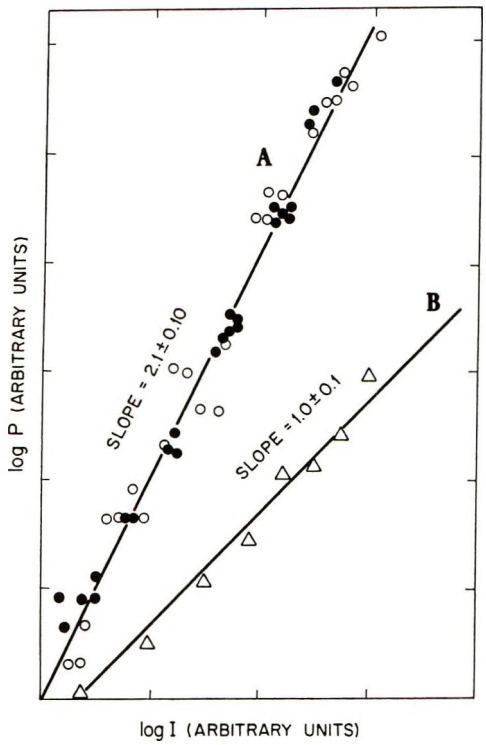

Figure 6. Dependence of peak photocurrent (P) on laser light intensity (I). A, ○, 2×10^{-3} M TMPD and 0.1 M naphthalene in isopentane; ●, 2×10^{-3} M TMPD and 0.1 M biphenyl in isopentane. B, △, 2×10^{-3} M pyrene and 0.1 M N,N-diethylaniline in acetonitrile.

extended below 500 nm, so that at present the relative absorbance of $^1T^*$ at 3371 Å cannot be estimated.

(2) *TMPD–Naphthalene and TMPD–Biphenyl in Nonpolar Solvents.* The fluorescence of TMPD in nonpolar solvents is quenched by aromatic electron acceptors such as naphthalene (N) and biphenyl (B), in a process leading to the formation of the corresponding charge-transfer fluorescent exciplexes.[8,9] With the purpose of establishing the role of the charge-transfer interaction in possible ionization processes we have submitted a 2×10^{-3} M TMPD–isopentane solution, in the presence of 0.1 M naphthalene or 0.1 M biphenyl, to pulsed laser experiments. The solutions were found to be photoconductive, the photocurrent exhibiting a second power dependence on the light intensity (Figure 6). Thus, biphotonic ionization is involved in process 2 as in the case of process 1. Figure 7 shows that the rise of photocurrent is faster than the ~15-nsec resolution of our apparatus. This is in keeping with the proposed biphotonic mechanism, yielding additional independent evidence in excluding spontaneous ionization of the thermalized fluorescent (~60 nsec) exciplex. It is interesting to note that the $P \sim I^2$ relation observed in the nonpolar TMPD exciplex systems is in contrast with the postulated monophotonic ionization following excited donor–acceptor interactions in polar solvents.[3] The latter behavior is in fact clearly demonstrated by the linear relation between photoconductivity and light intensity observed, for example, for the pyrene–diethylaniline pair in acetonitrile (Figure 6).

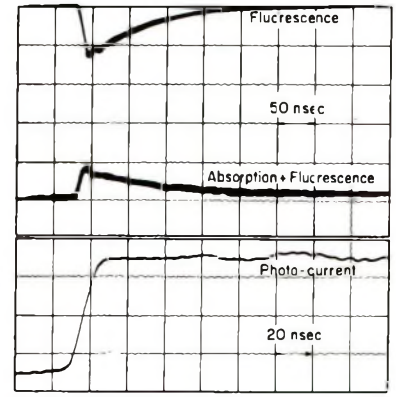

Figure 7. Oscillograms recorded in a 0.1 M biphenyl–2×10^{-3} M TMPD–methylcyclohexane solution showing: bottom, the rise of the photocurrent; top, the decay of the exciplex fluorescence at 610 nm recorded with no monitoring light (upper trace). The superposition of exciplex fluorescence and ababsorbance at 610 nm, recorded in the presence of the monitoring light beam (lower trace).

We have already pointed out that the photocurrents observed in TMPD–isopentane systems in the absence of electron acceptor quenchers cannot be accounted for by the simultaneous absorption of two photons. All ionization phenomena observed in TMPD systems in the presence of high biphenyl and naphthalene concentrations should thus be explained in terms of the absorbing species generated by the fast ($\tau \sim 5 \times 10^{-10}$ nsec) quenching process. We have accordingly carried out an absorption pulsed-laser photolysis study of both TMPD–naphthalene and TMPD–biphenyl systems. The transient absorbance changes upon pulsing are composed of a fast decay in the nanosecond region (see Figure 7), leaving (below 450 nm) a residual absorbance of microseconds lifetime. The fast decay matches the decay of the exciplex fluorescence ($\tau_{1/2} \cong 60$ nsec) and is therefore attributed to the exciplex absorption. The corresponding spectra are shown in Figure 8. The slowly decaying transients exhibit spectra identical with the known spectra of the triplets of naphthalene ($^3N^*$) and biphenyl ($^3B^*$).[10]

In previous studies[11] it has been shown that intersystem crossing following excited donor–acceptor interaction may be a fast process taking place in competition with the population of the thermalized (relaxed) fluorescent state of the exciplex, *i.e.*

(8) N. Yamamoto, Y. Nakato, and H. Tsubomura, *Bull. Chem. Soc. Jap.*, **40**, 451 (1967).

(9) H. Knibbe, Ph.D. Thesis, Free University of Amsterdam, 1969.

(10) Y. Novros, N. Orbach, and M. Ottolenghi, to be published.

(11) C. R. Goldschmidt, R. Potashnik, and M. Ottolenghi, *J. Phys. Chem.*, **75**, 1025 (1971); N. Orbach, R. Potashnik, and M. Ottolenghi, *ibid.*, **76**, 1133 (1972).

$$D^* + A \begin{cases} \nearrow {}^3D^* + A \text{ (or } D + {}^3A^*) \\ \searrow {}^1(D^+A^-)^* \end{cases}$$

It may thus be possible that $^3N^*$ and $^3B^*$ are already present during the laser pulse rather than being formed in the relatively slow processes

$$^1(T^+N^-)^* \longrightarrow {}^3N^* + T$$

and

$$^1(T^+B^-)^* \longrightarrow {}^3B^* + T$$

where $^1(T^+N^-)^*$ and $^1(T^+B^-)^*$ stand for the corresponding thermalized exciplexes. One should therefore consider the possibility that $^3N^*$ and (or) $^3B^*$ are involved in the biphotonic ionization similarly to $^3T^*$. The participation of $^3N^*$ can readily be ruled out since the naphthalene triplet state in solution does not absorb at 3371 Å.[12] The role of $^3B^*$ which exhibits a substantial absorption at the laser line ($\epsilon_{3371} \sim 10^4$ [13]) could be excluded by carrying out an analysis using piperylene as a selective triplet state quencher as it was previously done for the single TMPD molecule in the absence of electron acceptor quenchers. For the reaction between $^3B^*$ and piperylene we have established the value $k(^3B^* + \text{piperylene}) \cong 5 \times 10^9\ M^{-1}\ \text{sec}^{-1}$. Thus, piperylene concentrations of around $2 \times 10^{-2}\ M$ are needed to reduce the lifetime of $^3B^*$ so that $\tau_t \sim \tau_p$. Actually we have not observed any effect on the photoconductivity of the system as long as the concentration was above $\sim 2 \times 10^{-1}\ M$. Around 1 M piperylene we have measured a drop of ~35% in the photocurrent. However, a similar piperylene effect has been also observed in the TMPD–N system, where the role of $^3N^*$ has already been excluded. This makes the participation of $^3B^*$ in the photoionization quite unlikely, calling for a common explanation of the piperylene effect in both systems. We have observed that in the presence of ~1 M piperylene the initial fluorescence yield of both TMPD–B and TMPD–N exciplexes is lowered by ~25% (the emission lifetime is reduced from 60 to ~30 nsec). Excluding the corresponding triplets as possible photoactive intermediates and interpreting the biphotonic ionization in terms of the absorption of a second photon by the fluorescent exciplex, the effect of piperylene on the photocurrents can be at least partially accounted for by its effect in reducing the exciplex yield. It is possible that the rest of the effect may be attributed to specific solvent effects on the ionization cross section or on ionic mobilities.

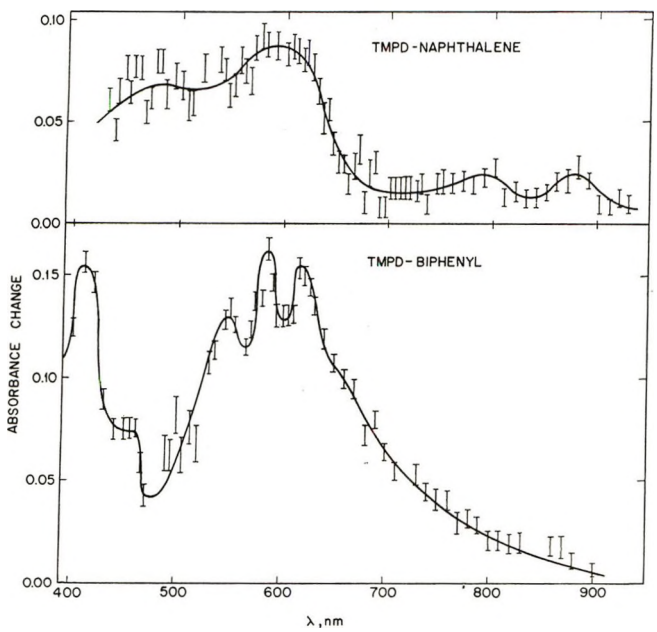

Figure 8. Exciplex absorption spectra recorded (20 nsec after triggering) in $2 \times 10^{-3}\ M$ TMPD–0.1 M biphenyl or naphthalene–methylcyclohexane solutions. The net absorbance change was obtained after substracting the contribution of fluorescence (see Figure 7).

(3) *Photoionization of the Exciplex.* (*a*) *The Exciplex Absorption Spectrum.* The previous analysis leads to the process

$$^1(D^+A^-)^* \xrightarrow{h\nu} D^+ + A^-$$

as the principal ionization path of donor–acceptor systems in nonpolar solvents. Further insight into the nature of the process in the system of the present work calls for an analysis of the exciplex spectra presented in Figure 8. It has been recently shown,[14] in the cases of various *N*,*N*-diethylaniline systems, that the corresponding exciplex absorption spectra should be interpreted in terms of four types of transitions

1. $^1(D^+A^-)^* \xrightarrow{h\nu} (D^{+*}A^-)$;
   localized excitation within the D^+ species
2. $^1(D^+A^-)^* \xrightarrow{h\nu} (D^+A^{-*})$;
   localized excitation within the A^- species
3. $^1(D^+A^-)^* \xrightarrow{h\nu} (^1D^*A)$; electron transfer to states in which the donor is locally excited
4. $^1(D^+A^-)^* \xrightarrow{h\nu} (D^1A^*)$; electron transfer to states in which the acceptor is locally excited

The various types of transitions can best be visualized by an approximate orbital diagram such as presented in Figure 9. Transitions belonging to types 1 and 2 lead to higher charge-transfer states of the exciplex, while

(12) G. Porter and M. W. Windsor, *Proc. Roy. Soc., Ser. A*, **245**, 238 (1958).

(13) W. Heizelmann and H. Labhart, *Chem. Phys. Lett.*, **4**, 20 (1969).

(14) R. Potashnik, C. R. Goldschmidt, M. Ottolenghi, and A. Weller, *J. Chem. Phys.*, **55**, 5344 (1971).

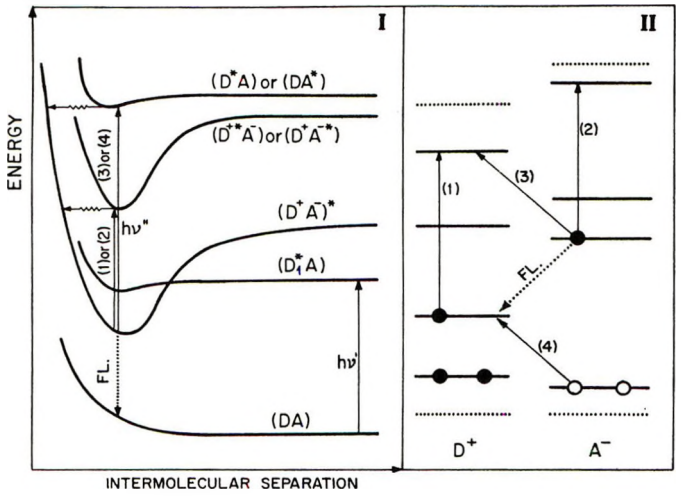

Figure 9. Schematic diagrams of potential energy curves (I) and molecular orbitals (II) of exciplexes in nonpolar solvents. The notations (1), (2), (3), and (4) refer to the exciplex absorption transitions described in the text. (Excited exciplex states such as $(D^{2+}\ A^{2-})^*$ and (D*A*) have been omitted since their contribution to the spectrum will be far out of our experimental observation range). $h\nu'$ denotes the absorption populating the lowest excited state of the TMPD donor (D_1^*). $h\nu''$ denotes the absorption of the second photon by the exciplex. Broken arrows denote radiationless transitions, dotted arrows the exciplex fluorescence.

types 3 and 4 are "reverse charge-transfer" transitions leading to locally excited states of low CT character. Accordingly, the exciplex absorption spectrum will exhibit a superposition of the spectra of the ground state D^+ and A^- radical ions. It will also include bands due to transition types 3 and 4, reflecting the energy gaps between the fluorescent state of the exciplex $(D^+A^-)^*$ and those corresponding approximately to higher excited (singlet) states of D and A.

In the case of TMPD–N, the contribution of the $TMPD^+$ transitions to the exciplex spectrum is evident in the form of the broad, nonresolved, 590-nm band which covers the range of the closely spaced maxima at 620, 580, and 540 nm, which characterize the $TMPD^+$ absorption.[15,16] The relatively weak absorption around 800 nm can be attributed to transitions to a ($TMPD^+$-N^{-*}) state. (The spectrum of the naphthalene negative ion is characterized by a band in the same region.[17]) The absorption in the 430–520-nm range cannot be accounted for by higher charge-transfer states and should thus be attributed to reverse charge-transfer transitions. The only possible contributor in this energy range is the locally excited state (TMPD·N*), due to the ~44.000 cm^{-1} $S_3(^1B_b)$ state of naphthalene, predicting an exciplex transition with 0–0 energy around 480 nm. The $S_2(^1L_a)$ naphthalene state is expected to yield an exciplex band at 850 nm, in fair agreement with the observed band around 880 nm.

The fit between expected and observed spectra is even more clear-cut in the case of the TMPD–biphenyl exciplex. Thus, all three bands (at 620, 580, and 540 nm) characterizing the $TMPD^+$ absorption are present, slightly shifted, in the exciplex spectrum. The shoulder around 650 nm and its tail in the red, as well as the intense 410-nm exciplex band, are correspondingly attributable to the relatively broad 630-nm band and to the more intense and sharper one at 400 nm, both characterizing the absorption of the biphenyl negative ion.[17] Among the upper locally excited states only one, involving the $S_3(^1B)$ biphenyl state, is predicted to yield an exciplex band in the 400–900-nm range, its 0–0 energy value being expected around 450 nm. This prediction fairly coincides with the 450-nm band in the exciplex spectrum.

(*b*) *The Photoionization Process.* A biphotonic ionization process involving the exciplex as the photoactive intermediate implies considerable exciplex absorbance around the 3371 Å laser line. Unfortunately, due to the interference of emissions and of the absorption of ground state TMPD, the exciplexes absorption spectra around 3371 Å could not be recorded. However, based on our previous analysis, we may predict a relatively strong contribution to the transition from the ($TMPD^+$*A^-) charge-transfer state for both exciplexes. This is due to the relatively high extinction ϵ $TMPD^+$ (3371 Å) $\cong 10^4$, which is comparable to that in the 530–620-nm region.[15] Transitions to anionic excited states ($TMPD^+A^{-*}$) are expected at 3371 Å for both biphenyl or naphthalene exciplexes. The contributions in the two cases are expected to be similar since for both N^- and B^- negative ions ϵ (3371 Å) $= 3 \times 10^3$.[17] It is difficult to predict to what extent transitions to locally excited states (types 3 and 4) will contribute to the exciplex absorption at 3371 Å. This is due to the fact that not all excited singlet energy levels of donor and acceptors are known with accuracy, as well as to the incapacity of predicting the intensities of types 3 and 4 bands in the exciplex spectrum.[14]

When considering the exciplex photoionization from a purely energetic aspect, we refer to the free energy gap between the fluorescent exciplex state $\Delta F(E)$ and the dissociated ion radical state $\Delta F(A^- + D^+)$ recently estimated by Taniguchi, Nishina, and Mataga,[18] for the pyrene–*N*,*N*-dimethylaniline exciplex in various solvents. In hydrocarbons with $\epsilon \cong 2$, $\Delta F(A^- + D^+) - \Delta F(E) \cong 1.6$ eV. A similar value is also ex-

(15) W. C. Meyer and A. C. Albrecht, *J. Phys. Chem.*, **66**, 1168 (1962).

(16) N. Yamamoto, Y. Nakato, and Y. Tsubomura, *Bull. Chem. Soc. Jap.*, **39**, 2603 (1966); R. Potashnik, M. Ottolenghi, and R. Bensasson, *J. Phys. Chem.*, **73**, 1912 (1969).

(17) J. Jagur-Grodzinski, M. Feld, S. L. Yang, and M. Szwarc, *ibid.*, **69**, 628 (1965); W. P. Weyland, Thesis, Free University of Amsterdam, 1958, p 82; J. Dieleman, Thesis, Free University of Amsterdam, 1962, p 11.

(18) Y. Taniguchi, Y. Nishina, and N. Mataga, *Bull. Chem. Soc. Jap.*, **45**, 3 (1972).

pected in our TMPD–acceptor systems. Since the energy of the 3371-Å laser quantum exceeds this value by more than a factor of 2, the basic requirement for a biphotonic ionization process involving the thermalized exciplex as the photoactive intermediate is satisfied.

Dealing with finer details of the exciplex photoionization process, one should consider two alternative mechanisms

$$(D^+A^-)^* \xrightarrow{h\nu} A + D^+ + e_s^- \longrightarrow A^- + D^+ \quad (I)$$

$$(D^+A^-)^* \xrightarrow{h\nu} A^- + D^+ \quad (II)$$

In the first case initial electron photoejection from the exciplex is followed by recapture by an acceptor molecule. In some respects this photoejection carries analogies to the formation of solvated electrons in the photolysis of radical anions in solution.[19] Mechanism II involves direct formation of the separated A^- and D^+ ions. This implies two assumptions. (a) In the internal conversion (wavy arrows in Figure 9) from higher exciplex states [$(D^{+*}A^-)$, (D^+A^{-*}), and possibly (D*A) or (DA*)], back to the fluorescent state $(D^+A^-)^*$, a considerable amount of electronic energy is transformed into relative kinetic energy of the solvated ions, D^+ and A^-, so that the system is above the ionization limit of the fluorescent state in the particular solvent involved. (b) This excess in kinetic energy is lost after a few diffusive displacements, so that if thermalization is complete only after an interionic separation of at least 20 Å is achieved, then pairing due to electrostatic attraction will be small and photocurrent will be observed. With respect to point b, mechanism I, with a solvated electron replacing A^-, appears more plausible. This is in view of the very high mobility of solvated electrons in hydrocarbon solvents[20] which may help obtaining large separations between D^+ and e_s^- before thermalization. In other words, a nonthermalized e_s^- is more likely to escape the field of D^+ than a nonthermalized A^-. However, a discrimination between mechanisms I and II is, at present, impossible.

We finally refer to the recent work by Taniguchi, *et al.*,[18] who observed monophotonic photoconductivity phenomena in relatively polar solutions of pyrene quenched by *N*,*N*-dimethylaniline, but did not record either mono- or biphotonic photocurrents in a low polarity hydrocarbon solvent such as *n*-hexene. Their failure to observe biphotonic ionization may be due to relatively weaker light intensities or, alternatively, to a low absorbance of the particular exciplex involved. This calls for a more detailed and comprehensive study of photoionization phenomena in intermolecular charge-transfer systems.

Acknowledgment. This work has been carried out under the sponsorship of the U. S. National Bureau of Standards. The authors are indebted to a referee for suggesting the process of electron photoejection from the exciplex.

(19) J. Eloranta and H. Linschitz, *J. Chem. Phys.*, **38**, 2214 (1963); L. J. Giling, J. G. Kloosterboer, R. P. H. Rettschnick, and J. D. W. Van Voorst, *Chem. Phys. Lett.*, **8**, 457 (1971); M. Fisher, G. Rämme, S. Claesson, and M. Szwarc, *ibid.*, **9**, 306 (1971).

(20) J. T. Richards and J. K. Thomas, *ibid.*, **10**, 317 (1971).

On the Photoionization of Aromatics in Solid Solutions: Ionization Potential Determinations

by A. Bernas,* M. Gauthier, and D. Grand

Equipe de recherches CNRS n° 98, Laboratoire de Chimie Physique de l'Université Paris VI, Centre d'Orsay, 91-Orsay, France *(Received December 28, 1971)*

Publication costs assisted by CNRS

The present study, based on photoionization experiments and neutralization luminescence recordings, reports some determinations of solid state ionization potentials I_{sol} for various aromatic solutes in the same rigid transparent solvent and for a definite solute in various solvents. When compared to the corresponding gaseous phase ionization potential I_g, I_{sol} is found to be reduced by an amount $\Delta I = I_g - I_{sol}$ which appears independent of the solute molecule but characteristic of the matrix. For the nonpolar or low polarity solvents used, ΔI is very close to hc/λ_{max}, λ_{max} being the wavelength at the absorption band maximum of the matrix trapped electron.

Introduction

It has long been stressed[1] that the ionization potential of a given molecule in a condensed phase, I_{sol}, is lowered by an amount ΔI with respect to the corresponding value I_g for the isolated molecule. Such a decrease has been considered as due to a polarization of the surrounding solvent molecules with a permanent or induced dipole moment. However, for most systems, the magnitude of ΔI is unknown.

The purpose of this work was to obtain systematic experimental determinations of ΔI for various aromatic solutes in the same rigid, transparent solvent and for a specific solute in various solvents.

As already observed by several authors,[2,3] near-ultraviolet irradiations of solid solutions may lead to solute photoionization, the mechanism being, in general, monomolecular and biphotonic: by intersystem crossing, the first photon $h\nu_1$ excites the solute molecule to its long-lived T_1 state which may then reabsorb a second photon $h\nu_2$. Provided the energy $h\nu_2$ is high enough, the ionization continuum is attained. By varying the second beam frequency, we have looked for the photoionization threshold; the ionization potential value is then given by the sum of the lowest triplet energy E_{T_1} and $(h\nu_2)_{thres}$. The ions were detected not at the stage of their formation but at the stage of their destruction; their neutralization is optically stimulated and the associated luminescence recorded as a function of ν_2.

We have paid particular attention to the two following points: (1) is ΔI characteristic of the matrix? and (2) how does it vary with the solvent polarity?

Experimental Section

Products. 3-Methylpentane (3-MP) and methylcyclohexane (MCH) were purified by passing through a column of activated silica gel and alumina. Methyltetrahydrofuran (MTHF) was purified according to Dainton and Salmon's method.[4] *tert*-Butyl alcohol was crystallized from the melt at room temperature.

Purity of solvents was tested by absorption and emission spectroscopy; their optically excited luminescence was found to be quite negligible.

N,N,N',N'-Tetramethyl-*p*-phenylenediamine (TMPD) was liberated from the hydrochloride salt with NaOH and purified by several sublimations. Aniline was distilled on zinc powder. Diphenylamine was recrystallized from methanol solutions, and triphenylamine was zone-refined.

Experimental Procedure. The liquid solutions (0.4 ml, 10^{-3} or 2×10^{-3} M) were degassed on a vacuum line, and the copper cell was opened under liquid nitrogen. A schematic diagram of the apparatus is presented in Figure 1. The sample S is simultaneously irradiated by two beams. The first beam—the frequency of which is set at a fixed value—gives a stationary concentration of solute triplet; the second, which leads to the ionization continuum, is produced by a xenon lamp through a grating monochromator. The bandwidth is of the order of 600 cm^{-1}.

After 1 or 2 min irradiation and a dark period of 90 sec, which allows the decrease of the phosphorescence and of the isothermal recombination luminescence, the xenon lamp is used to excite and release the matrix trapped photoelectrons. The stimulation frequency lies in the near-infrared region where the physically trapped electrons strongly absorb. The stimu-

(1) L. E. Lyons, *J. Chem. Soc.*, 5001 (1957).

(2) J. Joussot Dubien and R. Lesclaux, *C. R. Acad. Sci., Paris*, **248**, 4260 (1964).

(3) K. D. Cadogan and A. C. Albrecht, *J. Chem. Phys.*, **43**, 2550 (1965); *J. Phys. Chem.*, **72**, 929 (1968).

(4) F. S. Dainton and G. A. Salmon, *Proc. Roy. Soc., Ser. A*, **285**, 319 (1965).

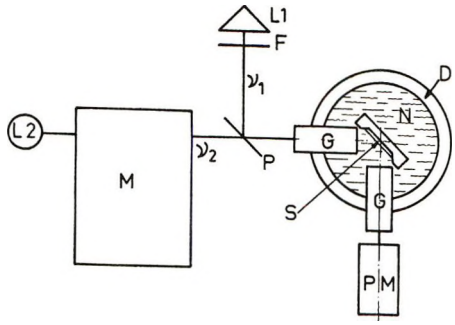

Figure 1. Experimental device: L1, low pressure Hg lamp; F, Corning filter no. 7.54 ($\rightarrow\lambda_1$ mainly 254 nm); L2, 450-W Xe lamp; M, grating monochromator Huet M25 operating with appropriate filters; P, semitransparent plate; D, styrofoam container; S, sample in copper container; N, liquid nitrogen; G, quartz light guides; PM, photomultiplier (radiotechnique 56 UVP).

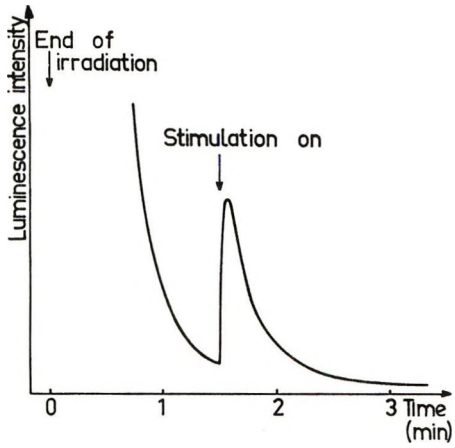

Figure 2. Neutralization luminescence signal.

lated luminescence is collected on a photomultiplier and recorded. As shown in Figure 2, the signal appears superimposed on the decaying spontaneous neutralization luminescence. The integrated intensity is proportional to the number of ions produced.

After 10–20 min bleaching, the sample is ready for another uv excitation. It has been checked that in such a sequence of experiments, no significant decrease of ion yield occurred for standard irradiation conditions. The absence of thermoluminescence, upon heating after about 15 irradiation–bleaching cycles, is also proof that all ionic species have been neutralized upon bleaching.

Results

(*a*) *TMPD in MCH.* Figure 3 displays typical ionization efficiency curves; the luminescence intensity is plotted *vs.* the second beam frequency ν_2 for a constant flux φ_2. Curve c corresponds to tetramethyl-*p*-phenylenediamine (TMPD) in methylcyclohexane (MCH).

In the two successive steps of the biphotonic ab-

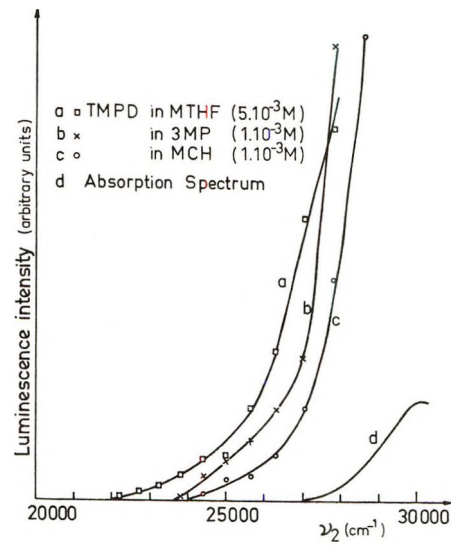

Figure 3. Ionization efficiency curves.

sorption, the first photon $h\nu_1$ is supposed to induce only the transition $S_1 \leftarrow S_0$ and the second photon $h\nu_2$, the transition from the lowest triplet state to the ionization continuum. However, because of the frequent spectral overlapping of the $S_1 \leftarrow S_0$ and $T_n \leftarrow T_1$ absorptions, the first light beam may also promote the second transition and the second beam, the first as well as the second transition. We have thus to correct the recorded signal for the contribution of the first beam acting alone, as well as for the second beam acting alone. The first correction has been made. The latter, however, has proved unnecessary in the ionization threshold region, where the second photon is not directly absorbed by the solute (curve d, Figure 3). The second correction does become important at frequencies greater than about 27,000 cm^{-1}.

It has been checked further that the intensity of the corrected luminescence is proportional to the intensity I_2 of the second beam and that luminescence curves corresponding to different I_2/I_1 ratios extrapolate to the same frequency value, which thus appears to be characteristic of a particular solute–solvent system.

The frequency threshold, taken as that corresponding to the onset of the neutralization luminescence, that is, the onset of the second beam ionizing efficiency, is found to be about 24,000 cm^{-1} (3 eV). Since E_T = 2.8 eV, the ionization potential of TMPD in a MCH matrix turns out to be 5.75–5.8 eV. From the value I_g = 6.6–6.7 eV,[5,6] ΔI would thus be about 0.9 eV.

(*b*) *Aniline and Diphenyl- and Triphenylamine in MCH.* To examine the variation of ΔI with the solute molecule for a given solvent, the various solutes have been chosen according to the following criteria: (1) they should be easily ionized; and (2) the expected

(5) G. Briegleb and J. Czekalla, *Z. Elektrochem.*, **63**, 6 (1956).
(6) R. Foster, *Nature*, **183**, 1253 (1959).

Table I: Ionization Potential I_{sol} and Corresponding ΔI Values for Various Solutes in a MCH Glass

Solute	E_T, eV	E_{thres}, eV	I_{sol}, eV	I_g, eV	ΔI, eV
TMPD	2.8[a]	2.95 ± 0.03	5.75 ± 0.03	6.6[b]–6.7[c,l]	0.85–0.95 (±0.03)
Aniline	3.32[d-f]	3.42 ± 0.03	6.74 ± 0.03	7.70[g,i]–7.69[h]	0.96 ± 0.03
Diphenylamine	3.12[e,f]	3.31 ± 0.03	6.43 ± 0.03	7.25[h]	0.82 ± 0.03
Triphenylamine	3.04[e,j,k]	3.0 ± 0.10	6.04 ± 0.10	6.86[h]	0.82 ± 0.10

[a] A. Kalantar and A. C. Albrecht, *Ber. Bunsenges. Phys. Chem.*, **68**, 361 (1964). [b] G. Briegleb and J. Czekalla, *Z. Elektrochem.*, **63**, 6 (1959). [c] R. Foster, *Nature (London)*, **183**, 1253 (1959). [d] D. S. McClure, *J. Chem. Phys.*, **19**, 670 (1951). [e] G. N. Lewis and M. Kasha, *J. Amer. Chem. Soc.*, **66**, 2100 (1944). [f] V. L. Ermolaev, *Opt. Spektrosk.*, **11**, 266 (1961). [g] K. Watanabe, J. Nakayama, and J. Mottl, *J. Quant. Spectrosc. Radiat. Transfer*, **2**, 369 (1962). [h] A. Terenin and F. Vilessov, *Advan. Photochem.*, **2**, 385 (1964). [i] R. Bralsford, P. V. Harris, and W. C. Price, *Proc. Roy. Soc., Ser. A*, **258**, 459 (1960). [j] W. G. Herkstroeter, A. A. Lamola, and G. S. Hammond, *J. Amer. Chem. Soc.*, **86**, 4537 (1964). [k] V. L. Ermolaev, *Sov. Phys. Usp.*, **80**, 333 (1963). [l] However, recent determinations give a somewhat lower value: 6.20 eV (Y. Nakato, *et al.*, *Chem. Phys. Lett.*, **6**, 615 (1971)).

$T_n \leftarrow T_1$ transition leading to ionization must not overlap the $S_1 \leftarrow S_0$ absorption of the ground state molecule. Considering the relative S_1, T_1, and ionization energies, only aromatic amines fulfill these conditions. Hence besides TMPD, aniline and diphenyl- and triphenylamine have been used.

The results for the luminescence threshold energies and the corresponding solid state ionization potentials are given in Table I together with some published values for gaseous ionization potentials I_g. To our knowledge, only semiempirical I_g values resulting from liquid phase charge-transfer experiments are available for gaseous TMPD. For the three other solutes both indirect charge-transfer determinations and direct gaseous photoionization measurements are available. In the latter case, only the direct determinations have been retained. The uncertainty on ΔI is then due mostly to a lack of accuracy of our own experimental determinations whereas for TMPD it is due mostly to the discrepancy in the I_g published values. Within these limits, the ΔI obtained for the four solutes are not significantly different and ΔI turns out to be approximately 0.9 eV in a MCH glass.

The fact that ΔI does not depend on the solute has also been found for a few polyaromatics dispersed in a boric acid matrix.[7a] In such a case however, the matrix has been reported as unhomogeneous and the electron traps consist mostly, if not entirely, of acid matrix protons.[7b-9]

(c) *TMPD in 3MP, MCH, MTHF.* The effect of polarity has been examined with TMPD as a solute for the pure solvents 3-methylpentane (3MP), methylcyclohexane, and methyltetrahydrofuran (MTHF) (Figure 3). The recourse to more polar solvents presents some difficulties. Besides the necessity for forming optically good glasses, the method described is obviously limited by two imperative conditions: (1) that upon detrapping, the electron does not become attached to the cage wall molecules and (2) that the neutralization act is luminescent.

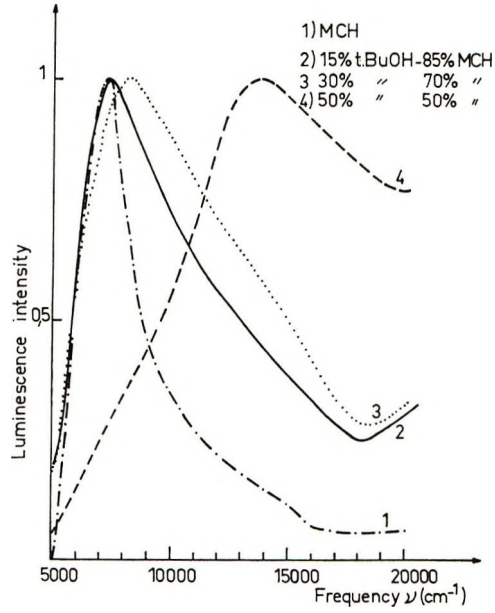

Figure 4. Stimulation spectra of electrons trapped in MCH–*tert*-BuOH mixtures (77 K).

Alcohols (except *tert*-butyl alcohol[10]), alkyl halides, nitriles, and amides are thus precluded.

tert-Butyl alcohol would fulfill the above conditions but it crystallizes upon cooling. We have thus tentatively used mixtures of *tert*-butyl alcohol (from 5 to 50%) with MCH.

The stimulation spectra given in Figure 4 show only one band for each particular mixture. From observations and considerations developed by Willard, *et al.*,[11]

(7) (a) R. Lesclaux and J. Joussot Dubien, *C. R. Acad. Sci., Paris*, 263, 1177 (1966); (b) R. Lesclaux, Thèse de Doctorat, Bordeaux, 1968.

(8) A. Bernas, D. Léonardi, and J. Roncin, *J. Chim. Phys.*, **66**, 249 (1969).

(9) R. Santus, *et al.*, *C. R. Acad. Sci., Paris*, 261, 117 (1965).

(10) R. G. Bennett, *et al.*, *J. Chem. Soc. A*, 1393 (1967).

(11) A. Eckstrom and J. E. Willard, *J. Phys. Chem.*, **72**, 4599 (1968).

it appears that these mixed systems can be considered as homogeneous. If the dielectric constant of the mixtures is assumed to be proportional to the *tert*-butyl alcohol concentration, the systems used cover a 2.0 to 6.4 (at 300°K) dielectric constant range.

The I_{sol} measured for TMPD in the pure or mixed solvents, as well as the corresponding ΔI values, are given in Table II.

Table II: Ionization Potential I_{sol} and Corresponding ΔI Values for TMPD in Various Rigid Matrices

Matrix	I_{sol}, eV (±0.03)	ΔI, eV[a] (±0.03)
MCH	5.75	0.85–0.95
3MP	5.75	0.85–0.95
MTHF	5.52	1.08–1.18
MCH + *tert*-BuOH 5%	5.67	0.93–1.03
MCH + *tert*-BuOH 15%	5.71	0.89–0.99
MCH + *tert*-BuOH 30%	5.55	1.05–1.15
MCH + *tert*-BuOH 50%	5.52	1.08–1.18

[a] The two values correspond, respectively, to $I_g = 6.6$ eV and $I_g = 6.7$ eV.

The ionization threshold determined for TMPD in 3MP (5.75 eV) appears to agree satisfactorily well with previous determinations by Cadogan and Albrecht[3] (5.9 eV) and Ewald[12] (5.6 eV).

The ΔI value is significantly larger for polar MTHF compared to the nonpolar 3MP and MCH; similarly, it increases slightly with increasing concentration of the polar alcohol in the *tert*-BuOH–MCH mixtures.

Discussion

The question arises as to a possible contribution of the triplet–triplet transition extinction coefficient ϵ_{TT} to the neutralization luminescence *vs.* frequency ν_2 curves. In other words, could the luminescence curves reflect the ϵ_{TT} *vs.* ν_2 variations rather than a photoionization cross section?

Two facts argue against such an interpretation. (1) The ϵ_{TT} *vs.* ν_2 curve obtained for TMPD in solid 3MP[13] is quite flat in the frequency region where the ionization threshold is located. (2) The neutralization luminescence curves for the various solutes in the same solvent lead to the same ΔI value; this would not be expected if the curves were reproducing an ϵ_{TT} *vs.* ν_2 variation.

Obviously, in the solid solutions where the photoelectron is not emitted out of the solid system, it is not rejected to infinity but, after thermalization, becomes localized in a matrix trap. Hence, the ionization energy we have experimentally determined does not represent the energy gap between a valence state and a zero energy free electron state. Besides its stabilization through polarization forces, the trapped electron may remain in the coulomb field of its paired cation. The cation–electron distances are distributed around average value d which has been estimated semiempirically, from luminescence kinetics data, as about 30 Å for TMPD in 3MP.[14,15] On the other hand, scavenging experiments in MCH, 3MP or MCH–isopentane mixtures have concluded that 50% of the photoelectrons travel 60–75 Å.[16–18] In such matrices the coulomb term is thus expected to be of the order of 0.25–0.1 eV. At any rate, whatever its exact value, the coulomb term E_{coul} cannot entirely account for 1-eV ΔI values.

Nor can the measured ΔI be attributed to differences between vertical and adiabatic ionization potentials. In the particular case of TMPD, for example, the values quoted in Table I are semiempirical. They combine liquid phase charge-transfer experiments and a calibration based on gaseous phase adiabatic ionization potentials. For the other solutes, the gaseous photoionization direct results reported in Table I also correspond to adiabatic ionization transitions.

Neglecting Pauli repulsion forces, the photoelectron is essentially subjected to two forces: the cation coulombic attraction and long-range electronic polarization interactions. Hence, the excess of ΔI over the residual coulomb term E_c should correspond to a polarization energy term which is found to increase with the solvent polarity, as expected, even though two opposite effects combine. The increase in dielectric constant is accompanied by a decrease in the cation-trapped electron mean separation.[16]

From our results on the pure solvents, for which the trapped electron (e_t^-) optical absorption band is well known, it appears that

$$\Delta I - E_{coul} \simeq hc/\lambda_{max} \qquad (1)$$

λ_{max} being the wavelength at the maximum of the e_t^- absorption band. If such an empirical relationship is confirmed for a wider range of solvents, the knowledge of the e_t^- absorption band would permit an estimate of ΔI.

It may be remarked that the trapped electron absorption band either coincides, more[19] or less[20] exactly, with the photobleaching and photoconductivity efficiency curves, or is energetically very close to the

(12) M. Ewald and B. Muel, *C. R. Acad. Sci., Paris*, **268**, 973 (1969).

(13) K. D. Cadogan and A. C. Albrecht, *J. Phys. Chem.*, **73**, 1868 (1969).

(14) A. C. Albrecht, 3ème Conférence Internationale de Photosensibilisation dans les Solides, Sarlat, 1971.

(15) D. Ceccaldi and J. Bullot, *Chem. Phys. Lett.*, **9**, 551 (1971).

(16) N. Yamamoto, Y. Nakato, and H. Tsubomura, *Bull. Chem. Soc. Jap.*, **40**, 451 (1967).

(17) M. Gauthier-Bodard and J. Bullot, *J. Chim. Phys.*, **65**, 1226 (1968).

(18) A. Bernas, M. C. Peraudeau, and J. Roncin, unpublished results; M. C. Peraudeau, Thèse de 3ème cycle, Paris, 1970.

(19) I. Eisele and L. Kevan, *J. Chem. Phys.*, **53**, 1867 (1970).

(20) A. Bernas, D. Grand, and T. B. Truong, *Chem. Commun.*, to be published.

photodetrapping threshold.[21-23] In either case, hc/λ_{max} would be close to the electron-binding energy. The latter should in turn involve two polarization energy terms—one corresponding to the instantaneous electronic polarization induced by the traveling photoelectron, the other to a slower structural relaxation of the trapping cavities.

Such a progressive deepening of the electron trap, as revealed by a blue shift of the e_t^- absorption with time,[24,25] would be of the order of 0.15 eV for a nonpolar 3-methylhexane matrix in the time range to 10^{-9} to 10^{-6} sec.[25] Obviously, this does not allow an extrapolation back to the 10^{-9} to 10^{-16} sec range.

On the other hand, the left-hand side term in relation 1, $\Delta I - E_{coul}$, is expected to contain two presumably equivalent electronic polarization terms[1] deriving from the simultaneous production of the positive and negative charges.

At this point, it seems premature to speculate further about the validity and physical significance of relation 1.

(21) A. Habersbergerova, L. Josimovic, and J. Teply, *Trans. Faraday Soc.*, **66**, 656 (1970).

(22) A. Bernas and D. Grand, *Chem. Commun.*, 1667 (1970).

(23) K. F. Baverstock and P. J. Dyne, *Can. J. Chem.*, **48**, 2182 (1970).

(24) J. T. Richards and J. K. Thomas, *Chem. Phys. Lett.*, **8**, 13 (1971).

(25) N. V. Klassen, H. A. Gillis, and D. C. Walker, *J. Chem. Phys.*, **55**, 1979 (1971).

Electronic Structure of Furanquinones. II. The Emission Spectra of Dinaphtho[2,1:2′,3′]furan-8,13-dione and Dinaphtho[1,2:2′,3′]furan-7,12-dione

by M. S. Walker,* R. L. Miller, and J. E. Kuder

Research Laboratory, Xerox Corporation, Rochester, New York 14603 *(Received October 29, 1971)*

Publication costs assisted by the Xerox Corporation

The relative position and nature of the low-lying molecular electronic states of the furanquinones dinaphtho[2,1:2′,3′]furan-8,13-dione (I) and dinaphtho[1,2:2′,3′]furan-7,12-dione (II) have been determined from their ultraviolet and visible absorption and emission spectra. The arrangement of states for these quinones is S_0, $T_1^{\pi-\pi^*}$, $T_2^{n-\pi^*}$, $S_1^{\pi-\pi^*}$, $S_2^{n-\pi^*}$. However, it is inferred that in polar media the $T_2^{\pi-\pi^*}$ and $S_1^{n-\pi^*}$ states invert. The $S_0 \rightarrow S_1^{\pi-\pi^*}$ transition in both molecules involves significant electron density rearrangement, as reflected by the solvent-induced frequency shifts of the transition observed in emission. The S_1 state dipole moments calculated for I and II, using the orientation polarization formula derived by Kawski, are in good agreement with values calculated by Hückel molecular orbital theory. Fluorescence quantum yields are dependent on both solvent and temperature, and phosphorescence yields in rigid media are of the order of 10^{-2} to 10^{-3}.

Introduction

The photophysical and photochemical behavior of polycyclic quinones has been related in general to the relative position and nature of their low-lying electronic states.[1] No fluorescence emission is observed from those quinones with a low-lying $n-\pi^*$ singlet state where intersystem crossing to the triplet manifold competes efficiently with this local symmetry-forbidden process.[2] The observation of a short-duration structured phosphorescence emission has led to an assignment of $n-\pi^*$ to the lowest triplet state of several quinones.[3]

Substitution in the quinone with electron-donor groups leads to participation of the substituent $2p_z$ electrons in conjugation (charge transfer) with the π-electronic system of the quinone. This gives rise to a new long-wavelength absorption band in the spectrum of the substituted quinone, designated $p_z-\pi^*$ or CT (charge transfer), and bathochromic and hypsochromic shifts in the $\pi-\pi^*$ and $n-\pi^*$ bands, respectively.[4] Fluorescence emission has been observed from such substituted quinones. Extensive π conjugation in the quinone also leads to low-lying $\pi-\pi^*$ states.[5]

(1) J. M. Bruce, *Quart. Rev., Chem. Soc.*, **21**, 405 (1967).

(2) G. Briegleb, W. Herre, and D. Wolf, *Spectrochim. Acta, Part A*, **25**, 39 (1969).

(3) A. Kuboyama and S. Yabe, *Bull. Chem. Soc. Jap.*, **40**, 2475 (1967).

(4) N. A. Shcheglova, D. N. Shigorin, and N. S. Dokunikhim, *Russ. J. Phys. Chem.*, **42**, 1449 (1968).

(5) M. Zander, *Naturwissenschaften*, **16**, 404 (1966).

Further, those molecules with low-lying n–π^* rather than π–π^* or CT states are the most photoactive of the quinones.[6]

Reported here are the emission characteristics of the furanquinones dinaphtho[2,1:2′,3′]furan-8,13-dione (I) and dinaphtho[1,2:2′,3′]furan-7,12-dione (II) (Figure 1), from which the low-lying electronic states of the molecules have been assigned. The electronic absorption spectra of these molecules were reported earlier.[7]

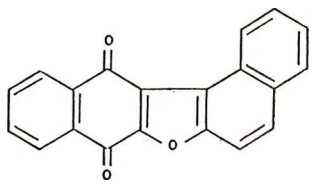

I

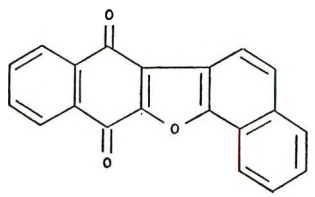

II

Figure 1. The molecular structure of dinaphtho[2,1:2′,3′]furan-8,13-dione (I) and dinaphtho[1,2:2′,3′]furan-7,12-dione (II).

Experimental Section

The synthesis and purification of dinaphtho[2,1:2′,3′]furan-8,13-dione (I) and dinaphtho[1,2:2′,3′]furan-7,12-dione (II) were described previously.[7]

Emission spectra were recorded on an Aminco-Kiers spectrophosphorimeter using either the ambient- or low-temperature attachment for this instrument. Spectra were corrected for the variation in sensitivity with wavelength of the detector assembly. Excitation wavelengths were 400 or 430 nm and excitation and emission band widths were 5 and 2 nm, respectively. Polarization spectra were measured as described earlier.[7] Fluorescence quantum yields were measured using the method due to Parker and Rees[8] and using fluorescein in 0.1 N NaOH, quantum yield 0.87,[9] as the standard. Solute concentrations were of the order of 10^{-5} M and solvents were Matheson Coleman and Bell Spectroquality reagent. Cells were 1 × 1 cm quartz and 1-mm diameter quartz tubes for ambient- and low-temperature studies, respectively. Solutions were deoxygenated by continuously bubbling dry nitrogen gas through the solvent. Ambient temperatures were 22 ± 1°.

Results

Fluorescence Spectra. The wavelength and quantum yield of fluorescence of furanquinones I and II are sensitive to both solvent polarity and temperature. Therefore, fluorescence spectra were recorded in ten aliphatic nonpolar and polar solvents at ambient temperature; aromatic solvents were excluded owing to the possibility of solute–solvent charge-transfer interactions in these solvents. Fuorescence quantum yields were also measured in several cases.

In nonpolar solvents a weak structured emission is observed with maxima at 475 nm and 453 nm for I and II, respectively (Figure 2). The vibrational spacing in the spectra is approximately 1000 cm^{-1}. The low intensity of the emission, and consequent poor resolution of the spectrum, prevented the determination of a more accurate value. The emission spectra also show a poor mirror-image symmetry with the corresponding absorption band (Figure 2). No change in the emission was noted on drying the solvents over sodium (*vide infra*).

In polar solvents a strong structureless emission is observed from both I and II. This emission shifts significantly to lower energies with increasing solvent polarity with no corresponding shift in the absorption edge. The fluorescence spectrum of I in dioxane is shown, for example, in Figure 2. The solvent-induced shifts were analyzed according to the formulas derived by Kawski[10] and rearranged by Chamma and Viallet,[11] *i.e.*

$$\nu_A - \nu_F = \frac{2}{hca^3}(\vec{\mu}_e - \vec{\mu}_g)^2 f(D, n) + \text{constant} \quad (1)$$

and

$$\frac{\nu_A + \nu_F}{2} = -\frac{2}{hca^3}(\mu_e^2 - \mu_g^2) \times \left[\frac{f(D, n)}{2} + f(n)\right] + \text{constant}' \quad (2)$$

where

$$f(D, n) = \left[\frac{2n^2 + 1}{n^2 + 2}\right]\left[\frac{D - 1}{D + 2} - \frac{n^2 - 1}{n^2 + 2}\right] \quad (3)$$

and

$$f(n) = \frac{3}{2}\frac{(n^4 - 1)}{(n^2 + 2)^2} \quad (4)$$

(6) H. H. Dearman and A. Chan, *J. Chem. Phys.*, **44**, 416 (1966).

(7) M. S. Walker, J. E. Kuder, and R. L. Miller, *J. Phys. Chem.*, **75**, 3257 (1971).

(8) C. A. Parker and W. J. Rees, *Analyst (London)*, **85**, 587 (1960).

(9) W. R. Dawson and M. W. Windsor, *J. Phys. Chem.*, **72**, 3251 (1968).

(10) A. Kawski, *Acta Phys. Pol.*, **29**, 507 (1966).

(11) A. Chamma and P. Viallet, *C. R. Acad. Sci., Ser. C*, **270**, 1901 (1970).

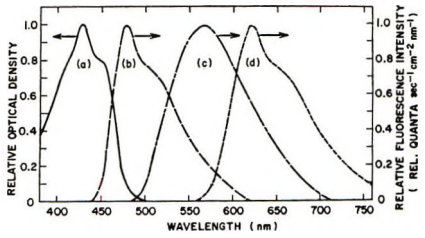

Figure 2. Emission spectra of dinaphtho[2,1:2′,3′]furan-8,13-dione (I): (a) absorption spectrum in pentane, (b) fluorescence spectrum in pentane, (c) fluorescence spectrum in dioxane, (d) phosphorescence spectrum in EPA glass (−196°).

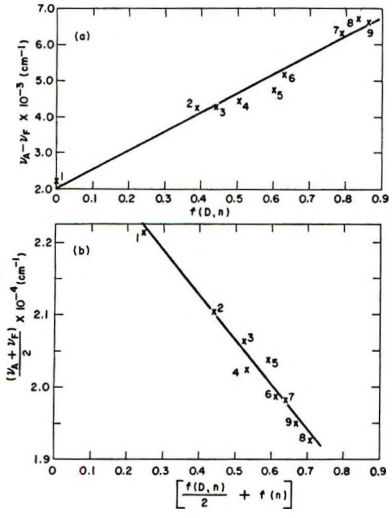

Figure 3. Solvent-induced fluorescence shifts plotted according to (a) eq 1 and (b) eq 2 for dinaphtho[2,1:2′,3′]furan-8,13-dione (I). Solvents: (1) hexane, (2) diethyl ether, (3) 1-bromohexane, (4) ethyl iodide, (5) ethyl bromide, (6) 1,2-dichloroethane, (7) acteone, (8) dimethylformamide, (9) acetonitrile.

ν_A and ν_F refer to absorption and emission frequencies, respectively, D and n are solvent dielectric constant and refractive index, and μ_g and μ_e are the solute ground- and excited-state dipole moments, respectively.

The fluorescence shift data for furanquinones I and II plotted according to eq 1 and 2 are shown in Figures 3 and 4, respectively. The lines drawn through the data are least-squares fits, and correlation coefficients are 0.985 or better in all cases.[12] With the assumption that the ground and excited dipole moments are parallel, the term $(\vec{\mu}_a - \vec{\mu}_g)^2$ in eq 1 reduces to $(\mu_e^2 + \mu_g^2)$. The ratio of the slopes from (1) and (2) is then a number expressed only in terms of μ_e and μ_g, whence for I and II values of μ_e equal to 12.2 μ_g and 14.6 μ_g, respectively, are obtained. By this method the need to estimate the solvent cavity radius, a, is circumvented. The values obtained above from the fluorescence data are compared with the dipole moments calculated by Hückel MO theory[7] in Table I.[13]

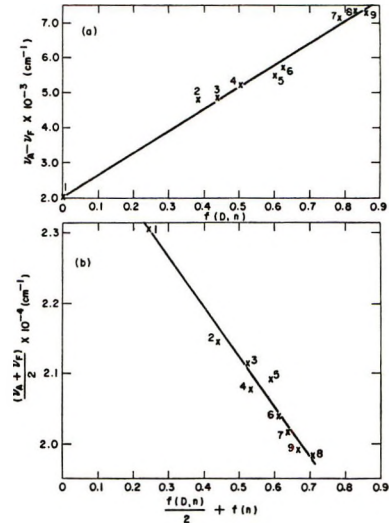

Figure 4. Solvent-induced fluorescence shifts plotted according to (a) eq 1 and (b) eq 2 for dinaphtho[1,2:2′,3′]furan-7,12-dione (II). Solvents as for Figure 3.

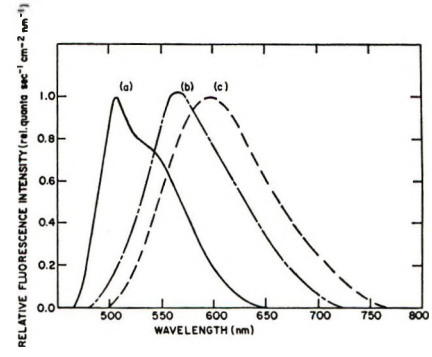

Figure 5. Fluorescence spectra of dinaphtho[2,1:2′,3′]furan-8,13-dione (I) in 2-methyltetrahydrofuran as a function of temperature: (a) −196°, (b) +45°, (c) −60°.

The fluorescence of both I and II in EPA and 2-methyltetrahydrofuran (2-MeTHF) glasses (−196°) is structured (frequency ~1000 cm^{-1}) and shifted to higher energies with respect to that measured in the same solvent at ambient temperatures and above (Figure 5). However, the emission is at lower energy than that recorded in a nonpolar solvent at ambient temperatures (*cf.* Figure 2). On lowering the tem-

(12) One of the referees has commented on the abrupt change in solvent properties between solvents 1 and 2 in Figures 3 and 4, suggesting that "filling in the gap" would be helpful in showing whether the fluorescent state is the same in all solvents. In fact, the plots of $(\nu_A - \nu_F)$ *vs.* $f(D, n)$ and of $^1/_2(\nu_A + \nu_F)$ *vs.* $[^1/_2 f(D, n) + f(n)]$ show abrupt changes between solvents 1 and 2 because $f(D, n)$ changes very rapidly when D and n are small. Furthermore, the observation that the point for emission in cyclohexane lies on the least-squares line is a necessary but not sufficient condition for the fluorescent state to be the same in this as in the other solvents, in view of the possibility of close-lying π–π^* and n-π^* states in compounds I and II.

(13) The low solubility of these furanquinones in nonpolar solvents precluded the measurements of μ_g from solvent–solute dielectric constants.

Table I: Measured and Calculated Dipole Moments of the Ground and First Excited Singlet States of I and II

Compound	μ_e,[a] D	μ_g,[b] D	μ_e,[b] D
I	$12.2\mu_g$	1.4	18.7
II	$14.6\mu_g$	1.9	24.3

[a] Determined from solvent-induced emission shifts. [b] Calculated using Hückel MO theory, taken from ref 7.

perature gradually between 20 and −70°, where the solvent is still fluid, the emission of I and II in 2-MeTHF shifts to lower energies before shifting to higher energies at −196° (Figure 5). No significant shift in the spectra of I and II was noted in EPA solvent in the range 20 to −70°.

Fluorescence Quantum Yields. The fluorescence yields for I or II in several solvents at ambient temperature are given in Table II. Within the limited number of polar solvents used there is a general decrease in yield with increasing solvent polarity concurrent with the shift of the emission to lower energies. The fluorescence yield in hydrocarbon solvents is significantly less than in polar solvents. However, addition of polar solvent to the nonpolar solvent produces an increase in fluorescence intensity and a gradual shift of the emission to longer wavelengths. At concentrations of polar solvent component below 1% the increase in yield is approximately linear with polar solvent concentration. The fluorescence yield also increases with decreasing temperature. The temperature dependence of the quantum yield (Q) of I in EPA (20 to −70°) was analyzed by the method of least squares according to

$$1/Q = A + Be^{-E/RT} \quad (5)$$

where A and B are constants and E is an activation energy. The value of E was determined to be ~6.0 kcal/mol.

A four- to fivefold increase in fluorescence yield was observed for both I and II on going from EPA solvent at ambient temperatures to −196°.

Table II: Fluorescence Quantum Yields of I and II

Compound	Solvent	Fluorescence max,[a] nm	Fluorescence yield[b]
I	3-Methylpentane	475	~0.002
	Dioxane	560	0.23
	Acetone	600	0.16
	Acetonitrile	620	0.11
II	3-Methylpentane	453	~0.001
	Dioxane	550	0.13
	Acetone	600	0.09
	Acetonitrile	615	0.08

[a] Error ±5 nm. [b] Error ±0.04.

Phosphorescence Spectra. A weak structured phosphorescence for both I and II in polar glasses at −196° was observed with maxima in EPA glass at 620 and 595 nm, respectively (Figure 2). The spacing between the maximum and shoulder is approximately 1000 cm^{-1} in both cases. No variation in wavelength of the emission was noted on going from an EPA glass to a 2MeTHF glass. Phosphorescence yields were estimated to be in the range 10^{-2} to 10^{-3} by comparison of phosphorescence and fluorescence intensities at −196°. The phosphorescence lifetime for II in EPA glass was estimated to be of the order of 50 msec. The emission intensity from I was too weak to measure its lifetime with the present apparatus, though several derivatives of I showed phosphorescence lifetimes of the order of 20–50 msec.

Phosphorescence excitation spectra corresponded closely to both fluorescence excitation and absorption spectra for both compounds. A low degree of polarization (P) was observed for the phosphorescence of II in EPA glass using wide excitation and emission bandwidths and excitation in the region 350 to 450 nm. No polarization spectra could be measured for I for reasons mentioned above. Addition of ethyl iodide to the polar glass increased the phosphorescence intensity of both molecules.

Discussion

In paper I[7] of this series it was reported that there was no evidence of n–π^* singlet states in the absorption spectra of the furanquinones I and II. The lowest excited singlet state of these molecules has π–π^* rather than n–π^* character. It is expected that the singlet n–π^* state lies at slightly higher energies than the lowest π–π^* state. The observation of fluorescence from I and II in both nonpolar and polar media is consistent with this assignment. However, the low fluorescence yield in nonpolar solvents is indicative of rapid intersystem crossing from the singlet state to the triplet manifold. This process, in these solvents, possibly involves crossing from the π–π^* state to an n–π^* triplet. Intersystem crossing rules for molecules containing carbonyl groups, where $S^{\pi-\pi^*} \rightarrow T^{n-\pi^*}$ is of the order of 10^3 times faster than $S^{\pi-\pi^*} \rightarrow T^{\pi-\pi^*}$, have been discussed by El-Sayed.[14] Alternatively, vibronic interaction between the lowest singlet π–π^* and n–π^* states may enhance intersystem crossing.[15] This effect is expected to be larger in hydrocarbon than in polar solvents due to an increase in the π–π^* to n–π^* splitting in the latter solvents.

It is unlikely that the emission from I and II in nonpolar media is due to the presence of trace quantities of polar impurities in the solvent (*vide infra*), as the emission yields were independent of hydrocarbon used

(14) M. A. El-Sayed, *Accounts Chem. Res.*, 1, 8 (1968).
(15) E. C. Lim and J. M. H. Yu, *J. Chem. Phys.*, 45, 4742 (1966).

(*i.e.*, hexane, isopentane, and 3-methylpentane) and did not change on drying the solvent over sodium. Further, the emission from these molecules in the hydrocarbon solvents is identified as π–π^* rather than n–π^* by the absence of any vibrational frequency corresponding to the C=O stretching frequency in the emission and by its structural similarity with the π–π^* fluorescence observed in polar glasses. The somewhat poor mirror-image symmetry between absorption and emission in the nonpolar solvents may be due in part to a change in nuclear configuration in these molecules on going from the ground to excited state.

In polar solvents the π–π^* singlet state is unequivocally identified as the emitting state. This is shown by the Stokes shift and increase in fluorescence yield in these solvents (Table II) and by the high positive degree of polarization of the emission when excited in the first π–π^* absorption band.[7] Further, the significant polar-solvent-induced Stokes shift in the fluorescence is consistent with the emitting state having intramolecular charge-transfer character, as was reported earlier for the lowest π–π^* state of these molecules.[7] Nonspecific polar solvent induced frequency shifts of fluorescence spectra have been discussed by several authors[16,17] and interpreted in terms of a generalized dipole–dipole interaction (orientation polarization) between solvent and solute in the excited state. A shift to lower energies analyzed in these terms implies a large increase in dipole moment on excitation and thus a greater solute–solvent stabilization in the fluorescent state than in the ground and Franck–Condon excited states. While dipole moments obtained from Hückel MO calculations are sometimes overestimated, the previously calculated values[7] are nonetheless in good agreement with the excited state dipole moments determined from the solvent shift data in the present work.

The shift of the emission of I and II in 2-methyltetrahydrofuran first to lower then to higher energies on lowering the temperature from ambient to −196° may be attributed to the temperature dependence of solvent reorientation.[18] At higher temperatures thermal motion inhibits solvent reorientation, while at −196° no solvent reorientation is possible during the lifetime of the fluorescence state. The result is that the shift in emission passes through a maximum as the temperature is decreased. Regardless of temperature, the emission from I and II is still significantly red shifted from the respective absorption edges, possibly due in part to specific solute–solvent interaction or again to differences in ground and excited state nuclear configurations. The approximate linear relationship observed between fluorescence intensity and concentration of polar components in predominantly nonpolar media is indicative of exciplex formation.[19] However, these results are preliminary and further study is necessary for any verification of exciplex states in these systems.

The large increase in fluorescence yield for I and II on going from nonpolar to polar solvents is indicative of a change in the intersystem crossing process from $S_1^{\pi-\pi^*} \rightarrow T^{n-\pi^*}$ to $S_1^{\pi-\pi^*} \rightarrow T^{\pi-\pi^*}$ in the latter solvents. In this case the significant stabilization of the $S_1^{\pi-\pi^*}$ state in polar media possibly results in an energetic inversion of the lowest singlet π–π^* and triplet n–π^* states. This order is consistent with the increase in phosphorescence yield from these molecules in the presence of ethyl iodide. Heavy-atom solvents induce spin–orbit coupling between the singlet π–π^* and triplet π–π^* states but not between the singlet π–π^* and triplet n–π^* states which are already strongly coupled. Thus, in the former case there is an increase of the singlet to triplet intersystem crossing rate with a resultant increase in phosphorescence yield. Within the limited number of polar solvents used here there is a general decrease in fluorescence yield, for both molecules, with increasing solvent polarity concurrent with the shift of the emission to lower energies. Similar dependences of fluorescence yield on solvent polarity have been reported for other molecules showing excited state solute–solvent interactions,[20,21] and interpreted as being a result of a solvent-dependent quasichemical[22] or internal conversion process.[23] Further, the high-temperature dependence of the fluorescence yield of I and II possibly reflects a large activation energy for such a process.

The weak phosphorescence emission from these furanquinones in polar glasses and their low solubility in hydrocarbon glasses makes any identification of their lowest triplet state difficult. The absence of any measurable shift in the phosphorescence on going from a 2-methyltetrahydrofuran to an EPA glass indicates that the emitting triplet state is of π–π^* character. Hydrogen bonding to the carbonyl oxygen in EPA glass would be expected to induce a shift to higher energies for an n–π^* triplet state which, however, is not seen. However, the measured phosphorescence lifetime of II is shorter than those reported for the π–π^* phosphorescence of substituted quinones[3,24] but still longer than n–π^* triplet lifetimes reported for *p*-quinones.[4] The triplet radiative lifetime which is the more reliable parameter for differentiating between

(16) E. Lippert, W. Luder, and H. Boos, *Advan. Mol. Spectrosc.*, 1, 443 (1962).

(17) N. Mataga, Y. Torihashi, and K. Ezumi, *Theor. Chim. Acta*, 2, 158 (1964).

(18) K. Brederick, Th. Förster, and H. G. Oesterlin in "Luminescence of Organic and Inorganic Materials," H. P. Kallmann and G. M. Spruch, Ed., Wiley, New York, N. Y., 1962.

(19) M. S. Walker, T. W. Bednar, and R. Lumry, *J. Chem. Phys.*, 47, 1020 (1967).

(20) E. N. Viktorova, *Opt. Spectrosc.*, 22, 206 (1967).

(21) Th. Förster and K. Rokos, *Chem. Phys. Lett.*, 1, 279 (1967).

(22) M. S. Walker, T. W. Bednar, R. Lumry, and F. Humphries, *Photochem. Photobiol.*, 14, 147 (1971).

(23) J. Eisinger and G. Navon, *J. Chem. Phys.*, 50, 2069 (1969).

(24) M. Sebti, F. Dupuy, J. Megel, and G. Nouchi, *C. R. Acad. Sci., Ser. B*, 272, 123 (1971).

$n-\pi^*$ and $\pi-\pi^*$ triplet states could not be calculated due to the lack of accurate values for the phosphorescence and S_1–T intersystem crossing yields. No conclusion can be drawn concerning the nature of the lowest triplet state from the phosphorescence polarization data due to the wide bandwidths needed to observe the emission. Tentative identification of the lowest triplet states of these molecules as $\pi-\pi^*$ is consistent with their low yields of photoreduction in alcohol solvents at ambient temperatures.[25]

The order and nature of the low-lying electronic states of the furanquinones I and II are therefore identified as S_0, $T_1^{\pi-\pi^*}$, $T_2^{n-\pi^*}$, $S_1^{\pi-\pi^*}$, $S_2^{n-\pi^*}$, ... in nonpolar solvents and S_0, $T_1^{\pi-\pi^*}$, $S_1^{\pi-\pi^*}$, $T_2^{n-\pi^*}$, $S_2^{n-\pi^*}$, ... in polar solvents. This order appears most consistent with the observed photophysical and photochemical behavior of these quinones. Further, the latter order is similar to that reported for other substituted *p*-quinones having low-lying intramolecular charge-transfer states.[4] It is of interest to note that fluorescence and a weak phosphorescence are also observed from single crystals of the furanquinones.[26]

Acknowledgment. The authors wish to acknowledge discussions on this work with Drs. A. R. Monahan and G. E. Johnson, and computer-programming assistance from A. Wilson.

(25) M. S. Walker, M. A. Abkowitz, R. W. Bigelow, and J. H. Sharp, to be published.

(26) M. S. Walker, R. L. Miller, C. H. Griffiths, and P. Goldstein, *Mol. Cryst. Liq. Cryst.*, **16**, 203 (1972).

Mercury Sensitization of the Isomerization of Diazines

by F. Lahmani and N. Ivanoff*

Laboratoire de Physico-chimie des Rayonnements, Université de Paris-Sud, Centre d'Orsay, 91 Orsay, France

(Received December 20, 1971)

Publication costs assisted by Centre National de la Recherche Scientifique

The Hg($6\ ^3P_1$)-sensitized isomerization of pyrimidine, 5-methylpyrimidine, 4,6-dimethylpyrimidine, pyrazine, and 2,5-dimethylpyrazine has been investigated; the quantum yields of the sensitized isomerization are respectively $(3.8 \pm 0.4) \times 10^{-2}$, $(5.2 \pm 0.5) \times 10^{-2}$, $(3.6 \pm 0.4) \times 10^{-2}$, $(2.08 \pm 0.2) \times 10^{-2}$, and $(2.1 \pm 0.2) \times 10^{-2}$. Quenching rate constants of the mercury $^3P_1$ atom by pyrimidine have been determined by physical and chemical methods; the value of k_q found is 9×10^{10} l./(mol sec). The addition of argon decreases the quantum yield of sensitized isomerization in the same way as that of direct isomerization. The phosphorescence of biacetyl sensitized by pyrimidine alone is low; it is increased in the presence of mercury and this effect is enhanced by the addition of argon. These results suggest that a high triplet state can be involved in the photoisomerization of diazines.

Introduction

The photochemical formation of unstable isomers leading to a shift of ring atoms seems to be a general process in the photochemistry of benzene compounds. We have found that an analogous reaction takes place in the case of the diazines,[1] *i.e.*

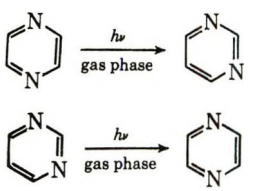

A previous investigation[2] on the mechanism of this reaction has shown the following points. (1) The quantum yield of isomer depends on the wavelength of excitation and is about 100 times higher at 253.7 nm (excitation of the second excited singlet state $S_{\pi\pi^*}$) than at 313 nm (excitation of the first excited singlet state $S_{n\pi^*}$). (2) The formation of the isomer is in competition with the collisional deactivation of a vibrationally excited species; in the case of the excitation of pyrazine in the $S_{\pi\pi^*}$ absorption band the quantum yield of isomer decreases when the pressure of an added inert gas increases while the phosphorescence $T_{n\pi^*} \rightsquigarrow S_0$ of pyrazine increases without any change in the fluorescence.

As the lifetime of the $S_{\pi\pi^*}$ singlet state can be sup-

(1) F. Lahmani and N. Ivanoff, *Tetrahedron Lett.*, 3913 (1967).

(2) M. Magat, N. Ivanoff, F. Lahmani, and M. P. Pilleni, paper presented at the 20ème Réunion de la Société de Chimie Physique, Paris, May 27, 1969; F. Lahmani, These, Facutlé des Sciences d'Orsay, Université de Paris, 1970.

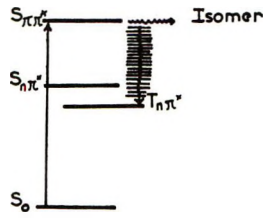

Figure 1. Schematic energy level diagram for diazine photoisomerization.

posed to be shorter than the time of collisions in the pressure range used, it was concluded from this study that the process competing with isomerization could be the vibrational relaxation of a highly excited triplet state according to the energy diagram of Figure 1.

In order to elucidate further the mechanism of the reaction, we have performed experiments on the mercury sensitization of diazines.

Experimental Section

Pyrazine, pyrimidine, and other diazines (Aldrich or Koch Light) were dried over BaO and distilled *in vacuo*. Argon, N_2O, butane, and propane were obtained from Air Liquide. Benzene (Prolabo RP) was purified by recrystallization, and biacetyl (Fluka), by fractional distillation.

Mercury Sensitization. Silica cells (Supracil; optical path 1 cm; volume ~10 ml; closed with a Teflon valve) were filled using a grease-free vacuum system. Mercury vapor was supplied by a small mercury droplet contained in the cell

All photolyses were carried out at room temperature using a low-pressure mercury resonance lamp (Claude Paz & Visseaux) and a chlorine filter. The relative light intensity absorbed by mercury was measured with a Zeiss spectrophotometer, the deuterium lamp being replaced by a low-pressure mercury lamp. This provided a relative means of measuring reproducibility of light absorption and permitted us to correct the effect of pressure broadening of the absorption.

The absolute measurement of light intensity was achieved either by using cis–trans isomerization of 2-butene[3] or by measuring the yield of nitrogen formed in the mercury-sensitized decomposition of nitrous oxide–*n*-butane mixtures.[4]

In the "physical" quenching experiments the cells were filled under a vacuum system with mercury vapor from a reservoir maintained at 0° and the experimental arrangement used a Zeiss spectrofluorimeter.

Analysis. Following the photolysis, the sample cell was connected to an aliquot of water cooled to liquid nitrogen temperature. The sample cell and the aliquot were isolated by a valve. The aliquot was evacuated to 10^{-3} Torr using a standard vacuum system. After evacuation the pumps were valved off from the aliquot and the valve to the sample cell was opened, allowing the products of the photolysis to be collected on the aliquot of refrigerated water. The vessel containing the mixture of water and products was then sealed. Under these conditions all the contents of the sample cell, except polymer, were collected in the water. After warming and agitating, the cell was opened and the sample was analyzed by gas chromatography on a Perkin-Elmer F6 apparatus using a flame ionization detector with a Carbowax 1500 column.

The identification of the products of photolysis has been previously done by trapping the new products after chromatographic separation and by comparing the uv absorption spectra of the eluted products with that of an authentic sample.[2]

The quantitative analysis was performed by reference to standard aqueous solutions of the diazines at concentrations in the same order of magnitude as that of the sample to be analyzed, the standard solutions being injected just before and after the sample of the photolysis products.

Results

When pyrimidine was irradiated at 253.7 nm in the presence of mercury under conditions such that no direct isomerization could be detected, the formation of pyrazine was easily observed.

The mercury-sensitized isomerization is also observed in the case of all the diazines that have been proved to isomerize in direct photolysis at the same wavelength (Table I).

In the case of 2,5-dimethylpyrazine the same isomeric pyrimidines are obtained in the same ratio for mercury sensitization as for the direct photolysis.

The quantum yields of mercury-sensitized isomerization are higher in all cases than those obtained in direct photolysis, as shown in Table I, while the ratio $\Phi_{isomer}/\Phi_{polymer} \approx 0.2$ seems to be the same.

To show that isomerization occurs *via* the mercury-sensitized pathway, we have determined the quenching rate constants of $Hg(^3P_1)$ excited atoms by pyrimidine, by the following physical and chemical methods.

(a) The intensity decrease of the resonance emission of $Hg(^3P_1)$ atoms was followed as a function of pyrimidine pressure. The experimental data were found to be consistent with the Stern–Volmer equation modified by Yang[5] (Figure 2)

$$Q_0/(Q_0 - Q) = \alpha + \beta[M]^{-1}$$

Q_0 and Q are the intensities of the resonance emission in the absence and presence of [M] mol/l of pyrimidine; α and β are experimental parameters whose ratio $\alpha/\beta = \tau k_q$; k_q is the quenching rate constant of $Hg(^3P_1)$ by pyrimidine; and τ is the mean lifetime of mercury atoms.

(3) R. B. Cundall and T. F. Palmer, *Trans. Faraday Soc.*, 1211 (1960).

(4) R. J. Cvetanovic, *J. Chem. Phys.*, 23, 1208 (1955).

(5) K. Yang, *J. Amer. Chem. Soc.*, 88, 4575 (1966).

Table I: Quantum Yields of Mercury-Sensitized and Direct Isomerization of Diazines

Initial compd	Isomer formed	$\Phi_{sens\ isom}$	$\Phi_{direct\ isom}$ (at 253.7 nm)
Pyrimidine	Pyrazine	$(3.8 \pm 0.4) \times 10^{-2}$	$(1.7 \pm 0.1) \times 10^{-3}$
4,6-Dimethylpyrimidine	2,5-Dimethylpyrazine	$(3.6 \pm 0.4) \times 10^{-2}$	$(4.6 \pm 0.4) \times 10^{-3}$
5-Methylpyrimidine	2-Methylpyrazine	$(5.2 \pm 0.5) \times 10^{-2}$	$(7 \pm 0.7) \times 10^{-3}$
Pyrazine	Pyrimidine	$(2.08 \pm 0.2) \times 10^{-2}$	$(7 \pm 0.7) \times 10^{-3}$
2,5-Dimethylpyrazine	4,6-Dimethylpyrimidine	$(7 \pm 0.7) \times 10^{-3}$	$(1.5 \pm 0.15) \times 10^{-3}$
	2,5-Dimethylpyrimidine	$(1.4 \pm 0.15) \times 10^{-2}$	$(3 \pm 0.3) \times 10^{-3}$

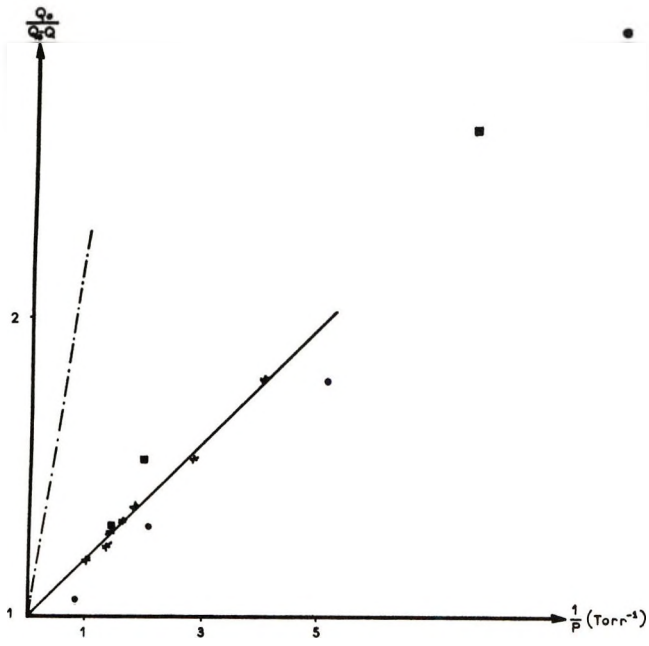

Figure 2. Quenching of $Hg(^3P_1)$ resonance radiation by diazines, $Q_0/(Q_0 - Q)$ against the reciprocal pressure of diazine: *, pyrimidine; ●, pyrazine; ■, 2,5-dimethylpyrazine; —·—, water.

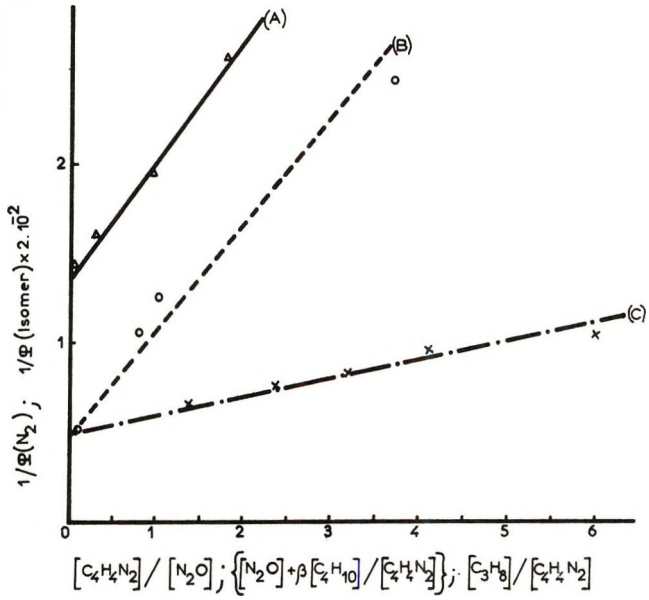

Figure 3. (A) (——) plot of $1/\Phi(N_2)$ against the pyrimidine to nitrous oxide ratio; (B) (- - -) plot of $1/\Phi$(pyrazine) $\times$ 2×10^{-2} againt the ratio of the mixture of nitrous oxide and butane to pyrimidine; (C) (—△—) plot of $1/\Phi$(pyrazine) $\times$ 2×10^{-2} against the propane to pyrimidine ratio.

The experimental value of τk_q(pyrimidine) was compared to the value obtained in the same geometrical arrangement with a standard molecule (H_2O) for which the quenching rate constant is known[6] (Figure 2). From the slope of the Stern–Volmer plot, one deduces k_q(pyrimidine) $\simeq 12 \times 10^{10}$ l./(mol sec), the corresponding cross section being 11 Å^2. Some experiments done with pyrazine and with 2,5-dimethylpyrazine have shown that the cross sections of these compounds approach that of pyrimidine.

(b) On the other hand, we have studied the mercury photosensitization of a ternary mixture of nitrous oxide, butane, and pyrimidine, according to the method of Cvetanovic.[4] On the basis of the mechanism described by this author, the reciprocals of the quantum yields of nitrogen and pyrazine produced are

$$1/\Phi_{N_2} = \alpha(1 + \beta[C_4H_{10}]/[N_2O] + \beta'[C_4H_4N_2]/[N_2O])$$

$$1/\Phi_{pyrazine} = \gamma\{1 + 1/\beta'([N_2O] + \beta[C_4H_{10}])/[C_4H_4N_2]\}$$

The values of α and β are, respectively, 1.28[4] and 0.255;[4] the ratio $[C_4H_{10}]/[N_2O]$ is 0.5 under our experimental conditions, while the value of γ ($1/\Phi_{pyrazine}$ in the absence of added compounds) is close to 25 (Table I); $\beta' = k_{C_4H_4N_2}/k_{N_2O}$ is the ratio of quenching efficiencies of the mercury $^3P_1$ state by pyrimidine and nitrous oxide; the partial pressures of pyrimidine, butane, and N_2O are, respectively, 6–8, 2.5–10, and 5–20 Torr.

The values of β' obtained from the slopes of plots of $1/\Phi_{N_2}$ and $1/\Phi_{pyrazine}$ are, respectively, 0.520 and 0.850 (Figure 3); assuming k_{N_2O} to be 14×10^{10} l./(mol sec),[6] the relative value of $k_{pyrimidine}$ would be 7.2×10^{10} or 11×10^{10} l./(mol sec). (In this calculation, we have neglected collisional deactivation of excited pyrimidine molecules by foreign gases. In fact, the value of β' would be even larger.) Considering that the discrepancy in the values of β' arises from the complexity of the ternary system and analytical difficulties,

(6) R. J. Cvetanovic, *Progr. React. Kinet.*, 2, 66 (1964).

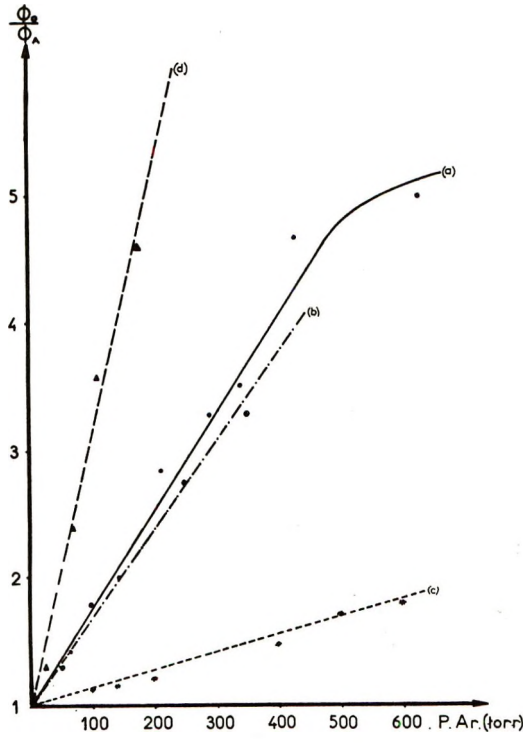

Figure 4. For the sake of comparison, Stern–Volmer plots of the quenching of isomerization by argon, in the case of direct excitation at 253.7 and 300 nm and for mercury sensitization: ——, mercury-sensitized isomerization of pyrimidine (a); –·–·–·–, mercury-sensitized isomerization of pyrazine (b); - - - - - - - -, isomerization of pyrazine at 253.7 nm (direct irradiation[2]) (c); — — —, isomerization of pyrazine at 310 nm[2] (direct irradiation[2]) (d).

an additional investigation was performed with a binary mixture of propane and pyrimidine. The value of $k_{\text{pyrimidine}}$ found was 9×10^{10} l./(mol sec) (Figure 3).

The quenching rate constants obtained by physical and chemical methods are in relatively good agreement, especially in view of the uncertainty of the absolute values of k_q for the standard molecule, and show that under our experimental conditions, the isomerization of pyrimidine to pyrazine in the presence of mercury at 253.7 nm may involve sensitization by excited mercury atoms.

Effect of Argon. When mercury sensitization of pyrimidine or pyrazine is performed in the presence of increasing pressures of argon, a decrease in formation of isomer is observed. This in turn leads to a Stern–Volmer linear relationship between $1/\Phi_{\text{diazine isomer}}$ and argon pressure (Figure 4). Argon does not quench excited mercury atoms and this effect observed can only be explained by the collisional deactivation of the excited diazine molecule. A similar effect was obtained in direct photolysis. However the efficiency of argon in reducing isomer formation is greater in the mercury-sensitized photolysis than in the direct one at the same wavelength. This shows that Hg(6 $^3P_1$) does not transfer all its energy to diazine and is in agreement with the results of Montague and Rowland for the mercury-sensitized decomposition of cyclobutanone,[7] where the average energy transferred from mercury-excited atoms has been evaluated to 105 kcal/mol.

Effect of Biacetyl. Since pyrimidine does not emit phosphorescence in the gas phase, the presence of a triplet state of pyrimidine can be detected by the addition of biacetyl and the observation of the sensitized phosphorescence of biacetyl. When biacetyl (0.6 Torr) is added to pyrimidine (1.5 Torr), the sensitized phosphorescence of biacetyl is very low for the excitation at 253.7 nm. In the presence of mercury, the sensitized phosphorescence of biacetyl is strongly increased and the effect is enhanced by the addition of argon. No phosphorescence of biacetyl is observed for mercury and biacetyl alone.[8] This experiment seems to indicate the presence of an excited triplet state of pyrimidine arising from mercury $^3P_1$ energy transfer, and the increase of sensitized phosphorescence of biacetyl with pressure of added argon can be related to the decrease of isomer formation.

Conclusion

The results converge to show that Hg($^3P_1$) atoms can produce *via* triplet–triplet energy transfer an excited triplet state of the diazine from which isomerization of the ring can occur. (*o*-Xylene has been shown to behave differently from diazine: Hg($^3P_1$) atoms are inefficient in sensitizing the formation of *m*- or *p*-xylene.) Attempts to sensitize the reaction from triplet benzene (E_T = 85 kcal/mol) or Cd($^3P_1$) atoms (E_T = 87.5 kcal/mol) have failed, showing that the reaction of isomerization is energy dependent. Finally it can be pointed out that the role of a highly excited triplet state in the reaction of isomerization of diazine does not exclude a possible role of hot ground-state molecule in a subsequent step.

(7) D. C. Montague and F. S. Rowland, *J. Amer. Chem. Soc.*, **91**, 7230 (1969).

(8) A. G. Harrison and F. P. Lossing, *Can. J. Chem.*, **37**, 1478 (1959); H. Ishikawa and W. A. Noyes, Jr., *J. Chem. Phys.*, **37**, 583 (1962).

Nitrogen-14 Nuclear Quadrupole Coupling and the Nitrogen Localized Electron Distribution in Diazirine

by J. M. Pochan and W. H. Flygare*

Noyes Chemical Laboratory, University of Illinois, Urbana, Illinois 61801 *(Received January 21, 1972)*

Publication costs assisted by the National Science Foundation

The high-resolution microwave spectra of $^{14}N,^{14}N$-diazirine has been recorded to obtain the diagonal elements of the ^{14}N nuclear quadrupole coupling constant tensor in the principal inertial axis system. The ^{14}N coupling constants are $\chi_{aa} = +0.196 \pm 0.150$ MHz, $\chi_{bb} = -3.010 \pm 0.150$ MHz, and $\chi_{cc} = 2.814 \pm 0.300$ MHz. The bonding in this ring compound is discussed in light of the ^{14}N local electronic field gradients.

I. Introduction

Recently the ^{33}S and ^{14}N nuclear quadrupole coupling in the ethyleneimine[1] and ethylene sulfide[2] rings, respectively, have been used as probes of the electronic structure of these small strained ring systems. Both the Walsh[3] and Coulson–Moffitt[4] LCAO–MO bonding schemes were used to interpret the electronic field gradients at the ^{33}S nucleus in ethylene sulfide[2] and at the ^{14}N nucleus in ethyleneimine.[1] The Walsh bonding scheme[3] was found to give an appropriate description of the bonding in the above two molecules.[1,2] The present work is an extension of the above study to diazarine H_2CN_2 which contains a nitrogen–nitrogen double bond in the ring. We report here accurate values of the ^{14}N nuclear quadrupole coupling constants. We also compare our results to the values obtained in a recent *ab initio* calculation of the ^{14}N field gradients in diazirine.

II. Experimental Section

Diazirine was prepared by the method of Ohme and Schmitz.[5] The only variation on the reaction was the final drying step. In this experiment the N_2 gas was passed through the reaction solution into a U-tube nitrogen trap. The sample was stored at liquid nitrogen. After an initial attempt at vacuum distillation, all samples were used after trapping without purification. During the course of the experimental work five explosions resulted from handling the compound. These explosions appeared to be caused by incomplete drying of the sample as one dried sample consisting of about 1 ml of neat liquid was used over a 3-week period with no problems.

The rotational spectra of three isotopic species of diazirine have been observed previously.[6] For this experiment the $4_{22} \rightarrow 4_{23}$, $3_{22} \rightarrow 3_{21}$, $5_{33} \rightarrow 5_{32}$, and $7_{35} \rightarrow 7_{34}$ transitions were observed in the most prevalent species. The $0_{00} \rightarrow 0_{01}$ transition of the ^{13}C species was also observed. The a axis is along the symmetry axis, and the c axis is out of the molecular plane. The microwave spectrometer used in this work has been described elsewhere.[7] All spectra, with the exception of one ^{13}C natural abundance line, were taken in a S-band absorption cell cooled to Dry Ice temperatures. The ^{13}C line was studied in an L-band absorption cell cooled to Dry Ice temperature.

The theory of two quadrupole interactions in a rotating molecule has been given previously.[8] Considering the quadrupolar nuclei with spins I_1 and I_2, the total angular momentum can be described by either of the two following coupling schemes

$$\begin{aligned} I_1 + J &= F_1 \\ F_1 + I_2 &= F_2 \end{aligned} \qquad (1)$$

or

$$\begin{aligned} I_1 + I_2 &= I \\ I + J &= F \end{aligned} \qquad (2)$$

Krusic[9] has written a computer program to calculate rotational transitions and hyperfine intensities in the coupling scheme of eq 1. Diazirine has a C_{2v} axis (a axis) in which protons may exchange positions under rotation. The proton spin statistics must, therefore, be included, in any calculation of transition intensities. Because of the difficulty in determining spin statistics with the coupling scheme in eq 1, the program was rewritten in the coupling scheme of eq 2. Spin statistics

(1) M. K. Kemp and W. H. Flygare, *J. Amer. Chem. Soc.*, **90**, 6267 (1968).

(2) R. L. Shoemaker and W. H. Flygare, *ibid.*, **90**, 6263 (1968).

(3) A. D. Walsh, *Trans. Faraday Soc.*, **45**, 179 (1949).

(4) C. A. Coulson and W. E. Moffitt, *J. Chem. Phys.*, **15**, 151 (1947).

(5) R. Ohme and E. Schmitz, *Chem. Ber.*, **97**, 297 (1964).

(6) L. Pierce and Sr. V. Dobyns, *J. Amer. Chem. Soc.*, **84**, 2651 (1962).

(7) W. H. Flygare, *J. Chem. Phys.*, **41**, 206 (1964); *ibid.*, **42**, 1157 (1965).

(8) J. Bardeen and C. H. Townes, *Phys. Rev.*, **73**, 97 (1948).

(9) P. J. Krusic, "Quantum Chemistry Program Exchange," Indiana University, Bloomington, Ind.

calculations can be done with relative ease using this coupling scheme. All transitions in the computer output are listed as

$$I,F \longrightarrow I',F'$$

where I and F represent the initial state and I′ and F′ the final state in the rotational transition. The observed splittings between hyperfine components are listed in Table I. The weaker components of the transitions have not been listed. Line widths on spectra vary from $\Delta\nu$ (half-width) $\cong$ 50 kHz on the 7 → 7 transition to $\Delta\nu \cong$ 25 kHz on the 3 → 3 transition. All experimental frequencies are accurate to ±10 kHz.

Table I: Observed and Calculated Splittings between Hyperfine Components of Rotational Transitions Observed in Diazirine[a]

Transition	Hyperfine components (I,F → I′,F′)				− (I,F → I′,F′)				kHz, obsd	kHz, calcd	Difference
$4_{22} \rightarrow 4_{23}$	2	2	2	2	1	4	1	4	331	318	13
	1	4	1	4	2	6	2	6	202	217	−15
	2	6	2	6	1	5	1	5	816	809	7
	1	5	1	5	1	3	1	3	243	259	−16
	1	3	1	3	2	5	2	5	162	145	17
$3_{22} \rightarrow 3_{21}$[b]	2	3	2	3	2	4	2	4	439	449	−10
	2	4	2	4	1	2	1	2	110	103	7
	1	2	1	2	1	4	1	4	234	240	−6
	1	4	1	4	2	2	2	2	393	378	15
	2	2	2	2	2	5	2	5	120	137	−17
	2	5	2	5	1	3	1	3	182	172	10
	1	3	1	3	2	1	2	1	313	308	5
$5_{33} \rightarrow 5_{32}$	2	5	2	5	2	6	2	6	285	291	−6
	2	6	2	6	1	6	1	6	120	121	−1
	1	6	1	6	2	4	2	4	98	101	−3
	2	4	2	4	2	7	2	7	202	203	−1
	2	7	2	7	0 5 0 5 / 1 5 1 5				65	70	−5
	0 5 0 5 / 1 5 1 5				2	3	2	3	82	81	1
$7_{35} \rightarrow 7_{34}$	2	7	2	7	2	8	2	8	730	735	−5
	2	8	2	8	2	6	2	6	422	372	50
	2	6	2	6	2	9	2	9	556	596	−40
	2	9	2	9	0 7 0 7 / 1 7 1 7				111	113	−3

[a] The calculated values were obtained with χ_{aa} = +0.196 MHz, χ_{bb} = −3.010 MHz, and χ_{cc} = +2.814 MHz. [b] There are many overlapping transitions in this rotational transition. Only the most intense have been listed for brevity.

To obtain the best fit of the observed spectra the data of Dobyns and Pierce[6] was initially used. Their values in the ^{15}N–^{14}N molecule are $\chi_{cc} - \chi_{bb} = 6.2 \pm 0.3$ MHz and $\chi_{aa} < |1.0 \text{ MHz}|$. χ_{ii} is the nuclear quadrupole coupling constant along one of the principal inertial axis of the ^{15}N–^{14}N molecule. As the trace of the field gradient tensor is zero, a relation can be set up between χ_{aa} and χ_{bb}. χ_{bb} and χ_{cc} can, therefore, be determined for various values of χ_{aa}. Because the ^{15}N–^{14}N system is in a slightly different axis system than the ^{14}N–^{14}N molecule, our values of $\chi_{cc} - \chi_{bb}$ and χ_{aa} for the ^{14}N–^{14}N species would be expected to be slightly different than the values given by Dobyns and Pierce on the ^{14}N–^{15}N species. Initially two sets of coupling constants would give an acceptable fit of the 3(2,2)–3(2,1) and 4(2,2)–4(2,3) transitions. These values were

$$\chi_{aa} = -1.375 \text{ MHz}$$
$$\chi_{bb} = -2.425 \text{ MHz} \quad (3)$$
$$\chi_{cc} = 3.800 \text{ MHz}$$

and

$$\chi_{aa} = 0.200 \text{ MHz}$$
$$\chi_{bb} = -3.000 \text{ MHz} \quad (4)$$
$$\chi_{cc} = 2.800 \text{ MHz}$$

There is no way of distinguishing between these two sets of coupling constants with only the Q-branch transitions. However, the 0(0,0)–1(0,1) transition depends only on χ_{aa}. We observed the 0(0,0)–1(0,1) transition in the ^{13}C–^{14}N–^{14}N species at 39,192.08 MHz (the ^{12}C normal species 0(0,0)–1(0,1) transition is outside of our available frequency range). After considerable difficulty the 0(0,0)–1(0,1) line width was narrowed to $\Delta\nu$ = 300 kHz, and there was no indication of asymmetry in the line shape. If the coupling constants in eq 3 were valid, splittings would have been observed. The coupling constants in eq 4 are, therefore, correct. After this experiment the 5(3,3)–5(3,2) and 7(3,5)–7(3,4) transitions were also observed and fit. The coupling constants were refined and a best fit of all data was obtained with χ_{aa} = 0.196 MHz, χ_{bb} = −3.010 MHz, and χ_{cc} = 2.814 MHz. A least-squares error of 0.150 MHz is assigned to χ_{aa} and χ_{bb}. The final results are listed in Table II. The results of the fit of the experimental data with these values are shown in Table I.

The ^{14}N nuclear quadrupole coupling constants in dimethyldiazirine have recently been reported.[10] Comparing results indicates that the presence of the methyl

Table II: Diagonal Elements of the ^{14}N Quadrupole Coupling Constant Tensor in Diazirine[a]

$$\chi_{aa} = +0.196 \pm 0.150 \text{ MHz}$$
$$\chi_{bb} = -3.010 \pm 0.150 \text{ MHz}$$
$$\chi_{cc} = +2.814 \pm 0.150 \text{ MHz}$$

[a] *a* and *b* axis in plane of the molecule. *a* axis coincident with the molecular symmetry axis.

(10) J. E. Wollrab, L. H. Scharpen, D. P. Ames, and J. A. Merritt, *J. Chem. Phys.*, 49, 2405 (1968).

groups has not appreciably altered the ^{14}N electronic field gradients (the inertial axes in both molecules have the same orientation, but the *b* and c axes are interchanged).

III. Discussion

The ^{14}N nuclear quadrupole coupling constants reported in diazirine are in fair agreement with the results of an *ab initio* calculation ($\chi_{aa} = -0.8$ MHz, $\chi_{bb} = -1.88$ MHz, and $\chi_{cc} = +2.69$ MHz).[11] Apparently the *ab initio* calculations underestimate the asymmetry in the electronic distribution near the N nuclei in diazirine.

We will now attempt a simple localized description of the bonding in diazirine to compute the ^{14}N electronic field gradients.

The nuclear quadrupole coupling constant (Table II) is a product of the nuclear quadrupole moment times the electronic field gradient about the nucleus. The nuclear quadrupole moment of ^{14}N is known to be[12]

$$Q = 0.77 \times 10^{-35} \text{ esu cm}^2 \tag{5}$$

Using this number, the electronic field gradients in the principal axis system are calculated to be

$$q_{xx} = q_{aa} = \left\langle 0\left|\frac{\partial^2}{\partial a^2}V\right|0\right\rangle = \left\langle 0\left|\frac{\partial^2}{\partial a^2}\left(\sum_i \frac{1}{r_i^2}\right)\right|0\right\rangle$$
$$= \left\langle 0\left|\sum_i \frac{3a_i^2 - r_i^2}{r_i^5}\right|0\right\rangle = -0.351 \times 10^{24} \text{ cm}^{-3}$$
$$q_{yy} = q_{bb} = \left\langle 0\left|\sum_i \frac{3b_i^2 - r_i^2}{r_i^5}\right|0\right\rangle = 5.395 \times 10^{24} \text{ cm}^{-3} \tag{6}$$
$$q_{zz} = q_{cc} = \left\langle 0\left|\sum_i \frac{3c_i^2 - r_i^2}{r_i^5}\right|0\right\rangle = -5.044 \times 10^{24} \text{ cm}^{-3}$$

The electronic field gradients in eq 6 will be interpreted on the basis of the ^{14}N localized atomic orbitals. The limitations of this assumption have been discussed previously,[1,2] and we feel that this interpretation can give some insight into the bonding of the molecule. Each ^{14}N orbital will contain some fraction of two electrons. The fraction will be calculated by assuming a set of orbitals and comparing the calculated with the observed field gradients. The 2p-type atomic orbitals which are used are

$$\chi_{2p_x} = \frac{1}{\sqrt{2}}(Y_1^1 + Y_{-1}^1)\phi_{2p}(r)$$
$$\chi_{2p_y} = \frac{1}{i\sqrt{2}}(Y_1^1 + Y_{-1}^1)\phi_{2p}(r) \tag{7}$$
$$\chi_{2p_z} = Y_0^1\phi_{2p}(r)$$

$$\phi_{2p}(r) = \frac{1}{\sqrt{6}}(2\xi)^{3/2}\xi r e^{-\xi r}$$

where Y_M^1 are normalized spherical harmonics, z is perpendicular to the molecular ring, $x = a$ is the axis that bisects the NCN angle, and the y axis is parallel to the N–N bond. χ_{2s} is not needed as spherically symmetric orbitals do not contribute to the field gradient. Using the orbitals in eq 7 and the operators in eq 6, the values of the necessary nonzero field gradient matrix elements are calculated to be

$$\left\langle \chi_{2p_x}\left|\left(\frac{q_{zz}}{e}\right)\right|\chi_{2p_x}\right\rangle = \frac{4}{5}\left(\frac{1}{r^3}\right)_{av}$$
$$\left\langle \chi_{2p_y}\left|\left(\frac{q_{zz}}{e}\right)\right|\chi_{2p_y}\right\rangle = -\frac{1}{2}\left[\frac{4}{5}\left(\frac{1}{r^3}\right)_{av}\right] \tag{8}$$
$$\left\langle \chi_{2p_z}\left|\left(\frac{q_{zz}}{e}\right)\right|\chi_{2p_z}\right\rangle = -\frac{1}{2}\left[\frac{4}{5}\left(\frac{1}{r^3}\right)_{av}\right]$$

where cyclic permutations of x, y, and z give all other values. If we assume the free atom value of $(1/r^3)_{av}$

$$\left(\frac{1}{r^3}\right)_{av}^{^{14}N} = 16.6 \times 10^{24} \text{ cm}^{-3} \tag{9}$$

orbitals can now be suggested and interpreted in light of their ability to reproduce the experimental field gradients.

Unhybridized Orbitals. The functions for the unhybridized model are given in Table III.

Table III: Unhybridized Functions

Function	No. of electrons in orbital
χ_{2s}	2.0 (lone pair)
χ_{2p_x}	n_x
χ_{2p_y}	1.0
χ_{2p_z}	n_z

Our assumption in this case is that two electrons do not enter the bonding schemes and remain isolated in the 2s orbital. We also assume that one electron from a nitrogen atom enters into a σ bond with the neighboring nitrogen atom. Letting $A = {}^4/_5(1/r^3)_{av}$ we can now obtain the field gradients in terms of the number of electrons in the $2p_x(n_x)$ and $2p_z(n_z)$ orbitals.

$$q_{xx} = -{}^1/_2 n_z A - {}^1/_2 A + n_x A = -0.351 \times 10^{24} \text{ cm}^{-3}$$
$$q_{yy} = -{}^1/_2 n_z A + A - {}^1/_2 n_x A = 5.395 \times 10^{24} \text{ cm}^{-3} \tag{10}$$

(11) H. Basch, M. F. Robin, N. A. Kuebler, C. Baker, and D. W. Turner, *J. Chem. Phys.*, **51**, 52 (1969).

(12) C. H. Townes and A. L. Schawlow, "Microwave Spectroscopy," McGraw-Hill, New York, N. Y., 1955.

$$q_{zz} = n_z A - {}^1/_2 - {}^1/_2 n_x A = -5.044 \times 10^{24}\ \text{cm}^{-3}$$

Since only two of the nuclear quadrupole coupling constants are independent, we need only two of these equations to solve for n_x and n_z. The third can be used as a check of the results. Combining the equations in eq 10 gives

$$\begin{aligned} n_z &= -0.53 \\ n_x &= -0.71 \end{aligned} \tag{11}$$

These results indicate that there is a depletion of electrons on the nitrogen atom and that the methylene group of the molecule must have a relative negative charge. In light of what is known about the molecule this distribution seems highly unlikely.[13]

Walsh Orbitals. The Walsh picture is obtained by taking linear combinations of the hydrogenlike orbitals of Table III. The results are shown in Tables IV and V.

Table IV: Walsh Orbitals, sp Hybrids

Function	No. of electrons in orbital
$\psi_1 = \frac{1}{\sqrt{2}}\chi_{2s} + \frac{1}{\sqrt{2}}\chi_{2p_y}$	2
$\psi_2 = \frac{1}{\sqrt{2}}\chi_{2s} - \frac{1}{\sqrt{2}}\chi_{2p_y}$	1
$\psi_3 = \chi_{2p_z}$	n_z
$\psi_4 = \chi_{2p_x}$	n_x

Table V: sp^2 Walsh Bonding Scheme

Function	No. of electrons in orbital
$\psi_1 = \frac{1}{\sqrt{3}}\chi_{2s} - \frac{1}{\sqrt{6}}\chi_{2p_x} + \frac{1}{\sqrt{2}}\chi_{2p_y}$	2 (lone pair)
$\psi_2 = \frac{1}{\sqrt{3}}\chi_{2s} - \frac{1}{\sqrt{6}}\chi_{2p_x} - \frac{1}{\sqrt{2}}\chi_{2p_y}$	1
$\psi_3 = \chi_{2p_z}$	n_z
$\psi_4 = \frac{1}{\sqrt{3}}\chi_{2s} + \sqrt{\frac{2}{3}}\chi_{2p_x}$	n_4

Referring to Table IV two electrons have been placed into a lone-pair sp orbital pointing away from the N atom in a line with the N–N bond. One electron has also been placed in the sp hybrid σ bond pointing toward the other nitrogen atom. The number of electrons in the other two orbitals is allowed to vary. Proceeding as before the following equations are obtained.

$$\begin{aligned} q_{xx} &= -{}^1/_2 A - {}^1/_4 A - {}^1/_2 n_z A + n_x A = -0.351 \times 10^{24}\ \text{cm}^{-3} \\ q_{yy} &= A + {}^1/_2 A - {}^1/_2 n_z A - {}^1/_2 n_x A = 5.396 \times 10^{24}\ \text{cm}^{-3} \\ q_{zz} &= {}^1/_2 A - {}^1/_4 A + n_z A - {}^1/_2 n_x A = -5.044 \times 10^{24}\ \text{cm}^{-3} \end{aligned} \tag{12}$$

Solving these equations gives

$$\begin{aligned} n_z &= 0.98 \\ n_x &= 1.21 \end{aligned} \tag{13}$$

indicating a normal nitrogen–nitrogen double bond and a slightly polarized nitrogen–carbon bond with the methylene group, slightly positive. Note that these results are contradictory to those of eq 11. The possibility of using sp^2 hybrid orbitals is now considered. The orbitals are listed in Table V.

In this case the bonding is described by an sp^2 hybrid system in the plane of the molecule with ψ_4 parallel to the a axis. ψ_3 is perpendicular to this plane. Again a lone pair of electrons is assumed in ψ_1, the orbital pointing away from the ring and a single electron is placed in ψ_2 for σ bonding to the adjacent nitrogen. Proceeding as before gives

$$\begin{aligned} n_z &= 0.94 \\ n_4 &= 1.02 \end{aligned} \tag{14}$$

The results should be compared to eq 13 for the sp model. The results in eq 14 demonstrate a bonding scheme in which there is negligible polarization of bonds (this is unlikely).

It appears that the results in eq 12 and 13 give the best description of the ^{14}N field gradients and bonding in diazirine. These orbitals appear to have the expected polarity in the C–N bonds as well as indicating a N–N double bond.

It is interesting to note that in both previous calculations of this type (see ref 1 and 2) the electron configuration that most accurately fits the observed electronic field gradients, showed the sp^2 Walsh system to be best, with the sp^2 system perpendicular to the molecular ring. The models also predict polarized bonds in ethyleneimine and ethylene sulfide. Our sp^2 Walsh model is different, in that it contains the sp^2 system in the plane of the molecule and exhibits a small polarization of the proposed bonds to match the observed ^{14}N field gradients. Larger polarization of the bonds is obtained with the sp model.

In summary, we have measured the ^{14}N quadrupole

(13) See measurement of the sign of the electric dipole moment in cyclopropene in R. C. Benson and W. H. Flygare, *J. Chem. Phys.*, 51, 3087 (1969).

coupling constants in diazirine and we have tried to fit the ^{14}N field gradients with sets of localized orbitals. Walsh orbitals having sp orbitals in the plane of the ring (one pointing away from the N and containing a lone pair of electrons; the other entering into a C–N σ bond) have been used with unhybridized p_z and p_y orbitals to describe the ^{14}N field gradients.

Acknowledgment. The support of the National Science Foundation is gratefully acknowledged.

Solid State Reaction Kinetics. III. The Calculation of Rate Constants of Decomposition for a Melting System Undergoing Volume and Surface Changes

by Ernest A. Dorko* and Robert W. Crossley

Department of Aero-Mechanical Engineering, Air Force Institute of Technology, Wright-Patterson Air Force Base, Ohio 45433 *(Received June 29, 1971)*

Publication costs assisted by the Air Force Institute of Technology

A new physical and mathematical model for autocatalytic decomposition of a solid which undergoes melting is described. The object of the new model is to allow the entire reaction to be described by one set of kinetic parameters. The model includes a time variant parameter, μ, which incorporates spatial distribution of reactants and products in the sensible region, reaction surface distribution, and phase, as well as total material loss. The mathematical manipulations and numerical operations performed to obtain values of μ and the kinetic parameters are presented. A computer program employing a grid search technique to determine Arrhenius activation parameters over short temperature ranges was also developed for use with the decomposition data. From the results of this program it is possible to distinguish regions of the reaction which are controlled by a single mechanism from those which are influenced significantly by competing mechanisms.

Introduction

The utilization of the differential scanning calorimeter operated in the isothermal mode to determine the decomposition history of organic materials which are initially in the solid state has been reported previously.[1a] The computer reduction of the data and the calculation of refined autocatalytic rate constants by a computer has also been described.[1b] In previous work,[1] a sigmoid decomposition history was demonstrated for the cupferron–tosylate system. It was concluded that the decomposition was autocatalytic. The factor contributing most significantly to the autocatalytic or sigmoid decomposition behavior was felt to be liquefaction. However, the kinetic analysis of the mechanism was based on the nondimensionalized parameters, reactant fraction, and product fraction. It was found that a correlation based on the Bernoulli differential equation could be made for this system that was analogous to the Prout–Tompkins[2,3] analysis for a system decomposing completely in the solid phase. Also analogous to solid phase decomposition, a change in kinetic parameters was noted at *ca.* 50% reaction.[4]

The present report describes analytical work related to a more comprehensive physical model than considered previously. The object of using the new model is to allow the entire reaction to be described by one set of kinetic parameters. The physical model is discussed in the next section, and the resulting differential equation is presented. Then, the derivation and numerical processing of the equations which make up the mathematical model is described. Finally, a method for finding Arrhenius parameters for the rate constants is presented.

The detailed application of the mathematical techniques described herein to specific systems will be reported subsequently.

Development of Physical Model

The physical model with which data are to be com-

(1) (a) E. A. Dorko, R. S. Hughes, and C. R. Downs, *Anal. Chem.*, **42**, 253 (1970); (b) R. W. Crossley, E. A. Dorko, and R. L. Diggs, "Analytical Calorimetry," Vol. 2, R. S. Porter and J. F. Johnson, Ed., Plenum Publishing Co., New York, N. Y., 1970, pp 429–440.

(2) E. G. Prout and F. C. Tompkins, *Trans. Faraday Soc.*, **40**, 488 (1944).

(3) D. A. Young, "The International Encyclopedia of Physical Chemistry and Chemical Physics," Vol. 1, Pergamon Press, New York, N. Y., 1966, p 49.

(4) L. G. Harrison, "Comprehensive Chemical Kinetics," Vol. 2, C. H. Bamford and C. F. H. Tipper, Ed., Elsevier, Amsterdam, 1969, p 395.

pared was extended from the work of Dubovitskii, Manelis, and Merzhanov.[5] These authors do not state explicitly their assumptions, but they appear to consider the disappearance of an extensive property of a specie to be proportional to some function of that property and functions of intensive properties of other species involved in the reaction. As applied to the present analysis, the model is (rate of disappearance of moles of reactant) $\sim$ (moles of reactant) + (mole fraction of condensed product X moles of reactant) or

$$-\frac{dA}{dt} = k_1A + k_2C_BA \tag{1}$$

Equation 1 is appropriate to systems in which mass may disappear from the experimental region of measurement by escape of gaseous products and in which the spatial distribution of the mass remaining in the experimental region may vary throughout the experimental time, *e.g.*, by such occurrences as melting, macroscopic particle shattering, and coalescence.

To bring eq 1 into a nondimensional form that is applicable to the experimental data, it is normalized with respect to the initial amount of reactant, A_0; the density of reactants plus condensed product is assumed constant; and C_B is recognized as

$$C_B = \frac{B}{A + B} \tag{2}$$

where B represents the moles of condensed product. B is expressed as

$$B = \frac{v}{v_0}(A_0 - A) = (1 - \mu)(A_0 - A) \tag{3}$$

where

$$\mu \equiv \frac{v_0 - v}{v_0} \tag{4}$$

v_0 is the initial volume of reactant, and v is a variable in time. Inserting eq 2 and 3 into eq 1 yields

$$-\frac{d(A/A_0)}{dt} \equiv -\frac{da}{dt} \equiv -\dot{a} = k_1a + k_2\frac{(1 - \mu)(1 - a)a}{1 - \mu(1 - a)} \tag{5}$$

Equation 5 is formally identical with eq 3 of ref 5a. However, the latter was derived assuming the amount of material departing the experimental region is proportional to the extent of reaction, and the μ there is defined as

$$\mu \equiv \frac{v_0 - v_f}{v_0} \tag{6}$$

where v_f is the final volume of condensed products. The μ of eq 6 is a constant related only to the total material loss. It would be determined by measuring the initial mass of reactant and final mass of condensible product. In contrast, the μ of eq 4 is based on the "effective volume" of reactants plus condensable products at each instant during reaction. This μ functions as a parameter incorporating spatial distribution of reactants and products in the sensible region, reaction surface distribution and phase, as well as total mass loss.

There would appear to be no way to measure μ of eq 4 experimentally; happily, its role is not to be measured. It is intended to serve as a parameter, variable throughout the reaction, that absorbs the nonchemical influences on the reaction rate. If successful, the rate constants, k_1 and k_2, will truly represent only chemical effects as they are intended to do. The method of determining μ in conjunction with the determination of k_1 and k_2 in eq 5 is presented in the next section.

Mathematical Analysis of Physical Parameters

The mathematical analysis of eq 5 to find k_1, k_2, and μ depends on experimental data giving the remaining reactant fraction, a, at each time throughout the reaction period. The method of processing the experimental data has been described previously[1b] and is incorporated in a computer program[6] dealing with the solution of eq 5. The program is able to calculate rate constants under the assumption of no mass loss ($\mu = 0$), measured total mass loss (μ constant as determined by eq 6), and parametric μ (eq 4). The analysis of the last case will be discussed next. Then, the specializations of that case to obtain the first two will be mentioned briefly.

The solution for the case of parametric μ at a fixed point in time consists of the successive solution of three simultaneous transcendental equations. These are derived as follows. First, eq 5, is rearranged algebraically to give

$$K \equiv \frac{k_1}{k_2} = \frac{k_1(1 - \mu)(1 - a)}{\left(-k_1 - \frac{\dot{a}}{a}\right)[1 - \mu(1 - a)]} \tag{7}$$

Next, eq 5 is integrated to give

$$(k_1 + k_2)t = \frac{k_2}{k_2(1 - \mu) - \mu k_1} \times \ln\left(1 + \frac{k_2(1 - \mu) - \mu k_1}{k_1}(1 - a)\right) - \ln a \tag{8}$$

In integrating eq 5 to obtain eq 7, μ is held constant. The underlying condition is that μ remain essentially constant relative to a over each time range of integration. This must be justified by the results in each ap-

(5) (a) F. I. Dubovitskii, G. B. Manelis, and A. G. Merzhanov, *Dokl. Akad. Nauk SSSR*, **121**, 549 (1958); (b) G. B. Manelis and F. I. Dubovitskii, *ibid.*, **124**, 475 (1959).

(6) This program which is a modification of program PARACT (QCPE No. 168, Quantum Chemistry Program Exchange, Bloomington, Ind.) is available on request from the authors.

plication of the analysis. Various forms of eq 5, including eq 7 and 9

$$k_2(1 - \mu) - \mu k_1 = \left(-k_1 - \frac{\dot{a}}{a}[1 - \mu(1 - a)]\right)\frac{1}{1 - a} \quad (9)$$

are inserted in eq 8 to eliminate k_2. The result after extensive algebraic manipulation is

$$k = \frac{1 - a}{at}\left(1 + \frac{k_1\mu(1 - a)}{-k_1 - \frac{\dot{a}}{a}[1 - \mu(1 - a)]}\right) \times \ln\left(\frac{k_1}{-\frac{\dot{a}}{a}[1 - \mu(1 - a)]a^{\mu Z - 1}}\right) - \frac{\dot{a}}{a^2}[1 - \mu(1 - a)] \quad (10)$$

where

$$Z \equiv 1 + \frac{k_1(1 - \mu)(1 - a)}{\left(-k_1 - \frac{\dot{a}}{a}\right)[1 - \mu(1 - a)]}$$

Finally, eq 5 is differentiated with respect to t. When $\ddot{a}$ is equated to zero and the resulting expression is rearranged, the result is

$$\mu = \frac{1 - \mu}{a_{max}}\left(\frac{1}{\sqrt{1 - \mu(1 + K)}} - 1\right) \quad (11)$$

where a_{max} is the value of time at which $\ddot{a} = 0$ (or $\dot{a}$ achieves its maximum). In deriving eq 11, μ was again held constant. The implication is that $d\mu/dt$ is negligible compared to $\dot{a}_{max}$. This also must be justified for specific applications.

The three equations to be solved are now eq 7, 10, and 11. The solution is started by numerically iterating eq 10 for k_1 with $\mu = 0$. Then, eq 7 is solved for an initial K, and eq 11 is numerically iterated for an initial nonzero μ. Equation 10 is then reiterated for k_1 with the nonzero μ. The cycle is repeated until the specified trial-to-trial agreements of k_1 and μ are obtained. Finally, k_2 can be obtained from the definition of K if desired.

When μ is a constant determined by eq 6 or an assumed constant (zero or nonzero), the solution of eq 7, 10, and 11 is much easier. Equation 11 becomes superfluous. Equation 10 is iterated with the specified value of μ until satisfactory trial-to-trial agreement of k_1 is achieved. Finally, k_2 is calculated once by eq 7.

Two final comments are in order in closing this section. First, the value of a_{max} used in the iteration is obtained directly from the experimental data and is thus an independent quantity in the iteration for k_1 and μ. Second, neither the particular forms of equations presented nor the order of iteration is unique. They have been chosen to obtain rapid convergence and to treat k_1 explicitly. This is necessary because k_1 is expected to be relatively small and sensitive to empirical or numerical uncertainties.

Calculation and Interpretation of Arrhenius Parameters

When the rate constants *vs.* time have been calculated, it is found that, at least within certain time periods during the reaction, they are essentially constant. When the rate constants in related regions have been calculated over a temperature range, it is desirable to express them in Arrhenius form. It has been the authors' experience[1] in working with compounds that decompose during melting that only small temperature ranges are possible and not insignificant scatter is probably unavoidable. Therefore, a grid search technique[7] to determine Arrhenius parameters for both the exponential, eq 12, and logarithmic (or linearized), eq 13, forms has been developed

$$S_{exp} = \sum_{i=1}^{N}(k_i - Ae^{-E_a/RT_i})^2 \quad (12)$$

$$S_{ln} = \sum_{i=1}^{N}\left(\ln k_i - \ln A + \frac{E_a}{RT_i}\right)^2 \quad (13)$$

Use of eq 12 implies that absolute errors are assumed equal, and use of eq 13 implies that relative errors are assumed equal. Neither case is demonstrably more realistic in the present situation, and the object of using both is to delineate cases of agreement or disagreement to gain insight into the underlying physical processes.

The grid search technique was developed to calculate the parameters efficiently and accurately and to obtain quantitative estimates of the uncertainties involved. The program prints S_{exp} and S_{ln} throughout a selected region of the (A,E_a) plane. Final minimum values on the S surfaces are found by constricting the search region around the last calculated minimum values. When the minimum values have been determined, absolute and relative errors and confidence limits are calculated based on the minima of S_{exp} and S_{ln} and the F statistic.[8] The ranges of the Arrhenius parameters corresponding to the calculated confidence limits can then be found by examining the sums of squares printed during the iteration process. The more data and the less scatter in it, the smaller will be the region of the S surface surrounding the minimum for a specified confidence level. The lower the confidence levels associated with either S_{exp} or S_{ln} which enclose the minimum of the other, the less sensitive are the results to details of the analysis.

(7) R. W. Crossley and E. A. Dorko, program ACTEN (QCPE No. 179, available from the Quantum Chemistry Program Exchange, Indiana University, Bloomington, Ind.).

(8) R. S. Burington and D. C. May, "Handbook of Probability and Statistics," Handbook Publishers, Inc., Sandusky, Ohio, 1958, p 158.

Finally, and of particular importance, if the analysis gives differences in the locations of $S_{\exp_{\min}}$ and $S_{\ln_{\min}}$ for a particular rate constant that are significantly greater than for the other rate constants, the "bad" rate constant can be given special attention. This should be directed two ways: to the details of determining the rate constant and to the implications of the poor result on the kinetic model itself.

Stability of the Extended Nernst–Planck Equations in the Description of Hyperfiltration through Ion-Exchange Membranes[1]

by Lawrence Dresner

Chemistry Division, Oak Ridge National Laboratory, Oak Ridge, Tennessee 37830 *(Received January 25, 1972)*

Publication costs assisted by Oak Ridge National Laboratories

Some mathematical questions are discussed which arise when the extended Nernst–Planck equations are used to describe hyperfiltration (reverse osmosis) through ion-exchange membranes. These questions concern the stability of the extended Nernst–Planck equations. A simple means of calculating ionic rejections in the limits of infinite membrane thickness or infinite water flux has been suggested. Circumstances have been identified under which a particular one of the counterions may be completely rejected. Other circumstances have been identified under which some counterions may be negatively rejected. An experiment is quoted exhibiting both of these phenomena.

1. Introduction and Historical Review

A number of authors have used the Nernst–Planck equations, extended to include convection, to describe ionic transport in ion exchangers.[2] In this paper, these extended Nernst–Planck equations (ENPE) are used to describe hyperfiltration (reverse osmosis) through ion-exchange membranes. The ENPE are highly nonlinear equations, the nonlinearity being caused by the electrical coupling of the various ionic fluxes.[3] Because of this nonlinearity, the solutions of the ENPE that describe hyperfiltration have some interesting properties. While it is difficult to discuss these properties without first laying a proper foundation, the brief summary of them given below may give the reader a foretaste of what this paper contains.

There are two different kinds of solutions of the ENPE; which one we get depends on the composition of the feed solution. They are distinguishable by their behavior in the limit of infinite membrane thickness. The limiting behavior of the first kind of solution may be calculated easily from certain algebraic equations related to the ENPE, but the limiting behavior of the second kind cannot. In the limit of infinite membrane thickness, there is *complete rejection* of a particular one of the counterions from any feed which leads to a solution of the second kind. Finally, under certain circumstances solutions of the first kind exhibit negative rejection of one or more of the counterions. (Negative rejection means that the effluent solution is more concentrated in the particular ion than the feed.) An example is discussed in which both of the latter phenomena have been observed.

Schlögl[2a] and Hoffer and Kedem[4] have solved the

(1) Research supported by the National Science Foundation-RANN under Union Carbide Corp. contract with the U. S. Atomic Energy Commission.

(2) (a) R. Schlögl, "Stofftransport durch Membranen," Dr. Dietrich Steinkopff Verlag, Darmstadt, 1964; (b) F. Helfferich, "Ion Exchange," McGraw-Hill, New York, N. Y., 1962.

(3) The reader may be aided in seeing this by noting that ϵ is a function of the ionic concentrations. If we multiply eq 1 by $z_i/\mathfrak{D}_i$, sum, and use eq 2 to show that $d\left(\sum_{i=1}^{N} z_i c_i\right)\Big/dx = 0$, we find

$$\epsilon = \sum_{i=1}^{N} \frac{z_i}{\mathfrak{D}_i}(j_i - \beta_i c_i J)\Big/\sum_{i=1}^{N} z_i^2 c_i \qquad \text{(A)}$$

Substituting (A) into (1) we have

$$\mathfrak{D}_i \frac{dc_i}{dx} = -j_i + \beta_i c_i J + z_i c_i \mathfrak{D}_i\left(\sum_{k=1}^{N} \frac{z_k}{\mathfrak{D}_k}(j_k - \beta_k c_k J)\Big/\sum_{k=1}^{N} z_k^2 c_k\right) \qquad \text{(B)}$$

(B) shows that the dc_i/dx are uniquely determined by the c_i. This means that for given j_i and J, there is one and only one solution of the ENPE having given values of c_i at some given value of x (uniqueness theorem).

(4) E. Hoffer and O. Kedem, *Desalination*, 2, 25 (1967).

only problem of hyperfiltration for which a solution of the ENPE is known in closed form: the problem of hyperfiltration of a two-component feed ("two-component" means water plus one binary electrolyte). Their solution is of the first kind mentioned above; for, as we shall see later (section 7), solutions of the second kind are possible only when there are three or more different kinds of ions present in the feed. Consequently, these earlier authors did not discover the solution of the second kind and the complete rejection associated with it.

In an earlier paper,[5] I found an *approximate* solution of the ENPE, which turns out to be an approximate form of the solution of the second kind. From this approximate solution, I recognized the possibility of complete rejection that is associated with solutions of the second kind in the present paper. The conclusions of the earlier paper imply those of the present paper regarding solutions of the second kind and more. The additional conclusions of the earlier paper were due to the restrictive assumption of good coion exclusion from the membrane, an assumption that is dropped in the present paper. The earlier paper is discussed further in section 9.

Hoffer and Kedem[4] observed that the explicit solution of the two-component problem permitted negative rejection of the solute. This negative rejection is different from that pointed out here; for, most simply, Hoffer and Kedem's negative rejection occurs for feeds *sufficiently concentrated* in the solute, that discussed here for feeds that are *sufficiently dilute* (see section 9).

2. Hyperfiltration[6]

Hyperfiltration is one of many possible membrane processes involving ionic transport. In all membrane processes, a membrane—always an ion-exchange membrane in this paper—separates two ionic solutions. Water and ions are transported through the membrane as the result of differences between the two solutions in composition, electrical potential, and pressure. The various processes are distinguished from one another by such things as what driving force is externally applied, what the compositions of the two solutions are, and whether an electric current flows or not. For conceptual simplicity, both solutions are usually taken to be infinitely well stirred so that concentration polarization at the membrane surfaces can be ignored.

In hyperfiltration, pressure is the externally applied driving force, no electric current flows, and all the ionic fluxes are in the same direction as the flux of water. When all the ionic fluxes are in the same direction as the flux of water, we can speak of the transported mixture. In hyperfiltration, the composition of the low-pressure solution, into which all the fluxes are directed, is the same as that of the transported mixture. The composition of the high-pressure solution (feed) can be specified arbitrarily.

Hyperfiltration is intended as a process to remove dissolved ions from brackish natural waters or industrial waste waters. What we should like to know is how the composition of the transported mixture (effluent solution) depends on the composition of the feed, the applied pressure, and the properties of the membrane. To get an idea, we try to describe hyperfiltration using the ENPE.

3. The Extended Nernst–Planck Equations

The ENPE can be written (see Appendix C for glossary of symbols)

$$j_i = \beta_i c_i J - \mathfrak{D}_i \frac{dc_i}{dx} + z_i c_i \mathfrak{D}_i \epsilon \quad (i = 1, \ldots, N) \quad (1)$$

j_i is the flux of the ith kind of ion through the membrane. In the steady state, it is independent of x, as we can see from the equation of continuity for the ith ion: $\partial c_i/\partial t + \partial j_i/\partial x = 0$. The right-hand side expresses j_i as the sum of contributions from convection, diffusion, and migration in the electric field. The convective contribution (first on the right) is slightly more general than that used by earlier authors owing to the inclusion of convective coupling coefficients (β_i).[5,6] Earlier authors, influenced by the Teorell–Meyer–Sievers model of ion exchangers,[7] treated the mobile ions in the wet membrane as though they were dissolved in the interstitial water. If this were so, the β_i would equal unity. The possibility exists, however, that in pure convection the ions might not be swept along with the same velocity as the water. For example, if there were transitory binding of the counterions by the fixed charges, the instantaneous concentration of *mobile* counterions would be less than the total concentration of counterions, and convection would be reduced. Thus β_i for counterions would be <1. Another kind of effect could occur in a porous ion-exchange membrane in which the pore diameter is comparable with the thickness of the electrical double layer. The mobile counterions would be concentrated near the charged walls of the pores where the water flow velocity is below average, while the coions would be concentrated away from the walls where the water flow velocity is above average. Thus β_i for the counterions would be <1, while β_i for coions would be >1.

To integrate the ENPE, we assume that the convective coupling coefficients β_i and the diffusion coefficients $\mathfrak{D}_i$ are constants independent of the ionic concentrations. This assumption applies as well to all activity coefficients. These are the same assumptions

(5) L. Dresner, *Desalination.*, **10**, 27 (1972).

(6) A general discussion of hyperfiltration may be found in J. S. Johnson, L. Dresner, and K. A. Kraus, "Principles of Desalination," K. S. Spiegler, Ed., Academic Press, New York, N. Y., 1966, Chapter 8.

(7) T. Teorell, *Proc. Soc. Exp. Biol. Med.*, **33**, 282 (1935); *Trans. Faraday Soc.*, **33**, 1053, 1086 (1937); K. H. Meyer and J. F. Sievers, *Helv. Chim. Acta*, **19**, 649 (1936).

made by earlier authors, for whom $\beta_i = 1$ as well. Thus the conclusions of this paper apply *a fortiori* to their earlier, less general version of the ENPE.

In addition to eq 1, we have the equation of electroneutrality in the membrane

$$\sum_{i=1}^{N} z_i c_i + qX = 0 \tag{2}$$

Equations 1 and 2 together determine the variation of the ionic concentrations c_i and the electric field across the membrane. At each solution–membrane interface, we apply the condition of membrane equilibrium to match the ionic concentrations just inside the membrane to those just outside the membrane. That is to say, if we pass from a point just inside the membrane (but outside any double layer formed at the interface) to a point just outside the membrane (and again outside any double layer), we pass through a succession of thermodynamic states that are all in equilibrium with one another. The conditions of thermodynamic equilibrium at each solution–membrane interface can be written

$$\frac{c_i\gamma_i}{c_{i(s)}\gamma_{i(s)}} = \exp\left(-z_i\frac{F\Delta\phi}{RT} - \frac{\Delta\mu_i^{(0)}}{RT}\right) \tag{3}$$

Here $\Delta\phi$ is the difference in electrical potential between a point just inside the membrane and the contacting solution (Donnan potential), $\Delta\mu_i^{(0)}$ is the difference between the chemical potential of the ith kind of ion in its standard state inside the membrane and the chemical potential of the ith kind of ion in its standard state in the contacting solution, and γ_i and $\gamma_{i(s)}$ are the respective ionic activity coefficients. (Use of the ENPE to describe ionic transport tacitly implies the constancy of γ_i in the membrane phase, an assumption that we note here explicitly.) Equations 2 and 3, together with the equation of electroneutrality in the external solution

$$\sum_{i=1}^{N} z_i c_{i(s)} = 0 \tag{4}$$

determine the ionic concentrations and the electrical potential just inside the solution–membrane interface in terms of those in the solution, and conversely. It will be convenient in what follows to call internal and external solutions in membrane equilibrium with each other *conjugates* of each other.

4. Preliminary Considerations

As noted before, in hyperfiltration the composition of the effluent solution is that of the transported mixture

$$(c_i)_{\text{effluent solution}} = \frac{j_i}{J} \tag{5}$$

If we choose an effluent solution, eq 3 determines the ionic concentrations just inside the membrane at the effluent–membrane interface. If we choose a water flux J, eq 5 determines the j_i, and we then have enough information to integrate eq 1 and 2 through the membrane.[3] This is not the case if we choose the feed composition, because although eq 3 gives us initial concentrations at the feed–membrane interface, we have no way of determining the ionic fluxes j_i. Thus direct solution of eq 1 and 2 by finite differences must proceed by advancing from the effluent to the feed.

I have carried out a number of such calculations, and I always found that when I integrated far enough into the membrane from the effluent–membrane interface, the ionic concentrations c_i and the electric field ϵ approached constancy. The distance into the membrane at which constant limits are approached is of the order of magnitude of $\mathfrak{D}_i/J$, as is clear from dimensional considerations. When such constant limits exist, they, too, are solutions of eq 1 and 2. But since they are constant (*i.e.*, independent of x), when they are inserted into eq 1 the derivatives vanish identically. The limiting concentrations can thus be calculated by dropping the terms in eq 1 in dc_i/dx and solving the resulting *algebraic* equations (henceforth called the algebraic ENPE) for the c_i.

In the next section I show rigorously that for each given set of $j_i/J > 0$ there is one and only one constant solution of eq 1 and 2 for which all the c_i are positive. In Appendix A, I show that *any* solution of eq 1 and 2 corresponding to the same set of j_i/J approaches this constant solution if we advance far enough *in the direction opposite to the fluxes*. In mathematical language, I prove that for any set of $j_i/J > 0$, eq 1 and 2 have one and only one equilibrium point for which all the c_i are positive, and it is asymptotically stable in the large.

These two theorems actually refer to membrane processes less restricted than hyperfiltration. The only assumption we make concerning the process is that all the fluxes be in the same direction, *i.e.*, $j_i/J > 0$. We do not use the hyperfiltration condition (eq 5), which equates the composition of the bath into which the fluxes are directed with that of the transported mixture, nor do we use the condition that no electric current flows.

5. Equilibrium Points

An equilibrium point of eq 1 and 2 is a solution for which $dc_i/dx = 0$, *i.e.*, a constant solution. We denote the ionic concentrations at an equilibrium point by $c_i^{(0)}$. From eq 1 it follows that

$$c_i^{(0)} = \frac{(j_i/Jz_i\mathfrak{D}_i)}{\eta^{(0)} + \beta_i/z_i\mathfrak{D}_i} \tag{6}$$

where for convenience we have introduced the symbol $\eta^{(0)} = \epsilon^{(0)}/J$. The equilibrium concentrations $c_i^{(0)}$ must obey the equation of electroneutrality (eq 2). Substituting (6) into (2), we find

$$\sum_{i=1}^{N} \frac{j_i/J\mathfrak{D}_i}{\eta^{(0)} + \beta_i/z_i\mathfrak{D}_i} = -qX \tag{7}$$

When cleared of fractions, (7) is an equation of Nth order in $\eta^{(0)}$. It has N roots corresponding to N different solutions of (1), but as we shall see, only one of these roots leads to values of $c_i^{(0)}$ that are all positive. Let us consider the left-hand side of (7) as a function $f(\eta^{(0)})$ of $\eta^{(0)}$. It has poles at the points $\eta^{(0)} = -\beta_i/z_i\mathfrak{D}_i$. Since $j_i/J > 0$, $f(\eta^{(0)})$ is negative just to the left of each pole and positive just to the right of each pole. The poles on the negative $\eta^{(0)}$ axis correspond to positive values of z_i; the poles on the positive $\eta^{(0)}$ axis correspond to negative values of z_i. A plot of $f(\eta^{(0)})$ *vs.* $\eta^{(0)}$ (which we henceforth call a pole diagram) looks like the sketch in Figure 1.

The equation $f(\eta^{(0)}) = -qX$ has one root between each pair of poles of $f(\eta^{(0)})$ and one root outside—to the left of all poles if $q = +1$; to the right of all poles if $q = -1$; for the equation has *at least* one root in each of these positions, and if it had more than one root in any of these positions it would have more than N roots.

We wish to find the root or roots for which all the $c_i^{(0)}$ are > 0. From eq 6 we see that if $c_i^{(0)}$ is to be > 0, $\eta^{(0)} + \beta_i/z_i\mathfrak{D}_i$ must have the same sign as z_i. Thus

$$\eta^{(0)} + \beta_i/z_i\mathfrak{D}_i > 0 \text{ or } \eta^{(0)} > -\beta_i/z_i\mathfrak{D}_i \text{ if } z_i > 0 \tag{8a}$$

$$\eta^{(0)} + \beta_i/z_i\mathfrak{D}_i < 0 \text{ or } \eta^{(0)} < -\beta_i/z_i\mathfrak{D}_i \text{ if } z_i < 0 \tag{8b}$$

Since the poles with positive (negative) z_i lie on the negative (positive) $\eta^{(0)}$ axis, the roots we seek must lie to the right of each pole on the negative $\eta^{(0)}$ axis and to the left of each pole on the positive $\eta^{(0)}$ axis. Thus the roots we seek must lie between the two poles that straddle the origin. There is always such a root, and furthermore there is only one such root. Hence to each choice of $j_i/J > 0$ there corresponds one and only one constant solution for which all the $c_i^{(0)}$ are > 0.

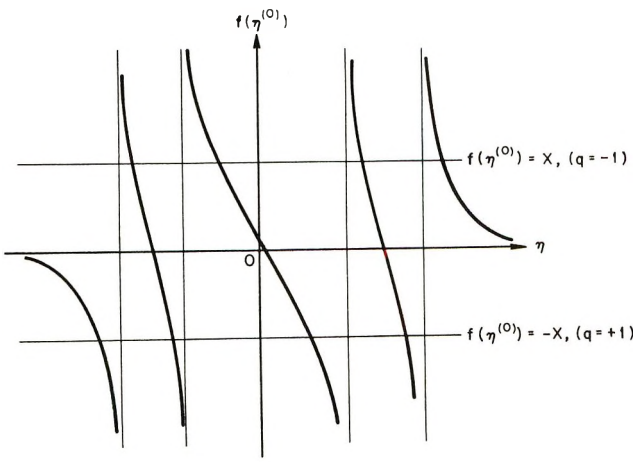

Figure 1. Sketch of a pole diagram.

6. The Method of Algebraic Equations. I

The next step in the logical development of the theory is the proof of the asymptotic stability of the equilibrium point found in the last section. However, the proof of stability is somewhat complicated, and rather than interrupt the flow of the ideas with it, it has been put in Appendix A. Granting asymptotic stability, we see that if we choose an effluent solution and integrate the ENPE away from the effluent–membrane surface far enough into the membrane, we always approach the constant solution. The importance of this fact is twofold. First, the constant solution is easy to calculate since only algebraic rather than differential equations need to be solved. Second, it provides us with information that is independent of the membrane thickness l, as we can see in the following way. The distance into the membrane we must go from the effluent–membrane interface before we approach the constant solution is of the order of magnitude of $\mathfrak{D}_i/J$, as we can see from dimensional considerations. If J is large enough, $l \gg \mathfrak{D}_i/J$, and the constant solution applies at the feed–membrane interface. We can then find the composition of the feed, which is conjugate to the constant solution, using the conditions of membrane equilibrium. Thus we have assumed an effluent and calculated the feed that produces it when J is large. Nowhere in this procedure did the actual value of l enter.

It would be even more convenient if we could invert this procedure. We would like to assume the feed, use the conditions of membrane equilibrium to calculate the concentrations $c_i^{(0)}$ of the constant solution, insert these in the algebraic ENPE, and evaluate j_i/J, the composition of the effluent in the limit of large J. Such information would be particularly useful in the study of hyperfiltration through dynamically formed ion-exchange membranes,[8] the thicknesses of which are generally not known. To carry out the solution, we multiply the algebraic form of the ENPE

$$\frac{j_i}{J} = \beta_i c_i^{(0)} + z_i c_i^{(0)} \mathfrak{D}_i \eta^{(0)} \tag{9}$$

by z_i, sum, and use eq 4 and 5 to show

$$\eta^{(0)} = -\frac{\sum_{i=1}^{N} \beta_i z_i c_i^{(0)}}{\sum_{i=1}^{N} z_i^2 c_i^{(0)} \mathfrak{D}_i} \tag{10}$$

(8) A. E. Marcinkowsky, K. A. Kraus, H. O. Phillips, J. S. Johnson, and A. J. Shor, *J. Amer. Chem. Soc.*, **88**, 5744 (1966); K. A. Kraus, H. O. Phillips, A. E. Marcinkowsky, J. S. Johnson, and A. J. Shor, *Desalination*, **1**, 225 (1966); A. J. Shor, K. A. Kraus, W. T. Smith, and J. S. Johnson, *J. Phys. Chem.*, **72**, 2200 (1968); J. R. Fryer, J. L. Hutchison, and R. Paterson, *J. Colloid Interface Sci.*, **34** (2), 238 (1970); K. A. Kraus, A. J. Shor, and J. S. Johnson, *Desalination*, **2**, 243 (1967); H. C. Savage, N. E. Bolton, H. O. Phillips, K. A. Kraus, and J. S. Johnson, *Water Sewage Works*, **116**, 102 (1969); J. J. Perona, F. H. Butt, S. M. Fleming, S. T. Mayr, R. A. Spitz, M. K. Brown, H. D. Cochran, K. A. Kraus, and J. S. Johnson, *Environ. Sci. Technol.*, **1**, 991 (1967); S. B. Sachs, W. H. Baldwin, and J. S. Johnson, *Desalination*, **6**, 215 (1969).

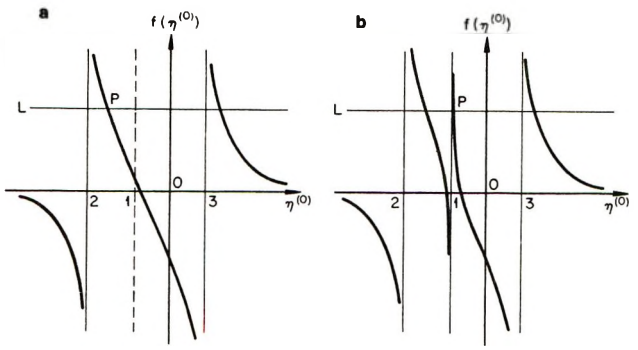

Figure 2. Pole diagram when $j_1/J = 0$ (case a) and when j_1/J is infinitesimally greater than zero (case b).

Knowing $\eta^{(0)}$ we can calculate j_i/J from (9).

It comes as a shock to learn that this inverted procedure sometimes gives absurd results, *i.e.*, sometimes gives values of j_i/J that are negative. Examples are not hard to find, but rather than demonstrate the failure of the inverted procedure by example, I present in the next section a deeper and more satisfying analysis.

7. The Region of No Constant Solution

To begin with, let us consider the special case of a feed solution that contains at most two counterions (call them 1 and 2) and one coion (call it 3). For the sake of definiteness, let us take the membrane to be a cation exchanger—the argument goes through as well for anion exchangers. Suppose further that $|\beta_1/z_1\mathfrak{D}_1| < |\beta_2/z_2\mathfrak{D}_2|$. Consider now a case in which $j_1/J = 0$, but $j_2/J \neq 0$ (j_3/J is determined by the condition of electroneutrality). The pole diagram for such a case looks like Figure 2a. The intersection P of $f(\eta^{(0)})$ with the line L: $\eta^{(0)} = -qX$ between the two poles that straddle the origin gives the value of $\eta^{(0)}$. The points marked 1, 2, and 3 designate the values $-\beta_1/z_1\mathfrak{D}_1$, $-\beta_2/z_2\mathfrak{D}_2$, and $-\beta_3/z_3\mathfrak{D}_3$ of the abscissa.

Now if we keep the value of j_2/J fixed and let j_1/J be *infinitesimally* different from zero, the pole diagram looks like Figure 2b. The value of $\eta^{(0)}$ must now lie to the right of the vertical line at point 1. This means that $\eta^{(0)}$ jumps discontinuously at $j_1/J = 0$. It follows from eq 6 that the $c_i^{(0)}$ also jumps discontinuously at $j_i/J = 0$.

It should be emphasized that such a discontinuity may, but need not necessarily, occur. For example, if point P in Figure 2a were to the right of line 1 to begin with, there would be no discontinuity. However, if j_2/J is small enough, point P in Figure 2a must lie to the left of line 1. To see this, first note that according to eq 5, if $j_1/J = 0$ (which is the case in Figure 2a), j_2/J and j_3/J are proportional. Now we can see from eq 7 that decreasing j_2/J by some given factor decreases $f(\eta^{(0)})$ by the same factor. This has the same effect on Figure 2a as if we had increased qX by the same factor, *i.e.*, as if we had raised the line L. Raising line L causes the point P to move to the left.

Finally, it should be clear that if $j_1/J \neq 0$, there is no discontinuity in $\eta^{(0)}$ or the $c_i^{(0)}$ at $j_2/J = 0$, nor can there be any discontinuity for any other values of j_1/J and j_2/J.

We can summarize the situation by making use of a plane in which the concentrations c_1 and c_2 of ions 1 and 2 are coordinates (c_3 is determined by electroneutrality). Each effluent solution, *i.e.*, each pair of values of j_1/J and j_2/J, can be plotted as a point in the first quadrant of this plane. We call such points E points. The *conjugate* of each constant solution can also be plotted as a point in this plane. We call such points F points. In section 5, we showed that every point in the first quadrant could serve as an E point, and that each E point *uniquely* determines an F point. From the above discussion, we see that the position of the F point depends continuously on the position of the E point except at the c_2 axis (where $c_1 = 0$). E points that lie on the c_2 axis have F points also on the c_2 axis, but E points infinitesimally to the right of the c_2 axis have F points a finite distance from the c_2 axis when j_2/J is small enough. Furthermore, no two E points can have the same F point. This follows at once from eq 9. For suppose that the E points j_i/J and $j_i'/J \neq j_i/J$ had the same F point. Then the two E points would have the same values of the $c_i^{(0)}$. Now, j_i/J and j_i'/J would both equal the right-hand side of eq 9. Since, by eq 10, $\eta^{(0)}$ is a unique function of the $c_i^{(0)}$, j_i/J and j_i'/J would have to be equal, contrary to supposition.

Consider now a short line segment in the first quadrant ending on a point Q on the c_2 axis. Suppose the points of this line segment are considered as E points. Each of these E points has an F point which we call its image. As we approach the c_2 axis along the line segment, the images approach a limit point Q′ whose coordinates depend on those of Q. As the point Q traverses the c_2 axis, Q′ describes a locus S (Figure 3), which for small j_2/J is removed from the c_2 axis by a finite interval.

All F points (*i.e.*, all points which are conjugate to a constant solution) must lie to one side of S. To see this consider the line EE′ in Figure 3 as a locus of E points. The images of these E points lie on a locus FF′. FF′ cannot cross S. For suppose it did at a point P. Then points on FF′ near P would be the images of points of EE′ in the neighborhood of some point E″ away from the c_2 axis as well as the images of points in the neighborhood of some point Q on the c_2 axis, a contradiction. But then all F points must lie on one side of S. If $j_2/J = 0$, it is easy to show that as $j_1/J \to \infty$, $c_1^{(0)} \to \infty$. Hence some, and therefore all, F points lie to the right of S.

These facts mean that eq 9 and 10 must fail for any set of $c_i^{(0)}$ whose conjugate lies in the region between the c_2 axis and the curve S. For if they did not fail, the j_i/J they determine would be an E point, the F

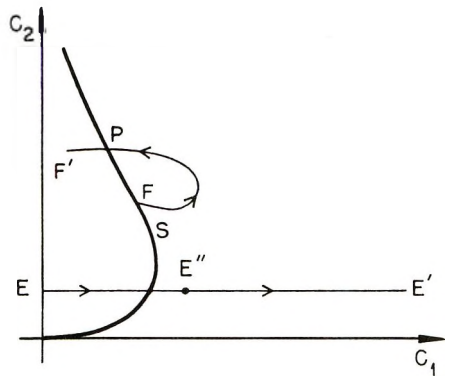

Figure 3. Sketch showing the locus S.

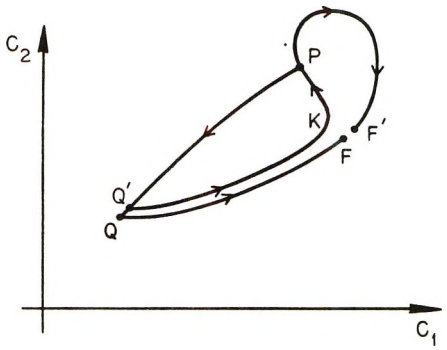

Figure 4. Sketch showing the effluent locus of P and the feed loci of Q and Q'.

point of which would lie to the left of S. This we have just seen is impossible. As mentioned before, the manner in which eq 9 and 10 fail is that one or more of the j_i/J are negative. We call the region between the c_2 axis and the curve S the region of no constant solution.

8. The Method of Algebraic Equations. II

We now return to a more rigorous discussion of the method of algebraic equations than that presented in section 6. Suppose we choose as feed a solution corresponding to a point P in the (c_1,c_2) plane lying to the right of curve S. Thus P can be an F point. Each thickness x of the membrane determines a pair of values j_1/J and j_2/J, *i.e.*, an effluent solution. As x increases from zero, the point corresponding to the effluent solution traces out a locus (curve PQ'Q in Figure 4). We call this locus the effluent locus of the feed P. We *assume* that as the membrane thickness approaches infinity, the composition of the effluent solution approaches a limiting composition corresponding to the point Q, which then becomes the end point of the effluent locus of P. The method of algebraic equations is based on the contention that P is the image (F point) of Q.

To prove this contention, let us suppose that another point F lying a finite distance from P is the image of Q. The line QF represents the locus of feeds that could produce Q as effluent; the membrane thickness increases from Q to F. We call QF the feed locus of the effluent Q. Consider now a point Q' near Q on the effluent locus PQ. It represents the effluent that would be produced from the feed P with a membrane of thickness x'. Let us consider the feed locus of Q'. We begin by proving that if Q' is close to Q, the feed locus of Q' is close to the feed locus of Q, at least for x not too large. For eq B (ref 3) shows that dc_i/dx is a continuous function of the j_i/J and c_i. At the effluent–membrane interface, the c_i are determined by the j_i/J through the conditions of membrane equilibrium (*i.e.*, they are conjugate). Because the values of the j_i/J for Q and Q' are very close, so are the respective values of dc_i/dx at the effluent–membrane interface. This means that as we integrate away from the effluent–membrane interface, the values of $c_i(x)$ on the two feed loci start out very close together. However, as we continue to integrate dc_i/dx on the two loci, the small difference *could* accumulate, increasing the difference in $c_i(x)$ on the two loci. However, if we choose a value of x beforehand, we can always choose Q' close enough to Q that $c_i(x)$ on the two loci differs by less than any preassigned amount for x smaller than the chosen value. Now, when $x = x'$, the feed locus of Q' must pass through P by the uniqueness theorem. Finally, it must end of F', which represents the image of Q'. Since the image of Q' must lie close to the image of Q when Q' is close to Q (proved in section 7), F' must lie close to F.

As Q' approaches Q, then the portion Q'K of the feed locus before the knee K approaches QF. K itself becomes sharper and approaches F, as does F'. In the limit KPF'F becomes a closed loop each point of which is an F point of Q. Since each E point has but one F point, this is a contradiction. Hence the assumption that P is not the same as F is false, and the method of algebraic equations is justified.

If P lies in the region of no constant solution, the effluent locus of P cannot end on a point Q in the finite part of the (c_1,c_2) plane. For if it did, by the above demonstration, P would be the image of Q, *i.e.*, it would be an F point and hence could not lie in the region of no constant solution, a contradiction. The contradiction disappears if Q lies on the c_2 axis. For then F, the image of Q, need not coincide with P. The previous proof breaks down at the point where it is asserted that F' approaches F as Q' approaches Q; for as we know an E point moves off the c_2 axis, its F point jumps discontinuously (see Figure 5). Since no other possibility exists, the effluent locus of feed points in the region of no constant solution must end on the c_2 axis. Thus in the limit of infinite membrane thickness feeds in the region of no constant solution produce effluents *from which ion 1 is completely absent.*

We can now describe the ionic concentration profiles in the membrane when the feed lies in the region of no constant solution. Let us consider a very thick mem-

brane producing the effluent Q′ from the feed P (see Figure 5). As we showed above, the feed locus of Q′ and that of Q can be made to differ by as little as desired over any given interval $(0,x'')$ adjoining the effluent–membrane interface by choosing Q′ close enough to Q. If we choose Q′ close enough to Q, we can also make $x'' \gg \mathcal{D}_i/J$. When $x \gg \mathcal{D}_i/J$ on the feed locus QF, the ionic concentrations are essentially those of the constant solution of Q, namely, $c_2^{(0)}(Q)$, $c_3^{(0)}(Q)$.

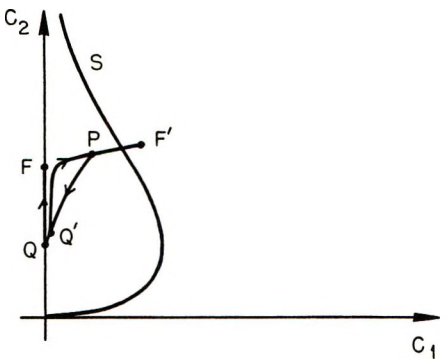

Figure 5. Sketch showing the effluent locus of a point P in the region of no constant solution.

Hence when $\mathcal{D}_i/J \ll x < x''$, the ionic concentrations in the membrane on the feed locus Q′PF′ can be made as close as desired to the values $c_1 = 0$, $c_2 = c_2^{(0)}(Q)$, $c_3 = c_3^{(0)}(Q)$ by choosing Q′ close enough to Q. Beyond x'' on the feed locus Q′PF′ the ionic concentrations differ from the values $c_1 = 0$, $c_2 = c_2^{(0)}(Q)$, $c_3 = c_3^{(0)}(Q)$ by more than the desired amount and eventually become equal to those of the solution conjugate to the feed P. Again on dimensional grounds, *most* of the change from the concentrations $c_1 = 0$, $c_2 = c_2^{(0)}(Q)$, $c_3 = c_3^{(0)}(Q)$ to those of the solution conjugate to the feed P takes place in an interval of thickness $\sim\mathcal{D}_i/J$ adjoining the feed–membrane interface. We can summarize the situation as follows: $j_1 = 0$ in the limit of an infinitely thick membrane for a fixed feed in the region of no constant solution. j_2/J and j_3/J then define a constant solution $c_2^{(0)}$, $c_3^{(0)}$. Adjoining each membrane–solution interface there is a region of thickness $\sim\mathcal{D}_i/J$ in which the ionic concentrations start at the interface from concentrations conjugate to the external solution and approach the limits $c_2^{(0)}$, $c_3^{(0)}$. In the center of the membrane, the ionic concentration profiles are virtually flat, the concentrations staying very close to those of the constant solution $c_2^{(0)}$, $c_3^{(0)}$. c_1 is vanishingly small everywhere in the membrane except in the region of thickness $\sim\mathcal{D}_i/J$ adjoining the feed–membrane interface. Finally, it should be clear from this discussion that the very long central part of the membrane corresponds to points on the feed locus Q′PF′ closely bunched near the knee.

9. Discussion of Results

We now turn to the meaning of the results, organizing our discussion around the following question: *Given a feed solution*, what is the limiting composition approached in the effluent as the membrane thickness becomes infinite? [We *assume* this limit exists. We have already *proved* that the composition of the feed solution required to produce a given effluent approaches a limiting composition as the membrane thickness becomes infinite (stability theorem). The latter limit is easier to prove than the former since specifying the effluent solution immediately determines the j_i/J, whereas specifying the feed solution does not.] We have seen that two different kinds of answers to this question exist, depending on whether or not the feed lies in the region of no constant solution. If it does not, the limiting effluent composition *must* be calculated from the algebraic ENPE; the ionic concentration profiles in the membrane are flat near the feed–membrane interface. If the feed does lie in the region of no constant solution, however, the ionic concentration profiles are not flat near the feed–membrane interface, and we *cannot* use the algebraic ENPE. Futhermore, the limiting effluent solution contains only counterion 2, *i.e.*, contains only the counterion with the larger value of $|\beta_i/z_i\mathcal{D}_i|$. In other words, $j_1 \to 0$ in the limit of infinite membrane thickness for feeds in the region of no constant solution. This means that there is complete rejection of ion 1 from this class of feeds in the limit of infinite membrane thickness.

We can display explicitly the solutions obtained from the algebraic ENPE. Using this explicit representation, we propose now to show that under reasonable assumptions regarding the conditions of membrane equilibrium, there are always feeds outside the region of no constant solution for which the effluent is more concentrated in ion 2 than the feed (negative rejection). To see this, we begin with eq 9, rewriting it as

$$R_i \equiv 1 - \frac{j_i/J}{c_i^{(0)}/D_i} = 1 - (\beta_i + z_i\mathcal{D}_i\eta^{(0)})D_i \quad (11)$$

where R_i is the rejection of the ith ion, and D_i is the distribution coefficient of the ith ion at the feed–membrane interface. If the effluent is to be more concentrated in ion 2 than the feed, $R_2 < 0$, which means $D_2 > (\beta_2 + z_2\mathcal{D}_2\eta^{(0)})^{-1}$. Since $\eta^{(0)} > -\beta_1/z_1\mathcal{D}_1$, R_2 will certainly be < 0 if

$$D_2 > (\beta_2 + z_2\mathcal{D}_2[-\beta_1/z_1\mathcal{D}_1])^{-1} = \frac{1}{\dfrac{z_2\mathcal{D}_2}{\beta_2} - \dfrac{\beta_1}{z_1\mathcal{D}_1}} \quad (12)$$

If the ionic strength of the feed solution is small enough, D_2 (which is the distribution coefficient of a counterion) can be made larger than any preassigned value. To

prove that R_2 can be < 0, it is then enough to show that there are feed solutions with arbitrarily small ionic strengths which can be treated with the algebraic ENPE, *i.e.*, to show that there are F points with arbitrarily small ionic strengths.

That there are such F point can be seen as follows. It is easy to show from eq 9 and 10 that *every* point on the c_1 axis is the F point of an E point also on the c_1 axis. In section 7 we showed that F points are continuous functions of their E points near the c_1 axis. Suppose we consider a point P on the c_1 axis that is the F point of an E point Q on the c_1 axis. We can choose the ionic strength of P as small as desired. Now consider an E point Q′ infinitesimally close to Q for which $j_2/J \neq 0$. Its F point P′ must be infinitesimally close to P, and thus is an F point (for which $c_2^{(0)} \neq 0$) with an ionic strength infinitesimally different from that of P. Thus we have shown that there are F points with arbitrarily small ionic strengths.

No explicit representation of the solution of the ENPE is available for feeds in the region of no constant solution, even in the limit of infinite membrane thickness. This lack of an explicit representation makes it difficult for us to explore in detail the properties of the solutions. All we know so far is that the counterion with the smaller value of $|\beta_i/z_i\mathfrak{D}_i|$ is completely rejected. In another place,[5] I have suggested a way of getting *approximate* solutions of the ENPE in the limit of infinite membrane thickness. The method is based on the assumption that coions are strongly excluded from the membrane and leads to explicit, if only approximate, formulas. I call it the method of good exclusion.

The solutions obtained with the method of good exclusion have properties that show that they can only be applied to feed points in the region of no constant solution: the concentration profiles are not flat near the feed–membrane interface, and ion 1 is completely rejected. This is not surprising since the method of good exclusion is a perturbation method based on an unperturbed condition in which the concentration profiles are not flat near the feed–membrane interface. We see now that the method of good exclusion can be used to get approximate solutions of the ENPE for feeds in the region of no constant solution, while the algebraic ENPE must be used for all other feeds. The chief property of importance of the good exclusion theory (aside from the total rejection of ion 1) is that if ion 2 is present in sufficiently low concentration in the feed, the effluent may be more concentrated in ion 2 than the feed, *i.e.*, ion 2 may be negatively rejected.[5] This conclusion, unlike those that preceded it above, is only approximate, being based on approximate integration of the ENPE.

All of the work from the beginning of section 7 to this point has been concerned with the case of two counterions and one coion. Let us briefly consider the case of two coions (call them 4 and 5) and one counterion (call it 6). Let $|\beta_4/z_4\mathfrak{D}_4| < |\beta_5/z_5\mathfrak{D}_5|$. As before, it is possible for $\eta^{(0)}$ and the $c_i^{(0)}$ to have a discontinuity at $j_4/J = 0$, but such a discontinuity need not necessarily occur. In fact, by a repetition of the argument given in the third paragraph of section 7, we can see that for sufficiently small j_5/J the discontinuity at $j_4/J = 0$ cannot occur. Furthermore, j_5/J being large enough is not a sufficient condition for a discontinuity to exist at $j_4/J = 0$; for if f(0) has the same sign as q, there can never be such a discontinuity, and f(0) has the same sign as q when $\beta_6 \geqslant \beta_5$. When the discontinuity does exist, *i.e.*, when $\beta_6 < \beta_5$ and j_5/J is sufficiently large, so does a region of no constant solution in the (c_4,c_5) plane. [It is interesting to note that when $\beta_6 < \beta_5$, $j_4 = 0$, and j_5/J is large enough, $q\eta^{(0)} < 0$, and the electric field *retards coions* and *accelerates counterions*.] Then, $j_4 = 0$ for feeds lying in the region of no constant solution in the limit of infinite membrane thickness.

When there are more than three ions present in the feed, the topological structure of the region of no constant solution becomes difficult to elucidate. The possibility arises that there may be solutions of the ENPE for feeds in the region of no constant solution for which several $j_i = 0$, the particular ones depending on the position of the feed point in the region of no constant solution. I have not succeeded in making a rigorous discussion of the general problem, but much useful information is contained in the following theorem. If in the limit of infinite membrane thickness $j_k = 0$ for a certain ion k contained in the feed, then $j_i = 0$ also for all ions with the same sign of charge for which

$$\left|\frac{\beta_i}{z_i\mathfrak{D}_i}\right| \leqslant \left|\frac{\beta_k}{z_k\mathfrak{D}_k}\right|$$

Proof: As we saw before, the concentration of ion k in the membrane is vanishingly small everywhere except in an interval of width $\sim\mathfrak{D}_k/J$ adjoining the feed–membrane interface. Now if we choose x to measure distance into the membrane from the feed–membrane interface ($x = 0$), then $j_i \geq 0$ and $J > 0$. The eq 1 can be written for ions k and i as

$$\frac{1}{c_k}\frac{dc_k}{dx} = \frac{\beta_k}{\mathfrak{D}_k}J + z_k\epsilon \tag{13a}$$

$$\frac{z_k}{z_i}\frac{1}{c_i}\frac{dc_i}{dx} \leqslant \frac{z_k}{z_i}\frac{\beta_i}{\mathfrak{D}_i}J + z_k\epsilon \tag{13b}$$

since z_i and z_k have the same algebraic sign. If we subtract eq 13a from 13b, integrate, and take exponentials, we get

$$\left[\frac{c_i(x)}{c_i(0)}\right]^{z_k/z_i}\frac{c_k(0)}{c_k(x)} \leqq \exp\left(\frac{z_k\beta_i}{z_i\mathfrak{D}_i}Jx - \frac{\beta_k}{\mathfrak{D}_k}Jx\right) = \exp\left(|z_k|Jx\left\{\left|\frac{\beta_i}{z_i\mathfrak{D}_i}\right| - \left|\frac{\beta_k}{z_k\mathfrak{D}_k}\right|\right\}\right) \tag{14}$$

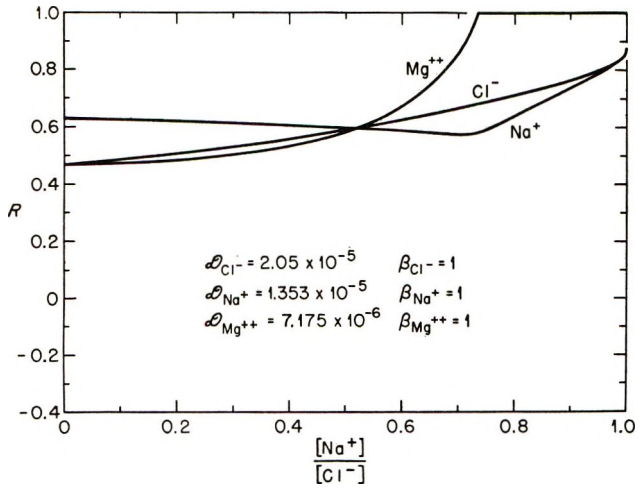

Figure 6. Ionic rejections calculated for the hyperfiltration through a cation-exchange membrane of NaCl–$MgCl_2$ solutions having a chloride concentration equal to 0.05 of the ion-exchange capacity. (Diffusion coefficients given in cgs units.)

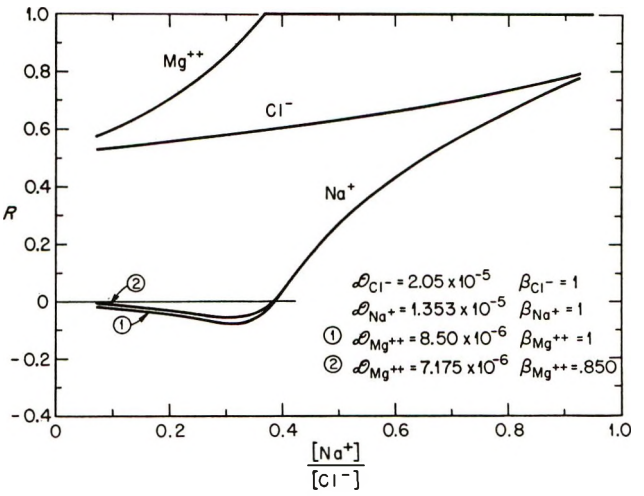

Figure 7. Ionic rejections calculated for the hyperfiltration through a cation-exchange membrane of NaCl–$MgCl_2$ solutions having a chloride concentration equal to 0.05 of the ion-exchange capacity. (Diffusion coefficients given in cgs units.)

When $x \to \infty$, the right-hand side of eq 14 remains bounded, so that if $\lim_{x\to\infty} c_k(x) = 0$, then $\lim_{x\to\infty} c_i(x) = 0$. But then $j_i = 0$.

The method of good exclusion leads to approximate solutions in which the only counterion for which $j_i \neq 0$ is that with the largest value of $|\beta_i/z_i\mathfrak{D}_i|$. Such a state of affairs is consistent with the theorem stated above. As before, if this counterion is present in the feed in sufficiently low concentration, it may be negatively rejected.

10. Example

The foregoing theory has led us to a practical recipe for calculating the rejection of dissolved ions by an ion-exchange membrane: use the algebraic ENPE for feeds outside the region of no constant solution and the method of good exclusion for feeds inside the region of constant solution. The rejections so obtained apply only in the limit of infinite membrane thickness, or what is the same thing, in the limit of infinite water flux J. [From dimensional considerations, we see that the limit of infinite membrane thickness is the limit in which l becomes very large compared with $\mathfrak{D}_i/J$ for fixed J. The same limit is achieved if l remains fixed and J becomes very large compared with $\mathfrak{D}_i/l$.] The rejections obtained from the algebraic ENPE are exact; those obtained from the method of good exclusion are valid only when there is good exclusion of coions from the membrane.

In this section, we use this calculational recipe to study hyperfiltration of a three-component feed solution (water plus two salts). The purpose of this study is to acquaint ourselves with the kinds of behavior allowed by the ENPE. For this purpose it is enough to choose reasonable values for the $\mathfrak{D}_i$ and β_i. We start by taking the $\mathfrak{D}_i$ equal to the ionic diffusion coefficients in dilute aqueous solution and the $\beta_i = 1$. We take all activity coefficients equal to 1 and assume $\Delta\mu_i^{(0)} = 0$.

Figure 6 shows ionic rejections calculated for the hyperfiltration through a cation-exchange membrane of NaCl–$MgCl_2$ feed solutions having a chloride concentration equal to 0.05 of the ion-exchange capacity of the membrane. Points on the left-hand side of the graph ($[Na^+]/[Cl^-] \leqq 0.735$) have been calculated using the algebraic ENPE; points on the right-hand side of the graph have been calculated using the method of good exclusion and correspond to feeds in the region of no constant solution.[9] On the right, the rejection of Mg^{2+}, the counterion with the smallest value of $\beta_i/z_i\mathfrak{D}_i$, is complete, as it should be. Figure 7 shows rejections for the same system, except that either the diffusion coefficient of Mg^{2+} has been raised by a factor $1.18 = 1/0.85$, or $\beta_{Mg^{2+}}$ has been lowered by a factor of 0.85. In both cases, the ratio $(\beta/z\mathfrak{D})_{Mg^{2+}}$ has been decreased by a factor of 0.85. More feeds now lie in the region of no constant solution as evidenced by the greater fraction of the composition axis on which there is complete rejection of Mg^{2+}. On the left, there is negative rejection of Na^+, a possibility we noted in

(9) As noted above, the results obtained from the algebraic ENPE are *exact* in the limit of infinite membrane thickness, while those obtained from the method of good exclusion are approximate. We can get a feel for the accuracy of the good exclusion results in Figures 6 and 7 as follows. The numerical results in the two regions seem to indicate that the rejections are continuous functions of composition, and they have so been shown in Figures 6 and 7. Thus the two halves of each curve should agree at the point at which we change from one approximation to the other. Now the two halves of the chloride rejection curves in Figures 6 and 7 differ by between 2 and 3% at this point. The smallness of this difference we take as an indication of the comparatively high accuracy of the good exclusion results in these cases. The accuracy of the good exclusion method is discussed further in ref 5.

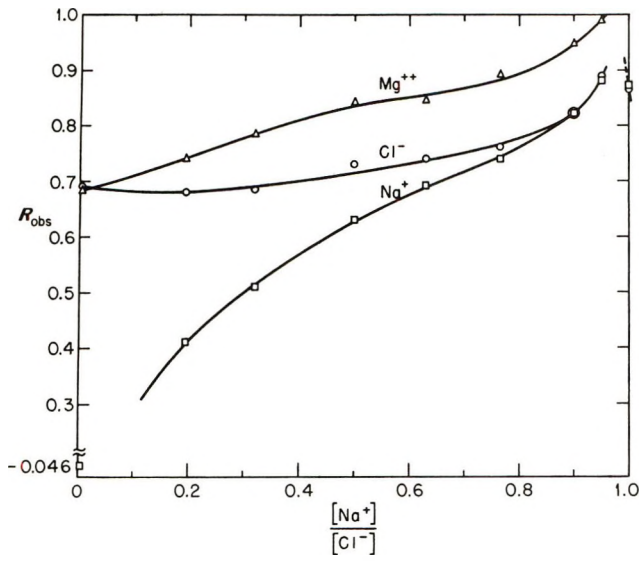

Figure 8. Ionic rejection measured in the hyperfiltration of $NaCl$–$MgCl_2$ solutions through a Zr (IV)oxide–polyacrylate dual-layer dynamic membrane; feed chloride concentration = 0.05 mol/l. Results of R. B. Bevan.

section 9. The extreme sensitivity of the rejection of Na^+ to the value of $(\beta/z\mathfrak{D})_{Mg^{2+}}$ is noteworthy.

R. B. Bevan of Oak Ridge National Laboratory[10] has measured the rejection of ions from $NaCl$–$MgCl_2$ solutions. He used as a membrane the dual-layer hydrous Zr(IV) oxide–polyacrylate dynamic membrane of Johnson, *et al.*[11] His results are shown in Figure 8. The strong resemblance to Figure 7 is unmistakable, although no quantitative comparison is possible. It seems likely that if $\mathfrak{D}_{Mg^{2+}}$ and $\beta_{Mg^{2+}}$ were to vary continuously from the values shown in Figure 7 to those shown in Figure 6 as the mole fraction of Na^+ in the feed increased, calculated curves very similar to those shown in Figure 8 could be obtained. Of particular interest is the very high rejection of Mg^{2+} at the extreme right of Figure 8 and the negative rejection of Na^+ at the extreme left.

11. Summary

Hyperfiltration of multicomponent solutions through ion-exchange membranes has been discussed using the extended Nernst–Planck equations. A simple means of calculating ionic rejections in the limits of infinite membrane thickness or infinite water flux has been suggested. Circumstances have been identified under which a particular one of the counterions may be completely rejected. Other circumstances have been identified under which some counterions may be negatively rejected. An experiment is quoted exhibiting both of these phenomena.

Appendix A

In this appendix we prove that the equilibrium points found in section 5 are asymptotically stable in the large. We begin by fixing on a choice of j_i/J. As we already know, the j_i/J uniquely determine a constant solution $c_i^{(0)}$. Suppose now that we consider any one-parameter family of solutions of eq 1 and 2, $c_i(x,\alpha)$, belonging to the same j_i/J. With no loss of generality we can take $c_i(x,0) = c_i^{(0)}$. If the dependence of $c_i(x,\alpha)$ on α is analytic, then $\lim_{x\to\infty} c_i(x,\alpha) = c_i^{(0)}$. (The positive direction of x has been chosen opposite to the direction of the fluxes, so that $x \to \infty$ means we have integrated the ENPE infinitely far into the membrane in the direction opposite to the fluxes. With this choice of positive direction, $J < 0$ and $j_i < 0$.)

The idea of the proof is to show that $c_i(x,\alpha)$ is asymptotically stable in all orders. We begin by expanding $c_i(x,\alpha)$ in a power series in α

$$c_i(x,\alpha) = \sum_{k=0}^{\infty} c_i^{(k)}(x)\alpha^k \tag{A1}$$

In view of relation A (ref 3) we can similarly expand $\eta \equiv \epsilon/J$ in powers of α

$$\eta(x,\alpha) = \sum_{k=0}^{\infty} \eta^{(k)}(x)\alpha^k \tag{A2}$$

If we substitute eq A1 and A2 into eq 1 and collect all terms in each power of α, we find

$$\frac{j_i}{J} = \beta_i c_i^{(0)} + z_i \mathfrak{D}_i c_i^{(0)} \eta^{(0)} \tag{A3a}$$

$$\frac{1}{J}\frac{dc_i^{(1)}}{dx} = \left(\frac{\beta_i}{\mathfrak{D}_i} + z_i\eta^{(0)}\right)c_i^{(1)} + z_i\eta^{(1)}c_i^{(0)} \tag{A3b}$$

$$\frac{1}{J}\frac{dc_i^{(k)}}{dx} = \left(\frac{\beta_i}{\mathfrak{D}_i} + z_i\eta^{(0)}\right)c_i^{(k)} + z_i\eta^{(k)}c_i^{(0)} + z_i\sum_{l=1}^{k-1} c_i^{(l)}\eta^{(k-l)} \qquad (k > 1) \tag{A3c}$$

Substitution of eq A1 into eq 2 gives

$$\sum_{i=1}^{N} z_i c_i^{(0)} + qX = 0 \tag{A4a}$$

$$\sum_{i=1}^{N} z_i c_i^{(k)} = 0 \qquad (k > 0) \tag{A4b}$$

Equations A3a and A4a are the same equations as those used in section 5 to determine the constant solution. Hence $c_i^{(0)}$ is the constant solution, as we intended it to be. Once we know $c_i^{(0)}$ and $\eta^{(0)}$, we can calculate $c_i^{(1)}$ and $\eta^{(1)}$. If we multiply eq A3b by z_i and sum over i, we find using eq A4b

$$\eta^{(1)} = -\frac{\sum_{i=1}^{N} z_i a_i c_i^{(1)}}{\sum_{i=1}^{N} z_i^2 c_i^{(0)}} \tag{A5a}$$

(10) Private communication.

(11) J. S. Johnson, R. E. Minturn, and P. Wadia, submitted to the *J. Electroanal. Chem. Interfacial Electrochem.*

where a_i is an abbreviation for the quantity $\beta_i/\mathfrak{D}_i + z_i\eta^{(0)}$

$$a_i = \frac{\beta_i}{\mathfrak{D}_i} + z_i\eta^{(0)} \qquad \text{(A5b)}$$

If we insert (A5a) into (A3b) and multiply the resulting equation by z_i, we obtain

$$\frac{1}{J}\frac{\mathrm{d}(z_ic_i^{(1)})}{\mathrm{d}x} = a_i(z_ic_i^{(1)}) - f_i\sum_{k=1}^{N} a_k(z_kc_k^{(1)}) \qquad \text{(A6a)}$$

where

$$f_i = \frac{z_i^2c_i^{(0)}}{\sum_{k=1}^{N} z_k^2c_k^{(0)}} \qquad \text{(A6b)}$$

We can write eq A6a in matrix form as follows

$$\frac{\mathrm{d}(z_ic_i^{(1)})}{\mathrm{d}x} = \sum_{k=1}^{N} M_{ik}(z_kc_k^{(1)}) \qquad \text{(A7a)}$$

where

$$M_{ik} = J(a_i\delta_{ik} - f_ia_k) \qquad \text{(A7b)}$$

Here δ_{ik} is Kronecker's delta ($\delta_{ik} = 1$ if $i = k$ and 0 if $i \neq k$).

To find out what kind of solutions eq A7 have, we need to know what the characteristic roots of the matrix M_{ik} are. The matrix M_{ik} has the property that the sum of its rows vanishes

$$\sum_{i=1}^{N} M_{ik} = 0 \qquad (k = 1, 2, \ldots, N) \qquad \text{(A8)}$$

$\left(\text{since } \sum_{i=1}^{N} f_i = 1\right)$. Furthermore, its diagonal elements are all negative and its off-diagonal elements are all positive (since $J < 0$ and $a_i > 0$, the latter inequality following from eq 8a and b of section 5). According to the theorem of Marcus and Minc,[12] the characteristic roots of M_{ik} have real parts that are ≤ 0. [To make this paper wholly self-contained, the proof of Marcus and Minc's theorem is given in Appendix B.] Since the rows of M_{ik} are linearly dependent, the determinant of M_{ik} vanishes. Thus at least one of the characteristic roots of M_{ik} is zero.

Let us consider the solutions of eq A7 that belong to a zero characteristic value. They are constants $c_k^{(1)}$ that satisfy the equations

$$\sum_{k=1}^{N} M_{ik}(z_kc_k^{(1)}) = 0 \qquad \text{(A9a)}$$

or equivalently

$$a_i(z_ic_i^{(1)}) = f_i\sum_{k=1}^{N}(z_kc_k^{(1)})a_k \qquad \text{(A9b)}$$

The sum on the right-hand side of eq A9b is a number; call it p. If $p \neq 0$, then $z_ic_i^{(1)} = (f_i/a_i)p$. Since both f_i and a_i are positive, all the $z_ic_i^{(1)}$ have the same sign. Hence they cannot sum to zero as required by eq A4b. Thus $p \neq 0$ leads to a contradiction, and $p = 0$. If $p = 0$, however, then $c_i^{(1)} = 0$. Thus the solutions of eq A7 that belong to zero characteristic values, vanish identically.

The nonzero characteristic values λ_k of M_{ik} all have negative real parts and the solutions corresponding to them are proportional to $e^{\lambda kx}$. The most general solution of eq A7 that obeys eq A4b expresses each $c_k^{(1)}$ as the sum of exponentials $e^{\lambda_i x}$ where λ_i is a complex number with a negative real part. This result is sufficient to yield first-order stability against small disturbances of $c_i(x,\alpha)$ from $c_i^{(0)}$.

The next step in the proof of stability is to show that if $c_i^{(1)}, c_i^{(2)}, \cdots, c_i^{(k-1)}$ and $\eta^{(1)}, \eta^{(2)}, \cdots, \eta^{(k-1)}$ are sums of exponentials of the type $e^{\lambda x}$ where λ is a complex number with a negative real part, so are $c_i^{(k)}$ and $\eta^{(k)}$. For convenience, we henceforth refer to a sum of exponentials $e^{\lambda x}$, $Re(\lambda) < 0$ as a *stable function*. We proceed as we did in the case of $k = 1$. If we multiply eq A3c by z_i and sum over i, we find

$$\eta^{(k)} = -\frac{\sum_{i=1}^{N} a_iz_ic_i^{(k)}}{\sum_{i=1}^{N} z_i^2c_i^{(0)}} - \frac{\sum_{i=1}^{N} z_i^2\sum_{l=1}^{k-1} c_i^{(l)}\eta^{(k-l)}}{\sum_{i=1}^{N} z_i^2c_i^{(0)}} \qquad \text{(A10)}$$

If we substitute this expression for $\eta^{(k)}$ into eq A3c and multiply the latter by z_i, we obtain after rearrangement

$$\frac{\mathrm{d}}{\mathrm{d}x}(z_ic_i^{(k)}) - \sum_{j=1}^{N} M_{ij}(z_jc_j^{(k)}) = J\sum_{l=1}^{k-1}\eta^{(k-l)}\left[z_i^2c_i^{(l)} - f_i\sum_{j=1}^{N} z_j^2c_j^{(l)}\right] \qquad \text{(A11)}$$

The general solution of eq A11 is the sum of any particular solution of eq A11 plus the general solution of the *homogeneous* equation

$$\frac{\mathrm{d}}{\mathrm{d}x}(z_ic_i^{(k)}) - \sum_{j=1}^{N} M_{ij}(z_jc_j^{(k)}) = 0 \qquad \text{(A12)}$$

The general solution of eq A12 is a stable function since, as before, any solution of eq A12 belonging to a zero characteristic value is identically zero. Our induction will therefore be complete if we can find a particular solution of eq A11 that is a stable function.

To find such a particular solution, we make a similarity transformation that puts the matrix M_{ij} in triangular form. This means we replace the dependent variables $z_ic_i^{(k)}$ by a linearly independent set of linear combinations $u_i^{(k)} = \sum_{j=1}^{N} W_{ij}z_jc_j^{(k)}$, where the matrix W has the property that the matrix product $T = WMW^{-1}$ has only zeros below the main diagonal and has the

(12) M. Marcus and H. Minc, "A Survey of Matrix Theory and Matrix Inequalities," Allyn and Bacon, Boston, 1964, p 159.

characteristic values of M along the main diagonal (triangular form of M).[13] Equation A11 then becomes

$$\frac{du_i^{(k)}}{dx} - \sum_{j=1}^{N} T_{ij}u_j^{(k)} = v_i^{(k)} \qquad \text{(A13)}$$

where the $v_i^{(k)}$ are linear combinations of the right-hand sides of eq A11 and are thus, by the inductive hypothesis, stable functions.

If we now consider the $i = N$ member of eq 21, we find it takes the form

$$\frac{du_N^{(k)}}{dx} - \lambda_N u_N^{(k)} = v_N^{(k)} \qquad \text{(A14)}$$

A particular solution of eq A14 is

$$u_N^{(k)} = e^{\lambda_N x}\int e^{-\lambda_N x} v_N^{(k)}(x)\, dx \qquad \text{(A15)}$$

Since $v_N^{(k)}(x)$ is a stable function, so is $u_N^{(k)}$.[14] The $i = N - 1$ member of eq A13 takes the form

$$\frac{du_{N-1}^{(k)}}{dx} - \lambda_{N-1}u_{N-1}^{(k)} = v_{N-1}^{(k)} + T_{N-1,N}u_N^{(k)} \qquad \text{(A16)}$$

A particular solution of (A16) is

$$u_{N-1}^{(k)} = e^{\lambda_{N-1}x}\int e^{\lambda_{N-1}x}(v_{N-1}^{(k)} + T_{N-1,N}u_N^{(k)})\, dx \qquad \text{(A17)}$$

Since $v_{N-1}^{(k)}$ is a stable function by hypothesis, and we proved $u_N^{(k)}$ is a stable function in the last step, $u_{N-1}^{(k)}$ is also a stable function.

Continuing in this way, we can generate a particular solution of eq A13 in which all of the $u_i^{(k)}$ are stable functions. Finally, the particular solution $z_i c_i^{(k)} = \sum_{j=1}^{N} (W^{-1})_{ij}u_j^{(k)}$ of eq A12 is a stable function. Since we proved above that $\eta^{(1)}$ and $c_i^{(1)}$ are stable functions, the induction is complete.

Appendix B

We prove the following theorem. If a matrix M_{ik} has the properties

$$\sum_{i=1}^{N} M_{ik} = 0 \qquad (k = 1, 2, \cdots, N) \qquad \text{(B1a)}$$

$$M_{ii} \leq 0 \qquad \text{(B1b)}$$

$$M_{ik} \geq 0 \qquad (i \neq k) \qquad \text{(B1c)}$$

then its characteristic values λ have real parts $Re(\lambda) \leq 0$.

The theorem stated by Marcus and Minc[11] is slightly different. In it, the column sums, $\sum_{k=1}^{N} M_{ik}$, vanish instead of the row sums, $\sum_{k=1}^{N} M_{ik}$. However, since a matrix and its transpose have the same characteristic values, in proving the theorem we can consider the transpose $\tilde{M}$ of the matrix M, for which the column sums vanish: $\sum_{k=1}^{N} \tilde{M}_{ik} = 0$. Again $\tilde{M}_{ii} \leq 0$, $\tilde{M}_{ik} \geq 0$ if $i \neq k$.

Suppose x_i is the eigenvector of $\tilde{M}_{ik}$ belonging to any characteristic value λ

$$\sum_{k=1}^{N} \tilde{M}_{ik}x_k = \lambda x_i \qquad (i = 1, 2, \cdots, N) \qquad \text{(B2)}$$

Suppose x_m is the component with the largest absolute value. Then choosing $i = m$, we find

$$|\lambda - \tilde{M}_{mm}| = \left|\sum_{\substack{k\neq m \\ =1}}^{N} \tilde{M}_{mk}\frac{x_k}{x_m}\right| \qquad \text{(B3a)}$$

$$\leq \sum_{\substack{k\neq m \\ =1}}^{N} \tilde{M}_{mk}\left|\frac{x_k}{x_m}\right| (\tilde{M}_{mk} \geq 0,\ m \neq k) \qquad \text{(B3b)}$$

$$\leq \sum_{\substack{k\neq m \\ =1}}^{N} \tilde{M}_{mk} = -\tilde{M}_{mm} \qquad \text{(B3c)}$$

Thus λ must lie in a circle of radius $-\tilde{M}_{mm} \geq 0$ centered on the point $\tilde{M}_{mm} \leq 0$. Therefore, $Re(\lambda) \geq 0$.

Appendix C

c_i, $c_{i(s)}$	= concentration of the ith kind of ion in the membrane and in an external solution, respectively (mol cm^{-3})
$\mathfrak{D}_i$	= diffusion coefficient of the ith kind of ion in the membrane (cm^2 sec^{-1})
D_i	= distribution coefficient of the ith kind of ion at a solution–membrane interface. Equals ratio $c_i/c_{i(s)}$ given in eq 3 (dimensionless)
$f(\eta^{(0)})$	= function defined by the left-hand side of eq 7
F	= the Faraday (96,500 C equiv^{-1})
j_i	= flux of the ith kind of ion through the membrane (mol cm^{-2} sec^{-1})
J	= volume flux of water through the membrane (cm^3 cm^{-2} sec^{-1})
l	= thickness of the membrane (cm)
R	= universal gas constant (8.315 J deg^{-1} mol^{-1})
q	= algebraic sign of the fixed charge: $+1$ for an anion exchanger, -1 for a cation exchanger
T	= absolute temperature (°K)
X	= fixed charge density in the membrane (equiv cm^{-3})
x	= distance into the membrane (cm)
z_i	= charge of the ith kind of ion (equiv mol^{-1})
β_i	= convective coupling coefficient; see references 5 and 6 (dimensionless)
γ_i, $\gamma_{i(s)}$	= ionic activity coefficients in the membrane and an external solution, respectively (dimensionless)
ϵ	= FE/RT, where E (V cm^{-1}) is the electric field in the membrane
η	= ϵ/J
$\mu^{(0)}$	= chemical potential of the ith kind of ion in its standard state (J mol^{-1})
ϕ	= electrical potential (V)

(13) H. Margenau and G. M. Murphy, "The Mathematics of Physics and Chemistry," Van Nostrand, Princeton, N. J., 1949, Section 10.15.

(14) A difficulty could conceivably arise if one of the exponentials in $v_N^{(k)}$ had the exponent λ_N. This can only happen as we can see from the form of the right-hand side of eq A11 if one of the characteristic values of M can be written as a linear combination with *positive integral* coefficients of two or more characteristic values. While possible, this will not generally be the case.

Molecular Orbital Theory of the Diatomic Molecules of the First Row Transition Metals

by W. F. Cooper,

Department of Chemistry, State University of New York at Buffalo, Buffalo, New York 14214

G. A. Clarke, and C. R. Hare*

Department of Chemistry, University of Miami, Coral Gables, Florida 33124 *(Received August 16, 1971)*

Publication costs assisted by the University of Miami

Extended Hückel molecular orbital calculations have been carried out on the diatomic molecules of the first row transition metals. A variation of the orbital parameters from reported values was necessary to obtain agreement with the experimental quantities. These calculations allow a critical evaluation of the orbital parameters and the basis sets required for the description of these simple molecules. The dissociation energy, equilibrium internuclear separation, and stretching frequency were found to be in good agreement with literature values for the extremes of the first row transiton metals (Sc, Ti, Co, Ni, and Zn) and poor for the middle of the series (Cr, Mn, and Fe). The bonding in these molecules arises predominantly from the overlap of the 4s and/or $3d_{z^2}$ σ orbitals. In a few cases π bonding is of some importance.

Introduction

Previously it was shown[1] that the extended Hückel theory of Hoffmann[2] gave an excellent description of the bonding and the potential energy surface of the diatomic copper molecule. The results were dependent on the orbital basis set and on the parameters required by the extended Hückel method. The usual basis set of 3d, 4s, and 4p atomic orbitals was found to reproduce best the molecular properties of the Cu_2 molecule. The 3d orbitals provided a core necessary to describe the repulsive region of the potential energy curve while the bonding arose from the interaction of the 4s orbitals. The inclusion of the 4p orbitals was necessary to give the proper value of the spectral transition.

The extended Hückel theory requires an approximation to the off-diagonal resonance or exchange integrals (H_{ij}). Four basic approximations were tested for the Cu_2 molecule and it was found that the Cusachs approximation[3] (eq 1) best described both the bonding and repulsive regions.

$$H_{ij} = 0.5(K - |S_{ij}|)(H_{ii} + H_{jj})S_{ij} \qquad (1)$$

The inherent dependence of the Cusachs approximation on the square of the overlap (S_{ij}^2) is a desirable property which approximates the kinetic energy (T_{ij}). The other approximations[4] lack this feature and therefore lead to less satisfactory results.

All of the homonuclear diatomic molecules of the first row transition metals are known to exist in the gas phase;[5-12] however, the Mn_2 molecule and possibly the Zn_2 molecule have been described as van der Waals molecules. Some of the properties of these molecules have been investigated by mass spectroscopy and information concerning the dissociation energy and the stretching frequency has been reported to an accuracy of about $\pm 30\%$. These dimers have dissociation energies between 0.5 and 2.5 eV and have stretching frequencies of approximately 300 cm^{-1}. Although accurate data are available only for the Cu_2 molecule, the experimental results for the other diatomics are sufficient to warrant molecular-orbital calculations and test the parameters and approximations required for the semi-empirical description of these simple molecules.

Methods and Results

The extended Hückel molecular orbital calculations reported here were carried out as in the case of Cu_2.[1] The Cusachs approximation (eq 1) was used exclusively for the calculation of the off-diagonal resonance integrals. The splitting parameter, K, used in the

(1) C. R. Hare, T. P. Sleight, W. Cooper, and G. A. Clarke, *Inorg. Chem.*, 7, 669 (1968).

(2) R. Hoffmann, *J. Chem. Phys.*, 39, 1397 (1963).

(3) L. C. Cusachs, *ibid.*, 43, 5157 (1965).

(4) R. S. Mulliken, *ibid.*, 16, 497, 675 (1949); M. Wolfsberg and L. Helmholz, *ibid.*, 20, 837 (1952); C. J. Ballhausen and H. B. Gray, *Inorg. Chem.*, 1, 111 (1962); W. A. Yeranos, *J. Chem. Phys.*, 44, 2207 (1966).

(5) D. N. Travis and R. F. Barrow, *Proc. Chem. Soc., London*, 64 (1962); M. Ackerman, F. E. Stafford, and J. Drowart, *J. Chem. Phys.*, 33, 1784 (1960); P. Schissel, *ibid.*, 26, 1276 (1957).

(6) A. Kant, *ibid.*, 41, 1872 (1964).

(7) A. Kant and B. Strauss, *ibid.*, 41, 3806 (1964); 45, 3161 (1966).

(8) A. Kant and S.-S. Lin, *ibid.*, 51, 1644 (1969).

(9) G. Verhaegen, S. Smoes, and J. Drowart, *ibid.*, 40, 239 (1964).

(10) A. Kant, S.-S. Lin, and B. Strauss, *ibid.*, 49, 1983 (1968).

(11) J. G. Winans, *Phys. Rev.*, 37, 898, 902 (1931).

(12) S.-S. Lin and A. Kant, *J. Phys. Chem.*, 73, 2450 (1969).

Cusachs approximation[3] was maintained at 2.0, the value which gave the best results in the Cu_2 calculations.

The dissociation energy of a molecule was calculated from the energy difference between the populated atomic orbitals at infinite separation and the populated molecular level at r_e (equilibrium internuclear separation). The stretching frequency ω_e, which reflects the width of the potential energy curve, was obtained from a best fit of the potential energy curve in the harmonic region by Morse's equation,[13] that is

$$V(r) = D_e\left[1 - \exp\left(-\omega_e\sqrt{\frac{\pi c\mu}{\hbar D_e}}\left(r_e - r\right)\right)\right]^2 \quad (2)$$

The value of r_e reported in the literature has frequently been given as the sum of the covalent radii. However, two other approximations can be used to calculate r_e. The Mecke–Morse[14] formula relates r_e to ω_e; *viz.*, $\omega_e r_e^3 = 3000$, while Badger's empirical eq[15,16] 3 introduces a parameter, d_{ij}, which depends only upon the position of the element in the periodic table.

$$k_e(r_e - d_{ij})^3 = 1.86 \times 10^5 \quad (3)$$

In most cases, Badger's internuclear distance lies between the values calculated by Mecke–Morse formula and by those obtained from the sum of the covalent radii. This, then, parallels the case of Cu_2, where the value of r_e found experimentally is somewhat less than the sum of the covalent radii.

The ionization potential in these calculations is given, according to Koopmans' theorem,[17] as the negative of the energy of the highest filled molecular orbital. This value can then be compared to the literature value which has been approximated as being 1–2 eV less than that of the atom. The spectral transition, Δ, was taken as the energy difference between the highest filled molecular orbital and the lowest unoccupied orbital of appropriate symmetry. The molecular orbital program does not explicitly account for the electron repulsions or a configuration interaction of the molecular terms. The absence of these terms forces the diatomic molecules of the first row transition metals to dissociate into atoms with a d^n rather than a $d^{n-1}s^1$ or $d^{n-2}s^2$ configuration when the d orbital is lower in energy than the s. Any extension of the basis set to include both 3p and 4p orbitals is prohibited in this calculation since the 3p and 4p orbitals are not set orthogonal in the program.[2,3]

As in every semiempirical molecular orbital calculation it is expected that the best set of orbital parameters (Coulomb integrals, H_{ii} and orbital exponents, ζ) used to describe the molecule will not in general be those of the free atom. Nevertheless, free atom orbital energies and exponents can be used as initial estimates of the molecular parameters. Two reasonable approximations for the Coulomb integrals available for the first row transition metals are the Hartree–Fock solutions of Clementi[18] and the valence state ionization potentials of Ballhausen and Gray.[19] The orbital energies of the diatomic molecules should be within the range of these extremes; also because several values of the orbital exponents are available (Clementi,[18] Clementi–Raimondi,[20] Burns,[21] Slater,[22] Veigele,[23] Cusachs[24]), the most appropriate values have been sought for the diatomic molecules and they should lie within the range of these values.

Zn_2. Diatomic zinc is known to exist,[11] but the binding energy between the two zinc atoms is quite small since both atoms contain two paired 4s electrons.

Table I: Comparison of Calculated and Experimental Properties of the First Row Transition Metal Homonuclear Diatomic Molecules[a]

		D_e, eV	r_e, Å	I.P., eV	Δ, eV	ω_e, cm^{-1}	Reference
Sc_2	calcd	1.25	2.20	5.50	0.34	250	
	found	1.13	2.50	5.7	...	230	9
Ti_2	calcd	1.88	2.30	5.3	0.51	250	
	found	1.40	2.50	5.8	...	288	7
V_2	calcd	3.05	2.10	5.6	...	300	
	found	2.48	2.32	5.7	...	325	8
Cr_2	calcd	2.6	1.90	7.9	0.40	300	
	found	1.90	2.22	5.8	...	400	7
Mn_2	calcd	1.22	1.90	8.0	0.25	325	
	found	van der Waals molecule					10
Fe_2[1]	calcd	3.10	1.90	8.9	...	...	
	found	1.0	2.22	5.9	...	365	12
Fe_2[2]	calcd	5.0	1.25	8.6	0.75	...	
	found	1.0	2.22	5.9	...	365	12
Co_2[3]	calcd	1.63	2.30	9.2	3.29	370	
	found	1.72	2.31	6.8	...	335	7
Co_2[4]	calcd	1.84	2.30	11.5	...	410	
	found	1.72	2.31	6.8	...	335	7
Ni_2	calcd	2.45	2.21	8.9	2.25	370	
	found	2.37	2.30	6.6	...	325	6
Zn_2	calcd	0.36	2.6	7.1	1.83	100	
	found	0.29	2.5	8.4	2.79	...	11

[a] [1] 3p, 3d, and 4s basis set, [3] H_{ii} (3d) = −10.0 eV; [2] 3d, 4s, and 4p basis set, [4] H_{ii} (3d) = −12.5 eV.

(13) P. M. Morse, *Phys. Rev.*, **34**, 57 (1929).
(14) R. Mecke, *Z. Phys.*, **32**, 813 (1925).
(15) R. M. Badger, *J. Chem. Phys.*, **2**, 128 (1934); **3**, 710 (1935).
(16) M. D. Dolgushin, *Opt. Spektrosk.*, **19**, 289 (1965).
(17) T. A. Koopmans, *Physica*, **1**, 104 (1933).
(18) E. Clementi, "Tables of Atomic Functions," International Business Machines, New York, N. Y., 1965.
(19) C. J. Ballhausen and H. B. Gray, "Molecular Orbital Theory," Benjamin, New York, N. Y., 1965.
(20) E. Clementi and D. L. Raimondi, *J. Chem. Phys.*, **38**, 2686 (1963).
(21) G. Burns, *ibid.*, **41**, 1521 (1964).
(22) J. C. Slater, *Phys. Rev.*, **36**, 57 (1930).
(23) W. J. Veigele, D. E. Stevenson, and E. M. Henry, *J. Chem. Phys.*, **50**, 5404 (1969).
(24) L. C. Cusachs, B. L. Trus, D. G. Carroll, and S. P. McGlynn, *Int. J. Quantum Chem. Symp.*, **1**, 423 (1967).

Table II: A Comparison of Coulomb Parameters, eV

	This work			Ballhausen-Gray[19]		Clementi[18]	
	3d	4s	4p	3d	4s	3d	4s
Sc[a]	−5.0	−6.15	...	−4.8	−5.7	−9.3	−5.7
Ti[a]	−5.0	−5.75	...	−5.6	−6.1	−12.0	−6.0
V[a]	−5.5	−7.0	...	−6.3	−6.3	−13.8	−6.3
Cr[a]	−8.0	−7.0	...	−7.2	−6.6	−15.5	−6.5
Mn[a]	−8.0	−7.0	...	−8.0	−6.8	−17.4	−7.0
Fe[a]	−10.0	−7.0	...	−8.7	−7.1	−17.6	−7.0
Fe	−10.0	−7.0	−4.0				
Co	−10.0	−7.4	−3.0	−9.4	−7.3	−18.4	−7.3
Ni	−10.1	−8.9	−4.0	−10.1	−7.6	−19.2	−7.5
Cu	−13.5	−6.45	−2.94	−10.7	−7.6	−13.5	−6.45
Zn	−21.3	−7.94	−4.80	...	...	−21.3	−7.94

[a] The Clementi Hartree–Fock orbital energy[18] was used for the 3p orbital.

As is general for this type of bonding (*e.g.*, He_2), the excited state is known to be more stable (that is, has a larger dissociation energy and smaller internuclear separation) than the ground state. Calculations on this molecule using the Clementi[18] Hartree–Fock orbital energies and −3.50 eV for the 4p orbital energy failed to show evidence for bonding. A lower energy for the 4p orbital (−4.80 eV) does, however, give a reasonable correlation with experiment (Table I). The orbital energies used for the Coulomb integrals are given in Table II and the exponents in Table III.

The Zn_2 molecule is not exactly like the He_2 molecule in that it is not completely repulsive. From these calculations its existence arises from a σ bond stabilized by the interaction of the low-lying 4p orbital with 4s, which does not effectively occur in He_2. The total overlap population (TOP), molecular orbital configuration, and molecular term for the ground state, are summarized in Table IV. The excited state, $^1\Sigma_u^+$, is definitely more bonding than the ground state and occurs at a smaller internuclear distance. Furthermore, the shape of the potential curves indicates that the excited state has a larger stretching frequency than the ground state. The calculated dissociation energy of the excited state is 2.02 eV which compares favorably with the estimated value, 1.7 eV.[25] The internuclear separation in this state is calculated to be 2.15 Å which is less than that of the ground state.

Table III: A Comparison of the Orbital Exponents

		CR[a] [20]	C[b] [18]	V[c] [23]	Cusachs[24]	Burns[21]	This work
Sc	3d	2.37	1.87	2.35		2.07	2.00
	4s	1.16	1.25	1.35		0.95	1.80
Ti	3d	2.71	2.01	2.56	2.10	2.28	2.20
	4s	1.20	1.30	1.51		1.08	1.60
V	3d	2.99	2.07	2.80	2.30	2.50	2.50
	4s	1.25	1.32	1.69	1.26	1.45	1.25
Cr	3d	3.25	2.34	3.02	2.43	2.72	2.71
	4s	1.28	1.40	1.83	1.31	1.32	1.20
Mn	3d	3.51	2.48	3.25		2.94	3.10
	4s	1.32	1.45	1.97		1.45	1.20
Fe	3d	3.73	2.62	3.47	2.55	3.15	2.65
	4s	1.36	1.55	2.13	1.41	1.57	1.45
Co	3d	3.95	2.75	3.70	2.59	3.37	2.20
	4s	1.39	1.60	2.28	1.46	1.70	1.40
Ni	3d	4.18	2.93	3.93	2.35	3.58	2.00
	4s	1.42	1.65	2.42	1.51	1.82	1.65
Cu	3d	4.40	3.16		2.70	3.73	3.16
	4s	1.46	1.75			1.92	1.75
Zn	3d	4.62	3.32			4.00	3.32
	4s	1.49	1.80			2.07	2.00

[a] CR = Clementi–Raimondi orbital exponents. [b] C = Clementi orbital exponents. [c] V = Veigele orbital exponents.

Ni$_2$. The properties of the Ni_2 molecule[6] are summarized in Table I. The use of the Clementi[18] orbital energies and dominant orbital exponents for the 3d, 4s, and 4p basis set calculations gave curve A, Figure 1, and does not predict the stable existence of the molecule. Even less evidence for bonding was obtained in calculations using Clementi–Raimondi[20] orbital exponents. The results, curve B, Figure 1, were improved by using the VSIP of Ballhausen and Gray[19] (−10.1 eV) for the 3d orbital. The potential energy curve is best reproduced by the parameters given in Tables II and III and is represented by curve C in Figure 1. Calculations with a 3d, 4s or a 3p, 3d, 4s basis set gave similar results and were less descriptive of the molecule, in that the dissociation energy was lower and the bond distance larger than observed.

Co$_2$. The Co_2 molecule has been observed and described by Kant and Strauss.[7] As in the case of Ni_2, Figure 1, the Clementi[18] parameters for the 3d, 4s, and 4p basis calculations were inadequate for the description of the molecule and a change to the Clementi–Raimondi[20] orbital exponents gave no minimum in the energy to 1.4 Å. Improvement was found by substituting the VSIP[19] for the Clementi 3d orbital energy. The best agreement with experiment is ob-

(25) G. Herzberg, "Molecular Spectra and Molecular Structure," Van Nostrand, Princeton, N. J., 1966.

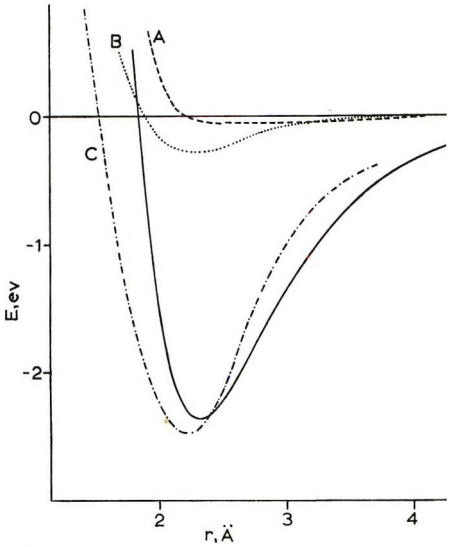

Figure 1. The dependence of the calculated potential energy of Ni_2 on the extended Hückel parameters. Curve A was calculated using a 3d, 4s, and 4p basis with the Clementi orbital energy and orbital exponents given in Tables I and II. Curve B was calculated using Clementi orbital exponents and Ballhausen–Gray VSIP for the 3d orbital and curve C with the "best" parameters of this work. The Morse curve was calculated using the data given in Table III.

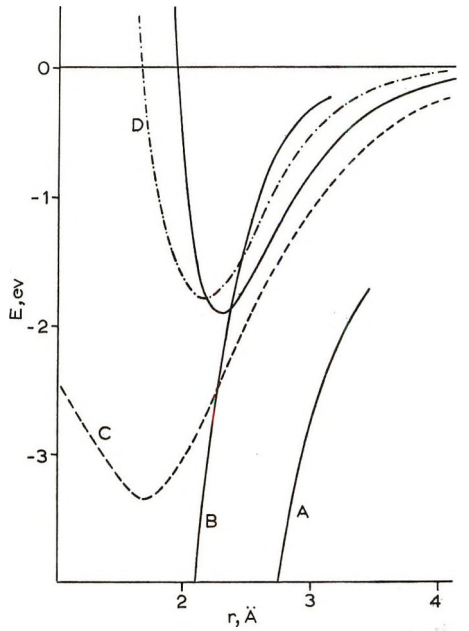

Figure 2. The dependence of the calculated potential energy of Ti_2 upon the extended Hückel parameters. Curves A, B, and C were calculated using a 3d, 4s, and 4p basis and Clementi, Clementi–Raimondi, and Ballhausen–Gray parameters, respectively (Tables I and II). Curve D was calculated with a 3p, 3d, and 4s basis set with the "best" parameters of this work. The Morse curve was constructed from the data given in Table III.

tained by using 3d and 4s orbital exponents very close to ones calculated by the method of Cusachs. An alternate set of parameters (−12.5, −7.3, −3.9 eV; 2.20, 1.40, 1.40 for the energies and exponents of the 3d, 4s, and 4p orbitals, respectively) is also capable of describing all the calculated molecular properties except the ionization potential, but predicts a double minimum for Co_2. Calculations carried out using a 3d and 4s or 3p, and 4s basis with the parameters in Tables II and III were less descriptive of the molecule, that is, gave a lower dissociation energy and a larger bond distance.

Fe_2. The properties of Fe_2 have recently been described by Lin and Kant.[12] Calculations using the Clementi parameters[18] or with Clementi–Raimondi exponents[20] for the 3d, 4s, and 4p basis were unsatisfactory. These results are only slightly improved by substituting the 3d VSIP.[19] The calculations were repeated using a 3p, 3d, 4s basis with the parameters given in Tables II and III. These results are unsatisfactory; however, the agreement with the experimental observations could be improved by increasing the core repulsions by use of −55.0 eV for the 3p orbital energy. This value of the 3p orbital energy seems unreasonable in view of the results on other molecules which use the Clementi[18] energy. All calculations using acceptable parameters on this molecule failed to give satisfactory agreement with the experiment.

Mn_2. This molecule has been described by Kant, Lin, and Strauss[10] as a van der Waals molecule because of its very low dissociation energy and large equilibrium internuclear separation. All calculations carried out on this molecule with reasonable parameters[18−20] for the 3d, 4s, and 4p basis set gave large dissociation energies at short distances. The 3p, 3d, and 4s basis calculations gave lower dissociation energies at larger distances but nevertheless predicts a stable molecule. Thus all calculations failed to satisfactorily reproduce the repulsions in the molecule.

Cr_2. The Cr_2 molecule is well known and has been studied in some detail by Kant and Strauss.[7] Calculations carried out using the 3d, 4s, and 4p basis with reasonable orbital parameters[18−20] were unsuccessful. The properties of the molecule can be described by calculations using a 3p, 3d, and 4s basis set with the parameters given in Tables II and III. The results are summarized in Table I. All calculations on Cr_2 are similar to those of the Ti_2 molecule which are illustrated in Figure 2.

V_2. The V_2 molecule has recently been described by Kant and Lin;[8] as in the case of the Cr_2 molecule, its properties are best calculated using a 3p, 3d, and 4s set. The parameters used for calculation are given in Tables II and III and the results are given in Table I. These results are similar to those of Ti_2.

Ti_2. Again, the 3d, 4s, and 4p basis with the appropriate parameters[18−20] gave unsatisfactory results when compared to experiment[7] (curves A + B, Figure 2). Calculations using a 3p, 3d, and 4s basis set with the parameters given in Tables II and III gave

results which are in good agreement with experiment, curve D, Figure 2 and Table I. Use of a 3d, 4s basis gave results which are similar to those obtained with a 3p, 3d, and 4s basis set (curve C).

Sc_2. As in the case of Ti_2 calculations with the 3d, 4s, and 4p basis with Clementi parameters, Clementi–Raimondi[18] exponents or the 3d VSIP[19] were unsatisfactory, Figure 2, when compared to experimental data.[9] The 3p, 3d, and 4s basis with the parameters given in Tables II and III gave results summarized in Table I. Apart from the uncertainty in r_e, agreement with the experimental quantities is satisfactory.

Discussion

In view of the approximations inherent in extended Hückel theory it is not surprising that the method cannot always describe molecular properties with the success previously reported for Cu_2.[1] It is also clear that optimizations of the parameters of one system do not ensure valid extensions to other systems unless some accommodation is made for electronic differences. In order to adequately approximate the molecular bonding region, the appropriate orbital exponents and Coulomb integrals must be used. In addition a proper selection of the basis set of atomic orbitals is required to calculate the potential energy surface of the molecule. The 3d orbitals are completely filled in the case of Cu_2 and Zn_2 and therefore contribute mainly to the repulsive region of the potential energy curve. For the other first row transition metals the 3d orbitals are only partially filled and therefore contribute to the molecular bonding. In order to adequately characterize the short range repulsions of these systems it was found necessary to reduce the 3d–4s orbital energy separation to increase the splitting of symmetry related molecular orbitals. In addition, when there are less than five electrons in the 3d atomic orbital, a 3p orbital core must be included in the basis set.

The parameters used to describe these molecules were close to, but in general not those of the atoms. The Hartree–Fock orbital energies and exponents of the atoms given by Clementi[18] poorly reproduced the molecular properties.

The use of Clementi–Raimondi orbital exponents[20] gave even less satisfactory results. The use of the valence state ionization potentials of Ballhausen–Gray[19] for 3d, 4s, and 4p Coulomb integrals gave results in better agreement with experiment. In a few instances, a small variation from the Ballhausen–Gray values was necessary to improve the results. The VSIP parameters are also best for the description of the ionization potential of the molecule because they are based on the ionization potential of the atoms. As a consequence the ionization potential of the molecules is not a useful criterion of the quality of the calculation. The Clementi–Hartree–Fock orbital exponent was satisfactory for the Zn and Ni calculations. For Co through to V, the Clementi–Raimondi 4s orbital exponents were used while for Sc and Ti the Veigele[23] 4s exponents were used. For the 3d orbitals, the orbital exponents which gave the best results correspond with the values of Burns[21] for the first half of the series (Sc to Cr) and with the best single-ζ Richardson exponents[26] which were calculated by the method of Cusachs, *et al.*,[24] for Fe to Ni. The trend for the 3d orbital exponents agrees with the predictions of Brown[27] for the 3d radial wave functions of the first row transition series. The 3p orbital energy used in all calculations was that of Clementi.[18] This is justified since the 3p orbitals would be best described by Hartree–Fock atomic energies which are relatively unperturbed core electrons. These values indicate that as the transition period is crossed, the 3p orbital drops rapidly in energy (from -42.0 eV for Sc to -89.0 eV for Ni) and therefore assumed a smaller role in the bonding.

The atomic Coulomb parameters used to obtain the best agreement with the molecular properties are summarized in Table II. For comparison, the Ballhausen–Gray[19] and Clementi[18] parameters are included. As expected, the 3d orbital is higher in energy than the 4s at the beginning of the transition series (Sc), but falls below the 4s after V. This trend is in accord with the parameters of Ballhausen–Gray, but not with the Clementi 3d orbital energies which for the series lie lower in energy than the 4s.

A Mulliken overlap population analysis at the equilibrium internuclear separation indicates that σ and π bonding is important to the description of Sc_2 and to a lesser extent in Ti_2. For the other molecules σ bonding predominates from the 4s and/or the $3d_{z^2}$ orbital.

The relatively poor solution for Fe_2 may be a result of the inability to expand the basis set. For Co_2 and Ni_2 the 3d, 4s, and 4p basis set was unquestionably superior to the 3p, 3d, and 4s set. However, for Sc_2 through Cr_2 the 3p, 3d, and 4s set gave the best results. For these molecules, it was necessary to include the 3p orbital in order to reproduce the repulsive region of the potential energy curve. For Fe_2, however, neither basis set gave an adequate solution. The 3d, 4s, and 4p basis set not only was less descriptive of the repulsive region but also gave an unreasonable value of D_e. On the other hand, the 3p, 3d, and 4s basis gave a somewhat better result for D_e and r_e but a substantially poorer one for the ionization potential. The calculation can only be improved by using an unrealistic value of -55.0 eV for the 3p orbital energy.

With the exception of Cr_2 and Ni_2, the ground state molecular term for these diatomics is $^1\Sigma_g^+$ (Table IV). The former have a $^3\Sigma_g^+$ term arising from a π^2 config-

(26) J. W. Richardson, W. C. Nieuwpoort, R. R. Powell, and W. F. Edgell, *J. Chem. Phys.*, **36**, 1057 (1962).

(27) D. A. Brown and N. J. Fitzpatrick, *J. Chem. Soc. A*, 941 (1966).

Table IV: The Overlap Population, Configuration, and Term Symbol of the Homonuclear Diatomic Molecules

Molecule	TOP	Configuration	Term	Term (exp't)[6-8,10,12]
Sc_2	0.516	$\sigma_{4s}^2 \quad \pi_{3d}^4$	$^1\Sigma_g^+$	$^1\Sigma_g^+$
Ti_2	0.599	$\sigma_{4s}^2 \quad \pi_{3d}^4 \quad \sigma_{3d}^2$	$^1\Sigma_g^+$	$^1\Sigma_g^+$
V_2	0.586	$\sigma_{3d}^2 \quad \pi_{3d}^4 \quad \delta_{3d}^4$	$^1\Sigma_g^+$	$^1\Sigma_g^+$
Cr_2	0.551	$\sigma_{3d}^2 \quad \pi_{3d}^4 \quad \delta_{3d}^4 \quad \sigma^*_{3d}{}^2$	$^3\Sigma_g^+$	$^1\Sigma_g^+$
Fe_2	0.354	$\sigma_{3d}^2 \quad \pi_{3d}^4 \quad \delta_{3d}^4 \quad \delta^*_{3d}{}^4 \quad \pi^*_{3d}{}^2$	$^3\Sigma_g^+$	...
Co_2	0.218	$\sigma_{3d}^2 \quad \pi_{3d}^4 \quad \delta_{3d}^4 \quad \delta^*_{3d}{}^4 \quad \pi^*_{3d}{}^4$	$^1\Sigma_g^+$	$^1\Sigma_g^+$
Ni_2	0.395	$\sigma_{3d}^2 \quad \pi_{3d}^4 \quad \delta_{3d}^4 \quad \delta^*_{3d}{}^4 \quad \sigma^*_{3d}{}^2 \quad \pi^*_{3d}{}^2$	$^3\Sigma_g$	$^3\Sigma_g$
Zn_2	−0.123	$\sigma_{3d}^2 \quad \pi_{3d}^4 \quad \delta_{3d}^4 \quad \delta^*_{3d}{}^4 \quad \pi^*_{3d}{}^4 \quad \sigma^*_{3d}{}^2 \quad \sigma_{4s}^2 \quad \sigma^*_{4s}{}^2$	$^1\Sigma_g^+$	...

uration. Only the Cr_2 result does not agree with the predictions of Kant,[6-8,10,12] although he concedes that the Cr_2 molecular state may indeed be of a higher multiplicity. The spectral transitions given for these molecules are undoubtedly too large especially for the 3p, 3d, and 4s basis set solutions. In the case of Cu_2, the 4p orbital was seen to be very important in the determination of Δ; without it, Δ became substantially too large. Therefore, the neglect of the 4p orbital in the 3p, 3d, and 4s basis set will result in an overestimation of the energies of the spectral transition. Furthermore, the neglect of configuration interaction among molecular terms will result in erroneous transition energies.

The molecular orbital description of the homonuclear diatomic molecules of the transition metals given here is by no means unique. This is exemplified by the calculations on Co_2, for which two different parameter sets satisfactorily reproduced the harmonic region of the potential energy curve. However, one of these solutions predicted a double minima in the potential energy curve and an ionization potential which agreed poorly with the experimental value. Furthermore, unreasonable 3d Coulomb integral (*i.e.*, a value between Hartree–Fock[18] and VSIP[19] energies) was required to obtain this solution. For these reasons, a solution of this nature was deemed unsatisfactory in predicting the bonding properties of the homonuclear diatomic molecules.

These calculations are generally descriptive of and consistent with a tentative assignment of the molecular parameters of the transition metal molecules. However, the method of calculation does not adequately describe the atomic repulsions for the molecules with incomplete valence shells. The transferability of these parameters to other systems is presently being tested on heteronuclear diatomic molecules including iteration to self-consistent charge.

Extended Hückel Calculations on the Color of Sulfur Chains and Rings

by B. Meyer* and K. Spitzer

Department of Chemistry, University of Washington, Seattle, Washington 98195 *(Received January 17, 1972)*

Publication costs borne completely by The Journal of Physical Chemistry

Extended Hückel calculations with Gouterman–Zerner parameters, using experimental spectra, structure, and ionization energy, were optimized to fit the energy levels of c-S_8. Structural data for other molecules and the parameters from S_∞ calculations were used to predict the energy levels of homologous series of sulfur rings, sulfur chains, sulfanes, and isomers of S_4. The results fit the spectral data for S_2, S_4, c-S_6, c-S_7, c-S_8, and c-S_{12} so well that calculations seem suitable for predicting the color and spectra of not yet discovered allotropes. Calculations on S_4 isomers and conformers indicate that a branched SO_3 structure is somewhat more stable than a chain, and thus revive the recurring postulate of branched chains of sulfur. Comparison of gas phase spectra with predicted spectra of rings and chains indicates that gas species with more than five atoms are rings. The calculations confirm recent suspicion that polymeric sulfur is not a diradical and suggest that polymeric sulfur can be a sulfane, a large ring, or a charge-transfer complex of the type (c-S_8–catena S_n–c-S_8)$_n$.

Introduction

Electronic energy levels of sulfur molecules have been computed by various methods. Miller and Cusachs[1,2] determined the energy levels of c-S_8, c-S_6, c-S_4, S_6^{2-}, H_2S, and H_2S_2, using 3s,p,d and 4s orbitals to ascertain the role of 3d orbitals and to explain the acid–base behavior of sulfur rings and chains.[3] Their calculations showed that 3d orbitals are only important for excited states. Buttet[4] used frontier molecular orbitals, applying the Wolfsberg–Helmholz method[5] to predict the diradical character of S_4, S_6, S_8, and S_{10} chains. Cruickshank[6,7] discussed the role of 3d orbitals and reviewed the results of Hartree–Fock SCF calculations on sulfur atoms, and sulfur in SF_6.[8] Energy levels of c-S_8 were classified by Palma[9] and by Clark,[10] and we have presented some preliminary results for extended Hückel calculations on a few select sulfur systems.[11] The best theoretical and experimental data are available for sulfanes, *i.e.*, polysulfide chains terminated with hydrogens. McGlynn[12] used 3s,p,d, and 4s orbitals to calculate the energy levels and transition energies of R_2S_n (n = 1 to 4), and examined the effect of 3d orbitals. Fehér[13] used a one-electron model to explain the bonding and spectra of the sulfanes which he first synthesized.

In the present work, extended Hückel calculations for four types of sulfur molecules are considered: sulfur rings, which are analogous to alkane rings; sulfur chains which are analogous to alkane diradical chains; sulfanes, which are analogous to unbranched alkane chains; and, finally, branched sulfur chains in which sulfur atoms have different oxidation states. The spectral data for S_8 are used to determine best fitting parameters for the calculations for S_8, and these parameters and the structural data for known rings, the sulfanes, polymeric sulfur, and S_2 are then used to compute electronic properties and energy levels for homologous series of rings and chains.

The purpose of this work was to use extended Hückel calculations as a simple, although crude, model for correlation of the energy levels of the various types of sulfur chains and rings. We were interested to see whether the spectral properties of S_2, S_3, S_4, c-S_6, c-S_8, and S_∞, and the qualitative data from the color of sulfur rings S_7, S_9, S_{10}, S_{12}, and S_{18} would obey systematic trends. If such trends were evident, then the color, transition energy, and stability of other, yet unknown allotropes could be predicted. We were curious to study the correlation between rings and chains of equal size in order to determine the structure of the vapor species, especially the molecular and electronic structure of the recently observed molecules S_3 and S_4,[14] and of the long known but little understood polymeric sulfur. A further important question regarded the contribution of d orbitals to sulfur–sulfur bonds.

Elemental sulfur can exist in an unusually large number of molecular forms which have widely different

(1) D. J. Miller and L. C. Cusachs, *Chem. Phys. Lett.*, **3**, 501 (1969).

(2) D. J. Miller, Ph.D. Thesis, Tulane University, New Orleans (1970).

(3) T. K. Wiewiorowski and F. J. Turro, *J. Phys. Chem.*, **70**, 3528 (1966).

(4) J. Buttet, *Chem. Phys. Lett.*, **1**, 297 (1967).

(5) M. Wolfsberg and L. Helmholz, *J. Chem. Phys.*, **20**, 837 (1952).

(6) D. W. J. Cruickshank, B. C. Webster, and D. F. Mayers, *ibid.*, **40**, 3733 (1964).

(7) D. W. J. Cruickshank, "Inorganic Chemistry of Sulfur," G. Nickless, Ed., Elsevier, Amsterdam, 1968.

(8) D. P. Craig and C. Zauli, *J. Chem. Phys.*, **37**, 601 (1962).

(9) A. Palma and N. V. Cohan, *Rev. Mex. Fis.*, **19**, 15 (1970).

(10) L. B. Clark, Ph.D. Thesis, University of Washington, Seattle (1963).

(11) B. Meyer, M. Gouterman, D. Jensen, T. V. Oommen, K. Spitzer, and T. Stroyer-Hansen, *Advan. Chem. Ser.*, **No. 110**, 53 (1972).

(12) S. D. Thompson, D. G. Carroll, F. Watson, M. O'Donnell, and S. P. McGlynn, *J. Chem. Phys.*, **45**, 1367 (1966).

(13) F. Fehér and H. Munzer, *Ber.*, **96**, 1131 (1963).

(14) B. Meyer, T. V. Oommen, and T. Stroyer-Hansen, *J. Mol. Spectrosc.*, **42**, 335 (1972).

colors. Over 44 sulfur allotropes have been reported,[15] but only very few are well characterized. The thermodynamically stable room temperature form is c-S_8, a crown-shaped ring.[16]

c-S_6 is long known[17] and the structure well determined,[18] but it cannot be easily stored, and its spectrum is not very well studied.[19] In very recent years, a series of other sulfur rings was discovered. c-S_{12} is quite stable[20] and has the same S–S–S angles and bond distance as c-S_8.[21] Other recently synthesized rings are S_7, S_9, S_{10}, and S_{18}.[22-24] Very little is known about these species except their molecular weight and structure.[25,26] All cyclic allotropes are yellow, except for the yellow-orange c-S_6. Polymeric sulfur is not a well-defined allotrope. Depending on temperature and history,[27] it consists of different mixtures of rings and chains with an average chain length between eight and several hundred thousand atoms. Liquid polymeric sulfur changes its color from yellow at the melting point to dark red at the boiling point. The color change is due to the formation of small sulfur molecules and thermal broadening of absorption.[19] Quenched polymeric sulfur is yellow at room temperature, and white, yellow, or red at −198°, depending on how quickly it was quenched.[19] Sulfur vapor contains molecules with the formulas S_2 to S_{12}. Cold vapor contains mainly S_8; at high temperature violet S_2 prevails, and at intermediate temperature and pressure red S_4 and green S_3 are abundant.[14] Mass spectroscopic studies yielded quite reliable thermodynamic data on the vapor species,[28,29] but it is not known whether gaseous molecules are rings or chains.[28]

Sulfanes, H_2S_n with n = 2 to 8, are pale yellow. They were added to our list because they can be prepared in pure form and their absorption spectra are known.[13]

Extended Hückel Model

The extended Hückel calculations used in this study follow the Wolfsberg–Helmholz method described by Zerner and Gouterman.[30,31] The computer program was written by E. Davidson of our department.

The form of the Hamiltonian is

$$H_{ij} = {}^1/_2 S_{ij}(H_{ii} + H_{jj})(k + (1 - k)\delta_{ij})$$

where S_{ij} is the basis set overlap. Calculations were done with k = 1.89. This value has been empirically determined to give the best values for other systems such as metalloporphyrins.[32] H_{ii}, the atomic orbital ionization potentials, were adjusted to suit the net atomic charge by an iterative self-consistent charge procedure, in the manner described earlier.[32] The extended Hückel parameters for sulfur and hydrogen are given in Table I. Included in this table are the orbital ionization potentials and orbital exponents for 3d sulfur orbitals.

Table I: Extended Hückel Sulfur and Hydrogen Parameters

	α_s	α_p	α_d	ξ_s	ξ_p	ξ_d
S^+	−33.8	−23.4	−9.2	2.1223	1.8273	0.84
S^0	−20.3	−10.4	−1.94	2.1223	1.8273	0.84
S^-	−11.1	−2.1	0.00	2.1223	1.8273	0.84
H^+	−15.3568	...	...	1.00	...	...
H^0	−13.5950	...	...	1.00	...	...
H^-	−0.7562	...	...	1.00	...	...

Molecular Geometries

Only a few of the structural parameters of the allotropes and compounds have been determined.[16] The X-ray geometries of the cyclic compounds S_6, S_7, S_8, and S_{12} are known.[18,21,25,26] The bond distance of S_2 is 0.1889 nm.[33] The structures of the other allotropes and compounds were assumed from known bond distances and angles in similar compounds. In S_3 the bond distance, extrapolated from the series O_3, SO_2, and S_2O is 0.198 nm and the bond angle is 120°. Longer diradical chains were assumed to be planar with a bond distance of 0.204 nm and a bond angle of 104°. Figure 1 shows the various forms and structures which we considered for S_4. Sulfanes have H–S distances of 0.140 nm; an S–S–H angle of 95°; an S–S distance of 0.204 nm, except for H_2S_2 where the distance is 0.195 nm; and an S–S–S angle of 104°.[13]

Results and Discussion

c-S_8. c-S_8 has been more extensively studied than any other sulfur allotrope. The ionization potential is

(15) B. Meyer in "Elemental Sulfur, Chemistry and Physics," B. Meyer, Ed., Interscience, New York, N. Y., 1965.

(16) J. Donohue, Chapter 2 in ref 15.

(17) M. R. Engel, *C. R. Acad. Sci.*, **112**, 866 (1891).

(18) J. Donohue and A. Caron, *J. Amer. Chem. Soc.*, **83**, 3748 (1961).

(19) T. V. Oommen, Ph.D. Thesis, University of Washington, Seattle (1970).

(20) M. Schmidt and E. Wilhelm, *Angew. Chem.*, **78**, 1020 (1966).

(21) A. Kutoglu and E. Hellner, *Angew. Chem., Int. Ed. Engl.*, **5**, 965 (1966).

(22) M. Schmidt, B. Block, H. D. Block, H. Kopf, and E. Wilhelm, *Angew. Chem.*, **80**, 660 (1968).

(23) M. Schmidt and E. Wilhelm, *J. Chem. Soc. D*, **17**, 1111 (1970).

(24) M. Schmidt and E. Wilhelm, unpublished data.

(25) I. Kawada and E. Hellner, *Angew. Chem. Int. Ed. Engl.*, **9**, 379 (1970).

(26) A. Caron and J. Donohue, *Acta Crystallogr.*, **18**, 562 (1965).

(27) R. E. Harris, *J. Phys. Chem.*, **74**, 3102 (1970).

(28) J. Berkowitz and J. R. Marquart, *J. Chem. Phys.*, **34**, 275 (1963).

(29) D. Detry, J. Drowart, P. Goldfinger, H. Keller, and H. Rickert, *Z. Phys. Chem. (Frankfurt am Main)*, **55**, 317 (1967).

(30) M. Zerner and M. Gouterman, *Theor. Chim. Acta*, **4**, 44 (1966).

(31) M. Zerner and M. Gouterman, *Inorg. Chem.*, **5**, 1699 (1966).

(32) A. Schafer, Ph.D. Thesis, University of Washington, Seattle (1972).

(33) G. Herzberg, "Molecular Spectra and Molecular Structure," Vol. I, Van Nostrand, Princeton, N. J., 1950.

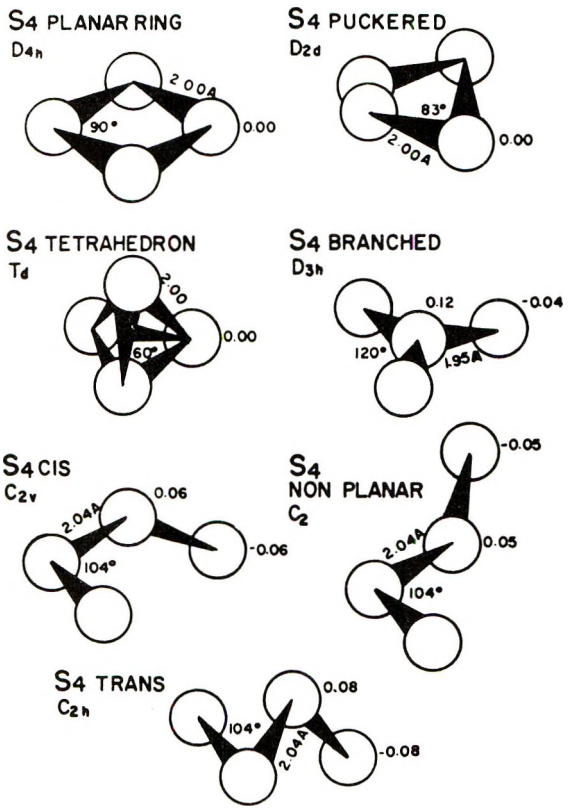

Figure 1. Seven isomers of S_4. Figure indicates bond distance, bond angle, and computed charge imbalance.

9.04 eV, as established experimentally by Berkowitz.[34] The electronic spectrum of c-S_8 crystals and solutions is known at room temperature and at 76°K,[19] and the first transition energy is approximately 4.0 eV.[10]

Semiempirical calculations on this allotrope neglected 3d orbitals, except for Cusachs and Miller.[1,2] These authors were able to compute correct experimental values for the ionization potential and the transition energy and established that the sulfur 3d orbitals do not contribute greatly to the filled molecular orbitals, but are important in the virtual orbitals.

We chose a method similar to that of Cusachs and Miller. The energy levels of S_8 computed with our Hückel program are shown in Figure 2. The most important differences in our approach are the choice of orbital exponents (Zed), the pure parameter k, and the valence state ionization potentials (VSIP). We used VSIP values from Moore's tables,[35] which are deduced from experimental data. Cusachs and Miller's values varied slightly from these values. Moreover, their formula for H_{ij} allows k to vary with the overlap S_{ij}, while in our calculations k was fixed at 1.89. Cusachs and Miller varied the orbital exponents of the sulfur 3s,p,d orbitals so that overlap population was maximized in the hypothetical c-S_4. Their value of Zed_{3d} of 1.70 implies that the molecular 3d orbitals are highly contracted compared to the free atom. In our calculations we used Zed_{3s} and Zed_{3p} from Clementi and Raimondi rules.[36] Zed_{3d} was varied to optimize the first transition energy. All calculations were performed with and without inclusion of 3d orbitals. Since energetically the 3d orbitals were found to contribute little to the filled orbitals, variations in Zed_{3d} affect the filled molecular orbitals little. As shown in Figure 2, Zed_{3d} was optimized to reproduce the experimental values for c-S_8. This occurred at Zed_{3d} of 0.84. This implies the 3d orbitals are more diffuse than those of Cusachs, more contracted than those of the free atom (Slater's rules), and similar to those predicted for SF_6.[8] The parameter values established for c-S_8 were used in all the rest of the calculations presented here. These values are shown in Table I.

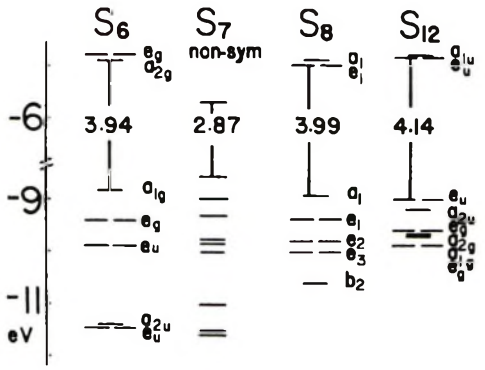

Figure 2. Energy levels of sulfur rings.

Other Rings. We have included in our calculations only those rings for which structural X-ray data are known.

The results of the computation on c-S_6 are shown in Figure 2. The transition energy, 3.9 eV, agrees with Cusach's value of 3.85 eV[1] but it is still slightly large for the absorption band at 350 nm.[19] The yellow-orange color of S_6 is caused by a flat red tail of the absorption which extends further towards the visible than that of c-S_8.

Figure 2 shows that the first transition of S_7 is predicted at 2.87 eV. This is too far to the red to be consistent with the light yellow color. However, the structural data for S_7 are not very reliable, and only the projection onto the xy plane is known.[25] c-S_7 is nonsymmetrical with unequal bond angles and distances. Small variations from the assumed bond distance in this distorted molecule could easily account for the missing transition energy.

The structure of light yellow S_{12} is well established.[21] The results of our calculation shown in Figure 2 produced a gap of 4.14 eV for the transition in accord with the color.

(34) J. Berkowitz and C. Lifshitz, *J. Chem. Phys.*, **48**, 4347 (1968).

(35) C. E. Moore, "Atomic Energy Levels as Derived from Analysis of Optical Spectra," Vol. I, U. S. Printing Office, Washington, D. C., 1949–1958.

(36) E. Clementi and D. L. Raimondi, *J. Chem. Phys.*, **38**, 2686 (1963).

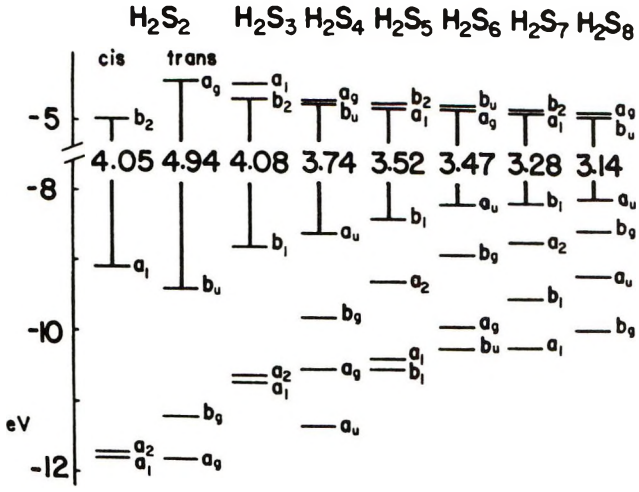

Figure 3. Energy levels of sulfane chains.

Sulfanes. The spectra of the sulfanes H_2S_n, with $n = 2$ to 8, have been published by Fehér[13] and coworkers, who also were the first to synthesize these compounds in pure form. The structure of these chains is not known. For our calculations we have assumed planar zigzag chains. The sulfanes are colorless with absorption edges converging toward 400 nm with increasing chain length. The results of the calculations are shown in Figure 3. In all sulfanes the gap between the top filled and lowest empty orbitals is large. The predicted transition energies are in excellent agreement with the published spectra, and the trend of the transitions of homologs parallel the trend of the absorption maxima. Figure 3 also shows the cis–trans effect for H_2S_2. Although there is little difference in total energy, the trans formation shows the largest gap between the top filled and lowest empty orbitals. It is conceivable that H_2S_2 has a conformation between these two extremes.

Sulfur Chains. Sulfur chains are diradicals. Diatomic sulfur has a $^3\Sigma_g^-$ ground state, like oxygen, and has a very short bond length of 0.1889 nm.[33] The structure of S_3 is not known. We assumed that it can be extrapolated from the structures of O_3, SO_2, and S_2O. For all longer chains we assumed, for simplicity's sake, planar zigzag structures. The results of the computations are shown in Figure 4. For longer chains, the lowest empty orbital is very close to the highest filled orbital. Our crude calculations do not include configuration interaction, so it is likely that the ground state of long chains is triplet. This would be consistent with the experimental esr spectrum of liquid sulfur.[37,38] Buttet used frontier orbitals in similar calculations on S_4, S_6, S_8, and S_{10} spiral chains to explain the Δ_g and hyperfine tensor elements in the esr spectrum.[4]

The transition energy between the second lowest unoccupied orbital and the highest filled orbital decreases from 5.9 to 3.1 eV with increasing molecular weight. This red shift results from the higher density of states

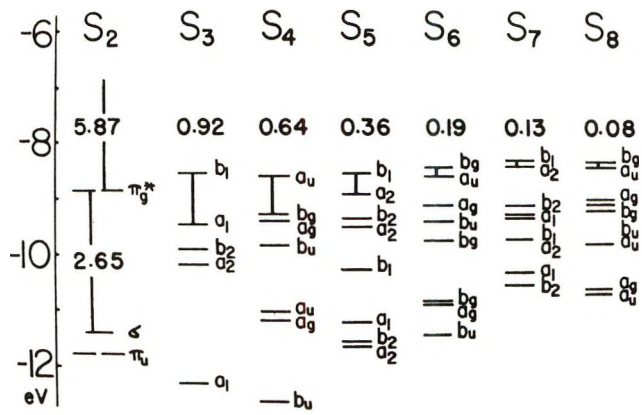

Figure 4. Energy levels of sulfur diradical chains.

in large molecules. It is consistent with the red shift which is experimentally observed in the spectrum of the series S_2, S_3, S_4.[11,14] However, all computed transition energies are somewhat larger than observed.

S_2 is included in our calculations for completeness sake. Our theoretical model is certainly not ideal for S_2. The highest filled and lowest empty orbitals of S_2 are theoretically degenerate. Since transitions in the near-uv occur from the lower filled orbitals to the degenerate orbitals, transitions to the higher empty orbitals in the vacuum-uv are molecular Rydberg transitions.

S_3 calculations indicate a transition energy of 0.92 eV. The visible transition at 430 nm which was recently observed in the gas phase[14] is probably from lower occupied orbitals. The transition at 0.92 eV corresponds to the lowest known transition of ozone at 1.24 eV.[33]

S_4 has a transition energy of 2.4 eV corresponding to the first strong absorption at 510 nm. It is, however, interesting to consider whether S_4 is really a planar zigzag chain, as assumed for this computation. Figure 1 shows seven conformers and isomers used to test for other possible structures. The results of the calculations are shown in Figure 5. The charge distribution is indicated in Figure 1. The structure for which our computations give the lowest total energy is the branched chain structure similar to SO_3. The energy gap is too large for a diradical species. The computed charge distribution suggests the resonance structure

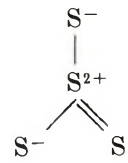

The cyclic S_4 shows no charge imbalance, while the chains have negative ends, as do all chain allotropes.

(37) D. M. Gardner and G. K. Fraenkel, *J. Amer. Chem. Soc.*, 78, 3279 (1956).

(38) D. C. Konigsberger, Ph.D. Thesis, Technische Hogeschool Eindhoven (1971).

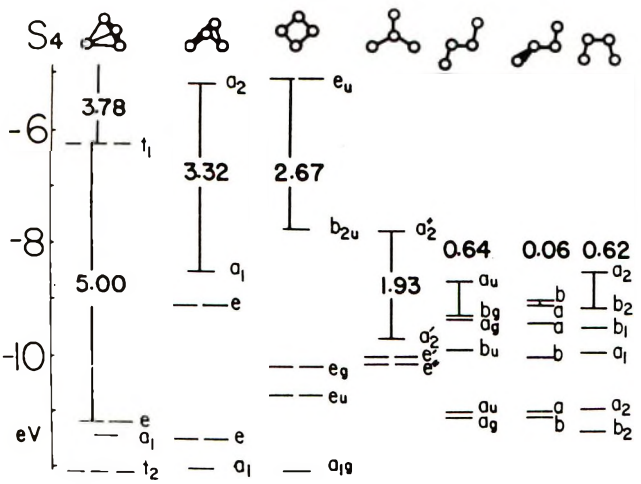

Figure 5. Energy levels of seven isomers of S_4.

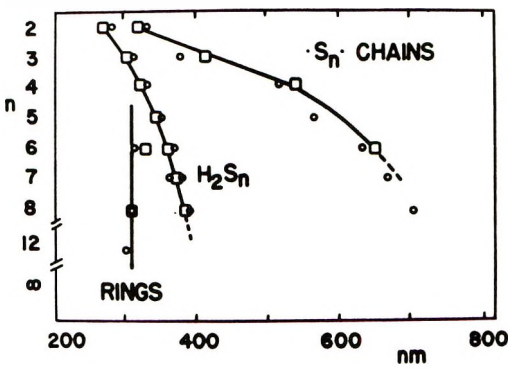

Figure 6. Calculated and observed first transition energy of sulfur allotropes. Circles indicate computed values, squares indicate observed absorption maxima. Diradical chain values are scaled.

The relative stabilities of the S_4 conformers, as obtained here, are branched chain > zigzag > cis > helical > cyclic planar > puckered cyclic > tetrahedron.

However, the total energy difference between the branched chain and the zigzag chain is merely 0.38 eV. While the branched structure is predicted to be green, the S_4 spectrum in matrices and the gas phase is more compatible with a chain. The theoretical stability of a branched S_4 reinforces an old, recurring hypothesis by many inorganic chemists and should encourage renewed search for methods to make such an isomer.

S_5 and longer chains are expected to absorb to the red of S_4. We have conducted experiments for the synthesis of S_6 in frozen solution and found an as yet insufficiently identified series of six bands at 620 nm with a vibrational spacing of 350 cm^{-1} which might well belong to this molecule.[14] The prediction of a red color for these molecules also led us to study the absorption of sulfur vapor, because mass spectra and vapor pressure measurements indicate their presence.[28] We found that the vapor never shows more than a weak shoulder on the S_4 spectrum. Thus, sulfur vapor must contain S_5, S_6, S_7, and S_8 as rings which absorb in the uv. It would be valuable but difficult to study the uv spectrum of vapor between 180 and 400 nm where all these rings should absorb.

Polymeric Sulfur. As mentioned above, viscosity and polymerization theory indicate that polymeric sulfur contains chains with up to 500,000 S_8 units. Figure 6 shows that extrapolation of our calculations on linear S_n chains leads us to predict that diradical species are dark red or black. However, it is well known that this allotrope is dark yellow in the liquid, and yellow at room temperature, and has an absorption peak at 360 nm.[19] Thus, the observed spectrum is not compatible with our calculations. Figure 6 shows that the transition at 360 nm lies also at the wrong end of the experimental data for the chain series S_2, S_3, and S_4. This violates basic knowledge of spectral behavior

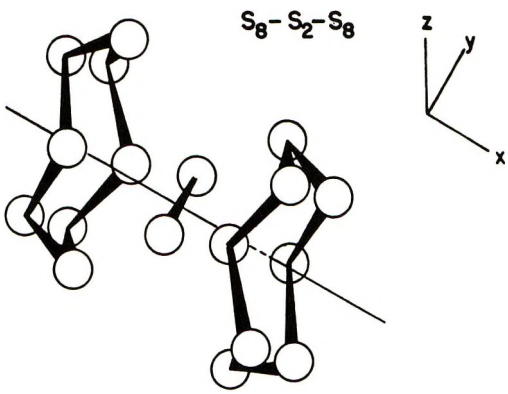

Figure 7. Geometry of c-S_8–S_2–c-S_8 charge-transfer complex.

of homologous molecules and raises suspicion about the widely adopted diradical model for polymeric sulfur. Similar doubts about the diradical nature have been provoked by esr studies[37,38] which yield unexpectedly weak signals.

Wiewiorowski[3] proposed that catena S_8 forms charge-transfer complexes with S_8 rings. Konigsberger[38] has used this model of (c-S_8–catena S_8–c-S_8)$_n$ and found good agreement with his new esr data. To test this suggestion by extended Hückel calculation is, for us, unfortunately, not practical. However, the question of c-S_8 ability to participate in charge-transfer complexes can be tested with smaller molecules. We did a number of calculations assuming S_2 sandwiched between two c-S_8, as shown in Figure 7. When the rings were at 0.4 nm or further away from S_2, no charge transfer took place, and the energy levels retained the characteristics of the separated molecules. When the rings were at 0.2 nm, *i.e.*, the closest ring atom at 0.34 nm, charge transfer also did not take place. However, when the S_2 was positioned 0.3 nm from the center of each ring, electron density shifted to S_2; the highest S_8

orbital and the S_2 lost their degeneracy, and a splitting of 0.35 eV resulted between the highest filled orbital and the lowest empty orbital. The next higher orbital was 3 eV higher. Since the filled orbitals were not greatly affected, the transitions expected would be similar to those of the separated molecules, but would appear slightly blue shifted. Thus, calculations confirm that c-S_8 has the ability to participate in charge-transfer complexes. It should be pointed out that our S_2 model is not a very realistic approximation for polymeric sulfur which contains long helical chains. However, if the splitting of the degeneracy of S_2 is in any way comparable to the splitting in S_8 and longer chains, the blue shift of the charge transfer is not nearly large enough to explain the yellow color of polymeric sulfur. Thus, according to our model, the S_8 ring–S_8 chain complexes would still be deeply colored. This raises doubts in this otherwise very convincing model for polymeric sulfur. Figure 6 leads us to suggest, however, another possible interpretation. The absorption of polymer fits the convergence limit of long sulfane chains extremely well. The presence of sulfanes is also compatible with the very weak esr spectrum. Furthermore, it is chemically quite likely that polymerization yields long sulfanes, because polymer forms above 160°, and at this temperature hydrocarbon impurities readily react with elemental sulfur.[39] High purity sulfur is at best 99.999% pure and chains with 500,000 sulfur atoms[14] can be saturated with as little as 10^{-6} wt % of an alkane impurity.

A further possibility, based on Figure 6, is that polymeric sulfur contains very large rings, perhaps intertwined helices. However, such interpretations are still quite speculative. In any case, our computations of chains and rings clearly confirm that liquid sulfur does not consist of long free radical chains.

Summary

A simple Hückel calculation, originally developed for metalloporphyrins,[30,31] can be used to compute transition energy and ionization energy of S_8. The S_8 parameters, combined with structural data or assumptions, lead to computation of homologous series of chains and rings which fit the experimental spectral data extremely well and allow prediction of unknown species. All rings and sulfanes are yellow, while chains absorb in the visible and, with increasing size, become darker and redder. Comparison of the vapor spectrum with our calculations shows that gas phase species larger than S_5 are cyclic, while S_4 is most likely a chain, or a branched chain. The prediction that long diradicals must be black is consistent with experiments and the behavior of analogous diradical species. Thus, polymeric sulfur cannot be a long diradical chain, as is often assumed. Instead, it is more likely a sulfane or a charge-transfer complex. The two latter models are compatible with the originally mysterious esr spectrum.[37,38]

Acknowledgment. The authors are indebted to Professor M. Gouterman, who suggested this project, and to Professor E. Davidson, who made his elegant computer program available. Without this program, computations would have been prohibitively expensive despite the support of the National Science Foundation and the Evironmental Protection Agency. K. S. was partly supported by a Chevron Research Fellowship.

(39) S. Oae, *J. Chem. Soc. Jap.*, in press.

Water Vapor Adsorption by Pure Silver Iodide above Ice Saturation[1]

by W. R. Barchet*[2] and M. L. Corrin

Department of Atmospheric Science, Colorado State University, Fort Collins, Colorado 80521 *(Received August 16, 1971)*

Publication costs assisted by the Atmospheric Science Program, National Science Foundation

Adsorption isotherms of water vapor on pure silver iodide are measured gravimetrically at equilibrium pressures between ice and water saturation. At −3.00° a stable adsorbed film exists at water saturation. However, at −6.50 and −10.00° nucleation of ice on the samples terminates the isotherms. Isosteric heats of adsorption and differential film pressures are calculated from smoothed isotherms. The shape of the isosteric heat curves indicates that the adsorbate is patchwise distributed on the surface. Kinks in the differential film pressure curves are evidence for a phase change in the adsorbate. Both the isosteric heats and film pressures indicate the presence of a liquidlike adsorbate–vapor interface prior to nucleation. The variation of embryo size, based on surface excesses, and the variation of supersaturation at nucleation with temperature are contrary to classical theory. The liquidlike interface may inhibit the nucleation of ice from the vapor at temperatures above −10°. Nucleation observed by this adsorption technique appears to occur after equilibrium adsorption and equilibrium size distributions of subcritical embryos have been attained. Supersaturations required to initiate ice crystal growth are much lower than previously found. Little experimental attention has been given to adsorption under saturated and supersaturated conditions. This study on pure silver iodide may serve as a base line against which further adsorption and nucleation studies on impure or doped materials can be compared.

Introduction

Since 1952 the interaction between water vapor and silver iodide has been extensively studied by adsorption techniques.[3−9] The purpose of these studies, either stated or implied, has been to determine the role of the silver iodide substrate in enhancing the vapor to solid phase transformation of water. Adsorption methods were employed to examine the energetics of the interaction between the surface and the vapor on as small a scale as possible. At low pressures of the vapor and correspondingly small surface coverages, adsorption thermodynamics provided a means of interpreting adsorption isotherm data in terms of the enthalpy of adsorption and thus gave the energy of the interaction between the surface and the vapor.

However, impurities in the silver iodide were recognized and shown[10−12] to affect the adsorption isotherms and, therefore, also the enthalpy of adsorption. Material containing ionic impurities, presumably coprecipitated from aqueous solution with the silver iodide, produced heats of adsorption curves with distinct low coverage minima and a gradual rise toward the heat of condensation as the coverage increased.[7,8] Such isosteric heat curves were considered characteristic of adsorption on and cluster formation around ionic impurity sites on the surface. On silver iodide powder presumably free of ionic impurities,[13] the adsorption isotherms led to isosteric heat curves with a very low coverage minimum, a maximum above the heat of condensation at just slightly higher coverages, and finally a decrease toward the heat of condensation with increasing coverage.[9] The behavior of the heat of adsorption in the case of pure silver iodide was interpreted as evidence for adsorption on patches of sites exhibiting a strong interaction with water vapor,[14] the remainder of the surface interacting weakly with the vapor.

These adsorption studies probably provide adequate models for the distribution of adsorbed vapor at relatively low coverages and well removed from saturated conditions. In only one instance, and that on impure silver iodide,[4] has adsorption been measured at high coverages in the vicinity of vapor saturation. Since the underlying goal of adsorption studies on the water vapor–silver iodide system is to increase our knowl-

(1) Based on a thesis by W. R. B. submitted in partial fulfillment of the requirements for the Ph.D. degree at Colorado State University, Fort Collins, Colo., March 1971.

(2) Address correspondence to this author at the Department of Meteorology, University of Wisconsin, Madison, Wis. 53706.

(3) M. L. Coulter and G. A. Candela, *Z. Elektrochem.*, **56**, 449 (1952).

(4) S. J. Birstein, *J. Meteorol.*, **12**, 324 (1955).

(5) N. N. Moskvitin, M. M. Dubinin, and A. I. Sarakhov, *Izv. Akad. Nauk SSSR, Otd. Khim. Nauk*, **12**, 2080 (1959).

(6) A. C. Zettlemoyer, N. Techeurekdjian, and J. J. Chessick, *Nature (London)*, **192**, 653 (1961).

(7) P. G. Hall and F. C. Tompkins, *Trans. Faraday Soc.*, **58**, 1734 (1962).

(8) N. Tcheurekdjian, A. C. Zettlemoyer, and J. J. Chessick, *J. Phys. Chem.*, **68**, 773 (1964).

(9) M. L. Corrin and J. A. Nelson, *ibid.*, **72**, 643 (1968).

(10) M. L. Corrin and N. S. Storm, *ibid.*, **67**, 1509 (1963).

(11) M. L. Corrin, H. W. Edwards, and J. A. Nelson, *J. Atmos. Sci.*, **21**, 555 (1964).

(12) M. L. Corrin, S. P. Moulik, and B. Cooley, *ibid.*, **24**, 530 (1967).

(13) M. L. Corrin, J. A. Nelson, B. Cooley, and B. Rosenthal, *ibid.*, **24**, 594 (1967).

(14) H. W. Edwards and M. L. Corrin, *J. Phys. Chem.*, **71**, 3373 (1967).

edge of the mechanism of nucleation of ice on this material, adsorption of the vapor must be measured up to the onset of nucleation. In contrast to measurements at low pressures which provide information on the surface–vapor interaction, measurements near the threshold of nucleation can provide an insight into the adsorbate–vapor interaction and the transition of the embryo into a growing nucleus as well.

This work is done on pure silver iodide to provide a base line against which further studies on impure or doped materials can be compared. Adsorption isotherms are measured gravimetrically to verify the patch model at the onset of nucleation, to determine the energetics of adsorption prior to nucleation, and to examine the transition of the adsorbed vapor into a growing ice nucleus.

Experimental Section

Materials. Silver iodide powders prepared by precipitation from aqueous solutions have been used in most adsorption studies. However, even the most careful preparation and washing of the precipitate was found not to remove coprecipitated ionic impurities.[10] To eliminate the ionic impurities a technique was developed for preparing silver iodide by the direct reaction between silver metal and iodine vapor.[13]

The reactants, reagent grade silver metal powder (Fisher Certified) and iodine crystals, were placed in a Pyrex vessel which was then evacuated, sealed, and placed in an oven at 140°. When the reaction was complete, the vessel was again evacuated to remove any unreacted iodine vapors. The silver iodide was separated from an excess of silver metal by dissolution in liquid ammonia; the liquid ammonia solution was siphoned off. A solid silver iodide–ammonia complex was obtained by allowing excess ammonia to evaporate. The complex, when pumped on and slightly warmed, explosively decomposed into a finely divided, extremely pure silver iodide powder. After additional pumping the powder was transferred in a water vapor free atmosphere to small, blackened, Pyrex ampoules which were then evacuated and sealed under high vacuum.

Silver iodide powders prepared in this fashion are presumably free of hygroscopic ionic impurities. The violent decomposition of the complex undoubtedly results in numerous surface dislocations and considerable strain; however, a direct measure of the dislocation count is not available.

One ampoule, prepared at the University of Arizona in 1967, provided all the silver iodide used in this study. Krypton adsorption isotherms were measured on this powder at liquid nitrogen temperature. A surface area of 0.49 $m^2\ g^{-1}$, standard deviation of 5%, was calculated by applying the BET relation to the measured isotherms.[10] No change in surface area was detected over the course of this work; the samples were well aged.

Distilled water, degassed on the adsorption system and distilled in the absence of other gases into a storage reservoir, served as the adsorbate vapor. The water (ice) in the storage reservoir was isolated from the adsorption system to prevent contamination of the water when the system was open to the atmosphere.

Method. The heart of the adsorption system was a Cahn electrobalance, Model RG, housed in a Pyrex vacuum jar. Viton O rings sealed the sample and tare hangdown tubes, the balance jar end cap, and the vacuum system to the balance jar. A mechanical fore pump, isolated from the system when not in use by a bellows sealed valve, was used to bring the system pressure down to a few milliTorr; a 13X molecular sieve trap prevented back-diffusion of pump oil vapors into the system. Final pumping was performed by an Ultek ion pump with the bellows valve closed; pressures less than 4 μTorr were maintained for several hours before each run to remove volatile material from the system. Large-diameter Pyrex tubing connected the pumping system and water reservoir to the balance jar.

The sample hangdown tube and water (ice) reservoir were immersed in separate thermostats which served to control sample temperature and the pressure of water vapor in the system, respectively, during an adsorption run. A mercury thermoregulator in the sample bath and a Sargent Thermonitor proportional temperature controller in the ice reservoir bath maintained bath temperatures against a constant cooling rate. Temperature control to $\pm 0.02°$ in the thermostats, measured by a platinum resistence thermometer calibrated by the National Bureau of Standards, permitted the pressure, saturation vapor pressure, and the relative pressures to be specified to less than 0.1% using empirical pressure–temperature relationships.[15,16] No attempt was made to measure the pressure of water vapor directly.

A small quantity of pure silver iodide, 0.7–0.9 g, was transferred in a water vapor free atmosphere to a 16-mm diameter, hemispherical, fused quartz pan. The pan was hung near the bottom of the sample hangdown tube on a quartz fiber attached to the balance; the adsorption system was closed and evacuated. Taring and calibration of the balance were carried out *in vacuo* at the start of each run; separate samples were used for each run.

To start an isotherm measurement, the stopcock isolating the ice reservoir from the system was opened. Adsorption of water vapor was detected as a change in weight of the silver iodide sample. The output of the electrobalance was displayed on an integrating digital voltmeter; a statistical treatment of the adsorption

(15) E. W. Washburn, *Mon. Weather Rev.*, **52**, 488 (1924).

(16) G. Jancso, J. Pupezin, and W. A. van Hook, *J. Phys. Chem.*, **74**, 2984 (1970).

data giving the mean and standard deviation of the amount adsorbed was possible. Data were not collected until the balance output remained steady in time. During this time, the temperature of the ice reservoir was kept constant to provide a constant pressure of the vapor in the system. Additional data points were obtained by stepwise increases of the ice reservoir temperature; the weight of the sample was allowed to reach a steady value after each increase in ice reservoir temperature. The weight of the sample at each ice reservoir temperature was corrected for balance calibration and adsorption on the balance. Minimum detectable weight changes were less than 10 μg.

Results

Water vapor adsorption isotherms measured on pure silver iodide at -3.00, -6.50, and $-10.00°$ could be divided into two groups, those with nucleation and those without. Nucleation of ice, detected as a rapid, unbounded increase in the weight of the sample, occurred at -6.50 and $-10.00°$. However, the amount of water vapor adsorbed at $-3.00°$, as shown in Figure 1, remained finite even at a pressure of the vapor equal to saturation over undercooled water. Surface excesses, coverages, are given in nanomoles per unit area (nmol cm^{-2}) based on the krypton surface area of the silver iodide powder. The isotherms at -6.50 and $-10.00°$, shown in Figure 2, covered a much smaller range of surface excesses and were terminated by nucleation on the sample at system pressures of 2.73 and 2.00 Torr, respectively. Condensation on the wall of the sample hangdown tube prevented measurements above water saturation pressure at $-3.00°$. The amounts adsorbed are much smaller than on contaminated[4,5,8] silver iodide and are close to previous low-pressure measurements on pure silver iodide.[9]

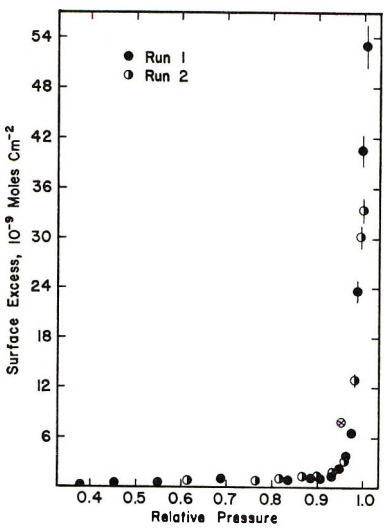

Figure 1. Water vapor adsorption isotherms at $-3.00°$ on pure silver iodide show a rapid increase in the amount adsorbed above a relative pressure with respect to the supercooled liquid which corresponds to saturation over ice. The amount adsorbed remains finite even at water saturation. Vertical bars indicate a one standard deviation error estimate about the mean data points.

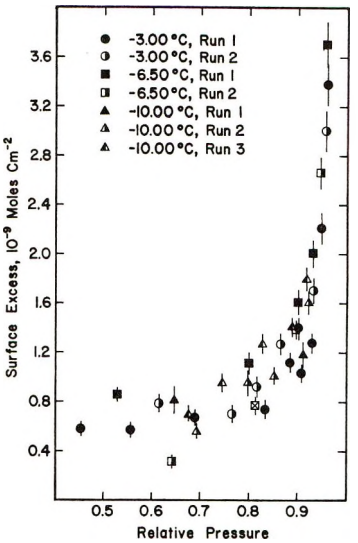

Figure 2. This composite of adsorption isotherms on pure silver iodide at -10.00, -6.50, and $-3.00°$ shows the similarity between the isotherms and the rapid rise in amount adsorbed as equilibrium relative pressures above ice saturation are attained. Isotherms at -10.00 and $-6.50°$ were terminated by nucleation on the sample at relative pressures of 0.930 and 0.967 with respect to water, respectively. Vertical bars indicate a one standard deviation error estimate.

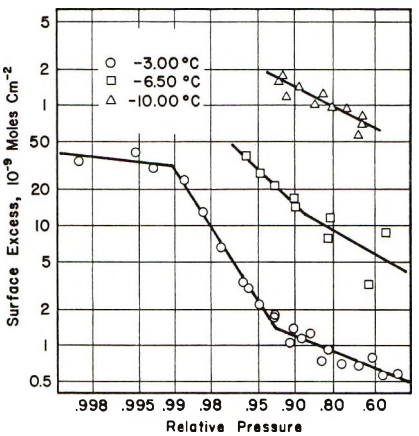

Figure 3. Smoothing of the adsorption data is based on this ln *vs.* ln ln plot of the surface excess and relative pressure. Values for the surface excesses at $-6.50°$ are increased by a factor of 10, while the scale is changed for the $-10.00°$ isotherm to permit all three isotherms to be clearly shown.

Mechanical noise on the output signal and undetectable changes in balance zero as well as inhomogeneities in the silver iodide that provided the samples for the adsorption work are possible causes for the scatter in the data for isotherms at the same temperature seen in Figure 2. To smooth the data, an empirical isotherm equation similar to the Frenkel–Halsey–Hill[17,18]

(17) T. L. Hill, *Advan. Catal.*, **4**, 211 (1952).

(18) C. Pierce, *J. Phys. Chem.*, **64**, 1184 (1960); C. Pierce and B. Ewing, *J. Amer. Chem. Soc.*, **84**, 4070 (1962).

Table I: Empirical Smoothing Isotherm Parameters

Isotherm	Straight line segment limits				Straight line parameters		
	Γ_{lower}[a]	Γ_{upper}[a]	p_{lower}[b]	p_{upper}[b]	a	b	n
−3.00°		1.386	1.670	3.423	−0.712	−0.396	1.53
	1.386	24.53	3.423	3.640	−3.857	−1.534	−0.35
	24.53	51.40	3.640	3.677	2.954	−0.107	8.34
−6.50°		1.250	1.493	2.490	−0.953	−0.567	0.76
	1.250	4.49	2.490	2.730	−1.740	−0.946	0.06
−10.00°		1.70	1.445	2.000	−0.804	−0.502	0.99

[a] Γ in nmol cm^{-2}. [b] p in Torr.

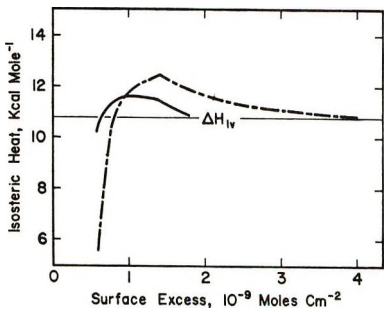

Figure 4. Isosteric heats of adsorption based on all three isotherms are shown as the solid curve. The peak in the isosteric heat is more evident in the curve based on the −3.00 and −6.50° isotherms given as the dashed curve.

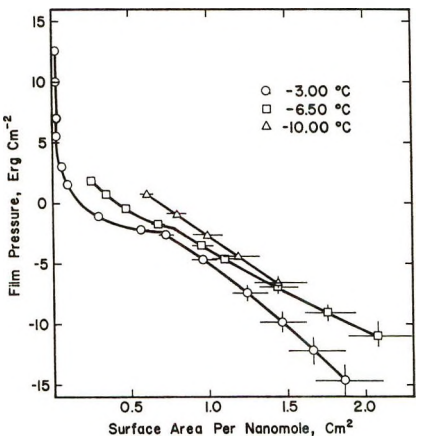

Figure 5. The surface free energy of the silver iodide–water vapor interface at ice saturation pressure is taken to be the reference state for the film pressure *vs.* surface area curve presented above. Horizontal and vertical bars give standard deviation error estimates.

isotherm was fitted to the data by a least-squares method. As Figure 3 shows, the −3.00 and −6.50° data lie on more than one straight line when the empirical isotherm is expressed as

$$\ln \Gamma = a + b \ln \ln p_0/p \qquad (1)$$

where Γ is the surface excess, p is the equilibrium pressure, p_0 is the saturation pressure over water, and a and b are the empirical straight line parameters. Table I gives the values of these parameters for the straight line segments.

Isosteric heats of adsorption, shown in Figure 4, are computed from isosteres given by the smooth isotherms using a Clausius–Clapeyron expression[17]

$$q_{st} = -R\left(\frac{\mathrm{d} \ln p}{\mathrm{d}(1/T)}\right)_\Gamma \qquad (2)$$

where T is the absolute temperature at which the isotherm was measured and R is the universal gas constant.

The empirical isotherm equation is also used to integrate analytically the Gibbs equation[17,19]

$$\Delta\pi = RT\int_{p_1}^{p_2} \frac{\Gamma}{p'}\mathrm{d}p' \qquad (3)$$

where $\Delta\pi$ is the differential film pressure. The reference state for the integration is taken, for convenience, to be the surface free energy of the adsorbent–vapor interface at ice saturation pressure, *i.e.*, p_1 is the saturation vapor pressure over ice at the isotherm temperature. Figure 5 shows the film pressure plotted against the surface area occupied per unit quantity of adsorbate.

Discussion

The differential nature of the isosteric heat of adsorption provides information on the energy of adsorption of molecules which "see" the adsorbent already covered with some adsorbate. At low pressures, when the adsorbent is nearly bare, the vapor will probably interact more strongly with the bare adsorbent than with previously sorbed molecules. On pure silver iodide this gives rise to a low coverage minimum in the isosteric heat curves.[9,14] Above this minimum, however, an increase in isosteric heat can only come from interactions between the vapor and the adsorbate; the strong adsorbent–vapor interaction sites have been occupied. The adsorption data presented here do not show a low coverage isosteric heat minimum because the adsorption measurements were

(19) G. Jura and W. D. Harkins, *J. Amer. Chem. Soc.*, **68**, 1941 (1946).

made only in the high coverage region. However, the rapid rise in adsorption energy to a maximum which occurs before statistical monolayer coverage,[20] 1.63 nmol cm^{-2}, is again indicative of a patchwise distribution of adsorbate on the surface. The trend toward the heat of condensation after the maximum in isosteric heat is attained indicates that the interface between the adsorbate and vapor becomes increasingly liquidlike with additional coverage, at least at temperatures above $-10°$.

Further evidence for a liquidlike film or interface is found in the film pressure curves in Figure 5. Kinks such as those seen in Figure 5 and in the isotherms as shown in Figure 3 have been interpreted as evidence for a change in phase of the adsorbed film.[18,19] Equation 1 may be transformed to

$$\Delta\pi = k\sigma^n + k' \qquad (4)$$

where σ is the surface area occupied per molecule and $n = -(b + 1)/b$. This is just a modified form of Jura and Harkins' condensed surface phase ($n = 1$).[19] As seen in Table I, n changes from a value near unity to a value much less than unity as the coverage increases. Such a transition corresponds to a change from a rigid structure ($n \approx 1$) to a more mobile structure ($n \ll 1$) of the adsorbate. However, this change need not necessarily extend through all of the adsorbed material. An alteration in the structure of the interface between the adsorbate and the vapor could account for the kinks and also for the peak in the isosteric heat curves.

The absence of a kink in the $-10.00°$ curve of Figure 5 means that either a transition in the adsorbate did not occur or the transition occurred so close to the termination of the $-10.00°$ isotherm that it could not be resolved. Recent theory on the surface structure of bulk ice calls for a liquidlike surface film to exist down to $-13°$ and possibly to $-30°$.[21]

The unbounded increase in amount adsorbed which led to the termination of the isotherms at -6.50 and $-10.00°$ was considered to be evidence for the nucleation of ice, the only stable phase possible at subzero temperatures and pressures below water saturation. If patches of sites that interact strongly with water vapor form the foundations for nucleation embryos, then those patches giving rise to the largest embryos will be favored in the nucleation process. Only one such embryo must reach the critical size and continue to grow for the adsorption method to detect nucleation. Adsorption parameters at the onset of nucleation are shown in Table II. There are several interesting features to these data.

The surface excess at nucleation clearly increases with temperature. It seems logical to assume that the number of embryos which may form on the patches which strongly adsorb water as well as the number of patches does not increase with temperature. Therefore, the increase in surface excess seems to indicate the embryos themselves are larger at warmer temperatures.

Table II: Adsorption Parameters at Nucleation

Parameter	$-3.00°$ [a]	$-6.50°$	$-10.00°$
p/p^0_{water}	1.000	0.967	0.930
p/p^0_{ice}	1.030	1.030	1.025
Γ, nmol cm^{-2}	51.40	4.486	1.073
$\Delta\pi$, erg cm^{-2}	12.49	1.83	0.84
q_{st}, kcal mol^{-1}		10.83	10.88

[a] Data for $-3.00°$, at which nucleation did not occur, are included for comparison.

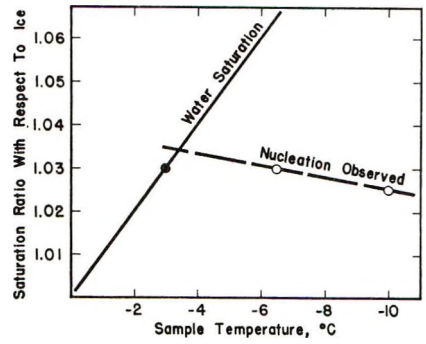

Figure 6. Extrapolation of the supersaturation data at nucleation to the water saturation curve gives nucleation thresholds on pure silver iodide. Nucleation did not occur at $-3.00°$.

A plot of the supersaturation with respect to ice *vs.* temperature is shown in Figure 6; a line which corresponds to water saturation is also shown. A very crude extrapolation of the nucleation data to the water saturation line gives the threshold temperature, $-3.5°$, and supersaturation, 3.4%, for the nucleation of ice from the vapor. Although based on only two points, the negative slope of the nucleation line is interesting; similar trends have been reported.[22] Classical nucleation theory[23] requires a positive slope, that is, a greater supersaturation to nucleate ice from the vapor at colder temperatures.

The increase in embryo size and the increase in supersaturation required to nucleate ice implies this liquidlike interface which apparently exists between the embryo and vapor at temperatures above at least $-10°$ inhibits the nucleation of ice from the vapor. Since the thickness of the liquidlike film is thought to be

(20) Based on surface area of 10.2 Å² occupied by a single adsorbed water molecule, given in ref 10.

(21) N. H. Fletcher, *Phil. Mag.*, **7**, 255 (1962).

(22) L. A. Madonna, C. M. Sciulli, L. N. Canjar, and G. M. Pound, *Proc. Phys. Soc. (London)*, **78**, 1218 (1961); C. E. Anderson in "Artificial Simulation of Rain," Pergamon Press, New York, N. Y., 1957, p 404.

(23) See review by N. H. Fletcher in "The Physics of Rainclouds," Cambridge University Press, New York, N. Y., 1962, Chapter 8.

strongly temperature dependent,[21] it is possible that the effect of this interface vanishes at temperatures below −13°. Below this temperature the supersaturation may again follow classical theory.

The supersaturation values reported here to nucleate ice are considerably smaller than the values of 12% and more mentioned in the literature.[24,25] One explanation is that here nucleation occurs after adsorption of the vapor by the substrate has reached an equilibrium value.[26] All embryos have attained their equilibrium size and only a small additional driving force is required to produce unstable growth. Also, the time scale for nucleation to occur is considerably longer in this study than in previous measurements of ice nucleation. A direct comparison to nucleation rate theory is not possible with the limited data presently available.

Conclusions

On this sample of pure silver iodide, the adsorbate, water vapor, is patchwise distributed on the surface at the onset of nucleation. Patches of adsorption sites exhibiting a strong affinity for water vapor form the foundations for nucleation embryos; the remainder of the silver iodide surface is relatively inactive in the adsorption process. As the amount of material adsorbed on the patches increases, a phase transition occurs in the adsorbate. It is not possible to determine if the transition extends through all the adsorbed material or affects only the adsorbate–vapor interface. However, this interface definitely assumes the energetic properties of a liquidlike surface prior to nucleation.

Nucleation of ice from the vapor on pure silver iodide is inhibited by the liquidlike interface between the embryo and the vapor. In this connection, the distinction between a freezing and a deposition mechanism for ice nucleation may depend on the definition of the phase of the adsorbed material. However, nucleation of a condensed phase occurred at pressures below saturation of undercooled water. Accordingly, the only condensed phase of water which can exist as a growing embryo under these conditions is ice.

It is quite clear that further detailed investigations of nucleation by adsorption studies on materials of all degrees of purity are necessary for understanding the mechanism of heterogeneous nucleation. Equilibrium as well as nonequilibrium adsorption and nucleation must be examined. Such studies over a much wider range of temperature and pressure than those undertaken here may show the temperature dependence of the effect of a liquidlike film on ice nucleation, the influence of the substrate on the number and size of nucleation embryos, and the effects of adsorption history on nucleation.

Acknowledgment. The research reported herein and publication of this manuscript were funded by the Atmospheric Science Program, National Science Foundation, NSF Grant No. GA-11309.

(24) G. W. Bryant, J. Hallett, and B. J. Mason, *J. Phys. Chem. Solids*, **14**, 189 (1959).

(25) G. R. Edwards and L. F. Evans, *J. Meteorol.*, **17**, 627 (1960).

(26) N. H. Fletcher, *Z. Angew. Math. Phys.*, **14**, 487 (1963).

Transport Phenomena of Polyelectrolytes in Solution under Electric Field

by Mitsuru Nagasawa,* Ichiro Noda, Toru Takahashi, and Noboru Shimamoto

Department of Synthetic Chemistry, Nagoya University, Chikusa-ku, Nagoya, Japan *(Received January 17, 1972)*

Publication costs borne completely by The Journal of Physical Chemistry

It is shown from transference number measurements that the mobility of counterions is very much affected by their interaction with polyion, whereas the mobility of by-ions is little affected. The degree of ion binding calculated based on the idea of Wall is found to be independent of the concentration of added salt. Moreover, the mobility of polyion calculated from transference number and specific conductivity well agrees with the mobility determined by a Tiselius electrophoresis apparatus. Based on these data of electrophoresis, transference number, and conductivity, a discussion is given to the contradiction between the theory of Hermans, Fujita, Overbeek, and Stigter on electrophoresis of polyion and the theory of Wall on counterion binding of polyion in transference phenomena. It is concluded that this contradiction arises from the prediction of uniform distribution of counterions inside polymer sphere in the theory of Hermans, *et al.*, but the conclusion of Hermans, *et al.*, that the polyion would be free draining in electrophoresis is still valid.

Introduction

Two different approaches have been reported to study the interaction between linear polyion and counterions in irreversible phenomena under applied electric field. One is the theory of Wall and his coworkers[1-3] in which a part of counterions is assumed to move together with polyion. This speculation was obtained by measuring the transference numbers of both polyion and counterions in the absence of added salt. The other is the theory of Hermans and Fujita,[4] Hermans,[5] and Overbeek and Stigter[6] on the electrophoretic mobility of polyion in the presence of a neutral salt. In their theory, it is concluded that the hydrodynamic interaction between segments, which is characteristic for linear polymers, would disappear at the limit of high ionic strength, and, hence, the polyion should move like a free draining sphere as if there were no effect from its ionic atmosphere. However, their theory is based on the assumption of the negligible relaxation effect of ionic atmosphere.

Thus, these two theories appear to conflict with each other. In this work, we determine the mobility of polyacrylate ion together with those of counter- and by-ions in solutions containing both a polyelectrolyte and a neutral salt by a modified method of Wall, *et al.*, and compare the observed mobility of the polyion with its electrophoretic mobility determined by a Tiselius electrophoresis apparatus. The agreement between the values determined by both methods is found to be satisfactory. Hence, the contradiction between both theories is in their theoretical predictions.

In the theory of Hermans, *et al.*,[4-6] the polyion is assumed to be a sphere in which segments are uniformly distributed. The electrophoretic mobility of polyion is then given in terms of two parameters; Debye's shielding ratio σ and the ratio of the radius of polyion sphere and the thickness of ionic atmosphere p, such as

$$U_p = \frac{e_s}{\xi}\left(1 + \frac{\sigma^2}{3p^2}\frac{2 + \sigma/p}{1 + \sigma/p}\right) \quad (1)$$

$$\sigma^2 = \nu\xi R^2/\eta \quad (2)$$

$$p = \kappa R \quad (3)$$

if both σ and p are large compared with unity. Here R is the radius of polyion sphere, ν the number of segments per unit volume in the polymer sphere, ξ the frictional coefficient of a segment, e_s the electronic charge number of a segment, and κ is the reciprocal thickness of ionic atmosphere defined by Debye and Hückel, *i.e.*

$$\kappa^2 = 8\pi e^2 N_A C_s/DkT \times 10^{-3} \quad (4)$$

N_A is Avogadro's number and C_s is the concentration of an added salt of uni-univalent type (moles per liter).

From eq 1, it is predicted that the mobility of polyion is equal to that of the segment (U_m) at the limit of high ionic strength since, in general, $p \gg \sigma$. That is

$$U_p = e_s/\xi \equiv U_m \quad (5)$$

Therefore, the polyion behaves like a free draining sphere at high ionic strengths, and its mobility is independent of molecular weight. This conclusion was well supported by experiments in previous works.[7-11]

(1) J. R. Huizenga, P. F. Grieger, and F. T. Wall, *J. Amer. Chem. Soc.*, **72**, 2636, 4228 (1950).

(2) F. T. Wall and M. J. Eitel, *ibid.*, **79**, 1556 (1957).

(3) F. T. Wall and W. B. Hill, *ibid.*, **82**, 5599 (1960).

(4) J. J. Hermans and H. Fujita, *Kon. Ned. Akad. Wetensch. Proc., Ser. B*, **58**, 182 (1955).

(5) J. J. Hermans, *J. Polym. Sci.*, **18**, 529 (1955).

(6) J. Th. G. Overbeek and D. Stigter, *Recl. Trav. Chim. Pays-Bas*, **75**, 543 (1956).

(7) J. J. Hermans, "The Structure of Electrolyte Solutions," Wiley, New York, N. Y., 1959, Chapter 21.

(8) S. A. Rice and M. Nagasawa, "Polyelectrolyte Solutions," Academic Press, New York, N. Y., 1961.

Moreover, eq 1 implies that U_p of a polyion should be independent of counterion species at high ionic strengths. The experimental test of this speculation may be particularly important, because U_p would be different with counterion species if a part of counterions were associated with polyion to decrease the net charge of the polyion.

However, it has often been pointed out that the sphere model employed by Hermans, *et al.*, is unrealistic, and the more realistic model for polyion may be a randomly coiled conformation whose skeleton is surrounded by a cylindrical ionic atmosphere.[6-12] Because of the effect of this ionic atmosphere, the electrophoretic mobility of polyion at high ionic strengths may not be equal to the mobility of a free segment. That is, U_m in eq 5 may be affected by ionic atmosphere around the fixed charges.[13-16] In contrast to the theory of Hermans, *et al.*, is is assumed in the theory of Wall and his coworkers that a part of counterions is associated with polyion and the charge density of polyion may be much lower than the analytical charge density. The contradiction between the theories of Hermans, *et al.*, and Wall, *et al.*, may arise from this neglect of the effect of ionic atmosphere around the skeleton.

Experimental Section

Samples. Fractionated poly(sodium styrene-*p*-sulfonate), P(NaSS), used in this work are the same as used in previous works.[17-19] The P(NaSS) solution purified was converted into the acid form P(SSA) by passage through a mixed bed ion-exchange resin column of Amberlite IR-120 and IR-400 and neutralized with aqueous solutions of the corresponding hydroxides to prepare various types of salts of P(SSA). The weight- and number-average molecular weights of P(NaSS) were determined by light scattering and osmotic pressure measurements in previous works.[17,19,20] Poly(sodium acrylates) P(NaA), used are also the same as used in the previous works,[10,20,21] but no special attention was paid to fractionation of P(NaA), since it is known that the electrophoretic mobility of P(NaA) is independent of molecular weight.[10] The number-average molecular weights of P(NaA) was determined by a high speed membrane osmometer Type 502 of Hewlett-Packard Co. The membrane used is gel cellophane No. 600. The molecular weights of the samples are listed in Table I.

The sample solutions containing a neutral salt of the same concentration as in the solvent used were prepared volumetrically by mixing the calculated volumes of a stock solution of the sample and the added neutral salt.

Electrophoresis. Electrophoretic velocities were determined at 25 ± 0.01° by using a Beckman Spinco Model H electrophoresis apparatus with the schlieren optical system. The cells used were standard 11-ml cells. Electric current used for measurements were varied from 0.1 to 13 mA, depending on the conductivity of the solution.[9] At ionic strengths lower than 3.5×10^{-3}, the current was reduced to 0.1 mA by using a shunt resistance between the electrodes. The error due to the change in the resistance of the sample solution was negligible. A silicone grease was used to prevent a current leakage in solutions of low ionic strength. The error in mobility due to the current leakage was less than 0.1% if checked with the leakage tester of the apparatus. The boundary velocity was determined by plotting the displacements of the peak of schlieren pattern against time. The velocities of ascending and descending boundaries were determined at three or more polymer concentrations and extrapolated to zero polymer concentration to obtain the electrophoretic mobility of the polyion.[9] At high ionic strengths, however, the average of the values from ascending and descending boundaries at one polymer concentration could be safely used. The velocity varied almost linearly with polymer concentration not only at high ionic strengths but also at low ionic strengths since the polymer concentrations were low enough. The polymer concentration dependence of the boundary velocity was similar to those reported in previous papers.[9,10] The electrophoretic mobility U_p

Table I: Samples

Sample name	of no.	$M_w \times 10^{-4}$
P(NaSS)	1	26
	2	48.5
	3	99
	4	260
P(NaA)		4.9[a]

[a] M_n.

(9) M. Nagasawa, A. Soda, and I. Kagawa, *J. Polym. Sci.*, **31**, 439 (1958).

(10) I. Noda, M. Nagasawa, and M. Ōta, *J. Amer. Chem. Soc.*, **86**, 5075 (1964).

(11) P. J. Napjus and J. J. Hermans, *J. Colloid Sci.*, **14**, 252 (1959).

(12) M. Nagasawa and I. Kagawa, *Bull. Chem. Soc. Jap.*, **30**, 961 (1957).

(13) U. P. Strauss, D. Woodside, and P. Wineman, *J. Phys. Chem.*, **61**, 1353 (1957).

(14) U. P. Strauss and S. Bluestone, *J. Amer. Chem. Soc.*, **81**, 5292 (1959).

(15) U. P. Strauss and P. D. Ross, *ibid.*, **81**, 5295 (1959).

(16) R. W. Armstrong and U. P. Strauss, *Encycl. Polym. Sci. and Technol.*, **10**, 781 (1969).

(17) A. Takahashi, T. Kato, and M. Nagasawa, *J. Phys. Chem.*, **71**, 2001 (1967).

(18) M. Nagasawa and Y. Eguchi, *ibid.*, **71**, 880 (1967).

(19) Y. Suzuki, I. Noda, and M. Nagasawa, *ibid.*, **73**, 797 (1969).

(20) A. Takahashi and M. Nagasawa, *J. Amer. Chem. Soc.*, **86**, 543 (1964).

(21) I. Noda, T. Tsuge, and M. Nagasawa, *J. Phys. Chem.*, **74**, 710 (1970).

($cm^2/(sec\ V)$) at each salt concentration was calculated from the limiting velocity by using the following equation

$$U_p = A\frac{\lambda}{i}\left(\frac{h}{t}\right)_0 \quad (6)$$

where $(h/t)_0$ is the velocity of the moving boundary at zero polymer concentration (cm/sec), A is the cross-sectional area of the cell (0.761–0.768 cm^2), λ is the specific conductance of salt solution against which the polymer solution was dialyzed, and i is the electric current. The values of A were determined from the weight of mercury filled in the cell, and λ was obtained from a table or determined by a Wagner bridge. The sample solutions were dialyzed against the solvent in a dialyzer consisting of a pair of glass cells at 25° until the Donnan equilibrium was reached. The specific conductivity of the deionized water used was 0.5–$1.1 \times 10^{-6}\ \Omega^{-1}\ cm^{-1}$.

Transference Experiments. The method of Hittorf, which was a basis for the method of Wall, *et al.*, was employed to determine the transference numbers of components. A cell consisting of three compartments, as shown in Figure 1, was used, to avoid the disadvantages discussed by Wall and Hill.[3] It was confirmed that no changes occur in the concentrations of polyelectrolyte and added salt in the middle compartment. The diameter of the glass tube was 16 mm, and three compartments were separated by two stopcocks which have the same diameter as the glass tube. The volumes of cathode, middle, and anode compartments were about 98, 69, and 95 ml, respectively.

Electrodes were Ag–AgCl electrodes, which were treated by the method of Washburn and McInnes.[22,23] The constant electric current, which was supplied from a d.c. source in the Beckman Spinco Model H electrophoresis apparatus, was from 0.4 to 3.0 mA. The electric amount passed was calculated from the intensity of electric current and time, but sometimes checked by a silver coulometer. The amounts of polyion and salt ions transferred were about 10% of the initial amount of each component in the compartment. Since the error due to deposit of polyion on the anode was not negligible, the amount of polyion transferred, as well as those of Na^+ and Cl^-, was calculated from the decrease in the polyion concentration in the cathode compartment. The apparatus was placed in an air thermostat at 25 ± 1°.

The reliability of this method was confirmed by measuring the transference numbers of Na^+ and Cl^- in NaCl solutions. One example of the experimental results is shown in Table II. Agreement between the observed transference number and the value in literature[24] is satisfactory.

Determination of Polyion, Na^+, and Cl^- Concentrations. After electrolysis, pH of the solutions was determined with a Beckman 1019 research pH meter.

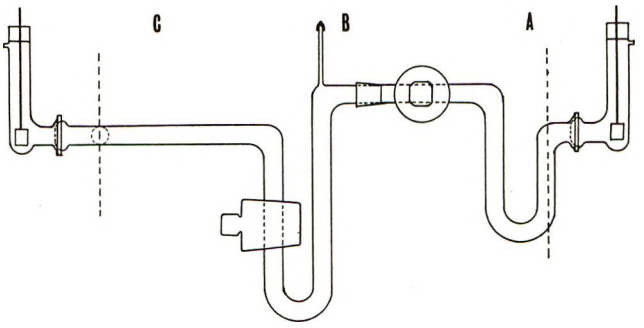

Figure 1. Cell for transference experiments: A, anode; B, middle; C, cathode.

The pH of the solutions in the cathode and middle compartments agreed with pH of the original solution within the error of ±0.02 pH unit except a few examples of 100% neutralized poly(acrylic acid) in which a difference of 0.25 pH at maximum was found.

Ion-exchange resin column methods were employed to determine the concentrations of polyion, Na^+, and Cl^- in each compartment. That is, a part of the solution taken out of the compartment after closing the stopcock was passed through an ion-exchange resin column of Amberlite IR-120, and the total acidity was determined by potentiometric titration with a standard NaOH. This gives the total concentration of HCl and poly(acrylic acid). Since no change in pH was found, this gives the concentration of Na^+. Another part of the solution was passed through a mixed-bed ion-exchange resin column of Amberlite IR-120 and IRA-400, and the acidity of the solution was determined by the same method as above. This gives the concentration of poly(acrylate). The difference between those two concentrations gives the concentration of Cl^-. Therefore, an error in the polyion concentration determination produces an error in the concentration of HCl.

The absorption of polyion on cation-exchange resin was negligible. Although there was a detectable amount of absorption of the polyion on the mixed-bed ion-exchange resin (about 4, 2, and 0% in 0.1, 0.05, and 0.01 N NaCl, respectively), the error due to the absorption could be minimized by determining the polyion concentrations in the original solution and the cathode compartment at the same experimental conditions. A few examples of preliminary experiments are shown in Table III.

The potentiometric titration was carried out in a nitrogen atmosphere with a Beckman 1019 research pH meter. A standard NaOH solution was delivered with a Tesa microburet of 0.001-ml division. Sampling of the sample solutions was carried out by weight.

(22) E. W. Washburn, *J. Amer. Chem. Soc.*, 31, 322 (1909).
(23) D. A. McInnes and M. Dole, *ibid.*, 53, 1357 (1931).
(24) R. A. Robinson and R. H. Stokes, "Electrolyte Solutions," Butterworths, London, 1959.

Table II: Determination of Transference Numbers of Na^+ and Cl^- in NaCl Solutions[a]

		In the cathode compartment	In the anode compartment	In the middle compartment
Concn, N		0.05166	0.04595	0.04882
Amount of solute in the compartments, mequiv	Before electrolysis	4.753	4.691	
	After electrolysis	5.031	4.416	
Change in the solute amount, mequiv		0.278	−0.275	
Transference number of sodium ion		0.388	0.384	
In literature		0.3877		

[a] Concn, 0.0488 N; electric current, 1.6 mA; time, 12 hr; electricity, 7.163×10^{-4} equiv; temp, 25.0 ± 0.1°.

Table III: Examples of Analysis of Salt Concentrations

Samples	P(NaA)	P(NaA) + NaCl	P(NaA) + NaCl
Concn, N	0.02	0.02 + 0.02	0.02 + 0.02
Ion-exchange resin column	H-type	H-type	Mixed-bed
Amount of solute in the sample solution, mequiv	1.204	2.306 (total)	1.486 P(AA)
Analytical result, mequiv	1.206	2.304	1.489
Error, %	0.2	−0.1	0.2

Calculation of Transference Number and Mobility. Let the changes in the amounts (equivalent) of Na^+, polyion, and, then, Cl^- in the cathode compartment be Q_{Na}, Q_p, and Q_{Cl}, respectively. Then, the transference numbers of the components are given by

$$t_p = \frac{Q_p F}{N_e} \cdot \alpha \tag{7}$$

$$t_{Na} = \frac{Q_{Na} F}{N_e} \tag{8}$$

and

$$t_{Cl} = 1 - \frac{Q_{Cl} F}{N_e} \tag{9}$$

where N_e/F is the amount of electricity passed, F is the Faraday constant, and α is the degree of ionization of the polyion, which is almost equal to the degree of neutralization. The ionic equivalent conductance Λ_i and electrophoretic mobility U_i (cm²/(sec V)) of component i are given by

$$\Lambda_i = \frac{10^3 \lambda t_i}{C_i} \text{ and } U_i = \Lambda_i / F \tag{10}$$

where λ is the specific conductance and C_i is the concentration of ith component (equiv/l.).

Conductivity Measurements. Electric conductivity of the sample solution was determined by a Wagner bridge at 1000 Hz using a cell of Jones and Bollinger's type.[25] The cell electrodes were black platinized. The cell constant (1.808 cm^{-1}) was determined with 0.1 D KCl ($\lambda = 0.0128524\ \Omega^{-1}\ cm^{-1}$).

Results

The electrophoretic mobilities of various salts of P(SSA) are compared with each other in Table IV. No practical difference can be found between these mobilities. This result is in perfect agreement with the theoretical conclusion of Hermans, *et al.*

Table IV: Electrophoretic Mobilities of Various Salts of Poly(styrenesulfonic Acid); Salt Concn, 0.100 N

Salt	$\Lambda°$	$U_p \times 10^4$, cm²/(sec V)
LiCl	115.03	3.4
NaCl	126.45	3.3
KCl	149.85	3.6
CsCl	153.61	3.3
$(CH_3)_4NCl$	121.27	3.4

The electrophoretic mobilities of P(NaSS) with different molecular weights at various ionic strengths are given in the sixth column of Table V and plotted against the weight-average molecular weights of the samples in Figure 2. It is clear from the figure that the mobilities of the polyions are independent of molecular weight within the limit of experimental error even at low ionic strengths. This is inconsistent with the prediction of Hermans, *et al.*, as is explained in the Discussion. In Figure 3, the average mobilities of the samples overall molecular weights are plotted against the square root of NaCl concentration. It is found that mobility of the polyion increases as the ionic strength decreases if the ionic strength is higher than about 0.005 equiv/l, but reaches a maximum. The same tendency was found in the mobility of poly(sodium vinyl sulfate) in NaCl solutions, too.[9] Although it is

(25) G. Jones and M. Bollinger, *J. Amer. Chem. Soc.*, 53, 411 (1931).

Table V: Electrophoretic Mobilities of Poly(sodium styrenesulfonate) in NaCl Solutions at 25°

NaCl concn, N	$M_w \times 10^{-4}$	$[\eta]$, dl/g	σ^2	p	$(U_p)_{obsd} \times 10^4$, cm²/(sec V)	$(U_p)_{calcd} \times 10^4$, cm²/(sec V)
0.1	26	1.00	61.0	27.2		3.50
	48.5	1.28	85.0	36.4	3.47	3.47
	99	2.32	112.0	56.4		3.40
	260	4.35	172.8	96.0		3.37
0.05	26	1.40	54.4	21.6		3.57
	48.5	1.74	77.67	28.5	3.70	3.50
	99	3.10	106.1	42.1		3.44
	260	5.03	164.8	71.1		3.40
0.02	26	1.96	48.6	15.3		3.74
	48.5	2.52	67.6	20.5	4.10	3.64
	99	4.55	89.6	31.6		3.50
	260	7.90	141.8	52.3		3.44
0.01	26	2.03	48.0	10.9	4.55	4.04
	48.5	3.31	61.9	35.8	4.48	3.77
	99	5.50	84.0	24.7	4.48	3.60
	260	12.80	120.4	43.6	4.50	3.47
0.005	26	3.45	40.3	9.21	4.85	4.17
	48.5	5.05	53.7	12.8	4.92	3.94
	99	9.52	70.0	20.0	4.71	3.67
	260	20.9	102.5	36.2	4.84	3.47
0.0035	48.5	5.70	51.2	11.2	4.04	4.04
	260	23.8	100.0	31.6	4.28	3.54
0.002	26	5.68	34.1	6.87	(4.35)	4.58
	48.5	7.94	46.1	9.48	4.35	4.24
	99	16.4	58.5	15.3		3.77
	260	35.4	85.9	27.3	(4.35)	3.57

Table VI: Mobilities of Polyion, Counterion, and By-ion[a]

No.	NaCl concn, N	Degree of neutralization	Transference numbers: t_p	t_{Na}	t_{Cl}	Specific conductance	$U_p \times 10^4$, cm²/(sec V)	Λ_{Na^+}	Λ_{Cl^-}	Mobility of polyion by electrophoresis, $U_p \times 10^4$, cm²/(sec V)	f
1		1.00	0.148	0.513	0.339	0.01156	4.11	27.7	60.4	3.11	0.34
2	0.09823	0.600	0.063	0.573	0.364	0.01129	2.86	33.1	65.9	3.08	0.39
3		0.200	0.015	0.612	0.373	0.01078	1.88	37.6	67.2	2.40	(0.12)
4		1.00	0.196	0.526	0.277	0.006553	3.09	19.7	70.2		0.29
5	0.04911	0.600	0.133	0.510	0.356	0.006306	3.37	29.9	65.5	3.60	0.47
6		0.200	0.042	0.538	0.420	0.005793	2.92	42.1	63.5		0.79
7		1.00	0.739	0.291	−0.03	0.002385	4.24	−1.2	70.6		0.32
8	0.009824	0.600	0.458	0.422	0.120	0.002134	3.92	7.2	91.7	4.65	0.39
9		0.200	0.206	0.325	0.469	0.001598	3.96	40.6	52.9		0.82

[a] Here, $U_p = \Lambda_p/96{,}500$. Concentration of poly(acrylic acid) in the original solutions is 0.04309 (monomer mol/1000 g).

our present opinion that a maximum may appear in the ionic strength dependence of the mobility of linear polyelectrolytes, the error in measurements of electrophoretic velocity at such low ionic strengths as 0.0035 of 0.002 equiv/l. is so large that we feel it difficult to conclude so without the slightest ambiguity.

Measurements of transference numbers by the Hittorf method were carried out in solutions of poly(acrylic acid) with 20, 60, and 100% degrees of neutralization in the presence of 0.01, 0.05, and 0.1 N NaCl. The polymer concentration was kept at about 0.04 monomer mol/1000 g. The change in the concentra-

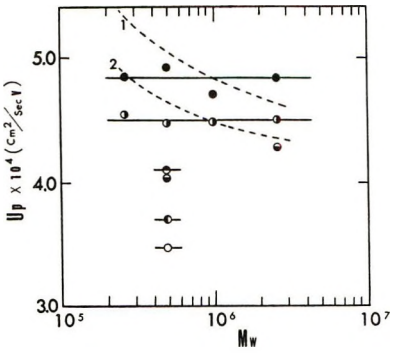

Figure 2. Molecular weight dependence of the electrophoretic mobility of sodium poly(styrenesulfonate) in NaCl solutions of various concentrations: NaCl concn (mol/l.), ⊙, 0.1; ◐, 0.05; ◓, 0.02; ◑, 0.01; ●, 0.005; ◒, 0.01; temp, 25°. Broken lines 1 and 2 denote the molecular weight dependencies of the mobility in solutions of 0.005 and 0.01 mol/l., respectively, calculated from the theory of Hermans and Fujita. The absolute values of those calculated lines are arbitrary.

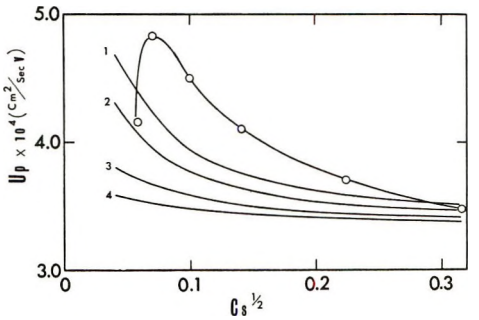

Figure 3. Ionic strength dependence of the electrophoretic mobility of sodium poly(styrenesulfonate) in NaCl solutions. The solid lines 1, 2, 3, and 4 denote the calculated values of Hermans and Fujita for M_w = 26, 48.5, 99, and 260 × 10^4, using the mobility at 0.1 mol/l. as a standard.

tion of each component in the middle compartment was usually 0.1–0.4%, though it reached 1% in some experimefts in 0.1 *N* NaCl.

The transference numbers of polyion, Na^+, and Cl^- obtained and their electrophoretic mobilities (or ionic equivalent conductances) calculated from the transference number and specific conductance of the sample solutions using eq 10 are listed in Table VI. The electrophoretic mobility of poly(acrylate) ion thus determined are compared with the values determined by the Tiselius electrophoretic apparatus (Beckman Spinco Model H) in Table VI. The agreement between both values must be considered satisfactory in view of the fact that the error in the transference number measurements is fairly high. Therefore, it may be concluded that the difference in conclusion reached from electrophoresis experiments and from transference experiments is not in the experimental results but is in the theoretical predictions.

The behaviors of counter- and by-ions are much more complicated than the behavior of polyion, as reported

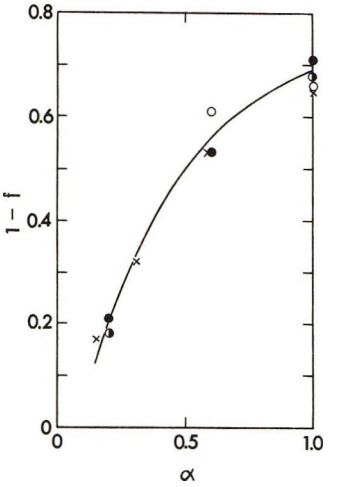

Figure 4. Degree of counterion association of sodium poly(acrylate) in NaCl solutions calculated from transference number measurements: α, degree of neutralization; NaCl concn, ○, 0.0982 *N*; ●, 0.0491 *N*; ◑, 0.00982 *N*; ×, salt free, by Wall, *et al.*[3] The data for 0.0982 and 0.00982 *N* at α = 0.6 are in coincidence.

by Wall, *et al.* The electrophoretic mobility of by-ion is not much affected by the presence of polyion, whereas that of counterion is very much decreased. This is similar to the behavior of ionic activity coefficients in polyelectrolyte solutions.[8,26] If we employ the assumption of Wall, *et al.*,[1] that a part of counterions is associated with polyion to decrease the charge density of the polyion, we have

$$-C_p\alpha(1-f)\Lambda_p + (C_p\alpha f + C_s)\Lambda_{Na}^\circ = (C_p\alpha + C_s)\Lambda_{Na} \quad (11)$$

where Λ_{Na} and Λ_{Na}° are the observed equivalent conductance of sodium ion and that of the unassociated ones, respectively, Λ_p is the observed equivalent conductance of the polyion, $1 - f$ is the fraction of carboxyl groups associated with sodium ions. C_s is the equivalent concentration of added neutral salt (NaCl), and α is the degree of ionization of the P(AA). Here, the contributions of H^+ and OH^- to the conductivity are assumed negligible.

If we assume the equivalent conductance (Λ_{Na}°) of "free" counterions in the solution to be equal to the values in NaCl solutions without polyelectrolytes (Λ_{Na}° = 47.9,44.4, and 42.3 at 0.01, 0.05, and 0.1 mol/l.),[27] we can calculate f from eq 11 as shown in Table VI and Figure 4. The reliability in f obtained is not high at high ionic strength and at low degree of neutralization. The value of f in the experiment no. 3 is abnormal because of unknown reasons. Nevertheless, it appears safe to conclude

(26) M. Nagasawa, M. Izumi, and I. Kagawa, *J. Polym. Sci.*, **37**, 375 (1959).

(27) These values were calculated from equivalent conductivities of NaCl and KCl, assuming that $\Lambda_{K^+} = \Lambda_{Cl^-}$ in KCl solutions and Λ_{Cl^-} is equal in both KCl and NaCl solutions at the same ionic strength.

from Figure 4 that the degree of counterion association $(1 - f)$ is independent of the concentration of NaCl added and is almost equal to the data of Wall, *et al.*, obtained in the absence of added salt.[3] This agrees with the experimental results of Wall and Eitel.[2]

Discussion

It is well known that thermodynamic properties of a polyelectrolyte solution can be well explained by assuming that a part of counterions is bound on polyion. In such cases, the degree of ion binding depends on counterion species or the radius of counterion. It is generally believed that no binding need be assumed if the counterion is a tetraalkylammonium ion.[28] Therefore, if the counterions were really bound on polyion so that the charge density of the polyion may be much lower than the analytical charge density in electrophoresis, the electrophoretic mobility of the polyion should differ with counterion species considerably. In practice, it is clear from Table IV that the mobility of P(SSA) is independent of counterion species and is as high as the mobilities of corresponding simple ions. This finding implies that the linear polyion coil is essentially free draining for solvent in electrophoresis, as predicted by Hermans, *et al.* The same conclusion was previously obtained from the fact that the electrophoretic mobility of polyion is independent of molecular weight if the ionic strength is high.[9,10] Here, however, it should be noted that the electrophoretic mobility of a poly(phosphate) differs considerably with different counterions according to Strauss, *et al.*[13] The interaction of sodium ion with phosphate group may be different from that between Na^+ and sulfonic acid group.

Quantitatively speaking, the fact that the mobility of P(NaSS) is independent of molecular weight even at low ionic strengths is inconsistent with the theory of Hermans, *et al.* If the ionic strength is low, a partially draining sphere model may be pertinent so that the mobility should depend on molecular weight according to the theory of Hermans, *et al.* To compare the experimental data with the theory of Hermans, *et al.*, it is necessary to know the radius of polymer coil R as a function of molecular weight and ionic strength. According to Flory and Fox,[29] the root-mean-square end-to-end distance $\langle r^2 \rangle^{1/2}$ is obtained from the intrinsic viscosity using eq 12

$$[\eta] = \Phi \frac{\langle r^2 \rangle^{3/2}}{M} \tag{12}$$

where Φ is 2.1×10^{21}. Although there is an ambiguity in the numerical value of Φ, it is not an important problem for the present purpose. R may be estimated from $\langle r^2 \rangle$ with the assumption of $R^2 = (5/18)\langle r^2 \rangle$. The parameters σ and p are calculated from eq 2 and 3 by using these values of R, and they are given in Table V. It is observed that σ and p are both large compared with unity at the present experimental conditions so that eq 1 may be applicable.

Assuming that the mobility of the polyion U_p observed at 0.1 N NaCl solution is equal to that of the polyion calculated from eq 1 with the σ and p values obtained for the polyion, the mobilities of the polyion at the other ionic strengths can be calculated from eq 1 as shown in Table V and also in Figure 3. The calculated mobility is found to depend on molecular weight at low ionic strengths beyond the uncertainty in the mobilities determined by electrophoresis ($\approx \pm 1\%$), in contrast to the experimental results.

One of the most important assumptions employed in the theory of Hermans, *et al.*, may be that the fixed charges are distributed uniformly in a sphere of radius R and, hence, the distribution of counterions around the polyion is also spherically symmetrical. It is evident from many theoretical and experimental studies that the counterions may be attracted cylindrically around the polyion skeleton rather than spherically around the porous sphere of polyion.[6,13,30] It is our opinion that the disagreement between the theoretical values of Hermans, *et al.*, and experiments in Figures 2 and 3 stems from this assumption of uniform distribution of fixed- and counterions.

However, this disagreement with experiments does not decrease the value of the theory of Hermans, *et al.*, which predicted that the polyion coil would be essentially free draining for solvent in electrophoresis, in sharp contrast to the fact that the polyion coil is essentially a nondraining sphere in viscosity, sedimentation, and diffusion. This disappearance of hydrodynamic effects in electrophoresis arises from the fact that the forces acting on a charged segment and a counterion must cancel each other if all counterions are present inside the polyion coil, regardless of the uniform or non-uniform distribution of counterions inside the polyion coil. Therefore, the free draining model may be applicable over the almost whole experimental range of ionic strength in electrophoresis.

From the above discussions, therefore, it may be concluded that the change in the mobility of polyion with ionic strength as observed in Figure 3 is not due to the effect of partial drainage through the polyion coil but may be attributed to the change in the mobility of a segment with ionic strength. If a fixed charge is regarded as a segment, the change of the mobility of an isolated segment with ionic strength can be approximately speculated from the ionic strength dependence of the mobilities of other simple electrolytes.[9] That is, the concentration dependence of equivalent conduc-

(28) H. P. Gregor, D. H. Gold, and M. Frederick, *J. Polym. Sci.*, **23**, 467 (1957).

(29) P. J. Flory, "Principles of Polymer Chemistry," Cornell University Press, Ithaca, N. Y., 1953.

(30) M. Nagasawa and I. Kagawa, *Bull. Chem. Soc. Jap.*, **30**, 961 (1957).

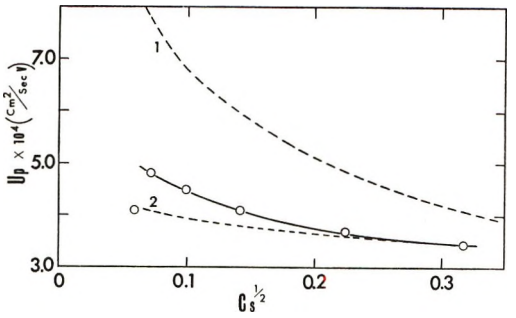

Figure 5. The effect of ionic atmosphere on the mobility of polyion skeleton at free drainage. The solid line denotes the experimental mobilities of P(NaSS) at various ionic stengths. The broken line 1 denotes the mobility of rodlike P(NaSS) calculated by using the theory of Henry.[32] The broken line 2 denotes the expected mobility of an isolated segment in NaCl solutions of various ionic strengths.

tance of a simple electrolyte is expressed as a function of its limiting equivalent conductance and ionic radii, though the parameters in the theory are not fully clarified.[24] The ionic strength dependence of U_m estimated from an analogy to the behavior of other ions is shown in Figure 5. The calculated values are much less dependent on ionic strength than the observed ones.

Another method to estimate the effect of ionic atmosphere on U_m may be to assume that a polyion is a rigid rod of infinite length. Its electrophoretic mobility is than approximately given by[31-33]

$$U_p \equiv U_m = D\psi_b/6\pi\eta_0 \qquad (13)$$

averaging overall possible orientations, though eq 13 is applicable only for such a thick rod as the thickness of ionic atmosphere can be neglected and, moreover, the relaxation effect is neglected in eq 13. Here, ψ_b is the electrostatic potential at the surface of the rod, D is the dielectric constant of water, and η_0 is the viscosity of solvent. The electrostatic potential around a cylinder $\psi(r)$ and, then, that at the surface ψ_b can be calculated from the Poisson–Boltzmann equation

$$\nabla^2\psi = -\frac{4\pi N_A e}{10^3 D} C_s[e^{-e\psi/kT} - e^{e\psi/kT}] \qquad (14)$$

where C_s is the molar concentration of added 1:1 electrolyte and N_A is Avogadro's number. In practice, the electrostatic potential at the position from which salt ions are excluded, ψ_a, can be determined from eq 14. There is a slight ambiguity in the relationship between ψ_a and ψ_b.[33] In this paper, however, we neglect the difference between ψ_a and ψ_b since a rod model is in any case a rough approximation for polyion.

The electrophoretic mobilities of P(NaSS) thus calculated with a = 10 Å (7.5 Å for polyion + 2.5 Å for Na^+) are plotted against the square root of NaCl concentration in comparison with experimental data in Figure 5. The ionic strength dependence of the calculated values are much stronger than that of observed values. It is reasonable that the observed values are found between both extreme cases, that is, between the calculated values for rod and those for an isolated monomer. Thus, it may be concluded that the electrophoretic mobility of polyion may vary with ionic strength even though the polyion is practically free draining for solvent over the whole range of ionic strength.

The term "counterion binding (fixation, association, etc.)" may cover various types of interaction between counterion and polyion: (1) formation of undissociated or complex molecules such as undissociated carboxylic acid or the interaction between carboxylate ion and Cu^{2+}; (2) trap of counterions inside the polyion domain; (3) ion-pair formation between counterions and fixed charges due to the electrostatic force, including the cylindrical ionic atmosphere strongly attracted around the polyion skeleton.[34-36] The condensation theory of Manning[37] may also be in this category. It was already pointed out that the second type of ion binding cannot explain the present interaction between counterion and polyion.[8] The third type of ion binding may be the most likely explanation. That is, the counterions are so strongly attracted around the polyion skeleton that a part of counterions may be treated as associated with fixed charges, just as ion-pair formation in simple electrolyte solutions. A feature of this type of ion binding is that the degree of binding as calculated from activity coefficient or osmotic pressure coefficient data is almost independent of the concentration of added salt.

The present experimental data on Λ_{Na} and Λ_{Cl} also show that the mobilities of counter- and by-ions are affected by the presence of polyion in such as way that a part of counterions appears to be associated with fixed charges and the degree of ion binding is independent of the concentration of added salt. This justifies the use of an effective charge density of polyion in discussing transport phenomena of polyelectrolytes.[38] However, this counterion binding should not be considered to be the undissociated or complex molecule formation in a strict meaning[36] (the first type of ion binding), since, if so, the electrophoretic mobility of polyion would be different with different ion species. Moreover, there is a clear experimental evidence that

(31) H. A. Abramson, L. S. Moyer, and N. H. Gorin, "Electrophoresis of Protein," Reinhold, New York, N. Y., 1942.

(32) D. C. Henry, *Proc. Roy. Soc., Ser. A*, 123, 216 (1929).

(33) T. Takahashi, I. Noda, and M. Nagasawa, *J. Phys. Chem.*, 74, 1280 (1970).

(34) A. Katchalsky, Z. Alexandrowica, and O. Kedem, "Polyelectrolyte Solutions," in "Chemical Physics of Ionic Solution," R. E. Conway and R. G. Barradas, Ed., Wiley, New York, 1966, p 295.

(35) L. Kotin and M. Nagasawa, *J. Chem. Phys.*, 36, 873 (1962).

(36) A. Katchalsky, *Pure Appl. Chem.* (preprint), 1971.

(37) G. Manning, *J. Chem. Phys.*, 51, 924, 934 (1969).

(38) G. Manning, *ibid.*, 47, 2010, 3377 (1967).

"bound" sodium ion has a finite mobility, though much lower than the mobility of "free" ions.[39] No experimental evidence has been found for a complex formation between $-COO^-$ and Na^+,[40] although a change in the hydration of counterion may be likely. It should also be noted that the electrophoretic mobilities of polyions discussed here are all as high as the mobilities of the corresponding monomer groups which can be estimated from the sizes of the ions[9] (approximately 3.0×10^{-4} cm^2/(sec V); *cf.* 3.35×10^{-4} for benzoate ion,[24] 3.6×10^{-4} for toluate and *p*-phenolsulfonate if estimated from the data of equivalent conductance of their sodium salts in International Critical Table).

However, this additivity of counterion mobility should not be taken too seriously,[41,42] since the mobility of "free" counterions (Na^+ in this case) cannot absolutely be the same as that in NaCl solutions. In practice, the mobility of by-ion (Cl^-) as well as its activity coefficient[26,43] is also affected by the presence of polyion.

(39) L. Kotin and M. Nagasawa, *J. Amer. Chem. Soc.*, **83**, 1026 (1961).

(40) L. C. Leyte, L. H. Zuiderweg, and H. J. Vledder, *Spectrochim. Acta, Part A*, **23**, 1397 (1967).

(41) J. W. Lyons and L. Kotin, *J. Amer. Chem. Soc.*, **87**, 1670 (1965).

(42) G. Manning, *J. Chem. Phys.*, **51**, 924 (1969).

(43) I. Kagawa and K. Katsuura, *J. Polym. Sci.*, **9**, 405 (1952).

Electrical Conductances and Ionization Behavior of Sodium Chloride in Dioxane–Water Mixtures at 50°

by Teik Huat Leong[1] and Lawrence A. Dunn*

Department of Chemistry, University of Tasmania, Hobart, Tasmania, Australia 7001 *(Received January 31, 1972)*

Publication costs borne completely by The Journal of Physical Chemistry

The ionization behavior of sodium chloride in various dioxane–water mixtures (0–81 wt % dioxane) at 50° has been studied by conductance techniques. Conventional ionization constants obtained from the measurements have been examined in terms of the complete constant (K^0), which incorporates the solvent as a reactant for the interpretation of equilibrium processes involving electrolytes. At 50° for sodium chloride, a net change (k) of 7.0 in waters of solvation on ionization and a log K^0 value of -11.13 are obtained. These values are shown to be consistent with previously published values for sodium chloride, both in dioxane–water (25–300°) and in water (400–800°) at pressures up to 4000 bars. For sodium chloride in dioxane–water over the temperature range 25–300°, the van't Hoff isochore yielded a constant value of -16.9 kcal mol^{-1} for the standard enthalpy change ΔH° for the complete equilibrium, $NaCl(aq) + kH_2O \overset{K^0}{\rightleftarrows} Na(aq)^+ + Cl(aq)^-$. With this value for ΔH° and the calculated values of ΔG° at each temperature, a constant value of -102.9 cal mol^{-1} deg^{-1} was obtained for the standard entropy change ΔS°. This negative value for ΔS° shows that order is increased by additional solvation on ionization of the electrolyte. These thermodynamic values have been compared with published data for the sodium chloride–pressurized water system over the temperature range 400–800°.

Introduction

The concept[2,3] of a complete isothermal ionization constant K^0 has been used successfully to describe the equilibrium behavior of electrolytes in both aqueous and mixed aqueous–nonpolar organic solvent mixtures,[4–9] the ionization behavior of water,[10,11] and to calculate the complete isothermal rate constants for several solvolysis reactions.[12] These studies cover the temperature range 25–800° and the pressure range 1–12,000 bars. The concentration of water in the equilibrium reaction

$$NaX(aq) + kH_2O \overset{K^0}{\rightleftarrows} Na(aq)^+ + X(aq)^- \quad (1)$$

has been altered by changing the pressure on the system, by changing the ratio of polar to nonpolar

(1) The work reported here summarizes a thesis presented by T. H. Leong in partial fulfillment of the requirements for the degree of Bachelor of Science with Honors in the University of Tasmania in October 1971. The receipt of a Colombo Plan Scholarship from the Commonwealth of Australia is gratefully acknowledged.

(2) W. L. Marshall and A. S. Quist, *Proc. Nat. Acad. Sci. U. S.*, **58**, 901 (1967).

(3) A. S. Quist and W. L. Marshall, *J. Phys. Chem.*, **72**, 1536 (1968).

constituents in the mixed solvents, or by doing both. These experimental conditions thus provide a rigorous test of the complete equilibrium constant concept.

The purpose of the present study was twofold: first, to evaluate k and K^0 for sodium chloride in dioxane–water mixtures at 50° by conductance methods and to establish whether these values could be related to published data for the same system at 25°,[13,14] 100°,[7,8] and 300°[9] and for sodium chloride in pressurized water from 400 to 800°,[4,6] and second, to evaluate $\Delta G°$, $\Delta H°$, and $\Delta S°$ for the sodium chloride–aqueous dioxane system from 25 to 300° for comparison with previously published data[6] for the sodium chloride–pressurized water system from 400 to 800°.

Experimental Section

The dioxane–water solvent mixtures were prepared by weight using AR grade p-dioxane (B.D.H. Chemicals Ltd.) and conductivity water, prepared by passing distilled water through a mixed-bed ion-exchange column. Experimental specific conductances (κ_0) of these solvent mixtures at 50°, for use as background conductances in this study, were measured and are given in Table I. The sodium chloride solutions were prepared gravimetrically from recrystallized AR grade sodium chloride (B.D.H. Chemicals Ltd.) and the various solvent mixtures. The sodium chloride was dried to constant weight at 120° before use. At least five molarities of sodium chloride in the range 0.0005–0.008 M were studied in each solvent mixture. The conductivity bridge has been described previously.[15] Two conductance cells of the Jones and Bollinger design,[16] with cell constants of 1.1145 and 0.2635 cm^{-1} at 50°, were used. These cells were calibrated with 0.01 and 0.1 demal potassium chloride solutions at 25°, followed by appropriate temperature corrections. Since it was found that platinized electrodes gave nonreproducible resistance readings (possibly due to some catalytic effect of the platinum deposit on the p-dioxane), bright platinum electrodes were used. For each solution, resistances were measured at five frequencies in the range 3.2–7.0 kHz. The resistances used in all calculations were obtained by plotting these measured resistances against $(\text{frequency})^{-1/2}$ for each solution, and extrapolating to infinite frequency.

Solvent densities and permittivities at 50° were interpolated from large scale plots of the density–composition data of Tommila and Koivisto[17] and Hovorka, Schaefer, and Dreisbach[18,19] and the permittivity–composition data of Åkerlöf and Short[20] and Tourky, Rizk, and Girgis.[21] The densities and permittivities of the experimental solvent mixtures are given in Table I. At 50° the viscosity of dioxane–water mixtures is unknown experimentally. The data and procedures described previously[7] were used to obtain viscosity data for 0, 20, 40, 60, 80, and 100 wt % dioxane mixtures at 50°. Solvent viscosities at the experimental compositions were interpolated from a large scale plot of these data and are included in Table I.

Table I: Properties of Dioxane–Water Mixtures at 50°

Wt % dioxane	d, g cm^{-3}	ϵ	η, cP	$10^6\kappa_0$, ohm^{-1} cm^{-1}
0.0	0.9881	69.88	0.547	0.2
14.7	0.9976	57.60	0.699	7.3
30.0	1.0062	45.35	0.875	5.9
44.7	1.0122	33.74	1.038	4.6
54.7	1.0142	26.28	1.103	3.9
60.2	1.0145	22.30	1.121	3.4
68.4	1.0137	16.70	1.111	2.2
75.1	1.0122	12.40	1.080	1.5
81.1	1.0101	8.90	1.036	0.9

Results and Discussion

The experimental equivalent conductances[22] of sodium chloride in various dioxane–water mixtures at 50°, together with the data of Chambers[23] for three sodium chloride concentrations in the range 0.009–0.03 M under identical conditions in aqueous solution at 50°, have been analyzed by various conductance equations using the procedures described previously.[4] In the composition range 0–60 wt % dioxane, the various conductance equations used gave essentially identical values, within the accuracy of the data, for the limiting equivalent conductances of sodium chloride at 50°. Accord-

(4) A. S. Quist and W. L. Marshall, *J. Phys. Chem.*, **72**, 684 (1968).
(5) A. S. Quist and W. L. Marshall, *ibid.*, **72**, 2100 (1968).
(6) L. A. Dunn and W. L. Marshall, *ibid.*, **73**, 723 (1969).
(7) L. A. Dunn and W. L. Marshall, *ibid.*, **73**, 2619 (1969).
(8) L. B. Yeatts, L. A. Dunn, and W. L. Marshall, *ibid.*, **75**, 1099 (1971).
(9) L. B. Yeatts and W. L. Marshall, *ibid.*, **76**, 1053 (1972).
(10) W. L. Marshall, *Rec. Chem. Progr.*, **30**, 61 (1969).
(11) A. S. Quist, *J. Phys. Chem.*, **74**, 3396 (1970).
(12) W. L. Marshall, *ibid.*, **74**, 346 (1970).
(13) R. W. Kunze and R. M. Fuoss, *ibid.*, **67**, 911 (1963).
(14) W. L. Marshall, *Rev. Pure Appl. Chem.*, **18**, 167 (1968).
(15) H. Bloom and I. A. Weeks, *J. Chem. Soc. A*, 2028 (1969).
(16) G. Jones and G. M. Bollinger, *J. Amer. Chem. Soc.*, **53**, 411 (1931).
(17) E. Tommila and A. Koivisto, *Suom. Kemistilehta B*, **21**, 18 (1948).
(18) F. Hovorka, R. A. Schaefer, and D. Dreisbach, *J. Amer. Chem. Soc.*, **58**, 2264 (1936).
(19) F. Hovorka, R. A. Schaefer, and D. Dreisbach, *ibid.*, **59**, 2753 (1937).
(20) G. Åkerlöf and O. A. Short, *ibid.*, **58**, 1241 (1936).
(21) A. R. Tourky, H. A. Rizk, and Y. M. Girgis, *J. Phys. Chem.*, **65**, 40 (1961).
(22) Experimental data at 50° will appear immediately following these pages in the microfilm edition of this volume of the journal. Single copies may be obtained from the Business Operations Office, Books and Journals Division, American Chemical Society, 1155 Sixteenth St., N.W., Washington, D. C. 20036, by referring to code number JPC-72-2294. Remit check or money order for $3.00 for photocopy or $2.00 for microfiche.
(23) J. F. Chambers, *J. Phys. Chem.*, **62**, 1136 (1958).

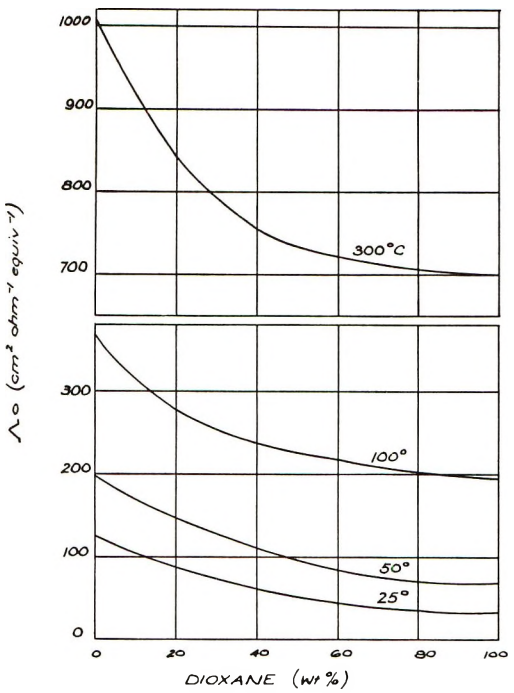

Figure 1. Variation of the isothermal limiting equivalent conductances of sodium chloride in several dioxane–water mixtures at 25, 50, 100, and 300° and 1 atm.

ingly, averaged Λ_0 values were used for this composition range. For solvent mixtures containing in excess of 60 wt % dioxane, agreement between the Λ_0 values from the various conductance equations was less satisfactory. Since it is expected that ion association would be important in this composition range, and since most of the conductance equations used make no allowance for this phenomenon, this is not entirely unexpected. Accordingly, values for Λ_0 in the composition range 55–81 wt % dioxane were calculated using only the Shedlovsky equation.[24,25]

The Λ_0 values over the whole composition range were fitted to the polynomial

$$\Lambda_0 = 198.76 - 2.761_1 W + 1.3087 \times 10^{-2} W^2 + 2.1359 \times 10^{-5} W^3 \quad (2)$$

by the method of least squares, where W is the wt % dioxane in the various mixtures. The standard deviation of fit was 1.88 cm² ohm⁻¹ equiv⁻¹. These smoothed Λ_0 values are given in Table II and are plotted in Figure 1, where they are compared with previously published data[7-9,13,14] for the same system at 25, 100, and 300°. The behavior of Λ_0 at these four temperatures is essentially the same in the dioxane-rich region, while marked variation occurs in the aqueous region. This is most likely associated with differences in the temperature variation of the density, viscosity, and permittivity of water and of dioxane.

Values of the conventional ionization constant (K) for the equilibrium

$$\mathrm{NaCl(aq)} \overset{K}{\rightleftharpoons} \mathrm{Na(aq)^+ + Cl(aq)^-} \quad (3)$$

in the various solvent mixtures at 50° were obtained from the Shedlovsky equation,[24,25] which includes an ionization constant. Using the experimental data[22] and the limiting equivalent conductances of Table II, the Shedlovsky equation reduces to only one parameter, the conventional ionization constant. Logarithms of the conventional ionization constants for sodium chloride in various dioxane–water mixtures at 50°, calculated by this procedure, are given in Table II. No physical significance is attached to the positive

Table II: Limiting Equivalent Conductances and Conventional Ionization Constants for Sodium Chloride in Dioxane–Water Mixtures at 50°

Wt % dioxane	Λ_0, cm² ohm⁻¹ equiv⁻¹	Log K
0.0	198.8	...
14.7	161.0	...
30.0	128.3	0.17
44.7	103.4	−0.82
54.7	90.4	−1.35
60.2	84.7	−1.59
68.4	78.0	−2.09
75.1	74.2	−2.90
81.1	72.3	−4.13

log K value for 30% dioxane. It most likely indicates that sodium chloride is completely dissociated under these conditions, and is included only for completeness.

For the equilibrium behavior of sodium chloride in aqueous dioxane at 25, 100, and 300°, and for a number of electrolytes in high-pressure supercritical water in the temperature range 400–800°, inclusion of the polar solvent species into the equilibrium expression yields a complete ionization constant (K^0) that is independent of isothermal properties of the solvent.[4-6] In the low-temperature aqueous dioxane system, it has been proposed[2,3,26,27] that the nonpolar dioxane acts essentially as a diluent, merely changing the concentration of the polar species involved in the equilibrium process. For sodium chloride under these conditions, the ionization process may be represented by eq 1 and 3, where k is the net change in the number of hydrating water molecules when one hydrated sodium chloride ion pair forms hydrated ions. Therefore, the complete equilibrium constant is given by

(24) T. Shedlovsky, *J. Franklin Inst.*, 225, 739 (1938).

(25) R. M. Fuoss and T. Shedlovsky, *J. Amer. Chem. Soc.*, 71, 1496 (1949).

(26) T. W. Davis, J. E. Ricci, and C. G. Sauter, *ibid.*, 61, 3274 (1939).

(27) A. Fratiello and D. C. Douglas, *J. Chem. Phys.*, 39, 2017 (1963).

Table III: Thermodynamic Data for the Sodium Chloride Equilibrium over the Temperature Range 25–800°

T, °C	k	Log K^0	ΔG^c, kcal mol^{-1}	ΔH°, kcal mol^{-1}	ΔS°, cal mol^{-1} deg^{-1}	Solvent
25	6.4	−10.00	13.64	−16.9	−102.9	$C_4H_8O_2$–H_2O
50	7.0	−11.13	16.46	−16.9	−102.9	$C_4H_8O_2$–H_2O
100	7.8	−12.70	21.68	−16.9	−102.9	$C_4H_8O_2$–H_2O
300	10.0	−16.00	41.96	−16.9	−102.9	$C_4H_8O_2$–H_2O
400	10.2	−17.10	52.70	−7.0	−88.3	H_2O
500	10.2	−17.31	61.20	−7.0	−88.3	H_2O
600	10.2	−17.52	70.00	−7.0	−88.3	H_2O
700	10.2	−17.70	78.80	−7.0	−88.3	H_2O
800	10.2	−17.83	87.60	−7.0	−88.3	H_2O

$$K^0 = K/C_{H_2O}{}^k \quad (4)$$

or

$$\log K = \log K^0 + k \log C_{H_2O} \quad (5)$$

where K is the conventional equilibrium constant and C_{H_2O} is the molar concentration of water. According to eq 5, a plot of log K *vs.* log C_{H_2O} should produce a straight line of slope k and intercept log K^0. Figure 2 shows that the data of Table II adhere to this relationship, giving values of 7.0 and −11.13 for k and log K^0, respectively, for sodium chloride in aqueous dioxane at 50°. Also included in Figure 2 is a plot of log K *vs.* (permittivity)$^{-1}$, which, according to conventional theory,[28,29] should be linear. These k and log K^0 values at 50° are plotted in Figure 3, where they are shown to

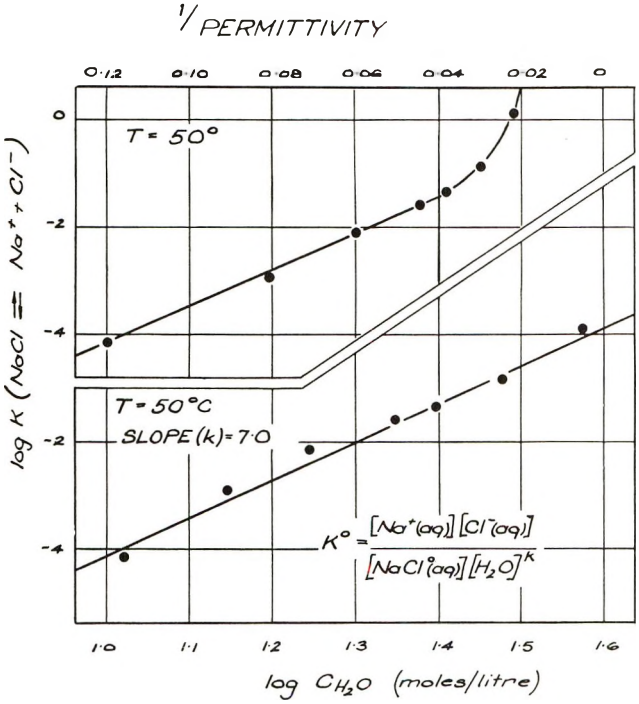

Figure 2. Variation of the conventional ionization constant of sodium chloride in dioxane–water mixtures at 50° with the molar concentration of water and with the reciprocal of the permittivity.

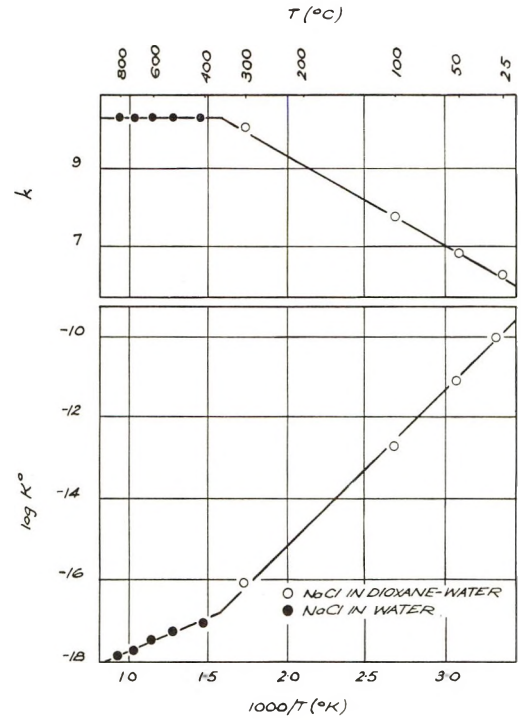

Figure 3. Variation with temperature of the complete molar ionization constant (K^0) and the net change (k) in waters of solvation for sodium chloride in aqueous solution, 25–800°.

be consistent with previously published values for sodium chloride in aqueous dioxane[7–9,13,14] from 25 to 300° and in pressurized water[4,6] from 400 to 800°. It is of interest to note that the two linear segments of the k–T^{-1} and log K^0–T^{-1} plots intersect at an average temperature of 369°, very close to the critical point of water. This suggests that the ionization behavior of sodium chloride exhibits a sharp change at about the critical point of water, rather than the smooth transition suggested earlier.[7,9,10,14] More detailed studies at higher temperatures in aqueous dioxane mixtures and in

(28) J. T. Denison and J. B. Ramsay, *J. Amer. Chem. Soc.*, 77, 2615 (1955).

(29) R. M. Fuoss, *ibid.*, 80, 5059 (1958).

aqueous solutions at temperatures closer to the critical point are needed to confirm this transition behavior.

From Figure 3, the van't Hoff isochore

$$\frac{\mathrm{d} \log K^0}{\mathrm{d}T^{-1}} = -\frac{\Delta H^\circ}{2.303R} \quad (6)$$

yielded a temperature-independent value of -16.9 kcal mol^{-1} for ΔH°, the standard enthalpy change for the sodium chloride ionization equilibrium in aqueous dioxane over the temperature range 25–300°. From the thermodynamic relationships

$$\Delta G^\circ = -RT \ln K^0 \quad (7)$$

$$\Delta G^\circ = \Delta H^\circ - T\Delta S^\circ \quad (8)$$

where ΔG° is the standard free energy change, the standard entropy change ΔS° for the complete equilibrium was also found to be essentially temperature independent, having an average value of -102.9 ± 0.4 cal mol^{-1} deg^{-1}. Similar temperature independent values of ΔH° and ΔS° for sodium chloride in aqueous solution over the temperature range 400–800° have been found previously.[6] A summary of the thermodynamic data for the sodium chloride ionization equilibrium from 25 to 800° is given in Table III. Since ΔS° for the sodium chloride equilibrium in the low-temperature aqueous dioxane system is more negative than for the high temperature aqueous system, increased solvation upon ionization of the ion pairs provides greater order in the aqueous dioxane solvent system than for the corresponding aqueous system.

Approximate Calculations of the Heats and Entropies of Hydration According to Various Models

by J. O'M. Bockris and P. P. S. Saluja*

Electrochemistry Laboratory, Department of Chemistry, University of Pennsylvania, Philadelphia, Pennsylvania 19104 *(Received April 15, 1971)*

Publication costs borne completely by The Journal of Physical Chemistry

Nmr spectroscopy has not yet been a decisive tool in investigations of the structure near an ion. Models used are, basically: (1) the CN is 4; no distinction between coordination number (CN) and solvation number (SN); (2) the CN is that obtained from X-rays; no distinction between CN and SN; (3) CN from X-rays; distinction between CN and SN is made. Three models of a structure broken (SB) region outside the first layer are calculated for each of the three basic models. The definition of CN is operational; that of SN is the number of water molecules per ion which remain for sufficiently long times attached to a given ion to accompany it on its translational movements. Heat calculations with model 3 give results in accord with experiment to better than ±18% for cations and ±8% for anions. Calculations with model 2 indicate values averaging 64% above the experimental values. Model 1 is inconsistent with X-ray data. Entropy calculations with the same models were carried out. Sound velocity measurements were used to estimate certain free volumes of model elements. Model 3, with a SB region of monomeric water, gives values averaging 25% above experimental values for cations and 12% for anions. Model 2 gives substantially higher values. Model 1 is inconsistent with X-ray data. Models in which SN is distinguished from a CN are numerically more consistent than those which do not make such a distinction.

Introduction

Spectroscopic studies[1-4] have contributed to the understanding of ion–solvent interactions. The criterion for the occurrence of separate nmr absorption peaks in different electronic environment is $\tau \gg 1/\Delta w$, where τ is the average time spent by the nucleus in a particular environment and Δw is the value of the difference in chemical shifts between the different environments through which the nucleus passes in exchange. The number of molecules nearest to an ion can then be obtained directly from the area under the

* Address correspondence to the Department of Chemistry, Cornell University, Ithaca, N. Y. 14850.

(1) J. E. Desnoyers and C. Jolicoeur, "Modern Aspects of Electrochemistry," Vol. 5, B. E. Conway and J. O'M. Bockris, Ed., Plenum Publishing Co., New York, N. Y., 1969, Chapter 1.

(2) C. Deverell, "Progress in N.M.R. Spectroscopy," Vol. 4, Pergamon Press, New York, N. Y., 1969.

(3) H. G. Hertz, *Angew. Chem. Int. Ed.*, 9, 124 (1970).

Table I: Comparison of Results of Number of Molecules in the First Shell of Ion from Various Nmr Methods

Ions	Broersma[a] (1958)	Hindman[b] (1962)	Hindman[b] (modified) (1962)	Fabricand[c] (1964)	Malinowski[d] (1966)	Creekmore,[e] *et al.* (1969)
Li^+	5 ± 2	-1.6	4	1 ± 1		3.4 ± 0.2[f]
Na^+	3 ± 1.2	3.1	3.1	3.6 ± 1	4.5 ± 1.3[f]	4.6 ± 0.2
K^+	1 ± 0.4	2.1	2.1	(6)		4.6 ± 0.2
Rb^+		1.6	1.6	9.9 ± 2		4.0 ± 0.2
Cs^+		1.0	1.0	14.6 ± 2		3.9 ± 0.2
F^-		1.6	1.6	9.9 ± 2		
Cl^-	2 ± 0.8	-1.1	0	13.2 ± 2	(0)	(0)
Br^-		-3.2	0	16.2 ± 2		
I^-		-7.5	0	21.8 ± 2		

[a] S. Broersma, *J. Chem. Phys.*, **27**, 481 (1957); **28**, 1158 (1958). [b] J. C. Hindman, *ibid.*, **36**, 1000 (1962). [c] B. P. Fabricand, S. S. Goldberg, R. Leifer, and S. G. Ungar, *Mol. Phys.*, **7**, 425 (1964). [d] E. R. Malinowski, P. S. Knapp, and B. Feuer, *J. Chem. Phys.*, **45**, 4274 (1966). [e] R. W. Creekmore and C. N. Reilley, *J. Phys. Chem.*, **73**, 1563 (1969). [f] Only sum of the values for cation and anion are obtained.

absorption peak. Unfortunately, a separate peak is not in practice obtained for monovalent ions.

An indirect way of deriving information on water in the first shell from nmr spectroscopy gave results shown in Table I. The discrepancies arise because the evaluations are based on *assumed* (but varied) structural models for water. Until these matters have been clarified, it is not possible to draw reliable conclusions on environment near anion from nmr studies.

X-Ray diffraction[1,5] can yield ion-to-water distances and the time-average coordination number. A systematic study of X-ray scattering patterns of aqueous solutions of alkali halides has been analyzed by Lawrence, *et al.*,[5] to obtain a CN for monovalent ions.

Lastly, ir and Raman spectral studies[1] have not been decisive in structural investigation because in concentrated solutions in which sufficient sensitivity is available, the interpretation becomes complicated, since librational bands have many components arising from $M^+ \ldots OH_2$ and $M^+ \ldots X^-$ interactions.

Krishnan and Friedman[6] state that the spectroscopic tools relied upon to resolve structural problems have not been decisive in respect to ion–solvent interactions. The reason seems to be the short lifetimes, $\simeq 10^{-12}$ sec, characterizing the hydrogen-bonded structures in liquid water and its ionic solutions.

An alternative approach to the model near an ion is through the interpretation of the physical properties of ionic solutions.[7] Relevant properties are summarized in Table II. This approach, however, seldom gives information on individual ions.

Various models[7-13] have been proposed for the region near an ion. Three representative models are summarized in Figure 1. It has hitherto not been possible to get experimental evidence which clearly favors one model over another. This difficulty[14] in the distinction among alternative structurals is contributed to by a lack of quantitative treatments of the models used.

In the following approximate calculations of heats and entropies of hydration have been made for chosen models. Recent X-ray measurements have been used to give the total number of water molecules in the first shell around an ion.

I. Heat of Hydration. A. Models

Three basic models of ionic hydration (together with variations of structure in the SB region), which differ from each other in respect to the characteristic structure in the first coordination shell, will be examined in this paper. Features of these models are in Table III. The notations chosen for models are: 1A, 1B, 1C; 2A, 2B, 2C; and 3A, 3B, 3C; where 1, 2 and 3 refer to three basic hydration models, and A, B, and C refer to the subdivision of the model for the SB region (Table III).

The model due to Bockris and Reddy[13] (see model 3 in Table III and Figure 1) recognizes a distinction between CN and SN. The significance of such a distinction was indicated by Conway, *et al.*,[1,15,16] who

(4) J. F. Hinton and E. S. Amis, *Chem. Rev.*, **67**, 367 (1967).

(5) R. M. Lawrence and R. F. Kruh, *J. Chem. Phys.*, **47**, 4758 (1967); R. M. Lawrence, Ph.D. Thesis, University of Arkansas (1965).

(6) C. V. Krishnan and H. L. Friedman, *J. Phys. Chem.*, **74**, 2356 (1970).

(7) J. O'M. Bockris, *Quart. Rev., Chem. Soc.*, **3**, 173 (1949).

(8) R. W. Gurney, "Ionic Processes in Solution," Dover Publications, New York, N. Y., 1962.

(9) J. D. Bernal and R. H. Fowler, *J. Chem. Phys.*, **1**, 515 (1933).

(10) D. D. Eley and M. G. Evans, *Trans. Faraday Soc.*, **34**, 1093 (1938).

(11) H. S. Frank and W. Y. Wen, *Discuss. Faraday Soc.*, **No. 24**, 133 (1957).

(12) O. Ya. Samoilov, "Structure of Electrolyte Solutions and Hydration of Ions," Engl. Transl., Consultants Bureau, New York, N. Y., 1965; *Discuss. Faraday Soc.*, **No. 24**, 141 (1957).

(13) J. O'M. Bockris and A. K. N. Reddy, "Modern Electrochemistry," Vol. I, Plenum Publishing Co., New York, N. Y., 1970.

(14) A. M. Holtzer and M. F. Emerson, *J. Phys. Chem.*, **73**, 26 (1969).

(15) B. E. Conway, R. E. Verrall, and J. E. Desnoyers, *Z. Phys. Chem. (Leipzig)*, **230**, 157 (1965).

Table II: Information Obtained for the First Shell from Various Experimental Data (Ref 7)

Authors	Method	Essence of method	Information intended to be obtained
Ulich[a]	Mobility	Stokes law used volume of solvation shell obtained	1. Number of molecules moving with the ion 2. Individual solvation number
Ulich[b]	Entropy of hydration	Entropy of solvation is equivalent to entropy of freezing of water (-6 eu mol^{-1})	1. Number of molecules acting as permanently solvated 2. It gives sum of SN
Darmois[c]	Density	Apparent molar volume, electrostrictional compression of solvation water	1. Number of molecules strongly electrostricted by ion 2. Sum of SN is obtained
Hasted,[d] *et al.*	Dielectric constant	Dielectric decrement attributed to the ions present, dielectric saturation	1. Number of molecules in first sheath which are dielectrically saturated 2. Sum of SN is obtained
Passyanski[e]	Compressibility	Solvation water has zero compressibility	1. Number of molecules fully compressed 2. Sum of SN is obtained
Wicke,[f] *et al.*, and Ackermann	Heat capacity	Loss of translational degrees of freedom on solvation	1. Number of molecules in the solvation shell 2. Sum of SN is obtained
Debye[g]	Ionic vibration potential	The potential difference is proportional to the difference of the effective masses of cations and anions	1. It should give the difference in SN of cation and anion 2. These results, when used with other methods, should give rise values for individual ions

[a] H. Ulich, *Trans. Faraday Soc.*, **23**, 388 (1927). [b] H. Ulich, *Z. Elektrochem.*, **36**, 497 (1930); *Z. Phys. Chem. (Leipzig)*, **168**, 141 (1934). [c] E. Darmois, *J. Phys. Radium*, **8**, 117 (1942). [d] J. B. Hasted, D. M. Ritson, and C. H. Collie, *J. Chem. Phys.*, **16**, 1 (1948); *cf. ibid.*, **20**, 1452 (1952). [e] A. Passyanski, *Acta Physicochim.*, **8**, 385 (1938). [f] E. Wicke, M. Eigen, and T. Ackermann, *Z. Phys. Chem. (Frankfurt am Main)*, **1**, 340 (1954); T. Ackermann, *Discuss. Faraday Soc.*, **No. 24**, 180 (1957). [g] P. Debye, *J. Chem. Phys.*, **1**, 13 (1933).

state that the converse calculation, *i.e.*, of estimating an hydration number, n, from apparent molar volume, using a value of the electrostriction of water per mole, is less satisfactory. n really measures rather the degree of partial loss of some property (volume in this case; compressibility or entropy in other cases associated with the solvent coordinated x-fold to the ion, than the true coordination number (CN) itself which probably varies less from (univalent) ion to ion than is indicated by the range of n values calculated in previous treatments of hydration.

In respect to the model with distinction between CN and SN, the solvational coordinated water (SCW), is defined as the number of fully oriented molecules, *i.e.*, $\cos\theta = 1$.

The concept of "nonsolvated coordinated water" arises in the following way.[13] The ion exists in two states in the solution. It is momentarily stationary or engaged in a diffusional jump. As it arrives at a new site, it is assumed to be coordinated by "SCW molecules" (*i.e.*, the molecules which accompanied during its movements).

"Solvation number" is defined as the number of water molecules which remain with the ion during its diffusive movements in solution. When the ion arrives at a new site, it may be there long enough to influence a number of the surrounding water molecules to be removed from the water structure and become solvated. Conversely, it may not have such effect on waters with which it is surrounded. These latter, still attached predominantly to the solvent structure, coordinate the ion but their dipoles have not had yet sufficient time (while they are neighbors of the ion) to rotate into the same ($\cos\theta = 1$) attractive position as that of the solvated coordinated waters, SCW. [Some development of a functional relation in terms of relaxation time connecting SN and CN is given in Saluja.[17]]

This model, in which some water molecules are firmly oriented toward the central ion whereas others have a less bound position somewhat, resembles the flip-flop model[18,19] of water on electrodes in the situation of water molecules is either strongly oriented in one direction towards the electrode or "flip-floppy" depending on the electrode charge.

(16) B. E. Conway, "Physical Chemistry, An Advanced Treatise," Vol. IXA, H. Eyring, Ed., Academic Press, New York, N. Y., 1970.

(17) P. P. S. Saluja, Ph.D. Thesis, University of Pennsylvania (1971); microfilm order No. 71-26,080.

(18) J. O'M. Bockris, M. A. V. Devanathan, and K. Muller, *Proc. Roy. Soc., Ser. A*, **274**, 55 (1963).

(19) K. Muller, Ph.D. Thesis, University of Pennsylvania (1965).

Table III: Models near an Ion (Also See Figure 1)

Model 1 First coordination shell	Model 2 First coordination shell	Model 3 First coordination shell
a. CN = 4 for all monovalent ions b. No distinction between SN and CN	a. CN ranges from 6 to 8 for monovalent ions b. No distinction between SN and CN	a. CN ranges from 6 to 8 for monovalent ions b. Distinction between SN and CN
Second layer (SB region): Model A, Model B, Model C	Second layer (SB region): Model A, Model B, Model C	Second layer (SB region): Model A, Model B, Model C
Molecules in the first shell are H-bonded to those in the SB region, rest of the solvent as bulk water	SB region consists of dimers formed from monomers drawn from liquid water	SB region consists of monomers some of which libirate with respect to molecules in the first shell

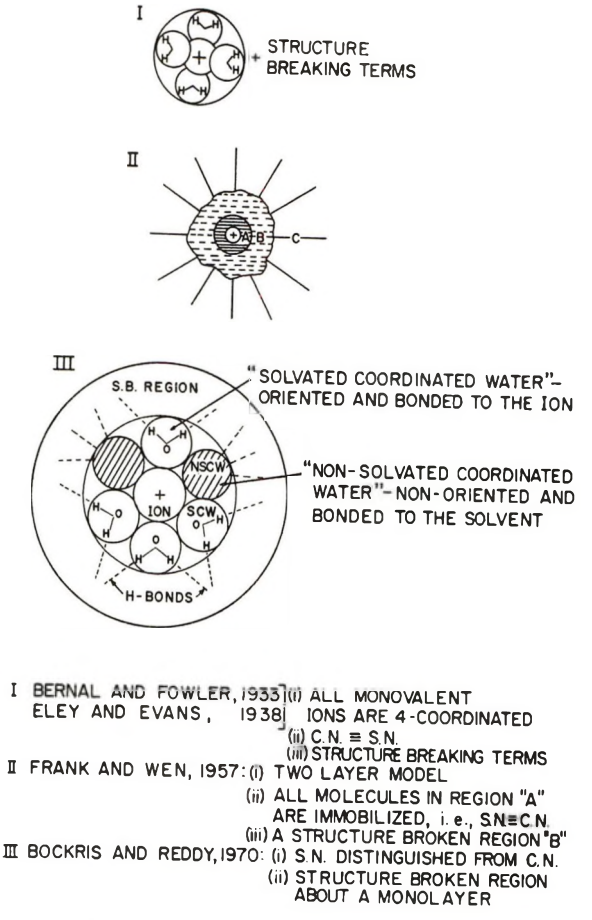

Figure 1. Models for the region near an ion.

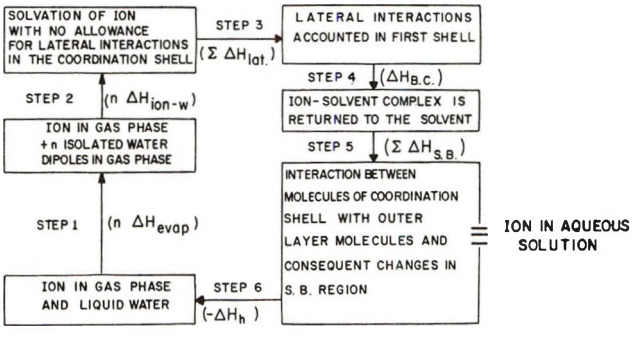

Figure 2. A cycle to separate out various contributions of ion–solvent interactions.

B. The Heat Changes Accompanying Hydration

The following steps in a hypothetical cycle (Figure 2) are carried out in the calculation of the heat of ionic hydration (ΔH_h): (1) the evaporation of the n water molecules from liquid water to the gas phase ($\Delta H_1 = n\Delta H_{evap}$) where n is the number of molecules in the first shell in a given model and ΔH_{evap} is the heat of evaporation (10.1 kcal mol^{-1}); (2) the gain on interaction of an ion with n water molecules in the gas phase ($\Delta H_2 = n\Delta H_{ion-w}$), where ΔH_{ion-w} is the ion–water interaction and is negative in sign; (3) a lateral interaction term: $\Delta H_3 = \Sigma\Delta H_{lat}$; (4) the phenomenon

Table IV: Relevant Quantities to Predict Heat of Hydration, ΔH_h

Ion	Li^+	Na^+	K^+	Rb^+	Cs^+	F^-	Cl^-	Br^-	I^-
r_{ion}, Å	0.60	0.95	1.33	1.48	1.69	1.36	1.81	1.95	2.16
$\Delta H_{ion-w} = H_{ion-SCW}$, kcal mol^{-1}	−29.92	−20.50	−14.75	−13.17	−11.38	−27.23	−18.67	−16.82	−14.51
ΔH_{i-NSCW}, kcal mol^{-1}	1.67	2.03	1.41	1.06	1.64	−10.94	−6.84	−5.99	−4.88
n_{CW}(X-ray)	(6)	(6)	(6)	(6)	(7)	(6)	(7)	(7)	(8)
n_{SCW}	(4)	(4)	(3)	(3)	(2)	(4)	(2)	(2)	(1.5)
n_{NSCW}	(2)	(2)	(3)	(3)	(5)	(2)	(5)	(5)	(6.5)
$(\Sigma E_{lat})_{CN-i}$ kcal	−2.3	−0.8	1.5	1.5	1.5	7.7	4.8	4.2	3.4
$(\Sigma E_{lat})_{CN-nCW}$ kcal	−20.7	−2.6	2.6	3.2	5.0	21.7	20.0	17.5	22.0
$(\Sigma E_{lat})_{SN \not\equiv CN}$ kcal	−2.3	−0.8	0.0	0.0	0.0	13.75	0.0	0.0	0.0
ΔH_{BC} kcal	−47.32	−42.91	−38.96	−37.59	−35.84	−38.68	−34.90	−33.87	−32.84
n_{SB}	23.6	28.7	34.8	37.4	41.1	35.3	43.4	46.0	50.2
$\Sigma\Delta H_{SB}$ (model 1A) kcal	−20.2	−20.2	−20.2	−20.2	−20.2	−20.2	−20.2	−20.2	−20.2
$\Sigma\Delta H_{SB}$ (model 2A) kcal	−30.3	−30.3	−30.3	−30.3	−35.4	−30.3	−35.4	−35.4	−40.4
$\Sigma\Delta H_{SB}$ (model 3A) kcal	−35.4	−35.4	−37.9	−37.5	−48.0	−32.8	−48.0	−48.0	−56.8
$\Sigma\Delta H_{SB}$ (model 1-3B) kcal	−64.5	−73.0	−83.0	−87.0	−92.75	−83.75	−96.25	−100.25	−106.7
$\Sigma\Delta H_{SB}$ (model 1C) kcal	−29.7	−31.7	−34.3	−35.3	−36.8	−34.4	−37.8	−38.8	−40.5
$\Sigma\Delta H_{SB}$ (model 2C) kcal	−40.0	−41.7	−44.3	−45.3	−51.8	−44.4	−52.8	−53.8	−60.5
$\Sigma\Delta H_{SB}$ (model 3C) kcal	−44.7	−46.8	−51.8	−52.3	−64.3	−46.9	−65.3	−65.8	−76.7

of Born-charging when the ion with its coordination shell is returned to the solvent ($\Delta H_4 = \Delta H_{BC}$); and (5) the interaction among the molecules in the first shell with molecules in the outer layer and, consequently, structural alterations in the SB region making a net contribution ($\Delta H_5 = \Sigma\Delta H_{SB}$).

The heat of ionic hydration, ΔH_h, can now be calculated as

$$\Delta H_h = \sum_{x=1}^{5} \Delta H_x \qquad (1)$$

When all the molecules in the coordination shell are treated as identical, *i.e.*, no distinction is made between CN and SN, ΔH_h will be

$$(\Delta H_h)_{SN\equiv CN} = n\Delta H_{evap} + n\Delta H_{ion-w} + (\Sigma\Delta H_{lat})_{SN\equiv CN} + \Delta H_{BC} + (\Sigma\Delta H_{SB})_{SN\equiv CN} \qquad (2)$$

When the SN is distinguished from the CN, ΔH_{ion-w} will differ for molecules referred to as solvational coordinated water (SCW), from those referred to as nonsolvational coordinated water (NSCW). ΔH_h will be

$$(\Delta H_h)_{SN \not\equiv CN} = n\Delta H_{evap} + n_{SCW}\Delta H_{ion-SCW} + n_{NSCW}\Delta H_{ion-NSCW} + (\Sigma\Delta H_{lat})_{SN \not\equiv CN} + \Delta H_{BC} + (\Sigma\Delta H_{SB})_{SN \not\equiv CN} \qquad (3)$$

Evaluation of the Energy Terms. $\Delta H_{ion-water}$. The interaction energy of an ion, with a water molecule oriented along the ionic field[13] is

$$\Delta H_{ion-w} = \Delta H_{ion-dipole} + \Delta H_{ion-quadrupole} + \Delta H_{ion-ind.dipole}$$

or

$$\Delta H_{ion-w} = \frac{-|z|e\mu_w}{\epsilon r^2} \pm \frac{zep_w}{2\epsilon r^3} - \frac{1}{2}\frac{\alpha_w(ze)^2}{r^4} \qquad (4)$$

where μ_w, p_w, and α_w are the dipole moment, quadrupole moment, and polarizability of the water molecule.[19a] r is the ion-water distance ($= r_i + r_w$) where r_i is crystal ionic radius and r_w is the radius of the water molecule. The ± sign in the ion-quadrupole term refers to cation and anion, respectively.

The question as to whether the anionic water molecules in the inner layer are symmetrical to the position obtaining near cation or, as suggested by Verwey[20] and Vaslow,[21] in a dissymmetric position with a dipole at an angle of 52° near cation and 120° near anion is not yet quite unambiguous. A recent discussion by Hertz[22] tends to favor the former structure which is that which has been used here.

Using values[23] of 1.84×10^{-18} esu cm, 3.9×10^{-26} esu cm^2, and 1.444×10^{-24} cm^3 $molecule^{-1}$ for μ_w, p_w, and α_w, respectively, eq 4 can be rewritten as (see Table IV for numerical values)

$$\Delta H_{ion-SCW}\ (\text{kcal mol}^{-1}) = 14.3976\left[\frac{-8.8357}{r^2} \pm \frac{9.3639}{r^3} - \frac{16.6487}{r^4}\right] \qquad (5)$$

(19a) Note Added in Proof. Other terms (not included in eq 4 and 6) for ion-water interactions such as higher moment terms, polarization, induction, ion-water repulsion, charge transfer, covalent bonding etc., though physically realized, have been neglected because these terms tend to compensate and thus their magnitude is not far from negligible in the present approximate calculations. However, it is suggested to utilize recent mass spectrometric data on ion-water clustering equilibria [see I. Džidić and P. Kebarle, *J. Phys. Chem.*, **74**, 1466, 1475 (1970)] in gas phase, to such calculations after accounting for the effect of the second and higher shell molecules on those in the first shell in aqueous media.

(20) E. J. W. Verwey, *Recl. Trav. Chim. Pays-Bas.*, **61**, 127 (1942).

(21) F. Vaslow, *J. Phys. Chem.*, **67**, 2773 (1963).

(22) H. G. Hertz, *Angew. Chem. Int. Ed.*, **9**, 124 (1970).

(23) A. D. Buckingham, *Discuss. Faraday Soc.*, **No. 24**, 151 (1957); *Quart. Rev., Chem. Soc.*, **13**, 183 (1959).

$\Delta H_{ion-NSCW}$. When SN $\neq$ CN, there will be two interaction energies: (a) the interaction energy of the SCW with the ion, $\Delta H_{ion-SCW}$; and (b) the interaction energy of NSCW with the ion, $\Delta H_{ion-NSCW}$. The $\Delta H_{ion-SCW}$ is given by eq 5. A NSCW does not give any average preferred orientation.[13,24] Before it has time to orient towards the ion, the latter has already left the site. Thus, NSCW is still a part of the water structure but, on the average, has a H-bonding position blocked by the ion. Thus, its net ion-dipole interaction energy is zero. The interaction energy of a NSCW with the ion arises from the ion-induced dipole, ion-quadrupole, and the dispersion interactions.[19a]

Thus

$$\Delta H_{ion-NSCW} = \Delta H_{ion-d_{ind}} + \Delta H_{ion-quadrupole} + \Delta H_{disp} \quad (6)$$

Thus

$$\Delta H_{ion-NSCW} = -\frac{1}{2}\frac{\alpha_w(ze)^2}{r^4} \pm \frac{zep_w}{2r^3} - \frac{3}{4}\frac{h\nu\alpha_{ion}\alpha_w}{r^6} \quad (7)$$

where α_{ion} is the polarizability of the ion. $\Delta H_{ion-NSCW}$, calculated from eq 7, is listed in Table IV.

ΔH_{lat}. The net lateral interactions in the coordination shell for a CN of 4 and 6 can be calculated from the following expressions due to Buckingham.[23] For $\Sigma\Delta H_{lat}$ for CN other than a $\Sigma\Delta H_{lat}$ *vs.* CN plot obtained for CN of 4 and 6, was extrapolated. Thus, $\Sigma\Delta H_{lat} \rightarrow 0$ when CN $\rightarrow$ 1, *i.e.*, there is no other molecule to interact with; and for CN 6, the extrapolation is made to follow the shape of the curve of $\Sigma\Delta H_{lat}$ *vs.* CN, obtained from the equation[9]

$$\Sigma\Delta H_{lat} = \frac{D_n\mu_w{}^2}{r^3} \quad (8)$$

where D_n is a purely geometrical factor depending on CN. When the SN differs significantly from the CN, the $(\Sigma\Delta H_{lat})_{SN \neq CN}$ arises mainly from the SCW. Thus, for large ions, which have a low SN, $\Sigma\Delta H_{lat}$ obtained from the $\Sigma\Delta H_{lat}$ *vs.* CN plot is no more than 0.5 kcal. Therefore, for large ions, $\Sigma\Delta H_{lat}$ has been neglected.

ΔH_{BC}. The Born-charging contribution is given by

$$\Delta H_{BC} = -\frac{N(ze)^2}{2(r_i + 2r_w)}\left[1 - \frac{1}{\epsilon} - \frac{T}{\epsilon^2}\left(\frac{\partial\epsilon}{\partial T}\right)\right] \quad (9)$$

Using accurate values of $(1/\epsilon)(\partial\epsilon/\partial T)$ $(= -0.485 \times 10^{-3})$ obtained independently by Rushe, *et al.*,[25] and Kay, *et al.*[26]

$$\Delta H_{BC} \text{ (in kcal mol}^{-1}) = -\frac{160.9z^2}{(r_i + 2r_w)} \quad (10)$$

where r_i and r_w are in angstrom units (see Table IV).

$\Sigma\Delta H_{SB}$ (*Model A*). This model (*cf.* Table III) considers H bonding between the molecules in the first layer and those in the SB region. The assumption that the SB region may be only one water molecule thick is based on the dielectric-distance plot[17] obtained from Booth's relation[27] which seems to indicate that the dielectric constant attains bulk value at a distance of beyond second layer around monovalent ions. The SCW, which is oriented towards the ion, has two H-bonding positions blocked by the ion and offers the remaining two sites for H bonding to the solvent molecules in the SB region (see Figure 1). The NSCW still attached predominantly to the solvent structure, but on the average has a H-bonding position blocked by the ion and thus can offer three H-bonding sites to molecules in the SB region. Thus, the net gain in energy contribution from H bonding between molecules in the SB region to those in the first layer will be $(2/2)E_{H-bond}$ for the SCW and $(3/2)E_{H-bond}$ for NSCW, *i.e.*

$$\Sigma\Delta H_{SB} \text{ (model A)} = n_{CW}((2/2)E_{H-bond}) \text{ [when SN} \equiv \text{CN]} \quad (11)$$

and

$$\Sigma\Delta H_{SB} \text{ (model A)} = n_{SCW}((2/2)E_{H-bond}) + n_{NSCW}((3/2)E_{H-bond}) \text{ [when SN} \neq \text{CN]} \quad (12)$$

where E_{H-bond} is energy of one H bond is equal to -5.0 kcal mol^{-1}. The numerical values are listed in Table IV.

$\Sigma\Delta H_{SB}$ (*Model B*). This model (*cf.* Table III) considers the SB region as consisting of dimers, which are formed from monomers drawn from liquid water. If the lowering in the potential energy due to formation of a dimer from two monomers is $\Delta E_{m\rightarrow d}$, then

$$\Sigma\Delta H_{SB} \text{ (model B)} = \frac{n_{SB}}{2}(\Delta E_{m\rightarrow d}) \quad (13)$$

where n_{SB} is the number of molecules in the SB region per ion, and $\Delta E_{m\rightarrow d}$ is taken as the energy of one H bond, *i.e.*, $(-5.0$ kcal mol$^{-1})$. Values of $\Sigma\Delta H_{SB}$ (model B) are listed in Table IV.

$\Sigma\Delta H_{SB}$ (*Model C*). The SB region is, in this model (*cf.* Table III), considered to consist basically of monomers. [This assumption is based on the quantitative treatment of the water structure, by Nèmethy and Scheraga,[28] that adjacent clusters in liquid water are separated, on the average by one or two layers of unbonded molecules. Bockris, *et al.*,[29] suggested a similar iceberg model for liquid silicates.]

(24) T. Anderson and J. O'M. Bockris, *Electrochim. Acta*, **9**, 347 (1964).

(25) E. W. Rushe and W. B. Good, *J. Chem. Phys.*, **45**, 4667 (1966).

(26) R. L. Kay, G. A. Vidulich, and K. S. Pribadi, *J. Phys. Chem.*, **73**, 445 (1969).

(27) F. Booth, *J. Chem. Phys.*, **19**, 391, 1327, 1615 (1951).

(28) G. Nèmethy and H. A. Scheraga, *ibid.*, **36**, 3382 (1962); *ibid.*, **36**, 3341 (1962).

(29) J. O'M. Bockris, J. D. Mackenzie, and J. A. Kitchener, *Trans. Faraday Soc.*, **52**, 299 (1956).

In respect to the existence of monomeric waters, a number of estimates have been made (25°): Eucken,[30] 11%; Hall,[31] 30%; Grjotheim and Krogh-Moe,[32] 50%; Wada,[33] 65%; Némethy and Scheraga,[28] 30%; Walrafen,[34] 30%.

However, Pople,[35] Stevenson,[36] and Wall and Hornig[37] argue that the percentage of monomeric molecules in water is much smaller than the values stated above.

Some distinction is offered by Horne[38] who pointed out that transport processes in liquid water should all have the same rate-determining step if the concentration of monomeric water is negligible. Whereas the converse is more likely, *i.e.*, different transport processes in liquid water entail a variety of rate-determining steps such as hole or vacancy formation and rotation of molecules. This view will be accepted in the present paper. Thus, in this paper, the main body of the water is in associated groups of 30 to 40 molecules. The monomeric water exists essentially between such groups.

Some of these monomers are H-bonded to the molecules in the first shell. The SCW and NSCW participate in two and three H bonds with molecules in the SB region.[38a] The formation of a SB region of monomers can be treated according to the following cycle

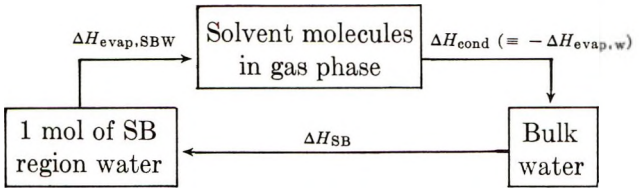

One can write

$$\Delta H_{SB} + \Delta H_{evap,SBW} + \Delta H_{cond,w} = 0 \quad (14)$$

or

$$\Delta H_{SB} = -\Delta H_{evap,SBW} - \Delta H_{cond,w} \quad (15)$$

or

$$\Delta H_{SB} = \Delta H_{evap,w} - \Delta H_{evap,SBW} \quad (16)$$

$\Delta H_{evap,SBW}$ can be approximately estimated obtained from free volume theory of liquids by using the following expressions,[39] provided the free volume in the SB region and the bulk are known

$$\ln V_{f,w} = 1 + \ln \frac{RT}{p_w} - \frac{\Delta H_{evap,w}}{RT} \quad (17)$$

and

$$\ln V_{f,SBW} = 1 + \ln \frac{RT}{p_{SBW}} - \frac{\Delta H_{evap,SBW}}{RT} \quad (18)$$

From eq 17 and 18

$$\ln \frac{V_{f,SBW}}{V_{f,w}} = -\left(\frac{\Delta H_{evap,SBW} - \Delta H_{evap,w}}{RT}\right) \quad (19)$$

on the assumption that the vapor pressure of the two forms of water are not significantly different. Using a value of $V_{f,SBW}$ (see section II) of 0.20 cm^3 mol^{-1} for water in the SB region and 0.40 cm^3 mol^{-1} for $V_{f,w}$[40]

$$\ln \frac{0.20}{0.40} = -\left(\frac{\Delta H_{evap,SBW} - \Delta H_{evap,w}}{RT}\right) \quad (20)$$

or

$$\Delta H_{evap,w} - \Delta H_{evap,SBW} = -RT \ln 2 \quad (21)$$

Substitution of values from (21) into eq 16 gives

$$\Delta H_{SB} = -RT \ln 2 = -0.41 \text{ kcal mol}^{-1} \quad (22)$$

Thus, for Li^+, where n_{SB} (see following section) is 24, the net contribution of ΔH_{SB} will be -9.8 kcal. Similar calculations can be carried out for other ions. The net contribution from $\Sigma\Delta H_{SB}$ (model C) will be

$$\Sigma\Delta H_{SB}(\Delta H_{SB}) = n_{SB}((2/2)E_{H-bond}) \quad [SN \equiv CN] \quad (23)$$

and

$$\Sigma\Delta H_{SB} \text{ (model C)} = n_{SB}\Delta H_{SB} + n_{SCW}((2/2)E_{H-bond}) + n_{NSCW}((3/2)E_{H-bond}) \quad [SN \not\equiv CN] \quad (24)$$

where, ΔH_{SB} in the first term is obtained from eq 21. The values of $\Sigma\Delta H_{SB}$ (model C) are listed in Table IV.

n_{SB}. The number of molecules in the SB region can be calculated by consideration of packing of water molecules on the area available on the sphere made up of ion and the first layer around it. Thus, the number of molecules of cross-sectional area, πr_w^2, will be given as

$$n_{SB} = \frac{4\pi(r_i + 2r_w)^2}{\pi r_w^2} \quad (25)$$

Values of n_{SB} are listed in Table IV.

Numerical Evaluation of ΔH_h. The heats of hydration of various monovalent ions have been calculated

(30) A. Eucken, *Nachr. Akad. Wiss. Goettingen*, 38 (1946).

(31) L. Hall, *Phys. Rev.*, **73**, 775 (1948).

(32) K. Grjotheim and J. Krogh-Moe, *Acta Chem. Scand.*, **8**, 1193 (1954).

(33) G. Wada, *Bull. Chem. Soc. Jap.*, **34**, 955 (1961).

(34) G. E. Walrafen, *J. Chem. Phys.*, **44**, 1546 (1966).

(35) J. A. Pople, *Proc. Roy. Soc., Ser. A*, **202**, 323 (1950); **205**, 163 (1951).

(36) D. P. Stevenson, *J. Phys. Chem.*, **69**, 2145 (1965).

(37) T. T. Wall and D. F. Hornig, *J. Chem. Phys.*, **43**, 2079 (1965).

(38) R. A. Horne, "Survey of Progress in Chemistry," Vol. 4, A. F. Scott, Ed., Academic Press, New York, N. Y., 1968, Chapter 1.

(38a) Note Added in Proof. The model C for the SB region receives a strong support from recent X-ray data on aqueous solutions of electrolyte [W. Bol, G. J. A. Gerrits, and C. L. van Panthaleon van Eck, *J. Appl. Crystallogr.*, **3**, 486 (1970)]. These authors could explain the peak in the electron distribution function at 4.2 Å only if they assume a second hydration shell of 12 ± 2 water molecules, which is the model utilized for SB region molecules interacting with SCW molecules.

(39) E. A. Moelwyn-Hughes, "Physical Chemistry," 2nd revised ed, Pergamon Press, Oxford, 1965, p 731.

(40) A. Stearn and H. Eyring, *J. Chem. Phys.*, **5**, 113 (1936).

Table V: Comparison of Experimental Values of ΔH_h with Those Predicted with Different Models

Ion	Model	Li^+	Na^+	K^+	Rb^+	Cs^+	F^-	Cl^-	Br^-	I^-
ΔH_h (calcd), kcal mol^{-1}	1A	−149.1	−103.9	−76.3	−68.6	−59.7	−119.7	−84.6	−76.8	−67.3
	2A	−217.2	−138.2	−94.6	−83.1	−75.1	−150.1	−110.2	−98.8	−86.5
	3A	−132.8	−94.7	−55.6	−49.7	−34.1	−134.5	−83.9	−74.8	−67.4
	1B	−193.4	−156.7	−139.0	−135.4	−132.3	−183.3	−160.6	−156.8	−153.8
	2B	−251.4	−180.9	−147.2	−139.9	−132.6	−203.5	−176.2	−168.7	−152.9
	3B	−156.8	−132.3	−100.7	−98.2	−78.9	−185.5	−132.2	−127.0	−118.6
	1C	−158.6	−117.0	−90.4	−83.7	−76.3	−133.9	−102.2	−95.4	−87.5
	2C	−226.9	−149.6	−108.6	−98.1	−91.6	−164.2	−127.7	−117.2	−115.2
	3C	−150.0	−107.8	−70.2	−65.6	−49.0	−142.0	−101.0	−92.6	−82.2
ΔH_h[a] (exptl)		−124.4	−97.0	−78.0	−71.9	−66.1	−120.8	−86.8	−80.3	−70.5

[a] Values are referred to $H_{h,H^+} = -260.7 \pm 2.5$ kcal mol^{-1}.[41]

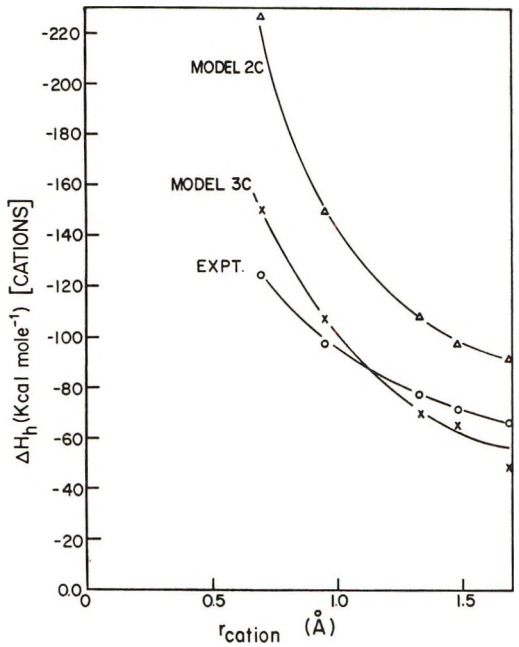

Figure 3. Heat of hydration against radius of cations.

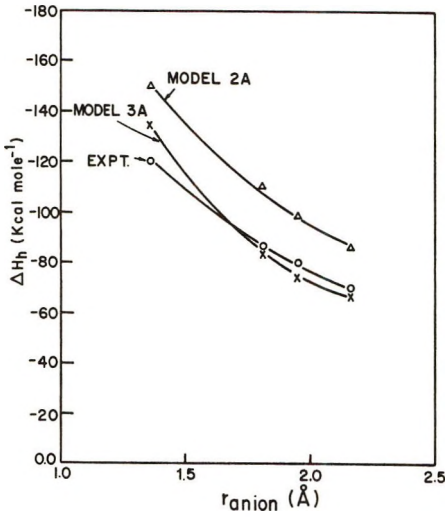

Figure 4. Heat of hydration against radius of anions.

for models by using (Table III) eq 2 and 3 and the parameters listed in Table IV. The results are shown in Table V and Figures 3 and 4.

C. Discussion

In considerations of the models most indicated by the comparisons of Figures 3 and 4 (Table V), we reject models 1A and 1C in spite of their good consistency, because of the clear evidence from the X-ray determinations of coordination numbers that the value is not uniformly 4, the basis of the calculations of model 1. [The model was pursued, however, because a CN of 4 has been used in most calculations of the solvation of ions in the literature.] The values of the solvation numbers have similar influence.[17] The models 2 are clearly least consistent with experiment.[5,17]

The models 3A and 3C are about equally consistent. The average deviation for anions is 8 and 9 kcal mol^{-1}, respectively. The deviations for the cations is 20 and 18 kcal mol^{-1}, respectively.

II. Entropy of Hydration. A. Models

The models for the region near an ion are shown in Table III.

Among models A, B, C (see Table III) for the SB region, model B (dimer model) was not calculated in detail. Thus, the entropy of hydration calculated for the model with no SB region[17] was found to be 40 to 60 eu mol^{-1} lower (more negative) than the experimental values (which range from −9 to −35 eu for monovalent ions). If model B were applicable the entropy of hydration would be *lowered* (made more negative) than that in the model in which no SB region is assumed.

B. Entropy Changes Accompanying Hydration

The ΔS_h is the entropy change for

$$\text{ion (in gas phase)} \longrightarrow \text{ion (in solution)} \qquad (26)$$

Thus

$$\Delta S_h = S_{i,s} - S_{i,g} \qquad (27)$$

(41) H. F. Halliwell and S. C. Nyburg, *Trans. Faraday Soc.*, **59**, 1126 (1963).

Table VI: Relevant Parameters in Calculations of the Entropy of Ionic Hydration

Ion	Li^+	Na^+	K^+	Rb^+	Cs^+	F^-	Cl^-	Br^-	I^-
$S_{i,g}$	31.8	35.3	36.9	39.2	40.6	34.8	36.7	39.1	40.6
ΔS_{BC}	−2.9	−2.6	−2.4	−2.3	−2.2	−2.4	−2.1	−2.1	−2.0
$\Delta S_{BC} - S_{i,g}$	−34.7	−37.9	−39.3	−41.5	−42.8	−37.2	−38.8	−41.2	−42.6
S_{rot}(SCW)	5.62	6.12	6.55	6.70	6.90	5.74	6.24	6.38	6.57
S_{vib}(SCW)	0.64	1.65	2.39	2.77	3.08	2.16	2.96	3.33	3.64
S(SCW)	6.26	7.77	8.94	9.47	9.98	7.90	9.20	9.71	10.21
S_{rot}(NSCW)	9.43	9.18	9.66	10.03	10.50	6.94	7.57	7.74	8.02
S_{vib}(NSCW)	0.89	2.30	3.36	3.85	4.33	3.14	4.27	4.74	5.16
S(NSCW)	10.32	11.48	13.02	13.88	14.83	10.08	11.84	12.48	13.18
$\Sigma\Delta S_{SB}$ (model 1A)	10.24	10.24	10.24	10.24	10.24	10.24	10.24	10.24	10.24
$\Sigma\Delta S_{SB}$ (model 2A)	15.36	15.36	15.36	15.36	17.92	15.36	17.92	17.92	20.48
$\Sigma\Delta S_{SB}$ (model 3A)	17.92	17.92	19.20	19.20	24.32	16.64	24.32	24.32	28.80
$\Sigma\Delta S_{SB}$ (model 2C)	32.8	40.4	49.6	53.5	58.6	50.3	62.1	65.9	72.2
$\Sigma\Delta S_{SB}$ (model 3C)	32.3	39.9	48.9	52.8	57.5	50.1	61.0	64.8	71.0

The second term in the right-hand side of eq 27 is the entropy of the ion in the gas phase and the first term represents the total entropy change caused upon the entry of the ion into the solution.[10] $S_{i,s}$ will be given as

$$[S_{i,s}]_{SN\equiv CN} = S_{tr,ion} + n_{CW}(S_{CW-i} - S_{w-w}) + \Delta S_{BC} + \Sigma\Delta S_{SB} \quad (28)$$

$$[S_{i,s}]_{SN\not\equiv CN} = S_{tr,ion} + n_{SCW}(S_{SCW-i} - S_{w-w}) + n_{NSCW}(S_{NSCW-i} - S_{w-w}) + \Delta S_{BC} + \Sigma\Delta S_{SB} \quad (29)$$

where $S_{tr,i}$ is the translational entropy of the ion, S_{CW-i} is the entropy of coordinated water in the first shell around the ion, S_{w-w} is the entropy of water in liquid water, ΔS_{BC} is Born-charging entropy, S_{SCW-i} and S_{NSCW-i} are, respectively, the entropy of SCW and NSCW near to the ion, and $\Sigma\Delta S_{SB}$ is the net entropy contribution of the structure-broken region around the ion.

The substitution into (27) of the values of $S_{i,s}$ from eq 28 and 29 gives the entropy of hydration.

Evaluation of Relevant Terms. $S_{i,g}$. This is calculated from

$$S_{i,g} = {}^3/_2R \ln M_{ion} + 26.0 \quad (30)$$

where M_{ion} is the mass of the ion (Table VI).

ΔS_{BC}. The Born-charging entropy is given by

$$\Delta S_{BC} = \frac{N_A(ze)^2}{2(r_i + 2r_w)}\frac{1}{2}\left(\frac{\partial\epsilon}{\partial T}\right) \quad (31)$$

which at 25° becomes[25,26]

$$\Delta S_{BC} = -\frac{9.787z^2}{(r_i + 2r_w)} \text{ (eu mol}^{-1}) \quad (32)$$

where r_i and r_w are in angstrom units (Table VI).

$S_{tr,ion}$. Now

$$f_{tr,ion} = \frac{(2\pi m_{ion}kT)^{3/2}}{h^3} V_{f,ion} \quad (33)$$

where m_{ion} is the mass of the ion, and $V_{f,ion}$ is the free volume available to the ion in solution. [The values of $S_{tr,ion}$ obtained by Eley and Evans (EE)[10] are too high to be reasonable (*ca.* 70% of gas phase values). There are two reasons. (1) EE[10] took the whole free volume of the solution as available to the solvent and solute molecules but neglected a detailed model of the region near the ion. (2) With respect to the temperature dependence of V_f, which is necessary to calculate $S_{tr,ion}$, EE[10] took the temperature dependence of V_f for water. The second factor alone contributes by $RT(\partial \ln V_f/\partial T)$, *i.e.*, 10 to 12 eu to the entropy of ion in solution.] Then

$$S = R \ln f_{tr,ion} + RT\frac{\partial \ln f_{tr,ion}}{\partial T} \quad (34)$$

Now

$$V_{f,soln} = x_{salt}V_{f,salt} + (1 - x_{salt})V_{f,water} \quad (35)$$

where $V_{f,soln}$, $V_{f,salt}$, and $V_{f,water}$ are the free volumes of solution, salt, and water, respectively, and x_{salt} is the mole fraction of the salt, eq 35 can be rearranged as

$$V_{f,soln} = V_{f,water} + x_{salt}(V_{f,salt} - V_{f,water}) \quad (36)$$

The plot of $V_{f,soln}$ *vs.* x_{salt} can then be used to calculate $V_{f,salt}$.

The $V_{f,soln}$ can be calculated from sound velocity by the expression[39,40]

$$V_{f,soln} = \left(\frac{U_g}{U_{soln}}\right)^3 V_{soln} \quad (37)$$

where U_g [$= (\gamma RT/M)^{1/2}$] is the velocity in the gas phase given by kinetic theory, U_{soln} as the sound velocity in solution, and V_{soln} is the molar volume of the solution. Equation 37 at 298.16°K, becomes

$$V_{f,soln} = \left(\frac{18.63 \times 10^4}{U_{soln}}\right)^6 \frac{V_{soln}}{M_{soln}^{3/2}} \quad (38)$$

where M_{soln} is the molar weight of the solution. The molar volume, V_{soln}, of a binary solution is given by[42]

$$V_{soln} = \frac{1}{\rho_i \Sigma w_i/M_i} \quad (39)$$

where w_i and M_i are the weight fraction and molar weight of the ith component, and ρ is the density of the solution. For NaCl, eq 39 reduces to

$$V_{soln} = \frac{18}{(1 - 0.6923w_2)} \quad (40)$$

where w_2 is the weight fraction of NaCl in solution. M_{soln} in eq 38 is given by

$$M_{soln} = x_{salt}M_{salt} + x_{solv}M_{solv} \quad (41)$$

where x^s are the mole fractions of salt and solvent in the solution. Using sound velocity measurements made in this laboratory,[17] V_{soln} from eq 40, M_{soln} from eq 41, $V_{f,soln}$ can be calculated from eq 38 for different mole fraction, x_{salt}, of the salt.

The $V_{f,salt}$ obtained from the slope of $V_{f,soln} - x_{salt}$ plot is -2.2 cm^3 mol^{-1}. [This result for the translational entropy of ions is surprising when compared with S_{trans} for monomeric water[43] (*ca.* 14 eu mol^{-1}). However, the monomeric water has available the total free volume of water in the calculation of the translational entropy. The ions themselves exist in a space, the free volume of which is diminished towards zero by their close association with the primary hydration sheath. The solvated ion also binds in upon itself the surrounding waters.] As $V_{f,salt}$ cannot be negative, it is taken that this value indicates a value of zero for the translational entropy of the ion. A similar result was obtained for the solvated complex.

S_{SCW-i}. The entropy of SCW is made up of librational ($S_{lib,i}$) and vibrational ($S_{vib,i}$) contributions. $S_{lib,i}$ can be calculated as follows.

$S_{lib-ion}$. The partition function, f_{rot}, under a field is[10]

$$f_{lib} = \frac{8\pi^2(8\pi^3 I_1 I_2 I_3 k^3 T^3)^{1/2}}{\sigma_w h^3} \frac{\sinh E_r/kT}{E_r/kT} \quad (42)$$

where I_1, I_2, and I_3 are the moments of inertia of the water molecules about three mutually perpendicular axes and E_r is the ion–water interaction energy. σ_w is symmetry factor and equal to 2 for water.

$$S_{lib} = \left[\frac{8\pi^2(8\pi^3 I_1 I_2 I_3 k^3 T^3)^{1/2}}{\sigma_w h^3} + \ln \sinh E_r/kT - E_r/kT + \coth E_r/kT + {}^5/_2\right] \quad (43)$$

For $E_r \gg kT$, in the case of water molecule oriented near to the ion, eq 43 becomes[10]

$$S_{lib} = R\left[\ln \frac{8\pi^2(8\pi^3 I_1 I_2 I_3 k^3 T^3)^{1/2}}{\sigma_w h^3} - \ln E_r/kT - \ln 2 + {}^5/_2\right] \quad (44)$$

Inserting numerical values of I_1, I_2, I_3 from a recent compilation,[44] S_{lib} at 298.16°K

$$S_{lib} = R[5.57 - \ln E_r/kT] \quad (45)$$

Substituting, ΔH_{i-w} for E_r from Table IV, $S_{lib,i}$ for SCW molecules near ions can be calculated. This quantity E_r represents ion–dipole, ion–quadrupole, and ion–induced dipole interactions.[19a] The contribution to E_r from lateral interactions were not calculated in detail. Their rough calculations suggest that they would made a maximum contribution of 5%.

In the computation of rotational entropy of SCW and NSCW near an ion, the only rotations which should be treated as librational are those about the axes perpendicular to the dipole axis.[28] The third rotation, *i.e.*, about the dipole axis, does not change the orientation of the dipole and will be close to a free rotation.[28] Thus, the entropy for this free rotation will be given by

$$f = \frac{2\pi}{\sigma}\left(\frac{2\pi I_\mu kT}{h^2}\right)^{1/2} \quad (46)$$

where I_μ is the moment of inertia of water molecule about the dipole axis and is[44] 1.9187×10^{-40} g cm^{-2}. Thus, $S_{rot,free} = 3.43$ eu mol^{-1} (Table VI).

Thus

$$S_{SCW,rot} = {}^2/_3 S_{lib,SCW} + 3.43 \quad (47)$$

$$S_{NSCW,rot} = {}^2/_3 S_{lib,SCW} + 3.43 \quad (48)$$

$S_{vib,i}$. $S_{vib,i}$ can be calculated from

$$f_{vib,i} = \left(2 \sinh \frac{h\nu}{2kT}\right)^{-1} \quad (49)$$

$$S_{vib,i} = R \ln \left(2 \sinh \frac{h\nu}{2kT}\right)^{-1} + R\left(\frac{h\nu}{2kT}\right) \coth \left(\frac{h\nu}{2kT}\right) \quad (50)$$

where ν is the vibrational frequency of water near to an ion. ν can be obtained from eq 51

(42) Reference 39, p 811.

(43) H. S. Frank and A. S. Quist, *J. Chem. Phys.*, **34**, 604 (1961).

(44) D. Eisenberg and W. Kauzmann, "The Structure and Properties of Water," Oxford University Press, Oxford, 1969.

$$\nu = \frac{1}{2\pi}\sqrt{k/\mu} \tag{51}$$

provided the force constant k, and the reduced mass, μ, are known.

Now

$$k = \left(\frac{\partial^2 U}{\partial x^2}\right)_{r=r_e} \tag{52}$$

Since

$$U_r = -\frac{ze\mu}{\partial r^2} + \frac{A}{r^9} \tag{53}$$

where n is 9 for water near the ion.[45] Now, at equilibrium ion–water separation

$$\left(\frac{\partial U}{\partial r}\right)_{r=r_e} = 0 \tag{54}$$

Thus

$$A = {}^2/_9 ze\mu r_e^7 \tag{55}$$

From eq 53, 55, and expressing the displacements from the equilibrium separation, r_e, as $r_e + x$ and $r_e - x$, one gets, k

$$k = \frac{14ze\mu}{r_e^4} \tag{56}$$

or

$$k = \frac{123.7 \times 10^{42}}{r_e^4} \text{ (in dyn cm}^{-1}\text{ if } r_e \text{ is in Å)} \tag{57}$$

[The fact that the force constant, k, has this form may be more generally seen from a formulation by Sutherland,[46] one finds $k = [mze\mu(n - m)]/(r_e^{m+2})$, where m and n are the exponents of attractive and repulsive terms. If $m = 2$ and $n = 9$, $k = 14ze\mu/r_e^4$.] Thus, ν can be evaluated by inserting k from eq 57 into eq 51. The values of ν, when substituted in eq 51, give $S_{\text{vib,i}}$ (Table VI).

S_{NSCW}. S_{NSCW} is made up of $S_{\text{lib,NSCW}}$ and $S_{\text{vib,NSCW}}$. The librational entropy of the NSCW can be obtained from eq 45 and 48 by inserting value of $\Delta H_{\text{i–NSCW}}$ for E_r from row 3 of Table IV (see Table VI).

$S_{\text{vib,NSCW}}$ can be calculated from eq 50 if ν_{NSCW} is known. The NSCW has as attractive force only an ion-induced dipole component (see ΔH_h). Thus, the force constant, k_{NSCW}, can be worked out by using eq 52–55. It is

$$k_{\text{NSCW}} = \frac{10(ze)^2}{r_e^6} \tag{58}$$

or

$$k_{\text{NSCW}} = \frac{332.9 \times 10^4 z^2}{r_e^6} \tag{59}$$

Substitution of k_{NSCW} in eq 51 gives ν_{NSCW} which, when used in eq 50, gives the vibrational contribution to the entropy of a NSCW near ions (see Table VI).

S_{SB} (*Model A*). In this model (see Table III), the hydrogen-bonded molecule of the SB region executes one free rotation about the H-bond axis, and two rotations about the axes perpendicular to the H-bond axis will be librational. $S_{\text{rot–H-bond axis}}$ can be obtained from eq 50 corresponding to a frequency of 60 cm^{-1} (or 1.80×10^{12} sec^{-1}) assigned[28] for the rotational band of a one hydrogen-bonded species. Thus

$$S_{\text{rot–H-bond axis}} = 4.48 \text{ eu mol}^{-1} \tag{60}$$

The entropy corresponding to two librations can be obtained by inserting the librational frequencies, $\nu_{\text{lib,1}}$ and $\nu_{\text{lib,2}}$ in eq 50. An assignment, based on the interpretation of the infrared spectrum for two libration frequencies,[28] are 4.35×10^{12} and 5.25×10^{12} sec^{-1}. Substituting these values in eq 50

$$(S_{\text{lib,1}})_{\text{SB}} = 2.74 \text{ eu mol}^{-1} \tag{61}$$

$$(S_{\text{lib,2}})_{\text{SB}} = 2.41 \text{ eu mol}^{-1} \tag{62}$$

The three vibrations, corresponding to the three translational degrees of freedom, for a molecule involved in a single H bond are assigned to have frequencies[28] of 1.80×10^{12} sec^{-1}. Thus, the entropy for these vibrations worked out from eq 50 is obtained to be

$$(S_{\text{vib}})_{\text{SB}} = 3[2.55] \text{ eu mol}^{-1} = 7.65 \text{ eu mol}^{-1} \tag{63}$$

From eq 60–63

$$(S_{\text{SB}})_{\text{H-bonded}} = 4.48 + 2.74 + 2.41 + 7.65 = 17.28 \text{ eu mol}^{-1} \tag{64}$$

Thus

$$S_{\text{SB}} \text{ (model A)} = n_{\text{SB,H-bonded}}(S_{\text{SB,H-bonded}} - S_{\text{w,w}}) \tag{65}$$

(See Table VI.)

S_{SB} (*Model C*). In this model (*cf.* Table III), the molecules in the SB region, which are not H-bonded to the first shell, are considered as unbonded molecules, *i.e.*, freely rotating monomers. These molecules are assigned three translational and three rotational degrees of freedom. The intramolecular bond stretching and bending modes are of high frequencies and do not contribute to the entropy of unbonded molecule.

One must know the free volume available to the unbonded molecule, $V_{f,\text{SB}}$, and its temperature dependence, so that the translational entropy may be calculated.

An approach to finding $V_{f,\text{SB}}$, may be made from sound velocity measurements. The concept is that if one takes a number of unassociated liquids, and plots

(45) Reference, 39, p 886.

(46) G. B. B. M. Sutherland, *J. Chem. Phys.*, **8**, 161 (1940).

Table VII: Comparison of Calculated Values of Entropy of Hydration with Experimental Values

Ion	Li^+	Na^+	K^+	Rb^+	Cs^+	F^-	Cl^-	Br^-	I^-
ΔS_h									
Model 1A	−63.42	−60.58	−57.30	−57.38	−56.64	−59.36	−55.76	−56.12	−55.52
Model 2A	−77.78	−71.92	−66.30	−65.32	−67.02	−70.44	−68.48	−67.31	−68.44
Model 3A	−67.10	−62.00	−50.20	−48.30	−36.30	−64.80	−48.90	−47.10	−40.80
Model 1C	−40.0	−29.6	−17.1	−13.3	−7.0	−13.4	−2.6	0.8	7.7
Model 2C	−60.4	−46.9	−32.1	−27.2	−26.4	−35.5	−24.3	−19.4	−17.2
Model 3C	−52.7	−40.0	−20.5	−14.6	−3.2	−31.4	−12.2	−6.6	0.7
ΔS_h (exptl)[a]	−33.7	−26.2	−17.7	−14.0	−14.0	−31.8	−18.2	−14.5	−9.0

[a] The experimental values are referred[1] to $S_{H^+}^\circ = 5.3 \pm 0.3$ eu mol^{-1}.

the free volume, V_f, obtained from sound velocity, against molar weight, an extrapolation through the molar weight of 18 will give rise to $(V_{f,SB})$, for freely rotating monomer.[17] The value of $(V_{f,SB})$ obtained through such an extrapolation is 0.20 ± 0.01 cm^3 mol^{-1}. A value of 0.2 cm^3 mol^{-1} for $V_{f,SB}$ has been used. The temperature dependence of $V_{f,SB}$ is obtained from the integration of

$$(C_v)_{SB} = RT^2\left(\frac{\partial^2 \ln V_{f,SB}}{T}\right) \quad (66)$$

which gives

$$T\frac{\partial \ln V_{f,SB}}{\partial T} = \frac{(C_v)_{SB}}{R} - \frac{x}{2} - 1.2 \quad (67)$$

where $(C_v)_{SB}$ is the heat capacity of the freely rotating monomers in the SB region; x is the number of degrees of freedom and −1.2 is the integration constant. In this model, $(C_v)_{SB}$ has a value of $(6/2)R$ arising from three translational and three rotational degrees of freedom. Thus, from eq 67

$$T\frac{\partial \ln V_{f,SB}}{T} = -1.2 \quad (68)$$

Using $V_{f,SB}$ of 0.20 cm^3 mol^{-1} and $T(\partial \ln V_{f,SB}/T)$ of −1.2, $S_{tr,SB}$ will be equal to

$$(S_{tr,SB})_{\text{freely rot}} = 7.0 \text{ eu mol}^{-1} \quad (69)$$

$S_{rot,SB}$ for three degrees of free rotations is equal to 10.48 eu mol^{-1}. Thus (Table VI)

$$S_{SB,\text{freely rot}} = 7.0 + 10.48 = 17.48 \text{ eu mol}^{-1} \quad (70)$$

$\Sigma\Delta S_{SB}$ (model C) =

$$n_{\text{H-bonded}}(S_{SB,\text{H-bonded}} - S_{w,w}) + (n_{SB} - n_{\text{H-bonded}})(S_{SB,\text{freely rot}} - S_{w,w}) \quad (71)$$

C. Discussion

In consideration of the models most indicated by comparisons of Table VII, as shown in Figures 5 and 6, it is necessary to reject model 1C in spite of its good numerical consistency because X-ray determinations of CN[5] indicate that the coordination number is not

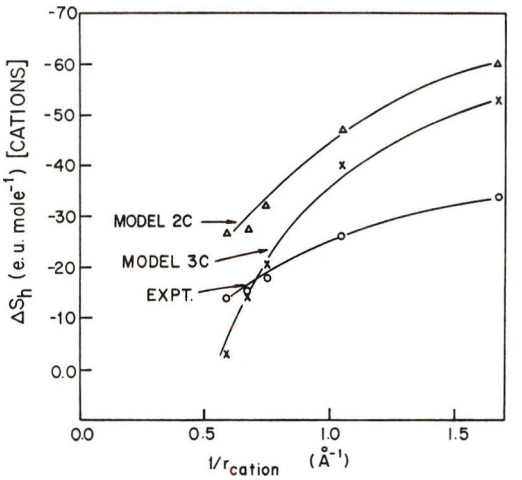

Figure 5. Entropy of hydration against reciprocal of ionic radius for monovalent cations.

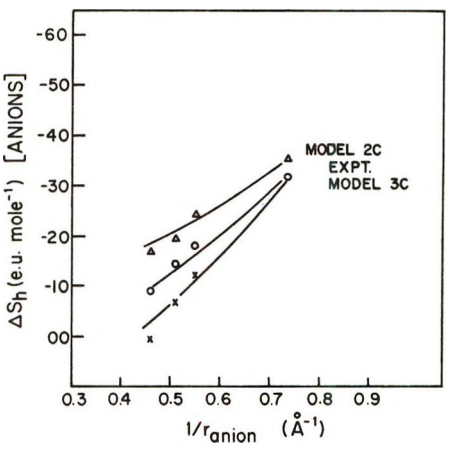

Figure 6. Entropy of hydration against reciprocal of ionic radius for halide ions.

4, but varies from 6 to 8 as a function of the ion. The experimental results on solvation numbers have similar inference, *i.e.*, a sharp distinction between the solvation numbers of larger and smaller ion is indicated (*i.e.*, the SN of Na^+ is 4, and that of I^- is 1.5).[17] Models 2A and 2C are the least consistent with the experiments (Figures 5 and 6).

The model 3C is most consistent for anions and is satisfactorily consistent for cations. The average deviation for anions is 4 eu mol^{-1}. The deviation for the cations is 10 eu mol^{-1}.

The model in which two different kinds of coordinating waters in the first shell have been assumed (*i.e.*, a "solvational" and a "nonsolvational" coordination number) gives numerically better consistency with experiment than do models lacking this feature. A CN of 4 for all monovalent ions, independent of ionic size, is unlikely.

The following conclusions are drawn. (1) A division of a region around the ion into two parts (Frank and Wen[11]) is supported. (2) In the first layer, one can distinguish two kinds of water molecules referred to as "solvated" and "nonsolvated." (3) The second layer is one water molecule thick and consists basically of monomers, some of which librate with respect to the first shell.

Conclusions 2 and 3 are new. The relative strength of the model used is shown in Figures 3–6 and Tables V and VII.[47–53]

Acknowledgments. The authors are grateful to the Office of Saline Water, Contract 14-01-0001-1467, for financial support. One of us, J. O'M. Bockris, wishes to acknowledge discussions with Professor B. E. Conway, University of Ottawa.

(47) Note Added in Proof. Ionic hydration has been a subject of a considerable theoretical interest with recent empirical[48] and quantum mechanical studies[49–51] One of the authors[52] is currently carrying out extensive quantum mechanical studies of ionic hydration in order to obtain a better understanding of binding forces between ion and water molecules. The recent experimental data[53] on ion–water clustering equilibrium is being utilized for the analysis of quantum mechanical results on solvation.

(48) S. Goldman and R. G. Bates, *J. Amer. Chem. Soc.*, **94**, 1476 (1972).

(49) R. E. Burton and J. Daly, *Trans. Faraday Soc.*, **67**, 1219 (1971); **66**, 1281, 2408 (1970).

(50) P. Russegger, H. Lischka, and P. Schuster, *Theor. Chim. Acta*, **24**, 191 (1972); **19**, 212 (1970); *Chem. Phys. Lett.*, **6**, 263 (1970); **11**, 35 (1971).

(51) G. H. F. Diercksen and W. P. Kraemer, *Theor. Chim. Acta*, **23**, 387, 393 (1972).

(52) P. P. S. Saluja and H. A. Scheraga, work in progress.

(53) P. Kebarle, "Ions and Ion Pairs in Organic Reactions," Vol. I, Michael Szwarc, Ed., Wiley-Interscience, New York, N. Y., 1972, Chapter 2; See also *J. Phys. Chem.*, **74**, 1466, 1475 (1970); *Can. J. Chem.*, **49**, 3308 (1971); **47**, 2619 (1969).

A Mass Spectrometric Study of the Vaporization of Cuprous Iodide

by T. E. Joyce* and E. J. Rolinski

Air Force Materials Laboratory (LPH), Wright-Patterson Air Force Base, Ohio 45433 *(Received December 28, 1971)*

Publication costs assisted by the Air Force Materials Laboratory

The vaporization of CuI has been investigated using mass spectrometric techniques. The vapor phase in equilibrium with CuI has been found to consist of Cu_3I_3 with smaller amounts of I, I_2, CuI, Cu_2I_2, and Cu_4I_4. The thermodynamics and partial pressures of the vapor species have been determined over the three solid modifications which exist in the temperature range of interest.

Introduction

The vaporization behavior of the copper chloride, bromide, and iodide systems has for some time been of interest to investigators active in the field of vaporization phenomena. Evidence was first provided by Brewer and Lofgren[1] for the complex nature of the vapor in equilibrium with the solid. Their study indicates that in the case of the chloride, and to a lesser extent the bromide, the predominant species in the vapor phase is the trimer, Cu_3X_3, with a smaller amount of monomer also present. The trimeric Cu_3Cl_3 molecule has also been studied employing electron diffraction techniques in order to determine its structure. Wong and Schomaker[2] report the trimer structure to be a planar six-membered ring. Rosenstock, Sites, Walton, and Baldock[3] have examined the vapors from CuCl, CuBr, and CuI mass spectrometrically. The samples in their experiment were placed on a platinum filament which was heated resistively. The resulting spectrum in each case was complex, including species indicative of the presence of tetrameric molecules over the chloride and bromide. Thermodynamic characterization of the vaporization of these compounds was

(1) L. Brewer and N. L. Lofgren, *J. Amer. Chem. Soc.*, **72**, 3038 (1950).

(2) C. Wong and V. Schomaker, *J. Phys. Chem.*, **61**, 358 (1957).

(3) H. M. Rosenstock, J. R. Sites, J. R. Walton, and R. Baldock, *J. Chem. Phys.*, **23**, 2442 (1955).

not attempted in their study. Sherwood and Turner[4] have recently reported the presence of a minor tetrameric species containing iodine while following a reaction between $I_2O_5(g)$ and Cu using a mass spectrometer.

Early vapor pressure data for the CuI system were reported by van Wartenberg and Bosse[5] and Jellinek and Rudat.[5] Subsequently, Shelton[7] has measured the vapor pressure of the same system using an effusion technique. Through indirect analysis he has concluded that in the region of interest the vapor is essentially trimeric and has analyzed his data on that basis. He further reports that while decompositon of the vapor molecules to the elements occurs outside the effusion cell, the degree of dissociation inside the cell is negligible.

The more recent observations of Sherwood and Turner[4] suggest that species which were previously unreported exist in the equilibrium vapor and that a detailed mass spectrometric investigation of the system might be helpful in resolving its behavior. Such a study has been carried out and the results of this study are reported here.

Experimental Section

The details of the mass spectrometric technique as applied to high-temperature vaporization phenomena have previously been discussed.[8] The instrument used in this study is a recently acquired Nuclide Analysis Associates 12-90-HT mass spectrometer. This instrument is a 90° sector, 30.5-cm radius of curvature, first-order direction focusing mass spectrometer which is equipped with a high-temperature Knudsen cell sample system. The resolution of the instrument was approximately $^1/_{1500}$ throughout the study.

Two types of Knudsen cell configurations were employed. The first type is a copper cell with a 0.05-cm diameter knife-edge orifice. The ratio of internal cell area to orifice area in this configuration is approximately 2700 to 1. The second type consists of an alumina cell in a copper holder. In the case of the ceramic cell, the orifice diameter is 0.1 cm and the length of the orifice is 0.15 cm. In this configuration the ratio of internal cell area to orifice area is 810 to 1.

Sample temperatures were determined using chromel–alumel thermocouples, the hot junctions of which were peened into blind holes in the bottoms of the cells or cell holders. The thermal emf's generated were referenced to the ice point and were measured using a Leeds and Northrup Type K-5 potentiometer. Prior to installation, the calibration of the thermocouples used was checked against a standard thermocouple. After installation, the calibration was again checked against the fusion point of zinc. Based on our observations, we take the error in our measurements of the temperature of the radiatively heated sample system to be ±1.0°.

All data were taken, except where noted, using 18-eV electrons with 0.5 mA emission current. The detector used in our instrument is a 16-stage electron multiplier with Cu–Be dynodes, the output of which is measured using a vibrating reed electrometer. A series of experiments was carried out using N_2^+, K^+, KCl^+, Ag^+, K_2Cl^+, $Cu_3I_2^+$, and $Cu_3I_3^+$ to assess the dependence of multiplier gain on the nature of the species impinging on the conversion dynode. The gain was measured using an insertable Faraday cup collector. Within our limits of error, the dependence of gain on the ionic mass and structure such as has been previously reported[9-11] was not observed. Such behavior is consistent with the findings of Gingerich.[12] Accordingly, we have taken the gain of our detector to be invariant for all ionic species reported in this work.

The samples used in this study were obtained from Alfa Inorganics. The material is "ultrapure" CuI with a purity of 99.9998%. The samples were used with no further treatment.

Results and Discussion

The mass spectrum of CuI at 430° was recorded using 18-eV ionizing electrons. The identity of the ionic species whose precursors had their origins in the effusion cell was ascertained by their mass to charge ratios, their shutterability and their isotopic abundances. The relative intensities of these species are given in Table I. In addition to 15 different ionic species composed of some combination of copper and iodine, four sets of peaks whose intensities were low compared to the more prominent Cu–I species were found. These were identified through isotopic abundance calculations and mass to charge ratios as being due to S, O, Cl, and Br impurities in the sample. The identities of SO^+ and SO_2^+ were further confirmed through appearance potential determinations.

Three weak peaks were observed in the mass spectrum which were quite diffuse, each peak extending over a mass range of up to ten mass units. The diffuse peaks appeared to have their maxima located at 347, 441, and 568 mass units with the diffuse peak at 347 being by far the most prominent. All three peaks were completely shutterable.

Each of these diffuse peaks has been attributed to decompositions giving rise to metastables. Using the

(4) P. M. A. Sherwood and J. J. Turner, *J. Chem. Soc. A*, 2349 (1970).

(5) H. van Wartenberg and O. Bosse, *Z. Elektrochem.*, 28, 384 (1922).

(6) K. Jellinek and A. Rudat, *Z. Phys. Chem. (Leipzig)*, 165, 117 (1933).

(7) R. A. J. Shelton, *Trans. Faraday Soc.*, 57, 2113 (1961).

(8) R. T. Grimley, "The Characterization of High Temperature Vapors," Wiley, New York, N. Y., 1967, pp 195–243.

(9) M. G. Inghram, R. Hayden, and D. Hess, *Nat. Bur. Stand. (U.S.), Circ.*, No. 522 (1951).

(10) M. G. Inghram and R. Hayden, Nuclear Science Series Report 14, 1954.

(11) P. Akishin, *Usp. Fiz. Nauk*, 66, 331 (1958).

(12) K. A. Gingerich, *Advan. Chem. Ser.*, No. 72, 291 (1968).

Table I: Relative Intensities of the Ionic Species Detected over CuI at 430°

Species	Mass no.	Relative intensity
Cu^+	63, 65	1
I^+	127	11
Cu_2^+	126, 128, 130	~0.1
Cu_3^+	189, 191, 193, 195	~0.2
CuI^+	190, 192	3
Cu_2I^+	253, 255, 257	40
I_2^+	254	1
Cu_3I^+	316, 318, 320, 322	3
CuI_2^+	317, 319	~0.2
$Cu_2I_2^+$	380, 382, 384	10
$Cu_3I_2^+$	443, 445, 447, 449	160
$Cu_2I_3^+$	507, 509, 511	~0.5
$Cu_3I_3^+$	570, 572, 574, 576	1000
$Cu_4I_3^+$	633, 635, 637, 639, 641	4
$Cu_4I_4^+$	760, 762, 764, 766, 768	3
SO^+	48	
SO_2^+	64, 66	
$Cu_3I_2Cl^+$	478, 480, 482, 484, 486	
$Cu_3I_2Br^+$	522, 524, 526, 528, 530	
Metastable no. 1	~347	
Metastable no. 2	~441	
Metastable no. 3	~568	

formalism presented by Hipple, Fox, and Condon,[13] the peak at mass number 347 has been identified as resulting from the reaction

$$Cu_3I_3^+ \longrightarrow Cu_3I_2^+ + I \qquad (1)$$

Based on the premise that both ionic species appearing in the decomposition also appear as normal ions in the mass spectrum and that the neutral product is a reasonable chemical species, we were unable to correlate the metastables appearing at mass numbers 441 and 568 with any possible normal decomposition process. It was furthermore not possible to establish unambiguously a decomposition reaction to explain these metastables by assuming a two-step acceleration process. These metastables must therefore remain unidentified.

All of the ionic species reported by Rosenstock, *et al.*,[3] were detected plus several others. Due to the conditions under which their data were taken, a quantitative comparison is meaningless.

Ionization efficiency curves were plotted for all shutterable species. The linear extrapolation method was used to determine appearance potentials. The energy of the ionizing electrons was calibrated by measurement of the appearance potential of Hg present as a background gas. The values determined for the appearance potentials of each of the species are listed in Table II. The maximum error of these determinations is estimated to be ±0.5 eV.

Based on the correspondence between the experimentally determined values for I^+ and I_2^+ and the values for their appearance potentials reported elsewhere,[14] it is concluded that these ions are produced by simple ionization of their respective parents, I and I_2. Likewise, the low values obtained for the $Cu_3I_3^+$ and $Cu_4I_4^+$ species lead us to conclude that they are products of the simple ionization of the trimer and tetramer, respectively. The Cu^+, Cu_2^+, Cu_3^+, Cu_2I^+, Cu_3I^+, CuI_2^+, and $Cu_2I_3^+$ ions all exhibited appearance potentials which are several electron volts higher than the $Cu_3I_3^+$ and $Cu_4I_4^+$ ions. Based on these observations, we have assigned these species to the trimer parent as fragments of a dissociative ionization process. The relatively low intensity of the $Cu_4I_4^+$ peak when compared to the $Cu_3I_3^+$ peak indicates that any contribution to these fragments from dissociative ionization of the tetramer is small.

Table II: Appearance Potentials of the Ionic Species Detected over CuI

Species	1st A.P., eV	2nd A.P., eV	Lit.[14] value, eV
Cu^+	15.2		
I^+	10.8		10.5
Cu_2^+	15.2		
Cu_3^+	17.0		
CuI^+	8.7	14.4	
Cu_2I^+	13.4		
I_2^+	10.1		10.0
Cu_3I^+	15.2		
CuI_2^+	16.1		
$Cu_2I_2^+$	9.3	14.8	
$Cu_3I_2^+$	10.8		
$Cu_2I_3^+$	13.6		
$Cu_3I_3^+$	9.1		
$Cu_4I_3^+$	9.5		
$Cu_4I_4^+$	8.7		

A definite break was noted in the ionization efficiency curves for both the CuI^+ and $Cu_2I_2^+$ species (see Figure 1). The first appearance potentials for the CuI^+ (8.7 eV) and $Cu_2I_2^+$ (9.3 eV) ions were taken to be indicative of the simple ionization of the corresponding neutral parents, CuI and Cu_2I_2. The second appearance potentials for both ions, marked by the discontinuity in the slope of the ionization efficiency curves, were taken in both cases to be due to the onset of dissociative ionization of the Cu_3I_3 molecule. Using appearance potential data alone, it is impossible to discern the parents of the $Cu_3I_2^+$ and $Cu_4I_3^+$ ions.

The intensity of each of the ions identified in the mass spectrum was recorded as a function of temperature and the logarithm of the intensity–temperature product was plotted for each species *vs.* reciprocal temperature. The use of the "proportionality rule" ad-

(13) J. A. Hipple, R. E. Fox, and E. U. Condon, *Phys. Rev.*, **69**, 347 (1946).

(14) J. L. Franklin, J. G. Dillard, H. M. Rosenstock, J. T. Herron, K. Droxl, and F. H. Fielol, *Nat. Stand. Ref. Data Ser., Nat. Bur. Stand. (U.S.)*, 26 (1969).

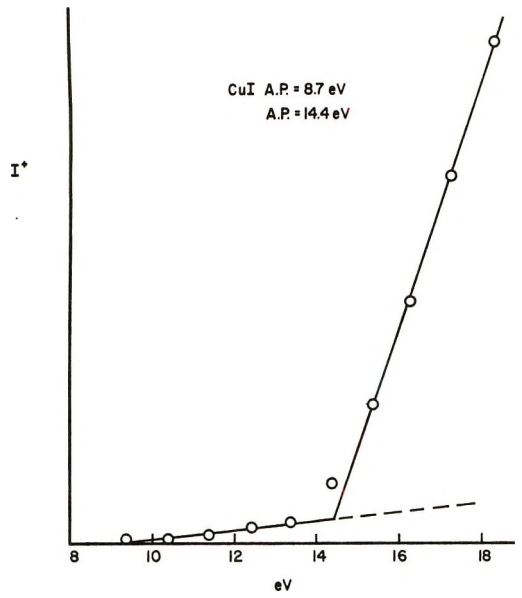

Figure 1. Ionization efficiency curve for the CuI^+ ion (intensity *vs.* electron energy).

vanced by Honig[15] along with the van't Hoff equation suggests that the enthalpy of sublimation obtained from the slope of such plots should be the same for all ions derived from a common neutral precursor. Comparison of the values obtained experimentally confirmed the assignments made on the basis of appearance potential data. The enthalpies of sublimation for the two unassigned peaks, $Cu_3I_2^+$ and $Cu_4I_3^+$, were compared to those for the $Cu_3I_3^+$ and $Cu_4I_4^+$ peaks (see Table III).

Table III: Apparent Second-Law Heats of Sublimation (kcal/mol) for $Cu_3I_2^+$, $Cu_3I_3^+$, $Cu_4I_3^+$, and $Cu_4I_4^+$ over α-CuI

	Experiment			
Species	3-15	3-16	3-17	3-18
$Cu_3I_2^+$	35.7 ± 1.4	37.1 ± 0.9	36.3 ± 1.4	38.3 ± 1.9
$Cu_3I_3^+$	34.7 ± 0.9	36.0 ± 0.4	35.8 ± 1.0	36.4 ± 1.0
$Cu_4I_3^+$	44.6 ± 2.2	47.2 ± 1.8	45.0 ± 2.1	44.9 ± 2.0
$Cu_4I_4^+$	41.4 ± 1.7	41.8 ± 1.1	41.3 ± 2.2	40.6 ± 1.0

A perusal of the enthalpies of sublimation obtained reveals that the $Cu_3I_2^+$ species has a higher apparent enthalpy of sublimation than does the $Cu_3I_3^+$ species, and the $Cu_4I_3^+$ species is similarly associated with a higher value than is the $Cu_4I_4^+$ species. The disparity in the values obtained for each of the species would seem to argue in favor of a Cu_3I_2 and Cu_4I_3 neutral species if the "proportionality rule" is universally valid. Such an assignment is not, however, consistent with the metastable transition which was observed and identified, which would indicate a dissociative ionization process.[16]

CuI is reported to exist in three solid phases in the temperature range over which this study was conducted.[17] The low temperature γ phase exists below 369° and has the zincblende structure. An intermediate phase, β-CuI, is present between 369 and 407°. The β phase has the wurtzite structure. Above 407° a high-temperature α phase appears. The structure of α-CuI has been proposed to be cubic. The heats of transition for the phase changes occurring in the solid have been determined. By utilizing a thermochemical cycle similar to that employed by Friedman,[18] additional information can, in principle, be obtained to further elucidate the origin of the $Cu_3I_2^+$ and $Cu_4I_3^+$ species.

By measuring the enthalpy of sublimation for the four species in question on either side of the $\alpha \rightarrow \beta$ transition point, the heat of transition was determined. The heats of sublimation were determined from the slopes of log I^+T *vs.* $1/T$ plots and are shown for all three phases in Table IV. Our results were compared to the calorimetrically determined values[17] as shown in Table V. The values obtained for the heats of transition which were obtained mass spectrometrically are in reasonable agreement with the literature values. In the case of the $Cu_3I_3^+$–$Cu_3I_2^+$ pair and with less certainty in the case of the $Cu_4I_4^+$–$Cu_4I_3^+$ pair, these data indicate that the members of each pair are vaporizing in the same way. If Cu_3I_2 and Cu_4I_3 are parents, they must be the product of a decomposition reaction of the type

$$Cu_3I_3(g) \longrightarrow Cu_3I_2(g) + I(g) \quad (2)$$

$$Cu_4I_4(g) \longrightarrow Cu_4I_3(g) + I(g) \quad (3)$$

Table IV: Experimentally Determined Values for Enthalpy of Sublimation of α, β, and γ Phases of Cu–I Systems

Species	$\Delta H(\alpha)$, kcal/mol	$\Delta H(\beta)$, kcal/mol	$\Delta H(\gamma)$, kcal/mol
$Cu_3I_3^+$	35.7 ± 0.5	37.8 ± 0.3	42.1 ± 0.2
$Cu_3I_2^+$	36.8 ± 1.0	38.6 ± 0.8	42.7 ± 0.8
$Cu_4I_4^+$	41.3 ± 1.3	45.2 ± 1.5	...
$Cu_4I_3^+$	45.4 ± 1.0	48.3 ± 1.3	...

Such decomposition reactions in the equilibrium vapor would account for the shutterable I^+ and I_2^+ signals which were observed. Because of the apparent problem of iodine's reacting with a copper Knudsen cell, a series of experiments was run using an alumina

(15) R. E. Honig, *J. Chem. Phys.*, **22**, 126 (1954).

(16) M. G. Inghram and J. Drowart, "Mass Spectrometry Applied to High Temperature Chemistry," Proceedings of the International Symposium on High Temperature Technology, Asilomar, Calif., 1959, McGraw-Hill Book Co., New York, N. Y.

(17) S. Miyake, S. Hashino, and T. Takinaka, *J. Phys. Soc. Jap.*, 7(1), 19 (1952).

(18) L. Friedman, *J. Chem. Phys.*, **23**, 477 (1955).

Table V: Comparison of Heats of Transition (kcal/mol) as Determined by Second-Law Heats of Sublimation and by Calorimetry

Species	$\Delta H_T(\alpha \rightarrow \beta)$	$\Delta H_T(\alpha \rightarrow \beta)_{cal}$	Parent
$Cu_3I_3^+$	−0.7	−0.77	Cu_3I_3
$Cu_3I_2^+$	−0.6	−0.77	Cu_3I_3
$Cu_4I_4^+$	−1.0	−0.77	Cu_4I_4
$Cu_4I_3^+$	−0.7	−0.77	Cu_4I_4
Species	$\Delta H_T(\beta \rightarrow \gamma)$	$\Delta H_T(\beta \rightarrow \gamma)_{cal}$	**Parent**
$Cu_3I_3^+$	−1.4	−1.7	Cu_3I_3
$Cu_3I_2^+$	−1.4	−1.7	Cu_3I_3

cell of the type described previously. The substitution of cell material had no effect on the relative intensities of the species reported in Table I.

In every case, when the high-temperature furnace assembly was removed from the mass spectrometer, a copper deposit was noted on the heater assembly and the interior of the heat shields. This observation is in accord with those of Shelton.[7] A decomposition to the elements apparently takes place outside the Knudsen cell. The possibility of such a decomposition inside the cell is not precluded, which suggests that the iodine in the equilibrium vapor could come from a decomposition reaction of the sort

$$(CuI)_x(g) \longrightarrow xCu(s) + xI(g) \quad (4a)$$

or

$$CuI(s) \longrightarrow Cu(s) + I(g) \quad (4b)$$

in addition to the decomposition proposed in eq 2 and 3. The failure of the cell material substitution to change the character of the mass spectrum can be accounted for by such an elemental decomposition in that the activity of Cu(s) is fixed at unity in either case.

A mass balance calculation was carried out, assuming reaction 2 to be the sole source of I(g) and I_2(g) in the cell. Based on the intensity ratios measured, the pressure of iodine would have to be increased by a factor of 3.5 to satisfy the conditions imposed by such a reaction. The failure to account for Cu_3I_2 by reaction 2 leads us to conclude that $Cu_3I_2^+$ and $Cu_4I_3^+$ are fragments of the dissociative ionization of the trimer and tetramer, respectively. The decomposition reaction in the cell then as given by reactions 4a or 4b is concluded to be the source of the iodine observed.

Since $Cu_3I_2^+$ and $Cu_4I_3^+$ are ion fragments, we must deal with the apparent breakdown of the "proportionality rule." The assignment of both $Cu_3I_3^+$ and $Cu_3I_2^+$ to the same parent and the assignment of both $Cu_4I_4^+$ and $Cu_4I_3^+$ to the same precursor is not consistent with the different second-law enthalpies obtained for the members of each pair. Others,[19] investigating the not dissimilar AgCl system, have contended that such results confirm the presence of the Ag_3Cl_2(g) species as a separate entity. In the case of the CuI system, we cannot accept such an interpretation.

The apparent breakdown of the "proportionality rule" has been reported previously.[20] The explanation favored by Berkowitz, *et al.*, for this phenomenon involves the assertion that the fragment ion is formed with excess kinetic energy and suffers discrimination in extraction from the ion source. These authors at the same time offer the conjecture that such behavior could be explained by a change in the Franck–Condon factors for ionization due to population of the first excited vibrational state of the parent molecule. While the former contention cannot be categorically refuted, we favor the latter in the case of the CuI trimer and tetramer.

The effect of temperature on the mass spectrum of hydrocarbons has been investigated by several workers.[21-24] Stevenson[22] and Reese, *et al.*,[24] both suggest that increased internal excitation of the parent molecule can result in a higher probability for dissociative ionization of the parent molecule and a decrease in the probability of formation of the molecule ion. Such observations are consistent with our data which indicate that at higher temperatures, a larger fraction of the parent trimer and tetramer molecules dissociate upon ionization to form fragment ions, having lost an iodine. Such a temperature-dependent electron impact ionization cross section for the formation of the individual species then gives rise to the unequal slopes encountered in the intensity–temperature plots. For purposes of calibration, we have taken the total ionization cross section for all ionization processes occurring for a given parent to be temperature independent and only the relative numbers of molecules undergoing simple *vs.* dissociative ionization are taken as temperature dependent.

In order to convert the intensity data to partial pressures for each species, a calibration of the mass spectrometer was necessary. In this case, two quantitative vaporization experiments were carried out in alumina cells. In the first, 20.875 mg of CuI was vaporized completely at 451.6°, leaving a copper residue weighing 100 μg. In the second, a 31.155-mg sample of CuI was vaporized at 452.0° leaving a copper residue weighing 190 μg.

The intensity of each of the shutterable ionic species was followed as a function of time and the resulting

(19) A. Visnapuu and J. W. Jensen, *J. Less-Common Metals*, **20**, 141 (1970).

(20) J. Berkowitz, H. A. Tassman, and W. A. Chupka, *J. Chem. Phys.*, **36**, 2170 (1962).

(21) R. E. Fox and J. A. Hipple, *ibid.*, **15**, 208 (1947).

(22) D. P. Stevenson, *ibid.*, **17**, 101 (1949).

(23) C. A. Berry, *ibid.*, **17**, 1164 (1949).

(24) R. M. Reese, V. H. Dibeler, and F. L. Mohler, *J. Res. Nat. Bur. Stand.*, **46**(2), 79 (1951).

Table VI: Pressure Equations and Second-Law Heats of Sublimation for Equilibrium Species over CuI

$$\log P(\text{atm}) = -\frac{A}{T°\text{K}} + B$$

Species	Phase	A	B	ΔH_s	T_{av}
CuI[a]	α	10,124.7 ± 516.7	5.9914 ± 0.7357	46.3 ± 2.4	702.6
Cu_2I_2[a]	α	8,750.2 ± 352.9	4.5928 ± 0.5028	40.0 ± 1.6	702.1
Cu_3I_3	α	7,732.6 ± 110.8	5.7159 ± 0.1578	35.4 ± 0.5	702.5
Cu_4I_4	α	9,511.4 ± 123.7	5.7807 ± 0.1762	43.5 ± 0.6	702.4
I_2	α	8,569.8 ± 200.4	4.0853 ± 0.2854	39.2 ± 0.9	702.6
Cu_3I_3	β	8,305.6 ± 72.4	6.5584 ± 0.1092	38.0 ± 0.3	660.9
Cu_4I_4	β	10,193.0 ± 149.0	6.7829 ± 0.2253	46.6 ± 0.7	661.8
Cu_3I_3	γ	9,253.4 ± 47.0	8.0344 ± 0.0768	42.3 ± 0.2	612.8
I[b]	...	8,404	4.8947		...

[a] Data obtained at 13 eV. [b] Calculated from the I pressure equation.

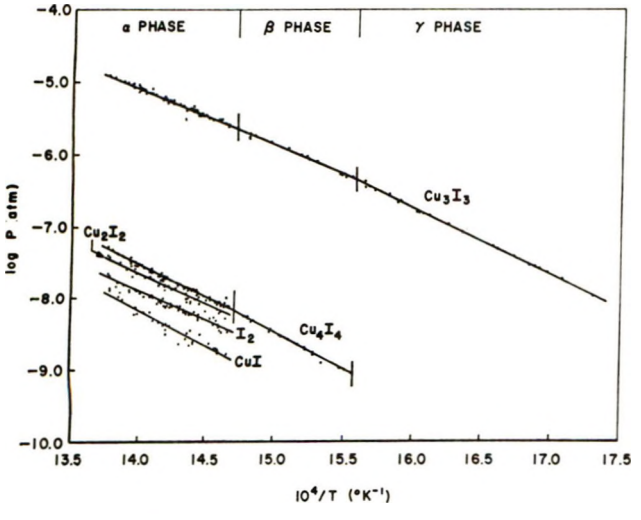

Figure 2. Partial pressures (atm) of the vapor species in equilibrium with CuI as a function of $10^4/T°\text{K}$.

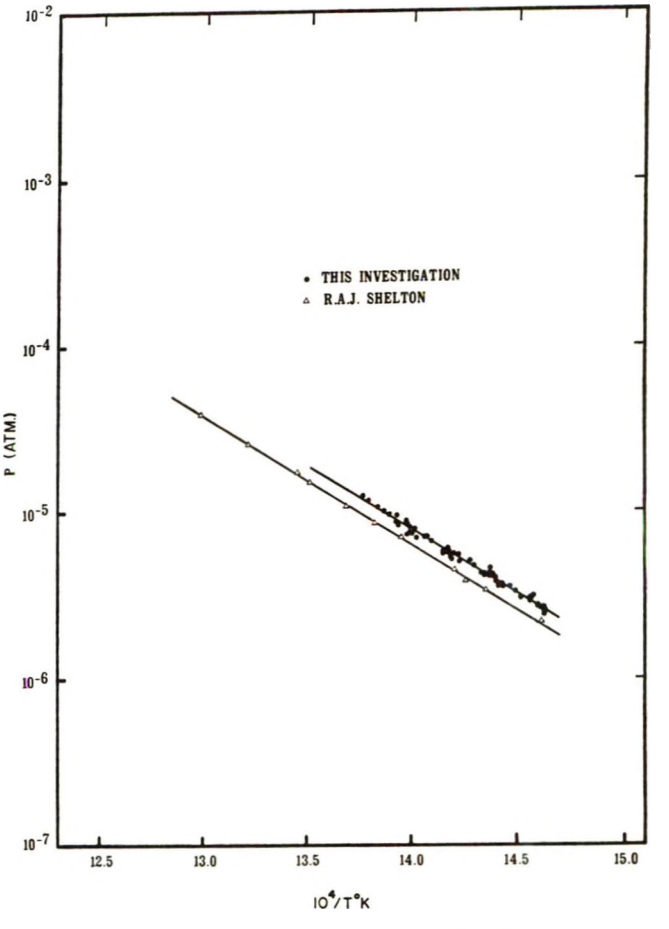

Figure 3. Comparison of pressures obtained by this work with those of Shelton.

intensity–time integrals were used to evaluate the sensitivity of the instrument. The rationale for the treatment of such data has been in part discussed previously.[8,25] A detailed consideration of these data has been published elsewhere.[26]

The additivity of atomic cross sections as proposed by Otvos and Stevenson[27] was accepted as valid as were the relative cross section values published by Mann.[28] Using the intensities measured during the early portion of the calibration experiments, a value for the pressure of the trimer at a reference temperature was obtained. The pressures of the other species were obtained through the relationship

$$P_1 = I_1{}^{+}T_1\left[\frac{P_2}{I_2{}^{+}T_2}\right]\left[\frac{\sigma_2}{\sigma_1}\right]\left[\frac{\Delta E_2}{\Delta E_1}\right] \qquad (5)$$

where P = partial pressure in atmospheres, T = temperature in °K, I^+ = isotope corrected intensity, σ = relative ionization cross section, and ΔE = energy of ionizing electrons minus the appearance potential.

The data from the second-law runs were forced to intersect the known pressure points. This was done by summing the intensities of all contributors from a given parent at each temperature and fitting the re-

(25) R. T. Grimley and T. E. Joyce, *J. Phys. Chem.*, **73**, 3047 (1969).

(26) T. E. Joyce and E. J. Rolinski, AFML-TR-71-262 (1971).

(27) J. W. Otvos and D. P. Stevenson, *J. Amer. Chem. Soc.*, **78**, 546 (1956).

(28) J. B. Mann, *J. Chem. Phys.*, **46**, 1646 (1967).

sultant set with a least-squares line. The results of this treatment are given in Table VI and Figure 2.

An inspection of Table VI shows that the partial pressure of I(g) is calculated. This calculation was carried out using the measured partial pressure of $I_2(g)$, the dissociation constant data of Perlman and Rollefson[29] and Murphy,[30] and the assumption of equilibrium inside the cell. This method of determination of the I(g) partial pressure was necessary as the intensity of I^+ as measured by our mass spectrometer is spuriously high.

When the molecular beam, composed mainly of Cu_3I_3 molecules, enters the ion source, a part of that beam collides with surfaces after entry. Deposits of copper have been seen in every region in the instrument where such collisions occur in high vacuum. It would appear then that a reaction of the sort

$$Cu_3I_3(g) \longrightarrow 3Cu(s) + 3I(g) \quad (6)$$

takes place inside the ion source. Because of the open nature of the source geometry, the probability of the iodine monomer's undergoing the reaction

$$2I(g) \longrightarrow I_2(g) \quad (7)$$

is remote. A shuttering procedure in this case, in addition to interrupting the molecular beam from the Knudsen cell, also stops this decomposition reaction. The intensity of the I^+ signal is thus enhanced with respect to the I_2^+ signal. Use of the dissociation constant, as suggested by Grimley,[8] to effect an instrument calibration would appear to be unreliable for this application.

Accepting the pressures calculated for the iodine species and the argument that all iodine in the equilibrium vapor comes from reactions 4a or 4b, it is possible to calculate the amount of copper which should remain in the Knudsen cell after the quantitative vaporization experiments. In the first, we measured 100 ± 20 μg in the cell. The residue calculated on the basis of the model proposed is 113 μg. In the second quantitative vaporization, we calculate a residue of 176 μg and found a residue of 190 ± 20 μg. We take these results to be in support of our iodine treatment.

The vapor pressure data of Shelton[7] are, to our knowledge, the only additional such data reported for the temperature range over which this investigation was carried out. His pressure data, calculated on the basis of an entirely trimeric vapor over the α phase, are shown along with our values for the trimer in Figure 3. The results of the two studies appear to be in reasonable agreement.

(29) M. L. Perlman and G. K. Rollefson, *J. Chem. Phys.*, **9**, 362 (1941).
(30) G. M. Murphy, *ibid.*, **4**, 344 (1936).

Viscous Flow in Simple Organic Liquids

by W. T. Laughlin[1] and D. R. Uhlmann*

Department of Metallurgy and Materials Science, Massachusetts Institute of Technology, Cambridge, Massachusetts 02139 *(Received August 23, 1971)*

Publication costs assisted by the Advanced Research Projects Agency

The viscosities of three organic liquids, salol, α-phenyl-*o*-cresol, and *o*-terphenyl, have been measured over a wide range of temperature using falling-sphere and bending-beam viscosimeters. The heat capacity *vs.* temperature relations for each of these materials have also been determined for the glass, liquid, and crystalline states, as have the thermal expansion coefficients of glassy and liquid α-phenyl-*o*-cresol. For none of the liquids investigated can the flow behavior over the full range of measured viscosity be adequately represented by any of the standard theoretical models. The agreement between molecular dynamics calculations and a modified free volume theory is combined with the close description of flow at high temperature by a free volume model to suggest that free volume theories are most appropriately used to describe flow in the high-temperature region rather than in the region around the glass transition. It is also suggested that a second, easier flow process becomes dominant in the low-temperature region. Flow data on several classes of liquids may be correlated by means of a corresponding-states parameter. Although limitations are recognized for the use of any such normalization factor, the most satisfactory corresponding-states parameter for liquid viscosity seems to be the glass-transition temperature.

I. Introduction

The nature of viscous flow has been the subject of extensive theoretical discussion for the past several decades. A significant portion of this discussion has been directed to flow in the high-viscosity region, as the glass transition is approached. In this region, the empirical Williams–Landel–Ferry (WLF) relation, originally used to describe relaxation in the vicinity of the glass transition, has been widely used and has become the representation of experimental data which theoretical models attempt to describe.

Despite the extensive theoretical interest in the area, relatively few experimental data are available on viscous flow in the high-viscosity region. Of the available data, most have been obtained on inorganic glass-forming liquids, which are sufficiently complex structurally that the application of the standard models in their description might well be questioned.

In the present paper, we shall report a study of viscous flow in a number of relatively simple organic liquids. Data will be presented on the heat capacities and thermal expansion coefficients of the materials in addition to their melt viscosities. The results will be compared with predictions of the standard models of viscous flow, and it will be shown that none of these models can provide an adequate description of the data over the full range of viscosity. It will be suggested that free volume theories can provide a useful description of flow at relatively high temperatures, but that a second, easier process—perhaps limited by transport over potential energy barriers—becomes dominant as the glass transition is approached.

II. Experimental Procedure

Viscosity measurements have been carried out on three relatively simple organic glass-forming liquids: α-phenyl-*o*-cresol, phenyl salicylate, and *o*-terphenyl. All three were obtained in the "highest purity" grade from the Eastman Chemical Co. The structural formulas of these materials are shown in Figure 1.

The measurements were carried out in a constant-temperature bath constructed of PMMA and styrofoam, which was provided with an outer cooling jacket as well as an inner sample chamber. The inner chamber, filled with methanol or 2-methylbutane, was provided with an immersion heater, a stirrer and a bimetallic strip temperature controller with a sensitivity of ±0.005°. Depending on the operating temperature desired, the outer cooling jacket was filled with ice and water, Dry Ice and alcohol, or liquid nitrogen. To permit visual observation, a vertical multilayered Plexiglass window was built through the cooling jacket into the side of the inner constant-temperature bath.

The temperature of the controlled bath was measured with a precision of ±0.1° using a copper–constantan thermocouple with a large insulated steel block at room temperature as a reference junction. Prior to each reading of the bath temperature, the thermocouple was placed in a freshly prepared crushed-ice bath and the potentiometer output reset to zero. During the course of a given viscosity measurement, temperature fluctuations in the bath were held to within ±0.05°.

The viscosities of α-phenyl-*o*-cresol and salol were measured over the viscosity range from 10^1 to $10^{13.5}$ P. A falling sphere was used for viscosities up to about 10^8 P. For higher viscosities, a beam-bending technique,

(1) Based in part on a thesis submitted by W. T. L. in partial fulfillment of the requirements for the Sc.D. degree in Materials Science, M.I.T., Jan 1969.

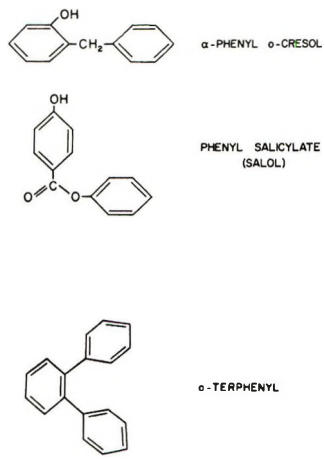

Figure 1. Structural units of the liquids studied in the present investigation.

similar to that used at higher temperature by Hagy,[2] was employed. In the case of *o*-terphenyl, data of other investigators[3] have been overlapped with present falling-sphere measurements and extended into the high viscosity region with the beam bending technique.

In the falling-sphere measurements, a test tube filled with molten sample was placed in the constant-temperature bath and allowed to equilibrate at the temperature of measurement. At the lowest viscosities, the time for an Al_2O_3 sphere, 1 mm in diameter, to pass between two reference marks was measured with a stop watch, while for higher viscosities the rate of fall of a Pt sphere was recorded with a cathetometer. At the highest viscosities, warming the sphere slightly was required for immersion in the bulk supercooled liquid, but no measurements were made until thermal equilibrium was established.

The viscosities were obtained from the falling-sphere data with the relation

$$\eta = \frac{2}{9}\frac{gr^2\Delta\rho}{u}f(r/R) \qquad (1)$$

where η is the viscosity, g is the gravitational acceleration, r is the diameter of the sphere, $\Delta\rho$ is the density difference between sphere and liquid, u is rate of fall of the sphere, and $f(r/R)$ is a correction factor[4] which accounts for the finite size of the container in which the sphere is falling

$$f(r/R) = 1.000 - 2.104(r/R) + 2.09(r/R)^3 - 0.95(r/R)^5 + \ldots \qquad (1a)$$

Here R is the radius of the container.

The accuracy of the falling-sphere measurements was verified by measuring the viscosity of standard oil N 190,000 purchased from the Cannon Instrument Co. Values of 9870 and 1915 P at 68 and 100°F, respectively, were verified to within 5%.

For the beam-bending method, cylindrical rods of the sample material, 5 cm in length, were cast into low-temperature graphite molds. After removal from the molds, the rods were transferred to a three-point loading device and placed in the constant-temperature bath. The center point of the loading device was a push rod extending above the bath for application of the load. The motion of a scribe mark on the push rod was then observed with a cathetometer, and the displacement recorded as a function of time.

The viscosities were obtained from the bending beam data with the relation[2]

$$\eta = \frac{gL^3}{144uI}M + \frac{m}{1.6} \qquad (2)$$

Here L is the length and m the mass of the beam between supports, u is the deflection rate at the center of the beam, I is the area moment of the beam, and M is the mass added at the center of the beam.

For measurements at viscosity levels above 10^{12} P, a period of time was allowed at the temperature of measurement for relaxation to the equilibrium liquid before application of the load. In accord with recent suggestions (*e.g.*, ref 5), this period was always more than 40 times the appropriate Maxwell relaxation time. After application of the load, delayed elastic effects were observed, with the initial bending rate being faster than the subsequent constant-deflection rate. The viscosity values reported below were calculated from the long-time constant flow rate.

Viscosity values from the beam-bending measurements are estimated to be accurate to better than ±20%. The possible errors in the high-viscosity region, where delayed elastic effects are significant, are higher than those in the lower viscosity region. In the region of viscosity where data from the falling-sphere and the beam-bending techniques overlap (the range about 10^8 P), the viscosity values determined by the two methods agreed within a few per cent.

The thermal expansion coefficients of glassy and liquid α-phenyl-*o*-cresol were measured using a dilatometer technique described in detail elsewhere.[6] Measurements of the change in specific volume with temperature were made at intervals of about 2° in both the glass and liquid states.

The heat capacities of glassy and liquid α-phenyl-*o*-cresol, salol, and *o*-terphenyl were measured with a Perkin–Elmer DSC-1B differential scanning calorimeter, using in all cases a heating rate of 10° min^{-1}. An Al_2O_3 calibration standard was run after each sample run over a common temperature interval.

(2) H. E. Hagy, *J. Amer. Ceram. Soc.*, **46**, 93 (1963).

(3) (a) J. N. Andrews and A. R. Ubbelohde, *Proc. Roy. Soc., Ser. A*, **228**, 435 (1955); (b) R. J. Greet and D. Turnbull, *J. Chem. Phys.*, **46**, 1243 (1967).

(4) H. Faxen, *Ann. Phys.*, **68**, 89 (1922).

(5) J. H. Li and D. R. Uhlmann, *J. Non-Cryst. Solids*, **1**, 339 (1969).

(6) W. T. Laughlin, Sc.D. Thesis, M.I.T., Jan 1969.

Table I: Viscosity Data

α-Phenyl-o-cresol				Salol		o-Terphenyl	
Temp, °C	Log η	Temp, °C	Log η	Temp, °C	Log η	Temp, °C	Log η
12.2	−0.01	−33.6	4.49	3.7	0.18	−6.0	5.51
9.8	0.09	−35.0	4.76	−0.4	0.45	−8.4	6.00
7.8	0.18	−35.7	5.05	−2.9	0.64	−10.9	6.51
5.1	0.32	−36.5	5.21	−5.3	0.83	−12.8	6.93
2.3	0.48	−38.2	5.55	−7.7	1.06	−14.8	7.43
−0.9	0.67	−39.9	6.08	−9.7	1.25	−22.2	9.42
−3.0	0.75	−41.9	6.47	−13.7	1.70	−24.0	9.85
−4.7	0.94	−43.7	7.09	−16.0	1.97	−24.6	10.01
−7.6	1.11	−45.1	7.48	−18.8	2.55	−25.0	10.25
−10.5	1.33	−47.3	8.27	−19.5	2.73	−25.8	10.47
−12.6	1.50	−49.6	8.75	−22.3	3.15	−26.4	10.59
−13.8	1.57	−50.1	8.98	−24.7	3.66	−26.9	10.80
−14.7	1.71	−51.7	9.43	−27.4	4.18	−27.6	10.88
−15.1	1.70	−52.6	9.83	−29.5	4.65	−28.2	11.04
−16.9	1.88	−53.7	9.98	−31.7	5.04	−28.5	11.20
−16.9	1.94	−55.2	10.32	−33.5	5.57	−28.9	11.28
−19.2	2.21	−55.9	10.46	−35.0	5.88	−29.1	11.48
−21.3	2.51	−56.6	10.72	−37.4	6.55	−29.6	11.54
−22.3	2.61	−57.7	11.18	−40.0	7.06	−30.1	11.84
−23.9	2.81	−59.1	11.77	−41.6	7.70	−30.5	11.81
−25.8	3.11	−60.1	11.82	−43.7	8.19	−31.1	12.18
−28.4	3.53	−62.1	12.40	−47.0	9.12	−31.4	12.22
−29.8	3.70	−62.3	12.69	−49.0	9.58	−31.6	12.35
−30.2	3.93	−63.8	13.31	−51.6	10.27	−32.0	12.43
−31.8	4.18	−65.2	13.68	−54.0	10.80	−33.1	12.88
−32.4	4.26			−57.4	11.93	−33.7	13.15
				−59.9	12.68		

III. Results

Viscosity data on the three liquids are summarized in Table I. The data for α-phenyl-*o*-cresol and salol exhibit curvature in the log η *vs.* $1/T$ relations for viscosities smaller than about 10^5 P, while for larger viscosities (from 10^5 P to the glass-transition region) Arrhenius behavior is exhibited.

No previous viscosity data are available for α-phenyl-*o*-cresol, with which the present data can be compared. In the case of salol, previous data are available in the range of high fluidities.[7] In the range of mutual overlap, from 10^0 to 10^4 P, these previous data are in close agreement with the results of the present investigation.

The data on *o*-terphenyl in the high-viscosity region exhibit slight curvature on a log η *vs.* $1/T$ plot. At lower viscosities, significantly larger curvature is observed. The data on this material in the high-viscosity region are quite close to values estimated[3b] from volume relaxation data. In the range of lower viscosities, the present results and those previous investigators[3] are in close agreement.

Heat capacity data on the three materials are shown in Figure 2. In all cases, the data have been obtained on both the crystalline and amorphous forms of the materials. In the case of *o*-terphenyl, the present data are in close agreement with the results of previous workers.[8]

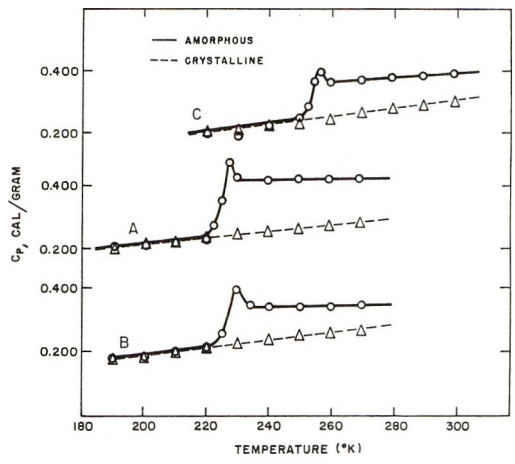

Figure 2. Heat capacity *vs.* temperature relation for crystalline and amorphous (a) α-phenyl-*o*-cresol, (b) salol, and (c) *o*-terphenyl.

The results of the present dilatometric study of α-phenyl-*o*-cresol are shown below, together with the corresponding results on *o*-terphenyl obtained previously.[3b]

Material	α_{liq}, °C^{-1}	α_{glass}, °C^{-1}
α-Phenyl-*o*-cresol	7.53×10^{-4}	2.45×10^{-4}
o-Terphenyl	7.49×10^{-4}	2.0×10^{-4}

(7) O. Jantsch, *Z. Kristallogr.*, **108**, 185 (1956).
(8) R. J. Greet and D. Turnbull, *J. Chem. Phys.*, **47**, 2185 (1967).

As shown here, the thermal expansion coefficients of both liquids are similar, while that of glassy *o*-terphenyl is somewhat smaller than the value for glassy α-phenyl. Both are, however, in the range frequently found for organic liquids, as is the value of $\Delta\alpha = \alpha_{liq} - \alpha_{glass}$.

IV. General Discussion

The increase in the heat capacity of amorphous salol, α-phenyl-*o*-cresol, and *o*-terphenyl occurs at temperatures about 8–10° higher than the temperature at which the viscosity is 10^{12} P. This reflects in part the relatively short time scale imposed by the heating rate selected and in part the difference between sample temperature and programmed temperature in the scanning calorimeter. For all materials studied, the heat capacities of the glassy and crystalline phases are found to be equal within experimental error. The peaks observed in the C_p *vs.* T relations of Figure 2 reflect the specimens being heated in the calorimeter more rapidly than they were originally cooled. For each material, the heat capacity increases by a factor of 1.5–2 on passing from the glass to supercooled liquid states. For each material, the difference in heat capacity between the liquid and the glass, ΔC_p, is observed to decrease with increasing temperature. This dependence can be represented by the linear relation

$$\Delta C_p = a - bT \tag{3}$$

Values of a and b appropriate from the glass-transition temperature, T_g, to $T_g + 100°$ are (material, a, b): α-phenyl-*o*-cresol, 0.362, 8.2×10^{-4}; salol, 0.343, 1.0×10^{-3}; *o*-terphenyl, 0.286, 6.8×10^{-4}.

The viscosity data on these three organic liquids illustrate two types of temperature dependences. For *o*-terphenyl, and also for tri-α-naphthylbenzene,[9] small curvature is observed in the log η *vs.* $1/T$ relation at high and low temperatures, with larger curvature being noted at intermediate temperatures. For salol and α-phenol-*o*-cresol, curvature is also observed at high and intermediate temperatures, but the low-temperature behavior is best described as Arrhenius.

These flow data may be discussed in terms of the standard theoretical models for liquid viscosity. Beginning with absolute rate theory,[10] the marked curvature in the log η *vs.* $1/T$ relations indicates that the apparent activation energies for flow must be taken as temperature dependent. In the intermediate- and high-viscosity regions of salol and α-phenyl-*o*-cresol, where straight-line log η *vs.* $1/T$ relations are observed (where absolute rate theory might conceivably apply), the apparent activation energies for flow are 63 and 66 kcal g-atom^{-1}, respectively. These values are larger than the corresponding heats of vaporization by a factor of 6 or 7 (estimated from the boiling points by Trouton's rule). The preexponential factors derived from flow in the high-viscosity regions are about 10^{-52} and 10^{-56} dyn sec cm^{-2} for salol and α-phenyl, respectively (far from the 10^{-3} dyn sec cm^{-2} expected from rate theory).

The very small values of the preexponential factor and large values of the apparent activation energy indicate that the flow process at high viscosities is not simply activated and that the simple absolute rate theory does not provide an appropriate description of the data. Similarly large apparent activation energies and small preexponential factors are also observed with *o*-terphenyl and tri-α-naphthylbenzene in the high-viscosity region, and present similar difficulties for the theory.

When the full range of temperature is considered, the free volume[11–14] and excess entropy[15–17] models are also inadequate for representing the complexity of form exhibited by the various log η *vs.* $1/T$ relations. Neither model can describe the Arrhenius behavior of salol and α-phenyl-*o*-cresol at low temperatures and two or more sets of constants, each appropriate over a limited range of temperature, are required to describe the data on *o*-terphenyl and tri-α-naphthylbenzene.

For each of the four organic liquids, the high-temperature data can be well represented by a relation of the Vogel–Fulcher form

$$\log \eta = A + \frac{B}{T - T_0} \tag{4}$$

This is shown in Figures 3–6. The values of the constants A, B, and T_0 obtained from the fit are tabulated in Table II. For each material the relation is seen to provide a close description of the data for viscosities smaller than about 10^4 P. The values of T_0 lie in the range of the experimentally determined glass transitions, being higher than T_g in some cases and lower in others. For viscosities higher than about 10^4 P, the

Table II: Values of Vogel–Fulcher Constants

Material	A	B	T_0
Salol	−2.74	148	226
α-Phenyl-*o*-cresol	−3.14	233	210
o-Terphenyl	−2.98	199	248
Tri-α-naphthylbenzene	−3.06	348	342.7

(9) D. J. Plazek and J. H. Magill, *J. Chem. Phys.*, **45**, 3038 (1966).
(10) S. Glasstone, K. J. Laidler, and H. Eyring, "The Theory of Rate Processes," McGraw-Hill, New York, N. Y., 1941.
(11) T. G. Fox and P. J. Flory, *J. Appl. Phys.*, **21**, 581 (1951).
(12) F. Bueche, *J. Chem. Phys.*, **30**, 748 (1959).
(13) M. H. Cohen and D. Turnbull, *ibid.*, **31**, 1164 (1959).
(14) D. Turnbull and M. H. Cohen, *ibid.*, **34**, 120 (1961).
(15) J. H. Gibbs and E. A. DiMarzio, *ibid.*, **28**, 373 (1958).
(16) J. H. Gibbs in "Modern Aspects of the Vitreous State," Vol. 1, Butterworths, London, 1960.
(17) G. Adam and J. H. Gibbs, *J. Chem. Phys.*, **43**, 139 (1965).

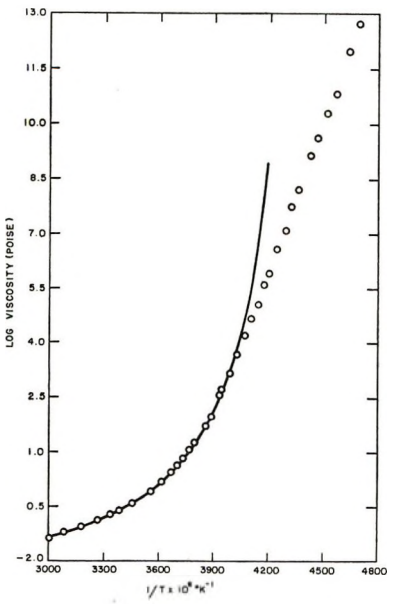

Figure 3. Viscosity–temperature relation for salol, based on data of ref 7 and present investigation; (——) Vogel–Fulcher curve with constants tabulated in Table II.

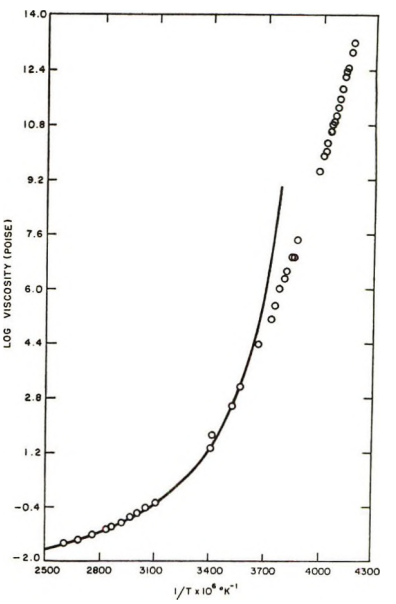

Figure 5. Viscosity–temperature relation for *o*-terphenyl, based on data of present investigation and ref 2 and 3; (——) Vogel–Fulcher curve with constants tabulated in Table II.

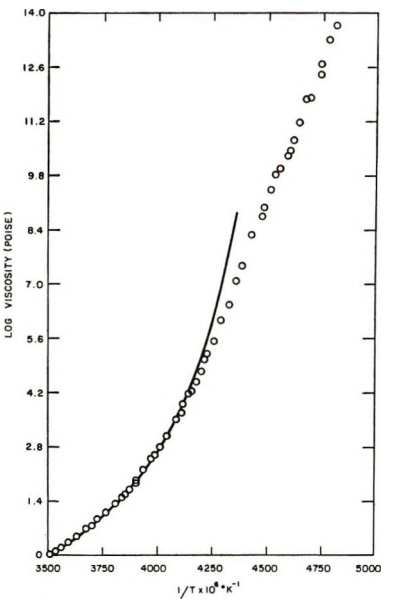

Figure 4. Viscosity–temperature relation for α-phenyl-*o*-cresol; (——) Vogel–Fulcher curve with constants tabulated in Table II.

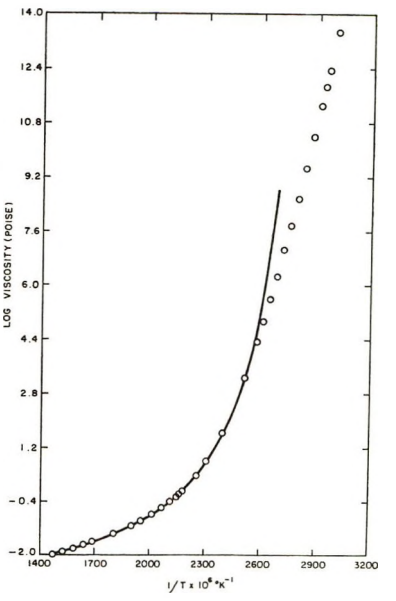

Figure 6. Viscosity–temperature relation for tri-α-naphthylbenzene, based on ref 9; (——) Vogel–Fulcher curve with constants tabulated in Table II.

high-temperature Vogel–Fulcher relation greatly overestimates the difficulty of flow for each of the materials.

In no case can the data in the region above the glass transition be described by the Williams–Landel–Ferry[18] relation, either with the original "universal" constants or with a modified constant based on the measured values of $\Delta\alpha$ for each material. In no case can the data be described over an extended range of temperature by the direct predictions of the excess entropy model. Evaluating the configurational entropy from the heat capacity data and the measured heat of fusion on each material, results similar to those shown in Figure 7 are obtained for the three liquids studied in the present investigation. As shown there, a curve of sigmoid shape is observed, rather than a straight line as predicted by the theory. In the case of tri-α-naphthylbenzene, the log η *vs.* $1/TS_c$ relation is quite linear over the range of high viscosity, and deviations from linearity are observed only at low viscosities.[19]

(18) M. F. Williams, R. F. Landel, and J. D. Ferry, *J. Amer. Chem. Soc.*, **77**, 3701 (1955).

(19) J. H. Magill, *J. Chem. Phys.*, **47**, 2802 (1967).

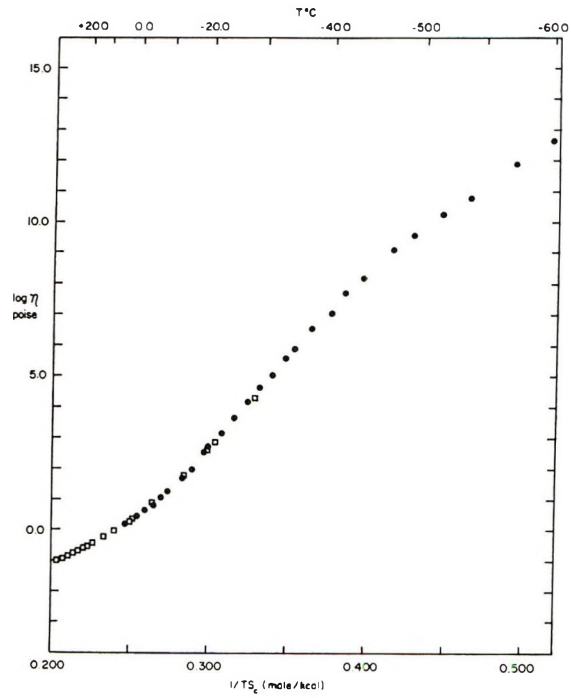

Figure 7. Variation of viscosity with configurational entropy for salol.

From the range of slopes of each log η *vs.* $1/TS_c$ relation, the corresponding range of the potential barrier to molecular rearrangement, $\Delta\mu$, can be estimated. Taking the entropy of the smallest region which can undergo a cooperative rearrangement as k ln 2, the values of $\Delta\mu$ shown in Table III are obtained. These values are in all cases much larger than any reasonable estimate of cohesive energies in the materials. The number of molecules in the smallest regions which can undergo rearrangement are estimated in all cases as less than a single molecule, a value which is too small to be physically meaningful.

Table III: Potential Barriers to Molecular Rearrangement

	$\Delta\mu Sc^*/k$, kcal g-atom^{-1}	$\Delta\mu$, kcal g-atom^{-1}
α-Phenyl	75–142	108–205
Salol	56–136	81–197
o-Terphenyl	62–103	90–149
Tri-α-naphthyl-benzene	310	450

Studies of the flow behavior of other organic liquids[20,21] have suggested linear log η *vs.* $1/T$ relations for viscosities in the range from 10^4 to 10^{12} P. The apparent activation energies derived from these data lie in the range from 15 to 35 kcal mol^{-1}. The Arrhenius behavior at high viscosities is similar to that of salol and α-phenyl-*o*-cresol, but experimental uncertainties leave open to question the form of the variation in the high-viscosity region.

V. Free Volume Theory, A High-Temperature Model

It is apparent from the preceding discussion that none of the standard models for flow can satisfactorily describe the behavior of simple organic liquids over the full range of measured viscosity. Such a failure of the standard models has previously been noted and discussed by several authors (*e.g.* see ref 22–26). It is also apparent that significant differences are found in the flow behavior of various materials, both within a given class (as the simple organics) and between different classes. Such differences may be illustrated by the following: A $0.60KNO_3$–$0.40Ca(NO_3)_2$ melt[25,27] exhibits flow behavior similar to that of salol and α-phenyl-*o*-cresol; glycerine[6] exhibits rather gradual curvature in the log η *vs.* $1/T$ relation over the full range of temperature; SiO_2 and GeO_2[28,29] exhibit Arrhenius or nearly Arrhenius behavior over the full range of temperature; and B_2O_3[24] exhibits apparently Arrhenius behavior at high and low temperatures, with an intermediate region of curvature.

These differences cannot be described by the standard theoretical models, which are based on rather simple pictures of the flow process and direct attention to universal features of flow. A more satisfactory theory seems almost certain, however, to be a more complex theory, considering factors such as the type of bonding in the liquid and the molecular shape and flexibility.

Despite these reservations, it seems significant that the flow behavior of all four organic liquids in the high-temperature region can be well represented by the free volume model. This result is well viewed in the perspective of recent extensions of free volume theory[30] and molecular dynamics (MD) calculations of transport in hard-sphere fluids.[31]

The MD calculations have indicated self-diffusion coefficients in good agreement with Enskog values (gaslike behavior) for low densities, but fall far below the Enskog estimates at the highest fluid densities.

(20) A. C. Ling and J. E. Willard, *J. Phys. Chem.*, **72**, 1918 (1968).
(21) A. C. Ling and J. E. Willard, *ibid.*, **72**, 3349 (1968).
(22) D. R. Uhlmann, in "Amorphous Materials," Wiley, New York, N. Y., 1972.
(23) M. Goldstein, *J. Chem. Phys.*, **51**, 3728 (1969).
(24) P. B. Macedo and A. Napolitano, *ibid.*, **49**, 1887 (1968).
(25) H. Tweer, N. Laberge, and P. B. Macedo, *J. Amer. Ceram. Soc.*, **54**, 121 (1971).
(26) H. Tweer, J. H. Simmons, and P. B. Macedo, *J. Chem. Phys.*, **54**, 1952 (1971).
(27) R. Weiler, S. Blaser, and P. B. Macedo, *J. Phys. Chem.*, **73**, 4147 (1969).
(28) R. Bruckner, *Glastech. Ber.*, **37**, 413 (1964).
(29) E. H. Fontana and W. A. Plummer, *Phys. Chem. Glasses*, **7**, 139 (1966).
(30) D. Turnbull and M. H. Cohen, *J. Chem. Phys.*, **52**, 3038 (1970).
(31) B. J. Alder and T. E. Wainwright, *Phys. Rev. Lett.*, **18**, 988 (1967); see also results cited in ref 30.

At high packing densities, diffusive motion is canceled to a large extent by back-scattering in locally dense portions of the system. At the highest densities, such back-scattering can cancel almost all diffusive motion and result in solidlike behavior.

The extension of the free volume theory has considered a variable diffusive displacement and associated a correlation factor with each magnitude of the displacement. This modified theory was found to describe well the results of the molecular dynamics calculations in the high density region.

In light of this agreement between the MD calculations and free volume theory in the range of density which corresponds to relatively high fluidity, as well as the useful representation which this theory provides of the flow of simple organic liquids in the range of rather high fluidity, it seems reasonable to suggest that free volume theories be used to describe flow behavior in the high-temperature range rather than in the vicinity of the glass transition. This suggestion is in keeping with the success of free volume theories in describing the temperature dependence of the flow of hydrocarbons[32] and the temperature and pressure dependence of the flow of rare gas liquids[33] in the range of high fluidities. Viewed in this way, the glass transition need not correspond to a state of constant free volume or configurational entropy; the failure of free volume theories to describe the pressure dependence of the glass transition[34] does not require refutation; and the inability of any simple model to represent the complexity of flow behavior in the high viscosity region is not unexpected.

A recent extension of this view[35] has indicated that the free volume theory with measured values of $\Delta\alpha$ provides a detailed and accurate description of the flow of all four organic liquids at high temperature. The quality of this description is far superior to that which is obtained by attempting to describe data over the full range of viscosity. The magnitudes of the preexponential constants derived from the high-temperature flow data are in close agreement with those predicted by the theory, and the departure of the experimental data from the predictions of the model (see Figures 3–6) occurs at a nearly constant value of the fractional free volume.

The free volume description of the high-temperature flow data grossly overestimates the difficulty of flow in the low-temperature region, and an easier mechanism of flow appears to become dominant in this region. While it seems attractive to represent such flow as transport over potential energy barriers, it is clear that this transport cannot be regarded as a simply activated process but must involve cooperative motion to an extensive degree.

VI. Corresponding States Parameter for Viscous Flow

Corresponding state relations have been used previously for correlating data on liquid viscosity. Use of the heat of vaporization as a normalization parameter was originally suggested[14] as a measure of the cohesion in different systems. It was found inadequate,[36] however, for correlating the data on two organic liquids, and the melting point of the corresponding crystal, T_M, was found to provide a superior normalization. Using T_M, different viscosity-reduced temperature relations were found for different classes of materials, and in some cases for different materials within a class.

It should be noted, however, that use of the melting point to correlate data on liquid viscosity presents conceptual difficulties. Specifically, the melting point depends on the thermodynamic properties of both crystal and liquid, rather than of the liquid alone, and it is difficult to rationalize *a priori* the dependence of liquid flow on characteristics other than those of the liquid phase alone.

Viscosity data on the three simple organic liquids reported in this paper, together with those on tri-α-naphthylbenzene, are shown in Figure 8, using the melting point as a corresponding states parameter. As seen there, this parameter fails to provide a satisfactory normalization of the flow data (only in the case of *o*-terphenyl and tri-α-naphthylbenzene do the data come close to superposition).

In contrast, the glass-transition temperature, T_g, seems to provide a useful normalization of the viscosity data on these liquids. This is illustrated by Figure 9, where T_g was taken as the temperature corresponding to a viscosity of 10^{15} P. Use of this value, like all characterizations of the glass transition, is somewhat arbitrary, but selection of a somewhat different viscosity level for T_g would not significantly affect the quality of the normalization.

The same normalization procedure has been applied to the viscosity data of other workers[20,21,37] on a number of organic liquids. The forms of the resulting curves are similar to those shown in Figure 9, but somewhat greater scatter is observed and a shift to somewhat lower values of T_g/T is suggested if a linear viscosity extrapolation is employed. The data on these materials are not, however, available to such high viscosities as those on the liquids shown in Figure 9, and extrapolation over a wider range of viscosity is required to evaluate T_g. One set of workers[20,21] suggested that a linear extrapolation of the log η *vs.* $1/T$ relation would probably underestimate the viscosity. Introduction of a slight curvature in this relation in extrapolating to T_g is sufficient to produce effective coincidence of these

(32) A. K. Doolittle, *J. Appl. Phys.*, **22**, 1471 (1951).
(33) J. Nagizadeh, *ibid.*, **35**, 1162 (1964).
(34) M. Goldstein, *J. Chem. Phys.*, **39**, 3369 (1963).
(35) M. Cukierman and D. R. Uhlmann, to be published.
(36) R. J. Greet and J. H. Magill, *J. Phys. Chem.*, **71**, 1746 (1967).
(37) A. J. Barlow, J. Lamb, and R. Matheson, *Proc. Roy. Soc., Ser. A*, **292**, 322 (1966).

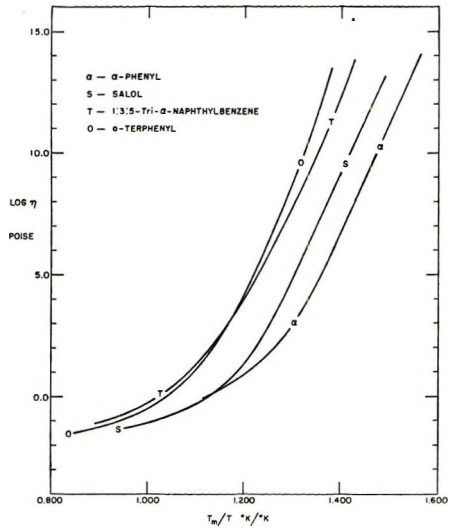

Figure 8. T_M/T normalization of viscosity data for simple organic glass-forming liquids: (S) data on salol from present study and ref 7, (α) data on α-phenyl-o-cresol from present study, (o) data on o-terphenyl from present study and ref 2 and 3, (T) data on tri-α-naphthylbenzene from ref 9.

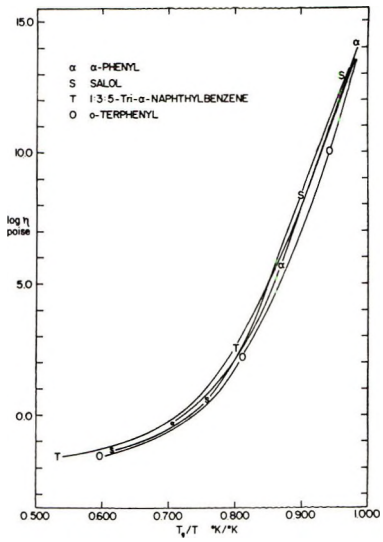

Figure 9. T_g/T normalization of viscosity data for simple glass-forming liquids: (S) data on salol, (α) data on α-phenyl-o-cresol, (o) data on o-terphenyl, (T) data on tri-α-naphthylbenzene.

data with those shown in Figure 9. The increase in T_g required to achieve such coincidence, relative to that obtained from linear viscosity extrapolation, is in the range of about 2–12°.

Applying the same corresponding-states analysis to viscosity data on familiar oxide glass formers, the results shown in Figure 10[28,29,38–44] are obtained. Also shown for comparison is the viscosity *vs.* reduced temperature relation for simple organic liquids from Figure 9. As noted in Figure 10, the viscosity *vs.* reduced temperature relation for SiO_2 is closely similar to that of GeO_2; both exhibit much less curvature than the corresponding relation for B_2O_3, sodium disilicate, potassium disilicate, the two standard NBS silicate liquids, and perhaps other silicate liquids; and these in turn display more shallow log η *vs.* T_g/T relations than the simple organic liquids discussed previously.

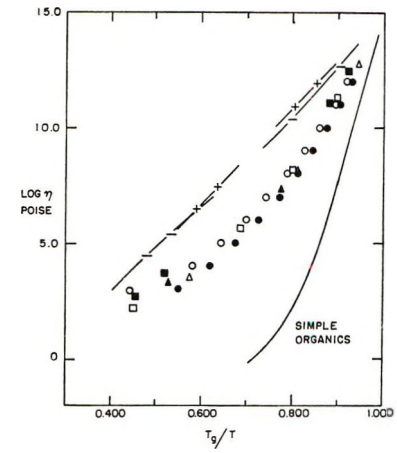

Figure 10. T_g/T normalization for inorganic oxide glass-forming liquids: (+) data on SiO_2 from ref 28 and 29, (−) data on GeO_2 from ref 29, (▲) data on B_2O_3 of ref 38, (△) data on B_2O_3 of ref 24, (■) data on $K_2O \cdot 2SiO_2$ of ref 39 and 40, (□) data on $Na_2O \cdot 2SiO_2$ of ref 39, 41, and 42, (o) data on NBS standard soda lime silicate glass of ref 43, (●) data on NBS standard lead silicate glass of ref 44, (SIMPLE ORGANICS) data on organic glass-forming liquids summarized in Figure 2.

Among other types of glass-forming liquids, the viscosity data on a Au–Si–Ge metal alloy[45] yield a log η *vs.* T_g/T relation similar to that of the organic liquids. This relation almost coincides with, but displays slightly more curvature than, that for o-terphenyl. The data on a KNO_3–$Ca(NO_3)_2$ melt[25,27] is also similar in form to that of the organic liquids, with the viscosity dropping somewhat more rapidly with decreasing T_g/T than that of o-terphenyl.

Use of the glass-transition temperature, T_g, as a corresponding-states parameter for liquid viscosity seems, then, to divide liquids into at least three classes with respect to their flow behavior. For each of these classes, the viscosity of the amorphous phase seems to increase in a similar manner as the temperature is decreased; and in this sense, the adoption of such a normalization parameter seems useful for categorizing materials and predicting the general form of their flow behavior.

(38) G. S. Parks and M. E. Spaght, *Physics*, **6**, 69 (1935).
(39) L. Shartsis, S. Spinner, and W. Capps, *J. Amer. Ceram. Soc.*, **35**, 155 (1952).
(40) N. W. Taylor and R. F. Doran, *ibid.*, **24**, 103 (1941).
(41) H. R. Lillie, *ibid.*, **32**, 367 (1949).
(42) J. P. Poole, *ibid.*, **32**, 230 (1949).
(43) A. Napolitano and E. G. Hawkins, *J. Res. Nat. Bur. Stand., Sect. A*, **68**, 439 (1964).
(44) A. Napolitano and E. G. Hawkins, *Nat. Bur. Stand. (U. S.) Misc. Pub.*, **No. 260**, 11 (1966).
(45) H. S. Chen and D. Turnbull, *J. Chem. Phys.*, **48**, 2560 (1968).

It should be noted, however, that any such simple categorization tends to obscure certain features of the available experimental data which are important for understanding the process of viscous flow. For example, within the group of simple organic liquids shown in Figure 9, two (salol and α-phenyl-*o*-cresol) exhibit Arrhenius low-temperature behavior while the other two are characterized by log η *vs.* $1/T$ relations having some slight curvature in this region.

VII. Conclusions

The following conclusions can be drawn from the present study. (1) No one of the standard models of liquid viscosity provides a satisfactory description of flow over the full range of viscosity. (2) In the high-temperature region, the Vogel-Fulcher relation provides a useful description of flow behavior for each organic liquid investigated. (3) The detailed agreement between a modified free volume theory and the results of molecular dynamics calculations, combined with the satisfactory description of flow at high temperatures, suggests that free volume theories be used to describe flow at low to intermediate viscosities rather than in the vicinity of the glass transition. (4) The free volume model used to describe flow at high temperatures overestimates the difficulty of flow in the high viscosity region, where a second, easier process seems to become dominant. (5) The glass-transition temperature seems to provide the most satisfactory corresponding-states parameter for correlating data on liquid viscosity.

Acknowledgments. Financial support for this work was provided by the Atomic Energy Commission. and by the Advanced Research Projects Agency. This support is gratefully acknowledged, as are stimulating discussions with Mr. M. Cukierman of M.I.T., who also provided valuable assistance with the data reduction, and Professor David Turnbull of Harvard University.

Laser Raman Spectroscopy of Surfaces[1]

by E. Buechler and John Turkevich*

Frick Chemical Laboratory, Princeton University, Princeton, New Jersey 08540 *(Received November 19, 1971)*

Publication costs assisted by the U. S. Atomic Energy Commission

Laser Raman spectroscopy was used to investigate the nature of silica surfaces, supported catalysts, rare earth and uranium zeolite catalysts, and adsorbed molecules. The results obtained are compared with those found using infrared technique. The Raman spectrum of water in 40-Å diameter pores of clean silica was shown to be identical with that of bulk water indicating that Raman spectroscopy is not sensitive to changes in the structure of water confined in pores or near surfaces. Adsorption isotherms were obtained of ethylene and propylene on silica. In many systems the interaction of the intense laser beam with adsorbed molecules leads to fluorescence which restricts the use of laser Raman spectroscopy.

Recent development of the laser has made Raman spectroscopy an important tool for the study of gases, liquids, and solids. Availability of a large number of exciting lines of great intensity, high monochromacy, and narrow collimation circumvents absorption and fluorescence problems normally associated with Raman work. Furthermore, the use of highly sensitive, fast response detecting devices permits characterization of species present in small concentration.[2-10] The first commercial laser spectrometer appeared in 1964. Therefore it was of interest to see whether laser Raman spectroscopy could be used to study surfaces, adsorbed species, or surface reactions much the same way as infrared spectroscopy has been used during the past two decades.[11,12]

The following publications have appeared on the application of Raman spectroscopy to adsorbed mole-

(1) This research was supported by the U. S. Atomic Energy Commission.

(2) (a) J. Brandmuller, "Einführung in die Ramanspektroskopie," Dr. Dietrich Steinkopff Verlag, Darmstadt, 1962; (b) N. B. Colthup, L. H. Daley, and S. E. Wiberly, "Introduction to Infrared and Raman Spectroscopy," Academic Press, New York, N. Y., 1964.

(3) H. A. Szymanski, Ed., "Raman Spectroscopy," Plenum Press, New York, N. Y., 1967.

(4) J. Brandmuller, *Naturwissenschaften*, **21**, 293 (1967).

(5) V. A. Zulov, M. M. Sushinskii, and I. I. Shuvalov, *Usp. Fiz. Nauk*, **89**, 49 (1966).

(6) I. R. Beattie, *Chem. Brit.*, **3**, 347 (1967).

(7) P. J. Hendra and P. M. Stratton, *Chem. Rev.*, **69**, 325 (1969).

(8) P. J. Hendra and C. J. Vear, *Analyst (London)*, **95**, 321 (1970).

(9) R. E. Hester, *Anal. Chem.*, **40**, 320R (1968); **42**, 231R (1970).

cules. Karagounis and Issa,[13] using mercury arc excitation and photographic detection, studied the fluorescence and Raman spectra of naphthalene, diphenyl, and paratriphenyl adsorbed in one to ten monolayers in aerosil powder, microporous glass, and potassium bromide. They reported quenching of fluorescence of aromatic compounds on adsorption, the equalization of intensities of all lines, and the appearance of lines normally forbidden in Raman spectra.

These results were disputed by Pershina and Raskin,[14] who observed the same spectra for adsorbed benzene, naphthalene, and 1,2,4,5-tetrachlorobenzene in the adsorbed state as in the liquid or solid phase. For acetophenone and acetonitrile there was a displacement of 10–15 cm^{-1} of their CO and CN band when the surface was half covered. In the case of $SbCl_3$, SbI_3, and dichloroethane, the ratio of intensity of deformation lines to valence lines increased with coverage. Examination of 1,2-dichloroethane showed variation in the ratio of the two conformation isomers with coverage.

Hendra and Loader[15] studied the laser Raman spectrum of adsorbed acetaldehyde, carbon disulfide, *trans*-dichloroethylene, and bromine. The spectra resembled those of the gaseous species except that in the case of acetaldehyde, para-aldehyde was observed in the adsorbed state.

Winde[16] found in acetone adsorbed on alumina ten lines, most of which are associated with those of liquid acetone. A new set of three lines was found and the 1710-cm^{-1} line associated with the CO vibration in liquid acetone was missing. The author ascribed the new lines observed in the adsorbed state to a chemisorption of the acetone on alumina *via* the carbonyl bond changing the character of the latter to a bond and a half.

Winde and Demme[17] investigated the Raman spectra of adsorbed nitrobenzene on porous glass, aerosol, alumina, and molecular 4Å zeolite. A mercury arc was used for excitation, and photographic recording was employed. Only the strong symmetrical valence band was found in the zeolite and this line was displaced to the 1348-cm^{-1} line in the adsorbed state from the 1346-cm^{-1} position in the liquid state. All the lines found in the liquid state except the weak 531-cm^{-1} line were found in the other absorbents. The normally Raman inactive 442-cm^{-1} line due to the NO_2 bending frequency was observed in the adsorbed state. However, the strong infrared CH line at 3080 cm^{-1} of the nitrobenzene and the 3750-cm^{-1} line of the surface OH were not recorded.

Study of surfaces with laser Raman effect involves basic experimental difficulties. Most catalysts are porous materials and consequently scatter light, making measurements at low wave numbers difficult. Pressed pellets (using KBr or similar material as a matrix) for transmission measurement would lower the interparticle scattering. However, such samples do not permit stringent control of surface purity nor ability to vary the amount of adsorbed vapors. Reflection measurements must be used. Under these conditions the laser beam may heat up the surface excessively either vaporizing the adsorbed species or decomposing them to produce fluorescent material. Hydrocarbon impurities adsorbed from ambient air or from vapors present in a conventional high-vacuum system give rise to fluorescence masking the Raman lines.

Material chosen for this investigation was porous Vycor glass (Corning 7930) usually in the form of rods 1.5 mm in diameter. This material has a continuous network of uniform pores of 40-Å diameter, a surface of over 150 m^2/g, and a pore volume of 40% of its geometrical volume. It is essentially silica with a small amount of boric oxide. The small size of its pores compared to the wavelength of exciting light minimizes scattering. The material has been used in a number of investigations in this laboratory to study surface reactions.[18]

Experimental Section

A conventional laser Raman spectrometer was used with the sample usually kept at room temperature (Figure 1). An argon–krypton laser (Coherent Radiation Laboratory, Model 52 Ion Laser) emits a number of lines from 4500 to 6764 Å. The strongest line at 4880 Å with a nominal output of 700 mW and the 5682-Å line were usually chosen as exciting lines. The slit width of the spectrometer (Spex Model 1400) was narrowed to the point that just did not change the band shapes visibly. The range of slit widths used was from 5 to 15 cm. The phototube (ITT Model FW 130) was cooled to about $-10°$ to minimize dark current and noise. The signal from the phototube was amplified by an electrometer (Victoreen VTE-1) and recorded on a strip chart.

Gas treatments were carried out using a conventional system capable of holding a vacuum of 10^{-6} Torr pressure. It was modified with greaseless stopcocks (metal–Viton O seals) or with stopcocks protected from the samples with liquid nitrogen traps. A quartz sample system could be cut off or sealed onto the gas handling system. All-metal valves (Granville-Phillips 203) were used. The sample system could be baked out

(10) B. J. Bulkin, *J. Chem. Educ.*, **46**, A859 (1969).

(11) L. H. Little, "Infrared Spectra of Adsorbed Species," Academic Press, London, 1967.

(12) M. L. Hair, "Infrared Spectroscopy in Surface Chemistry," Marcel Dekker, Inc., New York, N. Y., 1967.

(13) G. Karagounis and R. Issa, *Nature (London)*, **195**, 1196 (1962); *Z. Elektrochem.*, **66**, 874 (1962).

(14) E. V. Pershina and Sh. Sh. Raskin, *Opt. Spektrosk. Akad. Nauk SSR*, **3**, 328 (1967); *Dokl. Akad. Nauk SSR*, **150**, 1022 (1963).

(15) P. J. Hendra and E. J. Loader, *Nature (London)*, **217**, 637 (1968); **216**, 789 (1967).

(16) H. Winde, *Z. Chem.*, **10**, 64 (1970).

(17) H. Winde and V. Demme, *Z. Phys. Chem. (Leipzig)*, **244**, 283 (1970).

(18) J. Turkevich and Y. Fujita, *Science*, **152**, 1619 (1966).

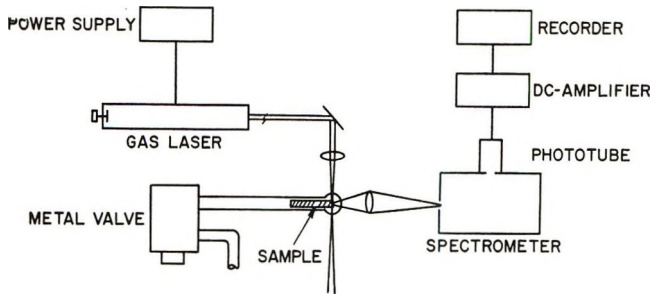

Figure 1. Schematic of apparatus.

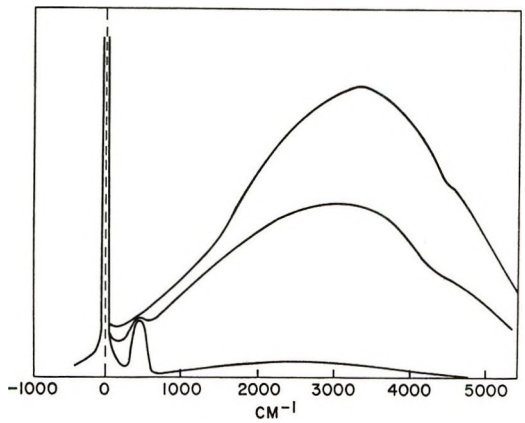

Figure 2. Spectrum of porous Vycor as received, contaminated, cleaned.

at 400°. Porous Vycor (Corning No. 7930) was subjected to the treatment described below. Chemicals used were either of reagent or spectroscopic grade purity. Liquids were vacuum distilled before use.

Results

Porous Vycor. The Raman spectrum of porous Vycor (Figure 2) excited with the 4880-Å line shows a relatively broad weak band around 500 cm^{-1} and a broad intense band extending over the whole "Raman range" with a maximum at 3000 cm^{-1} from exciting line. Changing the exciting line to 5682-Å yellow or to 6471-Å red leaves the position of the 500-cm^{-1} line unchanged. The broad band is shifted to lower wave numbers and decreased in intensity relative to the 500-cm^{-1} band (actually on a wavelength scale, the broad band remains almost unchanged in position while the narrow band shifts). The 500-cm^{-1} band is identified as a true Raman line while the broad band is a fluorescence band due to adsorbed impurities. This was confirmed by the following experiments. A porous Vycor rod that had been in contact with ambient air for several months and had become yellow showed a strong fluorescent band that completely blotted out the Raman line at 500 cm^{-1}. Fluorescence was to plague all work using laser Raman spectroscopy of materials of high surface area. It can be minimized by using a red exciting line and scrupulous cleanliness of materials.

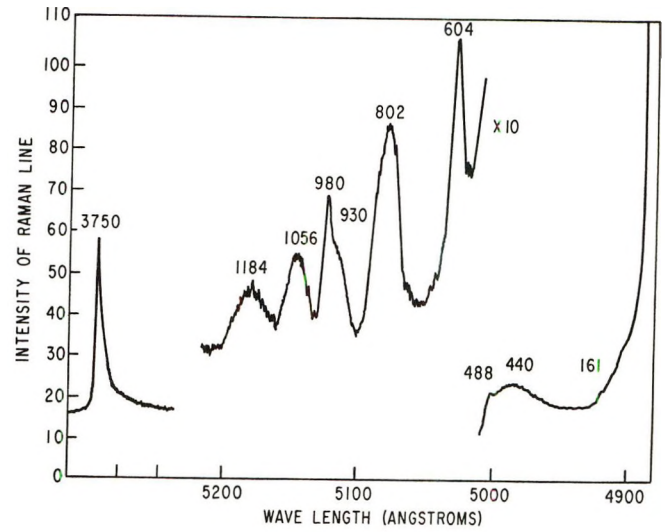

Figure 3. Spectrum of clean porous Vycor glass.

The fluorescence band was reduced to a low and constant level by treatment with 150 Torr of oxygen at 600–650°. Attempts to find milder or more effective cleaning procedures were unsuccessful. Treatment with 0.5 *N* NaOH for 0.5 hr and then with 2 *N* HCl prior to the heating in O_2 was not effective. Treatment by oxygen atoms (generated by a microwave discharge) at 25–200° was equally unsuccessful. Finally, boiling concentrated nitric acid did not remove the impurities adsorbed on the Vycor rod.

A detailed analysis of the Raman spectrum (Figure 3) shows many lines associated with fused silica or silica-rich glasses.[19-22] A weak 161-cm^{-1} band and a band at 185 cm^{-1} were reported by Hendra[15] for silica gel. The 440-cm^{-1} broad band is reported by Hass[23] for bulk silica at 410 cm^{-1} due to a bond-rocking motion with the oxygen atoms moving perpendicular to the Si–O–Si planes. This band is reported in the infrared as the strong 443-cm^{-1} band.[24]

The 488-cm^{-1} sharp band, reported by Hass for bulk silica as 496 cm^{-1}, is due to bond stretching of the nonbridging oxygens with the silicon atoms. The 604-cm^{-1} sharp band reported by Hass as the 600-cm^{-1} weak band may correspond to the 568-cm^{-1} broad but weak band in the infrared.

The 802-cm^{-1} band is identified with the 800-cm^{-1} band reported by Hass in the Raman and 814 cm^{-1} observed in the infrared. In some of our Vycor glass samples this band appeared as a doublet at 795 and 814 cm^{-1} and may represent a bulk and surface con-

(19) M. C. Tobin and T. Baak, *J. Opt. Soc. Amer.*, 58, 1459 (1968).
(20) P. Flubacher, A. J. Leadbetter, J. A. Morrison, and B. P. Stoicheff, *J. Phys. Chem. Solids*, 12, 53 (1959).
(21) N. C. Harrand, *C. R. Acad. Sci.*, 287, 784 (1954).
(22) G. B. Wilmont, Thesis, Massachusetts Institute of Technology, Cambridge, Mass., 1954.
(23) M. Hass, *J. Phys. Chem. Solids*, 31, 415 (1970).
(24) M. Miles, *Czech. J. Phys. B*, 18, 354 (1968).

figuration. The 800-cm^{-1} band is interpreted to be a bond bending vibration in which the oxygens move in the silicon–oxygen–silicon planes but at right angles to the silicon–silicon lines.

The 930- and 980-cm^{-1} bands are not reported by other workers in silica or silicate chemistry. The 1056-cm^{-1} band corresponds to the 1065-cm^{-1} band in the spectrum of Hass for solid silica and the strong 1061-cm^{-1} band of Miles in the infrared. The 1184-cm^{-1} band is reported by Hass for silica at 1200 cm^{-1}.

A strongly asymmetric band was observed at 3750 ± 2 cm^{-1} and assigned to the OH stretching vibration.[25] Unlike the corresponding band in the infrared, it is comparatively weak and cannot be resolved into components corresponding to SiOH and BOH. It does not change with adsorption of substances.

Its height increases slightly with a decrease in temperature of dehydration but there is no change in shape as the dehydration is carried out. Attempts to change the spectrum by varying the water treatment (H_2O and D_2O) vapor at 200–400° failed because the background scattering went up markedly. This was presumably due to uncontrolled contamination by organic material. In our spectrometer care had to be exercised in recording the 3750-cm^{-1} line when we used the 4880-cm^{-1} line for Raman excitation because of the presence of a spurious line. This was avoided by using the yellow 5682-Å line for excitation.

An attempt was made to methylate the hydroxyl band at 3752 cm^{-1} by treating it twice with hexamethyldisilazane at 130° for 1 hr and pumping in between at 130°. After final evacuation at 250° the Raman spectrum was taken. The silica lines at 489 and 609 cm^{-1} were found. Surprisingly the 3752-cm^{-1} hydroxyl line did not decrease appreciably in intensity. The dominant Raman lines were the strong 2906-cm^{-1} (polarized) and 2960-cm^{-1} (depolarized) bands due to CH_3 groups. The latter cannot be due to adsorbed hexamethyldisilazane $(CH_3)_3Si\cdot NH\cdot Si(CH_3)$ since the 578-cm^{-1} band whose intensity in the liquid hexamethyldisilazane is one-third of the 2906–2960-cm^{-1} doublet, is not seen in the Raman spectrum of the methylated solid. We must conclude that the hydrophobic action of hexamethyldisilazane is due to the covering with $Si(CH_3)_3$ groups of other than the hydroxyls seen in Raman effect. The spectrum of liquid hexamethyldisilazane has not been reported. It consists of the following bands in cm^{-1} which are all weak unless otherwise indicated as medium (m) or strong (s): 188.4, 2006 m, 273.0, 349.6, 578.6 s, 678, 688 Si–C stretch, 747.6 Si–$(CH_3)_3$, 839 m $Si(CH_3)_3$; 892.4 m SiOH bend; 1261.0 CH_2 rock, 1418.8 C–H bend; 2767; 2906 s CH stretch, 2960 s C–H stretch, 3100; 3389 m SiOH.

Water in Porous Vycor. There has been great interest in the behavior of water near surfaces or in pores because of the significance of such water in biological systems. It is quite possible that all chemical reactions may be affected if the reactants are subjected to strong surface forces undoubtedly present in thin layers or in small pores.[26-28] Nmr measurement carried out in the Princeton University laboratory by one of us in collaboration with Dr. L. Meecham has shown that the behavior of water as revealed by such criteria as line width, relaxation times, and their temperature dependence is different from bulk water for pores of 400 Å and smaller. A remarkably different Raman spectrum for water adsorbed in capillaries was reported by Lippincott, Stromberg, Grant, and Cessac.[26,29] They indicated the absence of bands at 3440 cm^{-1}, characteristic of the OH in ordinary water, and the presence of a strong band at 620 cm^{-1} which they ascribed to a new type of water, "polywater."

In order to see whether water condensed in pores of 40 Å on a clean silica surface showed a Raman spectrum different from that of water in the bulk we condensed water into pores of a cleaned porous Vycor sample rod at different vapor pressures. The Raman spectrum of Vycor glass whose pores were completely filled was found to be identical with that of water in the bulk in the region of 1000–4000 cm^{-1} (Figure 4). The 3440-cm^{-1} bands of water in pores may be slightly broader. This may be due to the pore effect or may be due to the laser beam heating the silica matrix more than liquid water and thereby distorting the 3440-cm^{-1} band. It must be pointed out that this band is composed of a number of peaks that are not resolved and their relative intensity depends on the temperature of the sample. This may account for the change in width of the 3440-cm^{-1} band of water in pores and in bulk.[30]

The 1645-cm^{-1} peak is two orders lower in intensity and is the same in both bulk and water. The silica bands at 482, 606, and 800 cm^{-1} observed in porous Vycor filled with water are within experimental error the same as those obtained with plain porous Vycor glass. It is unfortunate that the intermolecular interaction bands of water are of very low intensity and lie in this region so that they cannot be examined by Raman spectrum—60, 175, 450, and 780 cm^{-1}. Our results would indicate that there is certainly nothing unusual in the intramolecular vibrational spectrum of water in capillaries much smaller than those used by Lippincott, *et al.*, or in the small amount of polywater condensed on the surface of such capillaries after

(25) J. A. Cusumano and M. J. D. Low, *J. Phys. Chem.*, **74**, 1950 (1970).

(26) E. R. Lippincott, R. R. Stromberg, W. H. Grant, and G. L. Cessac, *Science*, **164**, 1482 (1969).

(27) B. V. Deryagin and N. V. Chureev, *Priroda (Moscow)*, **No. 4**, 16 (1968).

(28) D. L. Rousseau and S. P. S. Porto, *Science*, **167**, 1715 (1970).

(29) L. J. Bellamy, A. R. Osborn, E. R. Lippincott, and A. R. Bandy, *Chem. Ind. (London)*, 686 (1969).

(30) G. E. Walrafen, *J. Chem. Phys.*, **47**, 114 (1967).

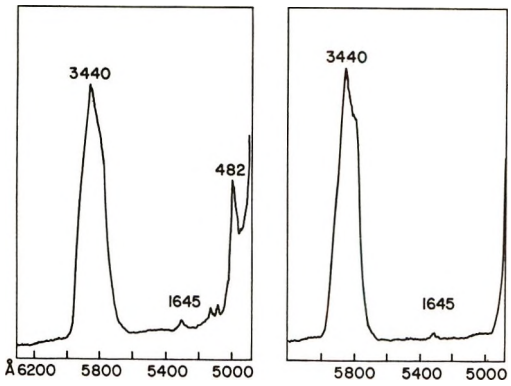

Figure 4. Spectrum of water in porous Vycor (left) and of bulk water (right).

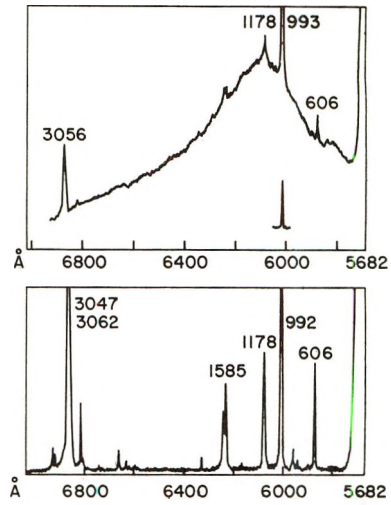

Figure 5. Spectrum of benzene in porous Vycor (upper) and of bulk benzene (lower).

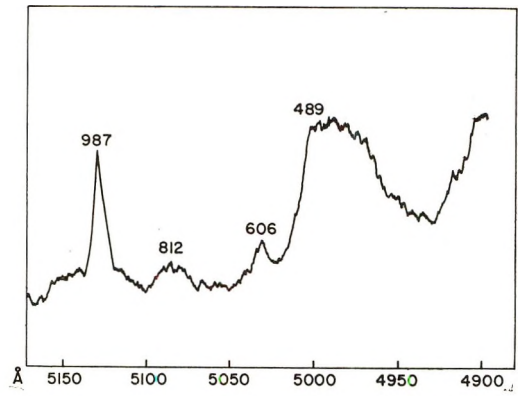

Figure 6. Spectrum of MoO_3 on porous Vycor.

evacuation. However, this does not preclude that low vibrational frequencies of water which characterize intermolecular forces may not be different in water present in capillaries and subject to the influence of surface forces. However, their detection is difficult both owing to interference of silica lines and possible local heating of the sample by the intense laser beam. At low and medium filling of the pores, spectra of poor quality were obtained owing to increase in the Raman background.

Benzene. The spectrum of the cleaned porous Vycor rod treated with 4–80 Torr of benzene at room temperature produced an intense, very broad, and unstructured fluorescence band which could not be removed by evacuation at 25 or 100°. It was concluded that benzene undergoes a polymerization to produce organic residues on the rigorously dehydrated silica surface, particularly when irradiated with a laser beam. The procedure for filling the pores was modified in the following way. After the 600° cleaning process, the sample was evacuated for 30 min and then treated for 2 hr at 650° with hydrogen gas. This has been found to be effective in removing adsorbed oxygen. The sample was then evacuated overnight at 500°, cooled, and filled at 4 Torr with high-purity helium to serve as a better heat-exchange medium. Raman spectra were recorded as benzene was introduced (Figure 5). The following lines were observed for benzene on porous Vycor compared with that of liquid benzene, presented in parentheses: 606 (606) (849) 993 (992 cm^{-1}) 1178 (1178), 1587, 1605 (1585, 1607), 3056 (3047, 3062 cm^{-1}). Thus all the important Raman lines found in bulk benzene were observed in benzene in 40-Å pores with no frequency shift. The Raman forbidden lines observed in infrared at 671, 1037, 1485, and 3099 cm^{-1} were not detected. As is seen in Figure 5, the broad fluorescence band was present. After several hours this broad band increased by an order of magnitude blotting out the benzene lines. The fluorescence band grew more rapidly when the sample was irradiated with the laser beam. Evacuation of the sample, which showed both the benzene lines and the fluorescence lines, removed the former but did not affect the latter.

These results indicate that highly cleaned surfaces are highly reactive to hydrocarbon vapors of such stable substances as benzene and that the fluorescence contaminants can be detected by Raman investigation at very low levels where gravimetric and infrared studies show only reversible surface interactions.[25]

The molybdenum oxide–silica used as an oxidation catalyst was prepared by impregnating a cleaned evacuated rod with a degassed solution of ammonium molybdate (40 g of $(NH_4)_6Mo_7O_{24}\cdot 4H_2O$ in 100 ml of H_2O) to give a coverage of 12% MoO_3.[31,32] The rod was rinsed superficially with water, dried at 120°, and heated in oxygen to 600° to remove ammonia and water. The sample so treated was colorless. The spectrum of the samples so obtained and that of MoO_3 are presented in Figure 6. The MoO_3 on porous Vycor has peaks char-

(31) A. C. A. M. Berijenberg, B. C. Lippens, and G. C. A. Schuit, *J. Catal.*, **4**, 581 (1965).

(32) F. Veatch, J. L. Callahan, S. C. Milberger, and R. W. Forman, *Actes Congr. Int. Catalyse, 2e Paris*, 1960, 2, 26 (1961).

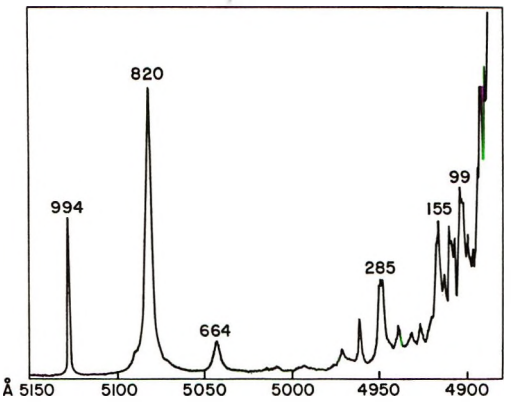

Figure 7. Spectrum of powdered MoO_3.

acteristic of the porous Vycor at 448, 486, and 604 cm^{-1} and the doublet at 795–812 cm^{-1}. A strong asymmetric peak is recorded at 987 cm^{-1} which can be resolved (DuPont Curve Resolver Model 310) into at least two components at 988 and 968 cm^{-1}. These must be related to the 994-cm^{-1} peak (Figure 7) in powdered MoO_3 assigned to the MoO stretching frequency. This indicates that the MoO on the surface on silica must have two very different environments since positions of Raman lines unlike the infrared are not usually sensitive to small variations in molecular environments. It is of interest to note that the strongest line of MoO_3, at 820 cm^{-1}, which is assigned to the Mo–O–Mo deformation frequency is not present in molybdenum oxide on porous Vycor silica. This is taken as evidence that the molybdena is dispersed in an atomic way with no appreciable number of molybdenum oxide clusters present since the shape of the broad silica band in the 900–700-cm^{-1} region of molybdenum oxide on porous Vycor is the same as that of porous Vycor itself.

Heating in hydrogen gas changed the color of the sample to yellow-brown at 400° and black at 500°. After heating for 4 hr at 530° the hydrogen was pumped off. The 4880-Å laser beam penetrated through half the diameter of the rod to give a weak and noisy spectrum. The 987-cm^{-1} band was 20% of its original intensity as compared to the porous Vycor 606-cm^{-1} line taken as an internal standard. No new bands were found. After oxidation at 550° for 4 hr, the original spectrum of MoO_3 on porous Vycor was obtained. Reduction at 370° for 8 hr followed with evacuation for 1 hr at 370° and for 9 hr at 470° was carried out to maximize the production of Mo^{4+}.[33] The rod was brownish black and was completely penetrated by the laser beam. No new bands were found; the band at 987 cm^{-1} was one-third of its original intensity and at same frequency. Thus Raman investigation of molybdenum oxide species under various oxidation–reduction conditions reveals only changes in Mo–O stretching band intensity.

Uranium oxide has also been used as a catalyst.[34] Three samples of 0.4, 2.0, and 10.0 wt % of UO_3 on porous glass were prepared by impregnation with uranyl nitrate solutions and then heated in oxygen at 600°. Their colors were yellow, light orange, and orange-red, respectively. All exciting lines with wavelengths less than 5682 Å gave a strong fluorescence. The red exciting light 6471-Å line was used since it did not excite fluorescence. The 10% sample has several sharp lines in the low-frequency region: 16.7, 21.5, 28.6, 39, 49.3, 55.8, 74.7, 82.0, 94.0, 99.2, 120.6, 125.5, and 191.0 cm^{-1}. These lines were seen at lower intensity on the cleaned Vycor using red-line excitation. It has not been established that these are porous Vycor lines or are due to small traces of uranium impurity in the porous Vycor. Furthermore, the porous Vycor bands above 500 cm^{-1} are reduced in intensity and a broad new band appeared at 689 cm^{-1}. Investigation of 0.4 and 2% samples did not give any new significant information not adduced from the 10% sample.

Europium(III) Y Zeolites. The samples were prepared by exchanging NaY zeolite with Eu(III) nitrate at 25 and 85° to give 12.8% Eu(III) and 14.4% Eu(III), respectively, on a dry basis.[35] Using the 4880-Å blue line both a Raman and a characteristic fluorescence spectrum was obtained. The 6371-Å red line excited the Raman lines only. No difference was observed between the two types of samples. Preliminary measurement for the Raman lines give the following values: 16, 36, 51, 55, 79, 92, 106, 118, 188, and 216 cm^{-1}. Eu_2O_3 powder showed Raman lines at 44, 47, 63, 90, 118, 157, and 335 cm^{-1}. Since the lines are of very low wave numbers, further work with other excitation is necessary to establish their validity as Raman lines. Three bands of the fluorescence spectrum of Eu(III) Y zeolite corresponds to $^5D_0$–$^7F_0$, $^5D_0$–$^7F_1$, and $^5D_0$–$^7F_2$ multiplet transitions.[36] Analysis of the bands with a DuPont Curve Resolver gives the following values for the transitions as shown in Table I. Within the accuracy of measurement and resolution of ±8 cm^{-1} the two samples, prepared at 25 and 85°, show the same fluorescence spectrum.

Platinum on Silica. A 0.2 and 1.0 wt % platinum on porous Vycor was prepared by impregnating porous Vycor with aqueous solutions of $H_2PtCl_2 \cdot 6H_2O$, drying, and heating at 600° in oxygen and then in hydrogen. The more dilute sample was brownish black, the other dark black. The 0.2% sample gave the following lines: 84, 120, 132, 175, 216, and 602 cm^{-1}. Their identification as platinum Raman lines is not complete at present. The dark black rod gave no Raman spectrum.

(33) C. Friedheim and M. F. Hoffmann, *Ber.*, **35**, 792 (1902).
(34) R. K. Grasselli and J. L. Callahan, *J. Catal.*, **14**, 93 (1969).
(35) H. S. Sherry, *J. Colloid Interface Sci.*, **28**, 288 (1968).
(36) G. E. Rindone in "Luminescence of Inorganic Solids," P. G. Goldberg, Ed., Academic Press, New York, N. Y., 1966, p 438.

Table I: Fluorescence Transitions of Eu(III) in Y Zeolite

	25°	85° exchanged
$^5D_0$–$^7F_2$	15,959	15,938 cm^{-1}
	16,032	16,027
	16,132	15,148
	16,255	16,253
	16,318	16,311
$^5D_0$–$^7F_1$	16,813	...
	16,894	16,900
$^5D_0$–$^7F_0$	17,282	17,280

Attempts to obtain a Raman spectrum of 5% Pd/Al_2O_3, 2% Pd on SiO_2, or 5% Pd on C in air or vacuum were unsuccessful. The focused laser beam produced either evaporation or oxidation. The 5% Pd on alumina saturated with hydrogen glowed with decomposition when irradiated with a laser beam line so that an isotherm could not be determined. Aluminum oxide, magnesium oxide, and zeolite powders when examined by the 4880-Å line gave no lines specific for these materials.

Ethylene Adsorption. Ethylene was admitted to cleaned porous Vycor at 23° at pressures of 50, 160, and 500 Torr and the intensity determined compared to that observed for gaseous ethylene at the same pressure in an empty tube. The Raman lines studied were the 1340.3-cm^{-1} C=C symmetrical deformation frequencies, 1619.2-cm^{-1} C=C symmetrical stretching vibration, and the 3014.4-cm C–H vibration. The position of the bands for the liquid are reported 2–5 cm^{-1} higher. An adsorption isotherm was constructed (Figure 8).

Propylene Adsorption. Propylene was adsorbed on cleaned porous Vycor at 22°. Lines were observed at 920, 1297, and 1647 cm^{-1}. These are to be compared with the following wavelengths for liquid propylene, 920, 1297, and 1648 cm^{-1}.[37] The only difference between the spectrum of the adsorbed propylene was the appearance of a broad shoulder at the high-frequency side of the C=C band at 1647 cm^{-1} which appeared at high pressure. The intensity of the Raman lines was an order of magnitude higher when present in the pores of the Vycor than when present at the same pressure in the gas. We can therefore consider the intensity of the Raman lines observed as proportional to the amount adsorbed. The isotherm so constructed is given in Figure 9.

The Raman spectrum of propylene on molybdenum–porous Vycor was examined at −36° in the pressure range up to 760 Torr. However, a decrease in intensity of the band and a development of a fluorescence was observed to take place with time. Dark spots were seen where the laser beam hit the rod. If the sample was moved by a millimeter, the original intensity was again observed with a subsequent decrease in intensity

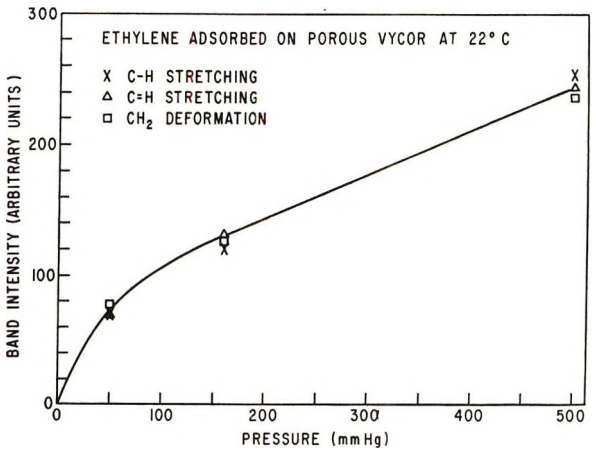

Figure 8. Adsorption isotherm of ethylene on porous Vycor at 22°.

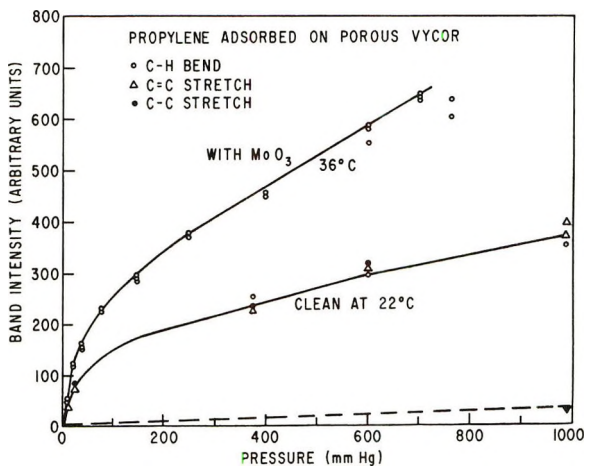

Figure 9. Adsorption isotherm of propylene on porous Vycor at 22° and on porous Vycor covered with MoO_3 at −36°. Dashed line is the Raman line intensity of gaseous ethylene in empty vessel of same size.

and development of fluorescence. This process was so marked at room temperature, independent of the exciting line, that an isotherm could not be determined. The colorless MoO_3 porous Vycor rod became yellow when contacted with propylene for several hours at room temperature. Either the heat generated by the laser beam or a specific photocatalytic process accelerated the surface polymerization of propylene.

The isotherm at −36° of propylene on molybdenum Vycor glass is presented in Figure 9, using the intensity of the 1297-cm^{-1} line. The 1647-cm^{-1} line showed the same behavior. Intercomparison of intensities is made difficult by variation of focusing of the laser beam on a solid sample.

Introduction of 40 Torr of oxygen into 60 Torr of propylene at room temperature did not slow down the surface contamination. The dark spots on the sample could be clearly recognized as dark blue and after 30

(37) R. Anantha Krishnan, *Proc. Ind. Acad. Sci.*, 3A, 527 (1936).

min the whole rod turned light blue. Without the radiation the system of propylene–oxygen turned the colorless molybdenum oxide–porous Vycor rod blue within a day. (Without oxygen it turned lightly yellow within the same time.) The colloidal "molybdenum blue" containing Mo(VI) and Mo(V) has probably been formed.

Adsorption of Carbon Monoxide on Pt on Porous Vycor. The 0.2 wt % platinum on porous Vycor was exposed to 13, 51, and 406 Torr of carbon monoxide at room temperature. The 2145-cm^{-1} band of CO was observed in the gas-phase part of the sample tube but no adsorbed CO was detected in the catalyst. Treatment at 250° for 2 days at 406° did not bring about a change in the spectrum. The platinum carbon monoxide band had been found at 478–480 cm^{-1} in the infrared spectrum of carbon monoxide adsorbed on platinum-containing catalysts. This is not the best of regions to examine by Raman because of the presence of the silicon–oxygen band from the porous Vycor glass.[38]

Acknowledgment. We wish to express our appreciation to Professor T. Spiro for the use of the Raman equipment and his helpful advice and that of his research group.

(38) While the manuscript was in the editorial offices of the journals, a publication by T. A. Egerton, A. H. Hardin, Y. Kayirovski, and N. Sheppard (*Chem. Commun.*, 887 (1971)), appeared in which the same oxygen treatment was proposed that we have used in our work. We would like to reemphasize the need not only to heat the sample in oxygen but also to avoid use of any stopcock grease in the system.

Mass Spectrometric Determination of the Bond Dissociation Energies of the Molecules CePd and CeC_2[1a]

by D. L. Cocke[1b] and K. A. Gingerich*

Department of Chemistry, Texas A&M University, College Station, Texas 77843 *(Received January 18, 1972)*

Publication costs assisted by the National Science Foundation and the Robert A. Welch Foundation

The mass spectrometric Knudsen effusion technique has been used to investigate the vapor phase over the Ce–Pd–C system. The new molecule, CePd, has been identified and third-law enthalpies, $\Delta H°_0$, of the reactions: (1) CePd(g) = Ce(g) + Pd(g), (2) CePd(g) + C_2(g) = CeC_2(g) + Pd(g), and (3) Ce(g) + 2C(graph) = CeC_2(g), have been evaluated as +76.8 ± 0.8, −78.0 ± 0.1 and +39.9 ± 1.9 kcal, respectively. The second-law value of $\Delta H°_0$, corresponding to reaction 1 is 74.0 ± 2.9 kcal and to reaction 3 is 41.9 ± 7.4 kcal. The dissociation energy, $D°_0$, of the molecule CePd has been obtained as 76.1 ± 4 kcal mol^{-1} and its heat of formation, $\Delta H_f°_{298}$ derived as 114 ± 5 kcal mol^{-1}. The dissociation energy of the CePd molecule is discussed in terms of the Pauling model of a polar bond and the Brewer–Engel theory.

Introduction

Studies concerning gaseous molecular species containing only metals have recently been reviewed.[2,3] The Pauling model of a polar bond[4] has been used to interpret the bonding for many gaseous diatomic intermetallic molecules where single bonding was assumed to occur.[3a,5-7]

The Brewer–Engel metallic theory[8,9] which has had success in predicting the structure and stability of metals and alloys, has recently been extended to the gas phase.[10,11] Intermetallic diatomic molecules between transition metals from the left side of the periodic table and platinum group metals are predicted to have unusually high bond energies due to multiple bonding involving d orbitals. The bond energies should therefore be larger than those calculated from the Pauling model of a polar bond where single bonding is assumed.

(1) (a) Work performed as part of the Ph.D. degree requirement by D. L. Cocke; (b) Phillips Petroleum Co. Fellow.

(2) B. Siegel, *Quart. Rev. Chem. Soc.*, 19, 77 (1965).

(3) (a) J. Drowart in "Phase Stability in Metals and Alloys," P. S. Rudman, J. Stringer, and R. I. Jaffee, Ed., McGraw-Hill, New York, N. Y., 1967, pp 305–317; (b) K. A. Gingerich, *J. Cryst. Growth*, 9, 31 (1971).

(4) L. Pauling, "The Nature of the Chemical Bond," 3rd ed, Cornell University Press, Ithaca, N. Y., 1960.

(5) M. Ackerman, F. E. Stafford, and G. Verhaegen, *J. Chem. Phys.*, 36, 1560 (1962).

(6) K. A. Gingerich and H. C. Finkbeiner, *ibid.*, 52, 2956 (1970).

(7) D. L. Cocke and K. A. Gingerich, *J. Phys. Chem.*, 75, 3264 (1971).

(8) L. Brewer, *Science*, 161, 115 (1968).

The present investigation of the dissociation energy of the CePd molecule allows the extension of the Brewer–Engel metallic theory to the gas phase to be tested.

Experimental Section

The high temperature mass spectrometer and procedure has been described elsewhere.[12] Palladium and cerium metals in atomic ratio 2.5:1 and an excess of graphite powder were contained in a graphite-lined tantalum Knudsen cell. The metals were physically separated by a carbon barrier about 1 mm in thickness fitted into the chamber of the graphite liner.

Temperatures were measured with a calibrated Leeds and Northrup optical pyrometer by sighting on a cylindrical cavity in the bottom of the Knudsen cell. The effective emissivity of this cavity was estimated as 0.97 as described by Williams.[13] Measured temperatures were also corrected for the interposed viewing window and deflecting prism.

Pertinent ions observed were Ce^+, Pd^+, $CePd^+$, CeC_2^+, C_1^+, and C_2^+. All ions were produced with ionizing electron energies and emission currents of 16 eV and 1 mA, respectively. An acceleration voltage of 4.5 kV was used along with a voltage at the entrance of the shield of the electron multiplier of 1.9 kV. The ions were identified by their mass to charge ratio, shutter effect, ionization efficiency curves, and isotopic distribution. Appearance potentials of all ions were determined by the linear extrapolation method using the value for silver, 7.57 eV, as a standard,[14] and are given in Table I. The appearance potentials are taken as evidence that all ions were formed by direct ionization of the corresponding neutral atoms or molecules and not by fragmentation.

Table I: Experimental and Estimated Parameters[a]

Ion	Appearance potential, eV	Relative ionization cross sections σ_i, Å²	Relative multiplier gains γ_i/γ_{Ag}	Intensity correction factor E_i	Calibration constant k_i, atm/A °K
Ag	7.57[b]	5.44[c]	1.00	1.00	0.36
Ag_2	7.4 ± 0.8	8.16	0.90	1.00	0.27
Pd	8.0 ± 0.4	6.55[c]	0.83	1.00	0.36
Ce	5.7 ± 0.3	11.70[c]	1.13	1.00	0.15
CePd	6.2 ± 0.5	13.69	1.13	1.00	0.13
CeC_2	5.6 ± 0.4	11.37	1.13	1.00	0.15
C_1	10.5 ± 1.0	1.73[b]	1.5	1.00	0.75
C_2	11.1 ± 1.0	2.595	1.8	1.27	0.54

[a] See text for details. [b] Reference 14. [c] Reference 17.

Pressure calibration was obtained by evaluation of the equilibrium $Ag_2(g) = 2Ag(g)$ over the temperature range 1294 to 1577 K after the method described by Grimley.[15] In this method, the k_{Ag} value is obtained from ion intensities and the dissociation energy of the dimer by the relation

$$k_{Ag} = \frac{\sigma_{Ag}\gamma_{Ag}}{\sigma_{Ag_2}\gamma_{Ag_2}} \frac{I_{Ag_2}+E_{Ag_2}n_{Ag}}{(I_{Ag}+E_{Ag}n_{Ag_2})^2 T} \times \text{antilog}\left\{\frac{-D^\circ_0 - T\Delta[(G^\circ_T - H^\circ_0)/T]}{2.303RT}\right\} \quad (1)$$

The general meaning of the terms in eq 1 are discussed below. Using a dissociation energy, D°_0, for Ag_2 of 38.0 kcal mol^{-1},[3b] k_{Ag} was obtained as 0.36 atm/A K. The k_i values for species i are given in Table I. They were calculated by the relation $k_i = k_{Ag}\sigma_{Ag}\gamma_{Ag}E_i/\sigma_i\gamma_i$. Here, σ_i is the relative maximum ionization cross section, γ_i is the relative multiplier gain, and k_i is the pressure calibration constant. E_i, which is given in Table I, is an empirical factor needed to correct the measured ion intensities to maximum ionization efficiency.

The reliability of this calibration procedure is indicated by evaluation of data taken on the carbon species C_1 and C_2 at the highest temperature, 2336 K, attained in this study. As seen in Table I, the pressure constant, k_{C_1} obtained using k_{Ag} = 0.36 atm/A K is given as 0.75 atm/A K. The k_{C_1} value obtained from the equilibrium $C_2(g) = 2C(g)$ at 2336 K is 0.47 atm/A K when using $D^\circ_0(C_2)$ = 142 ± 3 kcal mol^{-1}.[16] This value compares well with that from the silver calibration considering the uncertainty in the fragment contribution to the C_2^+ ion intensity. The calibration constant k_{C_1} obtained from the ion intensity of C_1^+ and the known carbon monomer vapor pressure[16] at 2336 K is 0.71 atm/A K. The calibration constants k_{C_1} calculated by this method is in reasonable agreement with that from the silver calibration. This indicates that the carbon is at unit activity and can be used as such in the formulation of reactions.

Absolute pressures, P_i, were obtained from the measured ion currents, I_i, for each species, i, by the relation $P_i = k_i I_i T_i$ where T_i is the absolute temperature and I_i has been corrected for isotopic fractional abundance.

Atomic ionization cross sections were taken directly from Mann.[17] Molecular ionization cross sections were calculated by multiplying the sum of Mann's atomic cross sections by 0.75.[18] Multiplier gains for

(9) W. Hume-Rothery, *Progr. Met. Sci.*, 13, 229 (1967).
(10) K. A. Gingerich and R. D. Grigsby, *Met. Trans.*, 2, 917 (1971).
(11) K. A. Gingerich, *High Temp. Sci.*, 5, 415 (1971).
(12) K. A. Gingerich, *J. Chem. Phys.*, 49, 14 (1968).
(13) C. S. Williams, *J. Opt. Soc. Amer.*, 51, 564 (1961).
(14) C. E. Moore, *Nat. Bur. Stand. (U. S.), Circ.*, 467, 48, 186 (1958).
(15) R. T. Grimley in "Characterization of High-Temperature Vapors," J. L. Margrave, Ed., Wiley, New York, N. Y., 1967, pp 195–243.
(16) JANAF Thermochemical Tables, Dow Chemical Co., Midland, Mich., 1965.
(17) J. B. Mann, *J. Chem. Phys.*, 46, 1646 (1967).

^{107}Ag, ^{106}Pd, and ^{140}Ce were measured as 1.82×10^5, 1.51×10^5, and 2.05×10^5, respectively. Multiplier gains for Ag_2, CePd, CeC_2, C_2, and C_1 were estimated as $0.9\gamma_{Ag}$, $1.0\gamma_{Ce}$, $1.0\gamma_{Ce}$, $1.8\gamma_{Ag}$, and $1.5\ \gamma_{Ag}$, respectively.

Results and Discussion

For calculation of the thermodynamic properties of the molecule CePd, the following reactions were considered

$$CePd(g) = Ce(g) + Pd(g) \quad (2)$$

$$CePd(g) + Cd(g) = CeC_2(g) + Pd(g) \quad (3)$$

$$Ce(g) + 2C(graph) = CeC_2(g) \quad (4)$$

Third-law enthalpies, $\Delta H°_0$, for reactions 2, 3, and 4 were calculated using the relation

$$\Delta H°_0 = -RT \ln K_p - T\Delta[(G°_T - H°_0)/T] \quad (5)$$

where K_p, R, and $-\Delta[(G°_T - H°_0)/T]$ represent the equilibrium constant, the gas constant, and the change of the free energy function for the corresponding reaction, respectively. The results of these calculations for reactions 2 and 3 are given in Tables II and III, respectively. The second-law enthalpy, $\Delta H°_{2120} = 79.0 \pm 2.9$ kcal, for reaction 2 was obtained using the relation

$$\Delta H°_T = -R\ \mathrm{d} \ln K_p/\mathrm{d}(1/T) \quad (6)$$

and, $\Delta H°_0 = 74.0 \pm 2.9$ kcal was obtained by using an estimated heat content change, $\Delta(H°_T - H°_0) = 5.0$ kcal mol^{-1}. The second-law procedure was not attempted for reaction 3 because of the few data. The second-law plot for reaction 4 is given in Figure 1. The corresponding second-law enthalpy $\Delta H°_{2106}$ was calculated as 37.8 ± 7.4 kcal and $\Delta H°_0 = 41.9 \pm 7.4$ kcal was obtained by using published heat content functions.[16,19,20] Over the temperature range 2010 to 2165 K, large fluctuations in the ion intensities of Ce and CeC_2 indicated condensed phase reactions were occurring. All data taken while the condensed phase reactions were in evidence were considered unreliable and were dropped from consideration.

Free energy functions, $-(G°_T - H°_0)/T$, used in the third-law treatments for reactions 2 and 3 were taken from the literature where available or calculated by means of statistical thermodynamics, using the rigid-rotator, harmonic oscillator approximation, from known or estimated molecular parameters. For Ce, Pd, and Ag, the necessary free energy functions were taken from Hultgren, *et al.*[19] For Ag_2, the free energy functions were calculated from molecular parameters given by Cheetham and Barrow.[21] The free energy functions for CePd were calculated from the following estimated molecular parameters: $r_e = 2.65$ Å and $\omega_e = 240.0$ cm^{-1}. Here, r_e was obtained by the sum of the Pauling metallic radii[4] for the atoms, and was subsequently corrected in proportion to the spectroscopically observed bond shortening in AlAu.[21] The vibrational frequency, ω_e, was calculated by use of the Guggenheimer relation[22] taking the z values as 4 and 6 for Ce and Pd, respectively. An electronic contribution to the free energy function for CePd was taken as 3 cal mol^{-1} K^{-1}.

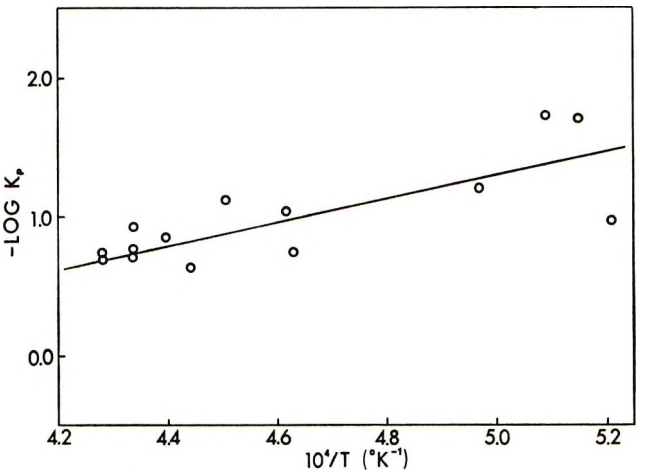

Figure 1. Second-law plot for the reaction Ce(g) + 2C(graph) = CeC_2(g).

Numerical values for the free energy functions of CePd are given in Table IV. The free energy functions for CeC_2 were taken from Balducci, *et al.*,[20] and for C_1 and C_2 were taken from JANAF Tables.[16]

For the average third-law enthalpies, $\Delta H°_0$, of reactions 2 and 3, the uncertainties given in Tables II and III are standard deviations. The estimated errors in the intensities, temperature measurements, the free energy functions, the relative multiplier gains, and the relative maximum ionization cross sections have been included in error limits on all final values derived from the third law. For all final values derived from the second law, the uncertainties in the temperature and intensities have been included in their error estimates.

The average third-law enthalpy, $\Delta H°_0$, for reaction 2 with overall uncertainties considered is 76.8 ± 4 kcal mol^{-1}, which also represents the dissociation energy, $D°_0$, for CePd. The second-law enthalpy for reaction 2 gives a dissociation energy $D°_0$ for CePd of 74.0 ± 6 kcal mol^{-1}. Giving more weight to the third-law enthalpy value for reaction 2, a final selected value of

(18) J. Drowart and P. Goldfinger, *Angew. Chem.*, **79**, 589 (1967); *Angew. Chem. Int. Ed. Engl.*, **6**, 581 (1967).

(19) R. Hultgren, R. L. Orr, and K. K. Kelly, "Supplement to Selected Values of Thermodynamic Properties of Metals and Alloys," University of California, Berkeley, Calif., Silver (1968), Palladium (1968), and Cerium (1967).

(20) G. Balducci, A. Capalbi, G. DeMaria, and M. Guido, *J. Chem. Phys.*, **50**, 1969 (1969).

(21) C. J. Cheetham and R. F. Barrow in "Advances in High Temperature Chemistry," Vol. I, L. Eyring, Ed., Academic Press, New York, N. Y., 1967, pp 7–41.

(22) K. M. Guggenheimer, *Proc. Phys. Soc.*, **58**, 456 (1946).

Table II: Third-Law Enthalpies for the Reaction CePd(g) = Ce(g) + Pd(g)

T, °K	Ion currents, A[a,b] $I(Ce^+)$	$I(Pd^+)$	$I(CePd^+)$	$-\log K_p$	$-\Delta[(G°_T - H°_0)/T]$, cal K^{-1}	$\Delta H°_0$, kcal
1940	5.55×10^{-11}	2.77×10^{-9}	5.02×10^{-13}	3.599	22.59	75.8
2208	2.64×10^{-10}	1.34×10^{-7}	1.20×10^{-11}	2.560	23.24	77.2
1964	1.03×10^{-10}	3.77×10^{-9}	1.11×10^{-12}	3.536	22.65	76.3
2010	7.08×10^{-11}	6.84×10^{-9}	9.22×10^{-13}	3.349	22.76	76.6
2165	3.89×10^{-9}	6.92×10^{-9}	9.75×10^{-12}	2.596	23.14	75.8
2219	3.02×10^{-9}	6.33×10^{-9}	6.78×10^{-12}	2.577	23.26	77.8
2251	4.68×10^{-9}	1.14×10^{-8}	1.29×10^{-11}	2.404	23.34	77.3
2336	2.24×10^{-9}	4.79×10^{-9}	1.37×10^{-12}	4.111	23.54	77.5
						Av 76.8 ± 0.8

[a] Ion intensities corrected for isotopic distribution. [b] $P_i = 0.361 I_i T_i \sigma_{Ag} \gamma_{Ag} / \sigma_i \gamma_i$ (in atm).

Table III: Third-Law Enthalpies for the Reaction CePd(g) + C_2(g) = CeC_2(g) + Pd(g)

T, °K	Ion currents, A[a,b] $I(CePd^+)$	$I(C_2^+)$	$I(CeC_2^+)$	$I(Pd^+)$	$\log K_p$	$\Delta[(G°_T - H°_0)/T]$, cal K^{-1}	$\Delta H°_0$, kcal
2251	1.29×10^{-11}	6.96×10^{-13}	6.82×10^{-10}	1.14×10^{-8}	5.846	7.95	−78.1
2336	1.37×10^{-12}	2.79×10^{-12}	3.00×10^{-10}	4.79×10^{-9}	5.484	7.82	−77.9
						Av	-78.0 ± 0.1

[a] Ion intensities corrected for isotopic distribution. [b] $P_i = 0.361 I_i T_i \sigma_{Ag} \gamma_{Ag} E_i / \sigma_i \gamma_i$ (in atm).

Table IV: Free Energy Functions $-(G°_T - H°_0)/T$ in cal mol^{-1} K^{-1} for CePd(g)

T, °K	$-(G°_T - H°_0)/T$, cal mol^{-1} K^{-1}
298	58.20
1800	73.42
1900	73.89
2000	74.34
2100	74.77
2200	75.18
2300	75.57
2400	75.95
2500	76.30

76.1 ± 4 kcal mol^{-1} or 318 ± 17 kJ mol^{-1} is taken for the dissociation energy, $D°_0$, of CePd.

Although reaction 3 was not considered in arriving at the final selected value for the dissociation energy of CePd, the reasons for which are discussed below, it is included as support for the high value of $D°_0$(CePd) obtained. The third-law value, $\Delta H°_0$, obtained for reaction 3 with all uncertainties included is −78.0 ± 6 kcal. To obtain the dissociation energy for CePd, from reaction 3, it is necessary to consider reaction 4. The appropriate combination of the standard enthalpy of formation for C_2(g), $\Delta H_f°_0 = 197 \pm 2$ kcal mol^{-1},[16] gives the following reaction

$$CeC_2(g) = Ce(g) + C_2(g) \qquad (7)$$

which can be used in conjunction with reaction 3 to yield the dissociation energy, $D°_0$, of CePd. Reaction 4 and consequently reaction 7, have been studied by Balducci, *et al.*,[20] who found the enthalpy, $\Delta H°_0$, for reaction 4 as 34.7 ± 1.1 kcal and for reaction 7 the $\Delta H°_0 = D°_0(Ce–C_2)$ value of 162 ± 2 kcal mol^{-1}. Combining the latter value with the third-law enthalpy, $\Delta H°_0$, for reaction 3 yields a dissociation energy $D°_0$(CePd) = 84.0 ± 8 kcal mol^{-1}. This value is seen to be rather high and prompted the evaluation of data taken in the present study on reaction 4. For 15 data points over the temperature range 1918 to 2336 K, the average third-law enthalpy $\Delta H°_0$ was obtained as 39.9 ± 1.9 kcal where the error is the standard deviation. Including all uncertainties, a value of 39.9 ± 5 kcal is obtained. The corresponding second-law enthalpy $\Delta H°_0$ was obtained as 41.9 ± 7.4 kcal where the error is the standard deviation. Owing to the large standard deviation in the second-law enthalpy, which is due to random error, especially of the end points of the plot of log K_p *vs.* $1/T$, the second-law value is considered less accurate than the third-law enthalpy. Combination of the third-law enthalpy obtained in this investigation, $\Delta H°_0$, for reaction 4, with the standard heat for formation of C_2(g),[16] yields a dissociation energy, $D°_0$, for the Ce–C_2 bond of 157 ± 5 kcal mol^{-1} which is lower than, but still in fair agreement with, the 162 ± 2 kcal mol^{-1} obtained by Balducci, *et al.*[20] However, the value obtained in this investigation lies between the value given by Balducci, *et al*,[20] and the value of 146 kcal mol^{-1} obtained by using the $\Delta H°_0 =$

51 kcal mol^{-1} given by Winchell and Baldwin[23] for reaction 4 and here, corrected from 2000 K.

Combining the third-law enthalpy $\Delta H°_0 = -78.0 \pm 5$ kcal for reaction 3 with the dissociation energy, $D°_0 = 157 \pm 5$ kcal mol^{-1}, for Ce–C_2 yields a dissociation energy, $D°_0$, for CePd as 79.0 ± 7 kcal mol^{-1}. This value is in agreement with that obtained from reaction 2 considering the uncertainty in the fragmentation contribution to the carbon dimer.

From the dissociation energy $D°_{298}$(CePd) = 76.8 ± 4 kcal mol^{-1} or 321 ± 17 kJ mol^{-1} and the standard heats of sublimation of cerium,[8] $\Delta H_v°_{298} = 101 \pm 3$ kcal mol^{-1} and palladium,[8] $\Delta H_v°_{298} = 90.0 \pm 0.5$ kcal mol^{-1}, the standard heat of formation $\Delta H_f°_{298}$(CePd) was obtained as 114 ± 5 kcal mol^{-1} or 477 ± 21 kJ mol^{-1}.

The high dissociation energy $D°_0$(CePd) = 76.1 ± 4 kcal mol^{-1} lends support to the extension of the Brewer–Engel theory to the gas phase. This is illustrated by applying the Pauling model of a polar bond[4] to interpret the bonding in CePd. Application of the Pauling model is possible since the dissociation energies, $D°_0$, of the homonuclear diatomic molecules Ce_2 and Pd_2 are known as 57 ± 4 and 25 ± 5 kcal mol^{-1}, respectively.[3] The arithmetic mean version of the Pauling model, which has worked well for interpreting the high stability of many diatomic intermetallic molecules[3,6] is given by

$$D(AB) = 1/2[D(AA) + D(BB)] + 23(\chi_A - \chi_B)^2$$

Here, the first term represents the covalent contribution to the bond energy D(AB), of the heteronuclear diatomic molecule AB. The second term is the ionic contribution to the bonding and involves the difference of the electronegativities χ_A and χ_B. Taking the electronegativities χ(Ce) = 1.3[6] and χ(Pd)[4] = 2.2 and the dissociation energies of Ce_2 and Pd_2 given above, a value for $D°_0$(CePd) = 59.6 kcal mol^{-1} is calculated. Single bonding is necessarily implied in using the Pauling model; however, the 16 kcal higher dissociation energy, $D°_0$, for CePd found in this study than calculated after the Pauling model suggests multiple bonding involving d orbitals. This is as predicted by the extension of the Brewer–Engel theory to the gas phase.

Acknowledgment. The authors are appreciative of the support given this work by the National Science Foundation under Grant GP-28937 and the Robert A. Welch Foundation under Grant A-387.

(23) P. Winchell and N. L. Baldwin, *J. Phys. Chem.*, **71**, 4476 (1967).

Gaseous Phosphorus Compounds. VIII. Thermodynamic Study of Antimony Monophosphide with a Mass Spectrometer

by J. Kordis and K. A. Gingerich*

Department of Chemistry, Texas A&M University, College Station, Texas 77843 *(Received January 19, 1972)*

Publication costs assisted by The Robert A. Welch Foundation

This article describes the measurement of the dissociation energy of the molecule SbP in the equilibrium vapor above the gadolinium antimonide-molybdenum phosphide-graphite system. The Knudsen cell mass spectrometric method was used for the experiments. From the measured equilibrium $2SbP(g) = P_2(g) + Sb_2(g)$, $\Delta H°_{298} = -(17.6 \pm 0.4)$ kcal and $\Delta S°_{298} = -(3.3_1 \pm 0.27)$ cal K^{-1} were obtained for this reaction. In combination with literature data, the following thermodynamic properties for the SbP molecule have been derived: $D°_0$(SbP(g)) = 84.5 ± 1.0 kcal mol^{-1} or $D°_{298}$(SbP(g)) = 85.3 ± 1.0 kcal mol^{-1}, $\Delta H_f°_{298}$(SbP(g)) = 57.7_8 ± 0.8 kcal mol^{-1}, and $S°_{298}$(SbP(g)) = 54.8_6 ± 0.14 cal mol^{-1} K^{-1}.

1. Introduction

The gaseous molecule SbP has not to our knowledge been previously identified. We have included the investigation of its thermodynamic properties in our program concerning gaseous phosphorus compounds. We were also interested in a reliable determination of its dissociation energy because we plan to use this molecule as a standard in current investigations of gaseous rare earth pnictides.

The condensed system gadolinium antimonide–

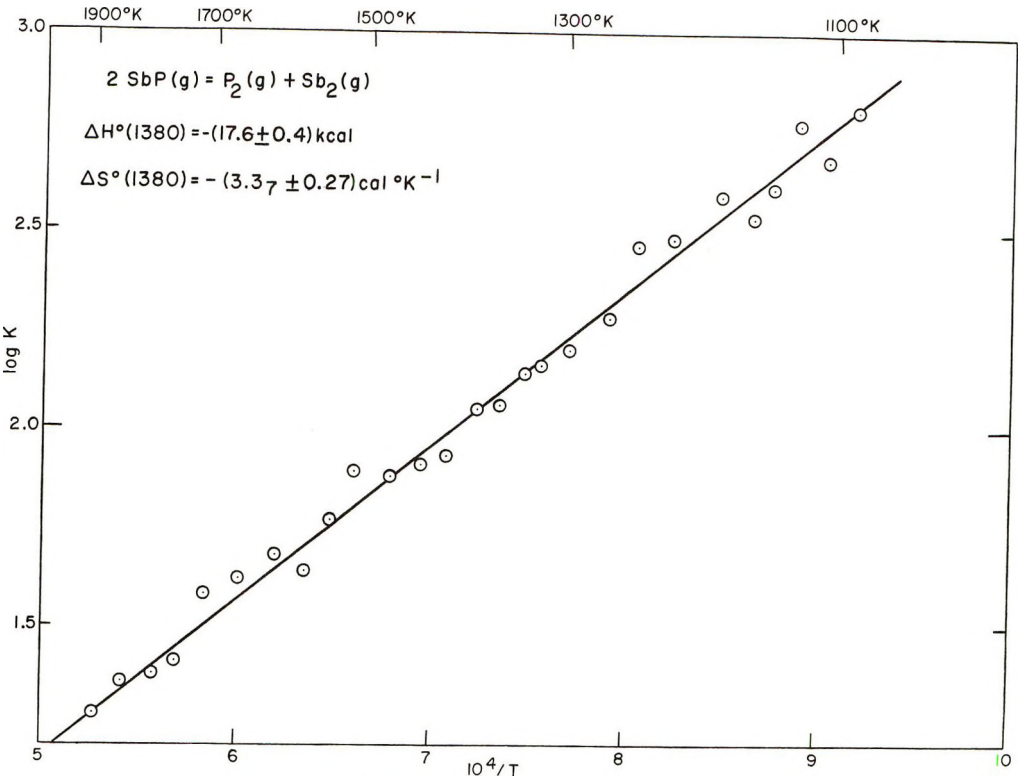

Figure 1. Second-law plot for the reaction $2Sb(g) = P_2(g) + Sb_2(g)$.

molybdenum monophosphide was chosen as a source of gaseous antimony and phosphorus. Under these conditions it could be expected that the activity of the respective group V elements would be sufficiently suppressed for the diatomic molecules Sb_2 and P_2 to be the predominant vapor species. Thus, the investigation of the pressure-independent reaction $2SbP(g) = P_2(g) + Sb_2(g)$ could be carried out without the disturbing effects of fragment contributions from gaseous Sb_4 or P_4 if the latter were to be present in significant concentrations. Furthermore, previous experiments with MoP[1] and PrSb[2] have shown that the activity of the respective group V element decreases further as the decomposition of either of these compounds proceeds toward a more metal-rich phase. Therefore, we could expect that molecular-flow conditions in the Knudsen cell would prevail over an exceptionally large temperature range, a condition favoring reliable determinations of the reaction enthalpies. As a source of antimony, gadolinium antimonide was chosen in preference to praseodymium antimonide in order to obtain preliminary information on its vaporization behavior.

2. Experimental Section

The investigation was carried out with a single-focusing magnetic deflection type of mass spectrometer. A graphite Knudsen cell was charged with a finely ground mixture of graphite, molybdenum phosphide, and gadolinium antimonide. A known small amount of silver was also added for calibration purposes. Temperatures of the Knudsen cell were obtained by sighting a calibrated optical pyrometer into a small blackbody hole at the base of the cell. Experimental window and prism reflector corrections were applied to the temperature measurements. The operating conditions of the mass spectrometer were standardized to 22 eV for the ionization energy, 4.0 kV for the accelerating voltage, and 2.0 mA for the emission current.

The initial heating of the Knudsen cell to above 700° yielded principally Sb_2 in the emanating vapor, followed by Sb and lesser amounts of Sb_4, Sb_3, and Ag. Temperatures above 800° were necessary before measurable intensities of P_2 and SbP were observed. Above 950° SbP_3 was also found, but no Sb_2P_2 or Sb_3P was detected under the restrictions of our experimental conditions. The P_4 molecule was observed as a minor species between 1000 and 1050°. The upper temperature limit for the equilibrium study of the $2SbP(g) = P_2(g) + Sb_2(g)$ reaction was set by the limits of detection of Sb_2 above 1600°. Wherever possible, the intensity measurements for all observed species were obtained. No gaseous compound of gadolinium and antimony was observed at temperatures up to about 2000°, at which point all the antimony had dissipated from the vapor.

Insofar as reactions within the condensed system are concerned, only the most tentative conclusions are possible. The interpretations are largely based on the

(1) K. A. Gingerich, *J. Phys. Chem.*, 68, 2514 (1964).
(2) K. A. Gingerich, *Proc. Conf. Rare Earth Res., 3rd*, 2, 245 (1964).

Table I: Third-Law Enthalpies of Reaction for $2SbP(g) = P_2(g) + Sb_2(g)$ over MoP–GdSb–C(graphite)[a]

T, K	Ion intensities, arbitrary units			$-\Delta G°_T/T$, cal K^{-1}	$\Delta(G°_T - H°_0)/T$, cal K^{-1}	$-\Delta H°_0$, kcal
	$I_{P_2^+}$	I_{SbP^+}	$I_{Sb_2^+}$			
1155	1.50	2.94	1670	11.592	3.339	17.24
1125	0.07	0.15	159	12.654	3.339	18.00
1177	0.525	0.81	414	11.858	3.339	17.89
1264	13.8	16.2	3070	10.429	3.339	17.40
1213	2.60	2.53	631	11.348	3.339	17.81
1089	0.105	0.090	43.1	12.878	3.339	17.66
1106	0.125	0.133	57.1	12.250	3.339	17.24
1142	0.310	0.288	92.3	11.938	3.339	17.44
1241	8.4	5.78	979	11.267	3.339	18.12
1297	44.8	25.9	2000	10.053	3.338	17.36
1338	212	76.0	3180	9.785	3.337	17.55
1322	91.5	19.7	525	9.901	3.337	17.50
1361	275	48.9	850	9.432	3.336	17.38
1383	520	69.5	878	9.365	3.336	17.56
1412	1080	131	1140	8.817	3.335	17.16
1440	584	50.7	304	8.742	3.334	17.39
1474	9.77	1.65	18	8.609	3.333	17.60
1515	10.4	2.00	25.6	8.668	3.332	18.18
1576	18.8	4.40	37.8	7.486	3.331	17.05
1546	11.3	1.34	7.93	8.096	3.331	17.67
1613	42.5	3.37	10.8	7.677	3.329	17.75
1663	116	7.72	18.3	7.426	3.328	17.89
1712	225	9.96	12.67	7.248	3.327	18.10
1758	216	10.3	10.6	6.430	3.326	17.15
1792	216	5.68	3.06	6.327	3.325	17.29
1848	760	10.83	2.99	6.216	3.324	17.63
1898	2010	19.3	3.02	5.872	3.323	17.45

[a] $\Delta H°_0 = -(17.6 \pm 0.3)$ kcal; $\Delta H°_{298} = -(17.5 \pm 0.3)$ kcal.

observed logarithmic variations of the partial pressures of Sb, Sb_2, P_2, and SbP as a function of the reciprocal temperature. It appeared that at the lowest temperature studied the MoP had been already reduced to $MoP_{0.7}$ since the observed P_2 pressures closely correspond to those obtained in an earlier study on the dissociation of the $MoP_{0.7}$ phase to $MoP_{0.7-a}$.[1] It seems also likely that at the same low temperatures GdSb reacted to give a ternary phase, Gd(Sb,P), which, with temperature increase, disproportionated to a more antimony- and phosphorus-deficient composition, $Gd(Sb,P)_{1-x}$. At about 1140° there was an abrupt decrease in the pressures of all the previously mentioned gaseous species, before increasing again with temperature. We attribute the pressure drops at 1140° to the onset of a reaction among $Gd(Sb,P)_{1-x}$, $MoP_{0.7-a}$, and carbon in a manner consistent with the observed reduction of the antimony and phosphorus activities. As a possible example, we present without consideration of stoichiometry, the solid-state reaction $Gd(Sb,P)_{1-x} + MoP_{0.7-a} + C \rightarrow (Gd,Mo)P_{1-y} + (Gd,Mo)Sb_{1-z} + GdC_2$. At about 1625°, there is another sudden drop in the partial pressures of SbP and Sb, leading to a gradual disappearance of these species from the gas phase as the temperature increases still further. For P_2 there is also yet another pressure drop but not till nearly 1790° is reached. From this we draw the general conclusion that GdP is more stable than GdSb, in keeping with the observation that PrP is more stable than PrSb.[2]

3. Results and Discussion

The results of our investigation of the reaction $2SbP(g) = P_2(g) + Sb_2(g)$ are presented in Table I and Figure 1. Equilibrium among the gaseous species in the Knudsen cell is tacitly assumed and is supported by the absence of any hysteresis in the equilibrium constant on thermal cycling at the lower temperatures (see Table I) where nonequilibrium conditions would be more likely to prevail.

The scatter of the points at the lower temperatures, as seen in Figure 1, derives largely from the low intensity of P_2 and, particularly, of the SbP species. Here, an average value for the intensity of SbP was obtained from the intensities of the two SbP isotopic species 152 and 154, after correction for isotopic abundance. In general, however, where intensities were reasonably

high, only the highest intensities of a given molecular species were considered. Another possible source of error prevalent at the more elevated temperatures was the marked decrease in the intensities of some of the species with time in response to corresponding activity changes in the condensed system. The difficulty was met by taking two or three sets of P_2, SbP, and Sb_2 intensities at close time intervals and interpolating the intensities to a convenient arbitrary setting on the recorder charts. Temperature readings were well reproducible and are not expected to have contributed significantly to the scatter in Figure 1.

The intensities as they appear in Figure 1 are uncorrected, save for the isotopic abundances with respect to the two isotopes of antimony, ^{121}Sb and ^{123}Sb. Additionally, corrections for the multiplier gain of secondary electrons and relative electron-impact cross sections need also to be applied. For lack of the necessary information it is generally assumed that in case of pressure-independent reactions these factors, to a first approximation mutually cancel each other.

The data needed for the evaluation of these correction factors in this investigation could be either measured or reliably estimated. The multiplier gains γ_{Ag}, γ_{Sb_2}, and γ_{Sb} were determined by the Faraday-cup positive-charge method, while from a previous investigation on a similar mass spectrometer relative values of γ_{Ag}, γ_{P_2}, and γ_P had been obtained[3] that made it possible to assign appropriate values of γ_{P_2} and γ_P for the present case. The multiplier gain γ_{SbP} was assumed to be the mean of γ_{P_2} and γ_{Sb_2}, and virtually the same value is obtained when it is assumed to be the mean of γ_P and γ_{Sb}. The relative maximum cross sections for singly ionized atomic species were obtained from the table by Mann.[4] For diatomic species, the cross sections are assumed to bear a simple proportionality to the monatomic species. The further assumption is made that the cross section σ_{SbP}, is the mean of the cross sections σ_{P_2} and σ_{Sb_2}. In the present instance of a pressure-independent reaction the aforementioned proportionality factor need not be known as it cancels out in applying it to the equilibrium constant. The maximum cross sections as given by Mann were empirically adjusted by a factor I_{max}/I to correspond to the value at the operating ionization energy of 22 eV. The respective values of I_{max}/I were obtained from our measured ionization efficiency curves. With reference to the ionization efficiency curves, it may be pointed out in an aside that the appearance potential of SbP was determined by the linear extrapolation method to be 9.9 ± 0.3 eV relative to that of silver of 7.57 eV as a standard.[5] The individual correction factors are summarized in Table II. The total corrections to the intensities are then proportional to $(I_{max}/I)/\gamma\sigma$. The full expression for the equilibrium constant for the reaction $2SbP(g) = P_2(g) + Sb_2(g)$ becomes

$$K = \left(\frac{\gamma^2_{SbP^+}}{\gamma_{P_2}\gamma_{Sb_2^+}} \frac{\sigma^2_{SbP}}{\sigma_{P_2}\sigma_{Sb_2}} \frac{(I_{max}/I)_{P_2^+}(I_{max}/I)_{Sb_2^+}}{(I_{max}/I)^2_{SbP^+}}\right) \times \left(\frac{I_{P_2^+}I_{Sb_2^+}}{I^2_{SbP^+}}\right)$$

The correction factor to K in the first set of large parentheses above amounts to about 1.18.

Table II: Measured and Estimated Pressure Correction Factors[a]

Species	Multiplier gain, γ	Rel max cross sections, σ	I_{max}/I
P_2	3.08×10^5	6.20	1.00
SbP	2.46×10^5	8.36	1.03
Sb_2	1.84×10^5	10.41	1.10

[a] See text for details.

The second-law enthalpy and entropy changes for the reaction $2SbP(g) = P_2(g) + Sb_2(g)$ were obtained from the plot of $\log K$ *vs.* $1/T$ according to the relationship $\log K = (-\Delta H^\circ_T/4.576T) + (\Delta S^\circ_T/4.576)$ (Figure 1). At temperature, these values are $\Delta H^\circ_{1380} = -(17.6 \pm 0.4)$ kcal and $\Delta S^\circ_{1380} = -(3.37 \pm 0.27)$ cal K^{-1}. For the evaluation of the third-law enthalpy, the free energy functions $(G^\circ_T - H^\circ_0)/T$ were taken from the literature for P_2[6] and Sb_2.[7] Those for SbP were calculated from estimated molecular parameters using the rigid-rotator harmonic-oscillator approximation. Here the equilibrium separation was estimated as 2.21 Å on the basis of the experimental and estimated triple-bond radii[8] for P and Sb, respectively, and by taking a slightly larger Sb–P distance than would correspond to the sum of the triple-bond radii. This latter correction was done in analogy to the measured r_e value for phosphorus.[9] The vibrational frequency of $\omega_e = 504.9$ cm^{-1} was calculated after Guggenheimer.[10] A $^1\Sigma$ electronic ground state was assumed in analogy to P_2 and Sb_2.[9] The numerical $-(G^\circ_T - H^\circ_0)/T$ values (in cal mol^{-1} K^{-1}) thus obtained are 60.252, 61.775,

(3) K. A. Gingerich, *J. Phys. Chem.*, **73**, 2734 (1969).

(4) J. B. Mann, *J. Chem. Phys.*, **46**, 1646 (1967).

(5) R. W. Kiser, "Introduction to Mass Spectrometry and Its Applications," Prentice-Hall, Englewood Cliffs, N. J., 1965.

(6) "JANAF Thermochemical Tables," Dow Chemical Co., Midland, Mich., 1965.

(7) R. Hultgren, R. L. Orr, and K. K. Kelley, "Supplement to Selected Values of Thermodynamic Properties of Metals and Alloys," Lawrence Radiation Laboratory, University of California, Berkeley, Calif., 1968.

(8) L. Pauling, "The Nature of the Chemical Bond," Cornell University Press, Ithaca, N. Y., 1960.

(9) G. Herzberg, "Spectra of Diatomic Molecules," Van Nostrand, Princeton, N. J., 1950.

(10) K. M. Guggenheimer, *Proc. Phys. Soc.*, **58**, 456 (1946).

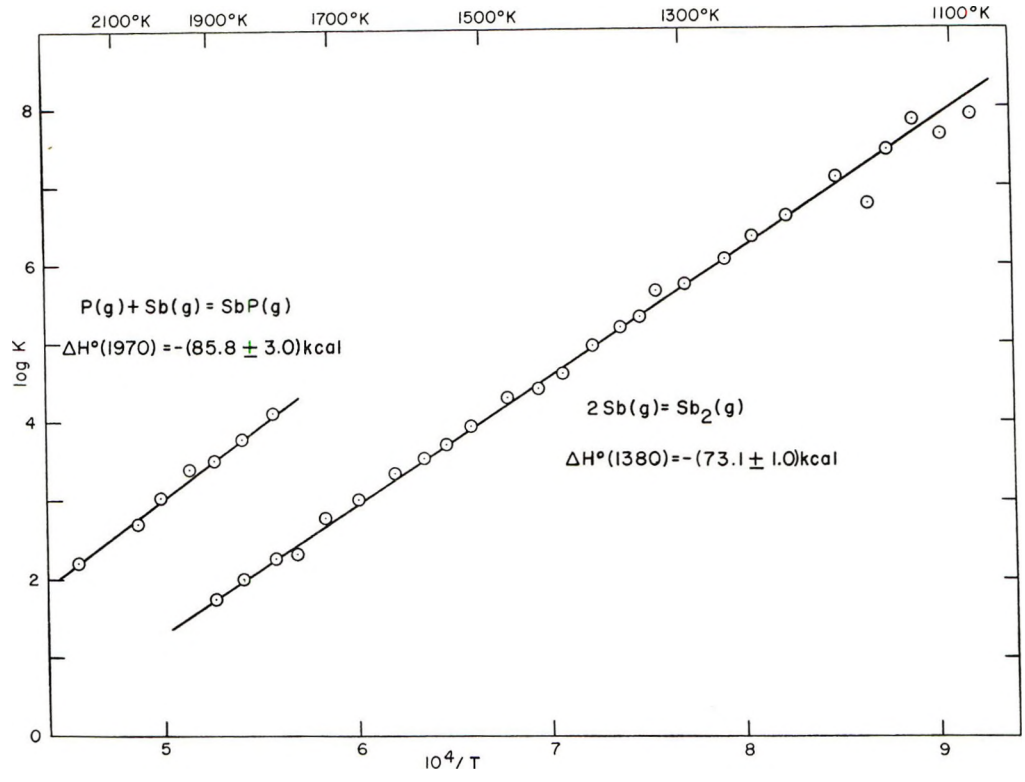

Figure 2. Second-law plots for the reactions $2Sb(g) = Sb_2(g)$ and $P(g) + Sb(g) = SbP(g)$.

63.076, 64.211, 65.217, and 66.122 for 1000, 1200, 1400, 1600, 1800, and 2000 K, respectively.

The changes in the free energy functions are included in Table I, together with $-\Delta G^\circ_T/T = 4.576 \log K$, from which it is then possible to obtain ΔH°_0 according to the relationship

$$\Delta H^\circ_0/T = (\Delta G^\circ_T/T) - [\Delta(G^\circ_T - H^\circ_0)/T]$$

After corrections to the standard temperature of 298 K, the third-law values $\Delta H^\circ_{298} = -(17.5 \pm 0.3)$ kcal and $\Delta S^\circ_{298} = 3.24$ cal K^{-1} compare very favorably with the second-law values $\Delta H^\circ_{298} = -(17.6 \pm 0.4)$ kcal and $\Delta S^\circ_{298} = -(3.30 \pm 0.27)$ cal K^{-1}. The error limits refer to standard deviations only. If no corrections for multiplier gain and electron-impact cross section had been applied to the intensities, the third-law enthalpy change would have been $\Delta H^\circ_{298} = -(17.1 \pm 0.3)$ kcal, and the second-law entropy would have been $\Delta S^\circ_{298} = -(3.62 \pm 0.27)$ cal K^{-1}.

In view of the fact that a theoretical free energy function of SbP had to be employed and some arbitrary, though reasonable, assumptions had to be applied in making corrections to the intensities, we prefer to regard the second-law enthalpy and entropy changes to approach more nearly the true values. We are reinforced in this belief by the large number of measurements (27) taken over a temperature range of 800° and the fact that the very minor temperature dependence of the enthalpy and entropy changes for this reaction could not impart any significant curvature to the second-law plot of $\log K$ *vs.* $1/T$.

For the determination of the atomization energy of SbP, literature values of the atomization energies of P_2, $D^\circ_0(P_2(g)) = 116.1 \pm 0.1$ kcal mol^{-1},[11] and of Sb_2, $D^\circ_0(Sb_2(g)) = 70.6 \pm 1.5)$ kcal mol^{-1},[12] were combined with the presently determined enthalpy changes for the dissociation reaction $2SbP(g) = P_2(g) + Sb_2(g)$. The value obtained for the atomization energy of SbP is $D^\circ_0(SbP(g)) = 84.5 \pm 1.0$ kcal mol^{-1} [353.5 ± 4.2 kJ mol^{-1} (1 cal = 4.184 J)] or $D^\circ_{298}(SbP(g)) = 85.3 \pm 1.0$ kcal mol^{-1} (356.9 ± 4.2 kJ mol^{-1}).

We also did study in the present investigation the equilibrium reaction $2Sb(g) = Sb_2(g)$ over the identical temperature range as the dissociation reaction of SbP. According to the second-law treatment (Figure 2), the enthalpy change for this reaction is $\Delta H^\circ_{1380} = -(73.1 \pm 1.0)$ kcal or $\Delta H^\circ_0 = -(71.4 \pm 1.0)$ kcal, which is in accord with the literature atomization energy of Sb_2 cited above.

In addition, the reaction $P(g) + Sb(g) = SbP(g)$ has also been studied over a narrower temperature range (Figure 2). The reaction enthalpy thus obtained by the second-law method, $\Delta H^\circ_{1970} = -(85.8 \pm 3.0)$ kcal or $\Delta H^\circ_0 = -(83.1 \pm 3.0)$ kcal, agrees well with the

(11) G. Herzberg, *Ann. Phys.*, 15, 677 (1932).

(12) G. DeMaria, J. Drowart, and M. G. Inghram, *J. Chem. Phys.*, 31, 1076 (1959).

selected value above for the atomization energy of SbP.

With recourse to appropriate literature data,[6,7] the molecule SbP was further characterized by the following thermodynamic parameters: $\Delta H_f^\circ{}_{298}(\mathrm{SbP(g)}) = 57.78 \pm 0.8$ kcal mol^{-1} (241.8 ± 3.3 kJ mol^{-1}) or $\Delta H_f^\circ{}_0(\mathrm{SbP(g)}) = 57.83 \pm 0.8$ kcal mol^{-1} (242.0 ± 3.3 kJ mol^{-1}) and $S^\circ{}_{298}(\mathrm{SbP(g)}) = 54.86 \pm 0.14$ cal mol^{-1} K^{-1} (229.5 ± 0.6 J mol^{-1} K^{-1}).[13]

Acknowledgment. We gratefully acknowledge the financial support of The Robert A. Welch Foundation under Grant A-387.

(13) NOTE ADDED IN PROOF. It has come to our attention that an emission spectrum of SbP had been obtained (K. K. Yee and W. E. Jones, *J. Mol. Spectrosc.*, **33**, 119 (1970)). The vibrational constants for $Sb^{121}P$ and $Sb^{123}P$ are 499.9 and 499.1 cm^{-1}, respectively, as compared to our estimate of 504.9 cm^{-1} for SbP. The free energy functions are affected but slightly by this revision and the derived thermodynamic data remain entirely unchanged. For the record, the revised free energy functions, $-(G^\circ_T - H^\circ_0)/T$, are 60.265, 61.790, 63.091, 64.226, 65.223, and 66.138 cal mol^{-1} K^{-1} at 1000, 1200, 1400, 1600, 1800, and 2000K, respectively.

COMMUNICATIONS TO THE EDITOR

Wavelength Dependence of Photobleaching of Trapped Electrons in 3-Methylpentane Glass[1]

Publication costs assisted by the U. S. Atomic Energy Commission

Sir: Early investigation[2] of the quantum yields of photobleaching of trapped electrons produced by γ irradiation of 3-methylpentane (3MP) glass at 77°K indicated initial yields of near unity at 950 nm and *ca.* 0.4 at 1300–1600 nm. A yield "indistinguishable from zero" was reported for measurements using a glow-bar source, said to emit 97% of its radiation at wavelengths greater than 1700 nm, in conjunction with a $^1/_{16}$-in. germanium filter said to transmit beyond 1700 nm. If most of the intensity from the glow-bar–germanium filter combination was actually above the upper limit of the electron absorption spectrum (*ca.* 2200 nm), rather than having the assumed "effective wavelength" of 1900 nm, the zero bleaching yield observed would be misleading.

Since threshold energies[3-5] for photobleaching of trapped electrons give some indication of the trapping energies, we have investigated bleaching from 1300 to 2150 nm in 3MP using a tungsten lamp source with a monochromator with a 100-nm bandwidth at half-height. We find nonzero quantum yields out to 2150 nm, the values at 1800 and 2000 nm being *ca.* 0.7 and 0.2 of the value at 1600 nm (Figure 1). The bleaching rate at 2150 nm was more than five times the minimum detectable rate. No bleaching was detected with the monochromator set at 2300 nm, indicating that none of the bleaching at shorter wavelengths was due to overtones or other impurity wavelengths.

The evidence for zero photobleaching yield[2] in the long wavelength portion of the trapped electron spectrum suggested transitions to bound excited states. However, the data of Figure 1 show that electrons are removed from their traps throughout the absorption spectrum, indicating that the entire spectrum may be the photodetachment continuum for electrons bound in their traps by *ca.* 0.53 eV. The decrease in the quantum yield at long wavelengths may be due to participation of transitions to bound excited states, but alternatively to a high probability for an electron to become retrapped if it is ejected from its trap with little excess energy.

If the trapped electron absorption spectrum is a continuum of direct transitions to unbound states, this can explain why it is so broad and does not change appreciably during thermal decay[6] or photobleaching. The spectrum may also include transitions to localized states which occur near the edges of conduction bands in amorphous solids.[7]

The bleaching experiments were done by observing, with repetitive scanning, the esr signal height from γ-irradiated samples of 3MP in 2-mm i.d. Suprasil tubes while illuminating them in a Varian 4531 esr cavity. A microwave power of 10 μW was used, partially saturating the electron singlet but allowing use of a resistive termination to prevent any dispersive contribution to the signal. Illuminations were started *ca.* 5 min after the end of irradiation and were continued until about one-third of the electrons were bleached.

(1) This work is supported in part by the U. S. Atomic Energy Commission under Contract AT (11-1)-1715 and by the W. F. Vilas Trust of the University of Wisconsin.

(2) D. W. Skelly and W. H. Hamill, *J. Chem. Phys.*, **44**, 2891 (1966).

(3) P. J. Dyne and O. A. Miller, *Can. J. Chem.*, **43**, 2696 (1965).

(4) A. Bernas and D. Grand, *J. Chem. Soc. D*, 1667 (1970).

(5) A. Habersbergerova, Lj. Josimovic, and J. Teply, *Trans. Faraday Soc.*, **66**, 656 (1970).

(6) (a) J. B. Gallivan and W. H. Hamill, *J. Chem. Phys.*, **44**, 1279 (1966); (b) R. A. Fass and J. E. Willard, unpublished results.

(7) M. H. Cohen, *J. Non-Cryst. Solids*, **4**, 391 (1970).

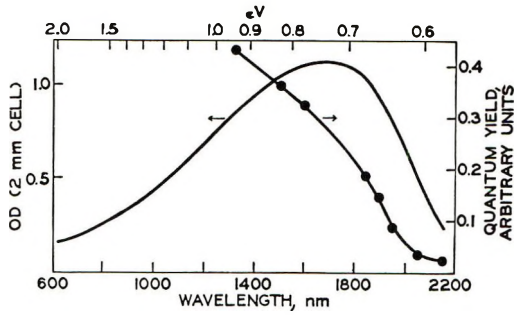

Figure 1. Relative photobleaching quantum yields in 3MP glass, and the absorption spectrum for trapped electrons in 3MP glass; γ dose 2×10^{19} eV g^{-1}. The relative quantum yield scale is set at 0.4 at 1300 nm to be in approximate correspondence with the reported yield[2] at this wavelength.

No thermal decay ($\ll 1\%$ min^{-1}) occurred at the temperature of operation (71 ± 2°K maintained by bubbling helium through the liquid nitrogen coolant). The relative photon intensities at different wavelengths were determined from thermopile measurements of the energy intensities. The fraction of the incident light absorbed at each wavelength was calculated from the absorption spectrum (Figure 1), assuming a 1.4 mm average light path through the cylindrical 2-mm i.d. sample tubes. The relative quantum yields of Figure 1 for $\lambda \geq 1800$ nm would be about 15% higher if corrected for reduction of the light intensity resulting from absorption by the vibrational bands of 3MP. The light source was a small-filament tungsten bulb operating at 15 W. The light was dispersed by the IR No. 2 grating of a Bausch and Lomb high intensity monochromator and passed through two Corning 7-56 filters (opaque for $\lambda < 850$ nm). For bleaching above 1600 nm a Corning 4-76 filter was added to give a combination opaque below 1450 nm. No impurity wavelengths were detectable (*i.e.*, <1%) by scanning the output light with a Cary 14 spectophotometer. γ Irradiations were for 5 min at a dose rate of 4×10^{18} eV g^{-1} min^{-1} under liquid nitrogen at 71 ± 2°K. The 3MP samples were prepared from Phillips pure grade by passage through a 0.5-m column of freshly activated silica gel, collection in a nitrogen atmosphere, bubbling with helium, freeze–pump–thaw degassing, pumping on the liquid, and storage over sodium–potassium alloy.

Acknowledgment. We wish to thank Dr. David Shooter for assistance with the low-power, low-temperature esr operation.

DEPARTMENT OF CHEMISTRY
UNIVERSITY OF WISCONSIN
MADISON, WISCONSIN 53706

JOHN R. MILLER
JOHN E. WILLARD*

RECEIVED FEBRUARY 10, 1972

Journal of Chemical and Engineering Data

JULY 1972, Vol. 17, No. 3

TABLE OF CONTENTS

Reprints from Chemical & Engineering News

On orders of $10 or less please remit check or money order

Keeping broadly informed challenges every person today. If you missed these features from recent issues of C&EN, you can still get copies by filling in the coupon below.

Population

A 2-part feature
David M. Kiefer, C&EN
Oct. 7 & 14, 1968 **75¢**

Mr. Kiefer finds that population is growing unchecked in much of the world, and that U.S. population will expand 50% in the next 30 years or so. Social as well as technological innovation is needed to thwart this advance. **10148**

Computers in Chemical Education

Dr. Frederick D. Tabbutt
Reed College
Portland, Oregon
January 19, 1970 **50¢**

A number of experiments with computers in education have been undertaken in the past few years. Some of the approaches to computer-assisted education now show promise as useful adjuncts as surrogate teachers. **11970**

Arthritis

A 3-part feature
Howard J. Sanders, C&EN
July 22, 29, & Aug. 12, 1968 **75¢**

Causes of arthritis are still a mystery, although more and more evidence points to infection as a possible trigger. Mr. Sanders discusses and examines the possible causes and the past, present, and future of treatment. **07228**

Industrial Research Careers

Howard Reiss
University of California
Los Angeles
June 29, 1970 **50¢**

A major concern of those beginning careers in science is, of course, where to carry out their careers—in a university, private industry, a foundation or wherever. An industrial research career can be a rewarding one, both professionally and financially. **62970**

Public Policy and the Environment

February 9, 1970 **50¢**

Speaking at the 158th ACS National Meeting, Lee DuBridge, Herbert Doan, and Barry Commoner urged cooperation among government, industry, and university in tackling environmental improvement. **02970**

Pollution Control Instrumentation

Michael Heylin, C&EN
February 15, 1971 **50¢**

Efforts to control air and water resources intelligently depends on the ability to detect and to monitor pollutants. The challenge to produce better instrumentation for this purpose is now receiving intense attention from industry and government researchers. **21571**

Allergy

Howard J. Sanders, C&EN
May 11, 1970 **50¢**

Although hay fever, bronchial asthma, and other allergies will not be conquered, they will be better understood and better treated. The expanding study of these diseases in fundamental scientific terms, using the latest research techniques, allergic disorders will yield more and more of their secrets that only a few years ago seemed almost unfathomable. **51170**

Food Additives

Howard J. Sanders, C&EN
October 10, 1966 **75¢**

Makers of food additives are keeping their eyes on the spectacular growth of new foods and the shifting moods of regulation-minded Washington. An array of chemicals enhances the wholesomeness, attractiveness, convenience, and nutritional value of American foods. **10176**

Technology Assessment

David M. Kiefer, C&EN
October 5, 1970 **50¢**

Technology assessment is an attempt—still halting and uncertain—to establish an early-warning system to control, direct, and, if necessary, restrain technological development so as to maximize the public good while minimizing the public risks. **10570**

Chemistry and the Atmosphere

Howard J. Sanders, C&EN
March 28, 1966 **75¢**

The earth's atmosphere is a vast, churning mixture of gases and trace quantities of liquids and solids. Held to the earth by the pull of gravity, it is the transparent envelope without which life on earth would cease to exist. **32866**

Career Opportunities The New Priorities

March 8, 1971 **50¢**

C&EN's annual career guide for chemists and chemical engineers. In the search for new priorities, new opportunities are emerging. Here C&EN looks at three such areas—food, shelter, and health. **03871**

Chaos in Science Teaching

Dr. Conrad E. Ronneberg
Professor Emeritus, Denison University
June 1, 1970 **50¢**

To many people familiar with the stiuation in teaching introductory science courses, both in high school and college, the situation is utter chaos. To place attempts to improve science teaching in proper perspective requires a brief review of the progress of science teaching since World II. **06170**

Artificial Organs

A 2-part feature
Howard J. Sanders, C&EN
April 5 and 12, 1971 **75¢**

The implanting of a total artificial heart in a human has been the most dramatic single advance to date in the field of artificial organs. In recent years, however, many other artificial organs have also been developed, and scientists foresee a vast increase in the number of body parts that, in the years ahead, will be replaceable by mechanical devices. **04571**

Scientific Societies and Public Affairs

K. M. Reese, C&EN
May 3, 1971 **50¢**

Scientific and engineering societies for many years have fostered research, published papers, and sponsored meetings without great regard for the world beyond their particular disciplines. Only in the past decade or so have the learned societies edged into the realm of public affairs. **05371**

1 to 49 copies—single copy price 50 to 299 copies—20% discount

Prices for larger quantities available on request

☐ 10148 ☐ 11970 ☐ 07228

☐ 62970 ☐ 02970 ☐ 51170

☐ 21571 ☐ 10176 ☐ 10570 ☐ 32866

☐ 03871 ☐ 06170 ☐ 04571 ☐ 05371

TO: REPRINT DEPARTMENT

ACS Publications
1155 Sixteenth St., N.W.
Washington, D.C. 20036

FROM:

Name _____

Street _____

City _____

State _____ Zip Code

Amount enclosed $ _____

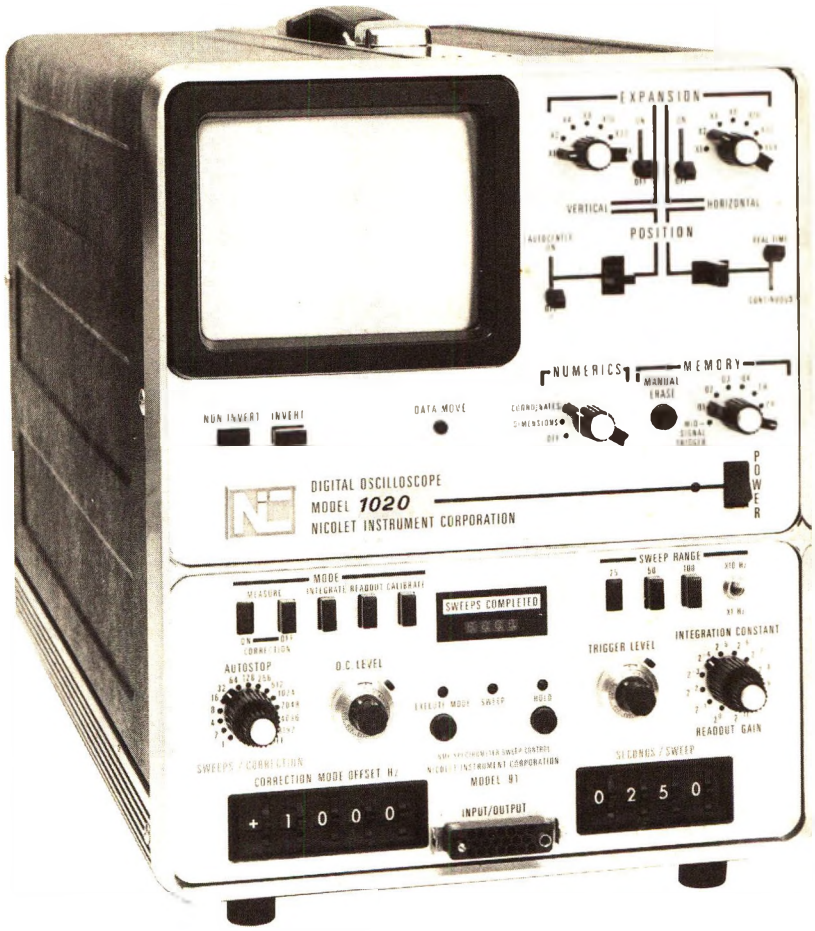

NEW low cost, state-of-the-art time averaging system for any cw nmr spectrometer

The Nicolet 1020 packs all these features into just 1.5 cubic feet of space:

- normalized averaging technique so signal remains constant while noise dimishes
- continuous, flicker-free display independent of sweep rates
- automatic field stabilization to correct for spectrometer drift
- display which can be expanded and shifted up to 64X on both time and intensity axes during measurement or display
- simultaneous analog display and numerical readout of any data point's intensity and address values
- 2048 words (data points) 24-bit memory
- preselectable number of sweeps
- digitally controlled baseline correction
- ability to store and display spectral data and integral data simultaneously
- output signals for X-Y and Y-T plotter
- easy-to-use controls labeled in context with spectrometer
- built-in 5" CRT
- light emitting diode sweep counter
- simple frequency scale calibration mode
- easily adapted for use with epr or other nmr spectrometers
- sweep rates adjustable from 1 second to 2,000 seconds in 1 second increments
- analog-to-digital converter resolution of 12 bits (one part in 4,096)
- PRICE IS ONLY $7,500.

NICOLET INSTRUMENT CORPORATION

5225 Verona Road, Madison, Wisconsin 53711
Phone 608/271-3333 TWX: 910-286-2713

Write or phone for more details or to arrange a demonstration in your laboratory.